Department of Chemical Engineering and Biotechnology

University of Cambridge

Miniaturisation of pH Holographic Sensors for Nano-Bioreactors

Leon CHAN Cong Zhi

- Churchill College -

Apr 2017

This dissertation is submitted for the degree of

Doctor of Philosophy

Name: Leon CHAN Cong Zhi

Dissertation Title: Miniaturisation of pH Holographic Sensors for Nano-Bioreactors

Abstract

Monitoring and controlling pH is of utmost importance in bioprocessing as it directly affects product yield and quality. Multiplexed experiments can be performed in nanobioreactors for optimisation of yield and cell heterogeneity in a relatively quick and inexpensive manner. In this thesis, a pH holographic sensor (holosensor) is miniaturised to 3.11 nL in volume and integrated into a PDMS-glass microfluidic chip for monitoring the growth of *Lactobacillus casei* Shirota. Although other established methods for monitoring cell cultures can be utilised, miniaturised holosensors enable real-time and non-consumptive monitoring of the bacterial cell culture growth medium.

The 2-hydroxyethylmethacrylate (HEMA)-co-2-(trifluoromethyl) propenoic acid (TFMPA) holosensor was fabricated using an adapted technique from photolithography, coupled with the use of a polymerisation inhibitor to control the gel polymerisation with diameters not exceeding a standard deviation of 0.067. The hologram brightness was optimised to 1.05 ms integration time with 36X magnification using a low power (0.290 mW) 532 nm green continuous wave (CW) laser with a devised beam-offset technique.

The holosensor was characterised with ionic strength balanced (9.50 mS/cm) McIlvaine pH buffers and a calibration curve plotted together with measured ionic strength, optical density at 600 nm (OD_{600}) and pH. Correspondingly, RGB-xyY transformed values were plotted in the CIE 1931 chromaticity diagram.

Later, a miniaturised 0.4ϕ HEMA-co-TFMPA holosensor and array was also demonstrated. Together with the 3.0ϕ holosensor, an accuracy parameter for the 0.4ϕ spot and array holosensors were calculated to be 99.08%, 99.38% and 97.77% respectively. Further work involved studying the issues associated with fabricating gels with unusually flat gel profiles.

Other preliminary results suggested the alternative of utilising polymers as a holosensor substrate, together with a dye-free method for hologram fabrication, outlined the prospective possibility of a miniaturised holosensor integrated into a polymer microfluidic chip with the flexibility of hologram colour customisation for cell culture monitoring.

Declaration

I hereby declare that this thesis is the result of my own work and contains no material, to the best of my knowledge and belief, previously published or written by another person, or is the outcome of work done in collaboration except where specifically indicated in the text. I further state that no substantial part of my dissertation has not been previously or concurrently for the award of any degree, diploma or its equivalent to any other University or Institution except where due acknowledgement has been made in the text.

This thesis comprises 256 pages (including front matter) that includes 129 figures, 5 tables, and around 65,000 words.

Acknowledgements

I would like to express my most heartfelt appreciation and gratitude to Emeritus Professor Christopher Lowe, who literally came to another side of the world in Singapore just to help me out with his invaluable advice and encouragement. Thank you for your continual guidance and belief in me to accomplish my work. I am also grateful to Dr Wang Zhiping for his support in helping me set up my lab in the cleanroom, providing me with the needed resources for my experiments, and dispensing advice during regular meetings in the office.

*I thank the A*STAR Graduate Academy (A*GA) for providing me the sponsorship to study in University of Cambridge, as well as the unwavering administrative support from Siti throughout my PhD.*

My journey down the rabbit hole of holography was insightful with the help, advice and friendship from our lab's walking encyclopaedia, Dr Colin Davidson, as well as Dr Jeff Blyth, whose enthusiasm in holography is especially infectious. Thank you for continually spurring my interest in holography.

I would never forget the hospitality and friendship I got from Jacky (Dr) since the first day in the lab. I am thankful for my friendship with my other lab mates: Jenny (Dr), Nan (Dr), Chen (Dr), Kheng (Dr) and Xu, and Ali (Dr) for his funny antics and random questions. I especially thank Gita (Dr) for her help in providing me with her MATLAB® RGB conversion programme.

I would also like to acknowledge the technical and administrative staff of IoB, especially Debby, Alan, Joe, Christine and Sue, as well as Chloe, Lyn, Laura, Hollie and Sophia, who are just a joy to talk to and so helpful when I approach for help. I will always remember Robin, who perks me up with his jokes and gives helpful advice with regard to IT and life in general. There is also Rebecca (Churchill College) who helps me in any way she can whenever I needed assistance, and never fails to wish me happy birthday before the year-end holiday break.

I am grateful for the help and assistance given to me by MMP staff such as Yeow Meng (Dr), Ruige (Dr) and Daphne and not forgetting Yong Hean who helped me with photolithography of the Ni moulds. I am thankful for Foundry personnel Chua, Han (for help with Ni plating) and Yong Chear, for providing me with useful advice and help whenever needed, including Sharon for assisting with my purchases and consumables; and especially Rahmad and Mohaime who respectively helped me mill PC, PMMA, and dice quartz and COC when I needed them urgently. I also thank Sharon and Pamela from SCEI for their assistance and advice with regard to my purchases and other finance matters.

Special mention to the warriors behind SIMTech Student's Club – Shuyun (Dr), Elizabeth, Wei Long and Aloysious. It was delightful working with like-minded people and organising events together. I am also touched, encouraged and inspired by their support and positivity.

I would also like to thank my parents and brothers for being supportive of my devotion to my PhD research, especially my Mum for instilling determination in me and showing me her love and care.

Last but definitely not least, I would like to express eternal gratitude to my wife, Wen Na, for her unfaltering support and belief in me, constantly reminding me of my purpose and priorities at work, encouraging me when I am demoralised, and making me a person of conviction and grit.

Table of Contents

Abstract i
Declaration ii
Acknowledgements iii
List of Figures xii
List of Tables xv
Acronyms xvi
Symbols xx
Naming conventions xxi

1 CHAPTER 1 INTRODUCTION 1

1.1 Microbioreactors (MBRs) 1
1.1.1 Types of microbioreactors (MBRs) 1
1.1.2 Advantages of microbioreactors (MBRs) 2
1.1.3 Commercialised systems 2
1.1.4 Features of MBRs 3
1.1.4.1 Microbioreactor (MBR) substrates 3
1.1.4.2 Volume of MBR chambers 4
1.1.4.3 Size of sensors in MBRs 4
1.1.5 Experimental requirements 4
1.1.5.1 Oxygen transfer rate (OTR) 5
1.1.5.2 Biomass and cell growth 5
1.1.5.3 pH and dissolved oxygen (DO) 6
1.1.5.4 Other analytes 6
1.1.5.5 Assays and products of interest 6
1.2 Microfluidics 7
1.2.1 Photolithography 7
1.2.2 Oxygen (O_2) plasma treatment 7
1.2.3 Fluid dynamics at the micro-scale 8
1.3 Holographic sensors (holosensors) 9
1.3.1 Alternative technologies 9
1.3.2 Constitutents of a holosensor 10
1.3.2.1 pH (biological) recognition element 11
1.3.2.2 Transducer 12
1.3.2.3 Display (holographic) 14
1.3.2.3.1 Brief history of holography 14
1.3.2.3.2 Latent image 15
1.3.2.3.3 Reflection hologram 15
1.3.2.3.4 Bragg's condition 16
1.3.2.3.5 Holographic signal offset 16
1.3.2.3.6 Holographic signal interrogation 17

1.4 Miniaturisation challenges and technology gaps 17
1.4.1 Process information available at miniaturised scale 17
1.4.2 Detectable limit of holograms 18
1.4.3 Buffering capacity of the holosensor 18
1.4.4 Dimensional control of gel 19
1.4.5 Effect of ionic strength on pH holosensors 19
1.4.6 Unbleached vs bleached holosensor 19
1.4.7 Tape mask fabrication method 19
1.4.7.1 Acrylic-based adhesive tape 20
1.4.7.2 Silicone-based adhesive tape 20
1.4.7.3 5.0ϕ HEMA-co-MAA holosensor 20
1.4.8 Other methods of gel fabrication 20
1.5 Holographic pH sensor in nanobioreactors 21
1.6 pH monitoring of *Lactobacillus casei (L. casei)* 22
1.7 Research scope 23
1.8 Aims and objectives 23
2 CHAPTER 2 MATERIALS AND METHODS 24
2.1 Materials 24
2.2 Laboratory equipment and apparatus 24
2.2.1 Custom-made commercial apparatus 24
2.2.1.1 Customised gel fabrication apparatus 24
2.2.1.2 Customised hologram fabrication apparatus 26
2.2.1.3 Customised holographic sensor interrogation apparatus 29
2.2.2 Laboratory-developed devices 31
2.2.2.1 Customised sample holders 31
2.2.2.1.1 Gel precursor solution vial holder 31
2.2.2.2 Customised sample-storage apparatus 31
2.2.2.3 Custom-made spin coater 32
2.2.2.4 Custom-made spectrophotometer enclosure 33
2.2.2.5 Customised hydrophobic-coating apparatus 33
2.3 Laboratory ware 34
2.4 Methods 34
2.4.1 Substrate preparation 36
2.4.1.1 Substrate patterning 36
2.4.1.1.1 Through-cut 36
2.4.1.1.2 Scribe-and-snap method 37
2.4.1.1.3 PDMS patterning via mould casting 37
2.4.1.2 Surface treatment 38
2.4.1.3 Surface modification 39
2.4.1.3.1 Silanisation of glass slides 39
2.4.1.4 Surface modification of polymers 40

2.4.1.4.1 Surface modification of polycarbonate (PC) 40
2.4.1.4.2 Surface modification of other common polymers 41
2.4.2 Gel fabrication 41
2.4.2.1 Preparation of gel precursors 41
2.4.2.2 Preparation of DMPA and HQ solutions 42
2.4.2.3 UV-initiated free radical polymerisation with masking tape mask 44
2.4.2.4 UV-initiated free radical polymerisation with photomask 45
2.4.2.5 Glass (quartz)-chrome vs film (acetate) photomask 46
2.4.2.6 Cover substrate for photo-polymerisation 46
2.4.2.7 Gel characterisation 47
2.4.2.8 Hologram fabrication 47
2.4.2.8.1 Experimental setup 47
2.4.2.8.2 Sample alignment 48
2.4.2.8.3 Preparation of developer 51
2.4.2.8.4 Fabrication procedure 51
2.4.3 Holosensor calibration 53
2.4.3.1 Microfluidic chip fabrication 53
2.4.3.2 Preparation of ionic-strength balanced McIlvaine buffer 54
2.4.3.3 pH characterisation of holosensors 55
2.4.4 Holosensor validation and application 57
2.4.4.1 Preparation of MRS media (agar and broth) 57
2.4.4.2 Culturing of Lactobacillus casei (L. casei) 57
2.4.4.2.1 *L. casei* cell culture 57
2.4.4.2.2 Preparation of *L. casei* batches 58
2.4.4.2.3 Cell count of *L. casei* against OD_{600} 59
2.4.4.2.4 Inoculation of *L. casei* 60

3 CHAPTER 3 INTEGRATED PH HOLOSENSOR IN A MICROFLUIDIC SYSTEM 61

3.1 Controlled polymerisation 61
3.2 Typical 3.0ϕ HEMA-co-TFMPA gel profiles 61
3.3 Holosensor brightness optimisation 63
3.3.1 Effect of vibrations and temperature variations on hologram brightness 63
3.3.2 Effect of polarisation on hologram brightness 64
3.3.3 Effect of orientation of optomechanical components 65
3.4 Integration of the 3.0ϕ HEMA-co-TFMPA holosensor into a microfluidic chip 66
3.5 3.0ϕ HEMA-co-TFMPA holosensor 67
3.5.1 Gold standard in hologram brightness 68
3.5.2 Comparison of holosensor to gold standard 68
3.6 Holosensor pH calibration 68
3.6.1 Choice of pH calibration buffer 68
3.6.2 Calibration technique 69
3.6.3 Holosensor reliability 71

3.6.4 Normalisation of holographic signal 71
3.6.5 Holosensor interrogation angle 71
3.6.6 RGB to xyY colour space 72
3.6.7 Holosensor at its pK_a 72
3.6.8 Modified Henderson-Hasselbalch (H-H) calibration curve 74
3.7 Difference in pK_a between solution and gel matrix-bound TFMPA 76
3.8 Effect of ionic strength on the calibrated holosensor 76
3.9 Monitoring of bacteria growth 78
3.9.1 Morphology and growth characteristics 78
3.9.2 Experimental parameters 78
3.9.3 Repeatability of inoculation duration to reach OD_{600}=1.0 78
3.10 *L. casei* 3.0ϕ HEMA-co-TFMPA holosensor interrogation 80
3.10.1 Difference between measured and predicted pH 81
3.11 Standard curve for the 3.0ϕ HEMA-co-TFMPA holosensor 82
3.11.1 Effectiveness of holosensor 84
3.11.1.1 Allowable error 84
3.11.1.2 R^2 ratio 84
3.12 Ionic-strength correction for the 3.0ϕ HEMA-co-TFMPA holosensor 86
3.13 Conclusions 87

4 CHAPTER 4 MINIATURISED PH HOLOSENSOR ARRAY 88

4.1 Buffering capacity of the holosensor 88
4.2 Typical 0.4ϕ HEMA-co-TFMPA gel profiles 89
4.2.1 Effect of solvent in gel precursor solution 89
4.2.1.1 Cage effect and gel porogen 89
4.2.1.2 Chain transfer agent 89
4.2.1.3 Dielectric constant 89
4.2.2 Photoinitiator (DMPA) concentration 90
4.2.2.1 1/18 DMPA for 3.0ϕ HEMA-co-TFMPA holosensor 90
4.2.2.2 1.0 DMPA for 0.4ϕ HEMA-co-TFMPA holosensor 90
4.2.3 0.4ϕ HEMA-co-TFMPA gel recipe 91
4.3 0.4ϕ HEMA-co-TFMPA holosensor 92
4.3.1 Gel miniaturisation 92
4.3.2 Determination of hologram fabrication offset angle 92
4.3.3 Hologram fabrication for 0.4ϕ HEMA-co-TFMPA gels 93
4.4 0.4ϕ HEMA-co-TFMPA holosensor observations 94
4.4.1 Gel expansion 95
4.4.2 Gel contraction during purging 96
4.4.3 Maximum holographic signal 96
4.5 0.4ϕ HEMA-co-TFMPA holosensor pH calibration 96
4.6 Calibration curve for 0.4ϕ HEMA-co-TFMPA holosensor 98

4.7 Effect of ionic strength on 0.4ϕ HEMA-co-TFMPA holosensor 99
4.7.1 RGB to xyY colour space 99
4.8 Monitoring *L. casei* with 0.4ϕ HEMA-co-TFMPA holosensor 101
4.9 *L. casei* 0.4ϕ HEMA-co-TFMPA holosensor interrogation 101
4.10 Standard curve for 0.4ϕ HEMA-co-TFMPA holosensor 103
4.11 Predicted pH vs measured pH (0.4ϕ HEMA-co-TFMPA holosensor) 104
4.12 Ionic strength correction for the 0.4ϕ HEMA-co-TFMPA holosensor 106
4.13 0.4ϕ HEMA-co-TFMPA holosensor array 107
4.14 pH characterisation for 0.4ϕ HEMA-co-TFMPA holosensor array 108
4.15 Calibration curve for 0.4ϕ HEMA-co-TFMPA holosensor array 114
4.16 *L. casei* growth curve for 0.4ϕ HEMA-co-TFMPA holosensor array 115
4.17 *L. casei* interrogation with 0.4ϕ HEMA-co-TFMPA holosensor array 115
4.18 Standard curve for 0.4ϕ HEMA-co-TFMPA holosensor array (whole array) 119
4.19 Discussion – Concentric ring patterns 124
4.19.1 Point scatterers and spherical waves 124
4.19.2 Diffraction of light from nano-periodic structures 125
4.19.3 Air wedge interference and Newton's rings 125
4.19.4 Effect of Airy disk 126
4.19.5 Effect of multiple reflections and interference 126
4.19.6 Effect of the Laguerre Gaussian mode 127

5 CHAPTER 5 FURTHER HOLOSENSOR DEVELOPMENTS 129

5.1 Flat gel profile exploration 129
5.1.1 "Bat-wing" gel profile 130
5.1.2 Flatness ratio (FR) 131
5.1.3 Effect of UV power intensity 131
5.1.4 Effect of cover substrate 132
5.1.4.1 Choice of cover substrate 132
5.1.4.2 Hydrophilicity and hydrophobicity of cover substrate 133
5.1.4.3 Difference between both sides of injection moulded COC 133
5.1.5 Effect of varying DMPA:HQ ratio 133
5.1.6 Effect of evaporation and solvent 133
5.1.7 Effect of O_2 plasma treatment 134
5.1.8 Effect of extrinsic experimental factors 134
5.1.8.1 Solvent overflow technique 134
5.1.8.2 Vibration length and frequencies 135
5.1.8.3 N_2 purge and reverse-pipetting technique 135
5.1.9 Flat profile (FR) anomaly 136
5.2 Surface roughness 138
5.2.1 Roughness and waviness parameters 138
5.2.2 Cut-off wavelength, λ_c (ISO 4288-1996) 138

5.2.2.1 Determination of cut-off wavelength for < 0.4 mm evaluation length 139
5.3 Cover substrate surface texture analysis 140
5.3.1 Flat gel profile anomaly criteria 141
5.4 Types of gel profiles 142
5.4.1 HEMA-co-DMAEM gel nano-indentation 143
5.4.1.1.1 3.0ϕ HEMA-co-DMAEM gels 143
5.4.1.1.2 0.4ϕ HEMA-co-DMAEM gels 144
5.5 Miniaturised 0.4ϕ HEMA-co-DMAEM holosensor 144
5.5.1 pH characterisation of 0.4ϕ HEMA-co-DMAEM holosensor 145
5.5.2 Calibration curve for 0.4ϕ HEMA-co-DMAEM holosensor 148
5.6 Miniaturised 0.4ϕ HEMA-co-TFMPA holosensor on PC 149
5.6.1 Adhesion of gel to PC substrate 149
5.6.2 Adhesion of PC to PDMS 150
5.6.3 Visualisation of the PC-embedded 0.4ϕ HEMA-co-TFMPA holosensor 151
5.6.4 Utilising the PC-embedded 0.4ϕ HEMA-co-TFMPA holosensor 151
5.7 Violet laser for hologram fabrication 152
5.8 Outcomes 153

6 CHAPTER 6 FINAL DISCUSSION 154

6.1 Current bioreactor sensors 154
6.2 Current holographic sensor technology 155
6.3 Controlling the gel volume 156
6.4 Maximising the signal-to-noise ratio 157
6.5 Performance comparison of the miniaturised holosensors 159
6.6 Final Conclusions 161

APPENDICES 162

Appendix A: Absorbance graphs 162
A-1 Absorbance spectra of chemicals for gel fabrication 162
A-2 Absorbance spectra of gel and dyes 163
Appendix B: RGB to xyY conversion 164
Appendix C: Using tape as a mask for gel fabrication 165
Appendix D: CO_2 laser cutting machine recipes for various substrates 167
Appendix E: PDMS Mould Fabrication 168
SU-8 glass mould 168
Nickel-plated glass mould 169
Appendix F: Calculation for gel precursor ratio 170
Appendix G: Summarised procedure for hologram fabrication 171
Appendix H: Recipe for ionic strength balanced (9.50 mS/cm) 0.1M McIlvaine buffers 172
Appendix I: Derivation of the modified Henderson-Hasselbalch equation 173
Appendix J: UV LED emission spectrum, power equivalence graph, substrate UV attenuation and transmittance 177

Appendix K: Ionic strength correction for 3.0ϕ HEMA-co-EDMA-co-TFMPA (91.0:3.0:6.0 mol%) holosensor spot 178
Appendix L: Minimum chamber volume required to mitigate buffering capacity of holosensor 179
Appendix M: Relative proportion of DMPA (by size) 180
Appendix N: Ionic strength correction for 0.4ϕ HEMA-co-EDMA-co-TFMPA (91.0:3.0:6.0 mol%) holosensor spot 181
Appendix O: 0.4ϕ HEMA-co-TFMPA holosensor array 182
O-1 Holograms of 0.4ϕ HEMA-co-TFMPA array – pH calibration 182
O-2 Holograms of 0.4ϕ HEMA-co-TFMPA array – Monitoring of *L. casei* growth 184
Appendix P: CIE 1931 chromaticity diagrams of 0.4ϕ HEMA-co-TFMPA holosensor array 186
P-1 0.4ϕ HEMA-co-TFMPA holosensor array CIExyY diagrams (pH characterisation) 186
P-2 0.4ϕ HEMA-co-TFMPA holosensor array CIExyY diagrams (*L. casei* interrogation) 187
Appendix Q: Graphs for 0.4ϕ HEMA-co-TFMPA holosensor array 188
Q-1 pH response (peak wavelength) of 0.4ϕ TFMPA holosensor array – pH calibration 188
Q-2 Normalised average intensity & slope 190
Q-3 pH characterisation curves (using modified H-H equation) 192
Q-4 Standard curve (Measured pH vs predicted pH) 194
Q-5 Measured pH vs OD_{600} curve (Ideal case) 196
Q-6 Predicted pH vs OD_{600} curves 197
Appendix R: Flat profile exploration 199
R-1 Naming conventions and schematics for flat profile exploration 199
R-2 Graphs for flat profile exploration (varying parameters) 200
Appendix S: Surface roughness and cut-off wavelength (λ_c) 202
S-1 Definitions of different surface roughness parameters 202
S-2 Cut-off wavelength (λ_c) 202
Appendix T: Determination of cut-off wavelength (λ_c) for 0.4ϕ HEMA-co-DMAEM gels 203
Appendix U: Ideal recipes for flat gel (0.4ϕ HEMA-co-DMAEM) profiles 204
Appendix V: Gel nano-indentation 205
V-1 3.0ϕ HEMA-co-DMAEM gel nano-indentation 205
V-2 0.4ϕ HEMA-co-DMAEM gel nano-indentation 206
Appendix W: Transverse modal field distribution for a circular waveguide 207
Appendix X: FTIR interrogation for residual HQ/DMPA detection in DMAEM gel 208
Appendix Y: Obstacles and challenges 209
Y-1 Challenges associated with $\geqslant$ 3.0ϕ holosensors 209
Y-2 Challenges associated with miniaturized 0.4ϕ holosensors 210
Appendix Z: Spectra of light sources for hologram interrogation 211
Appendix AA: Holosensor issues and challenges 212
3.0ϕ holosensors 212
Colour of reduced Ag^0 gel 212
Coffee stain (ring) effect 212
Polychromatism 213

Mini hologram in big spot 213
Major challenges for the 3.0ϕ holosensor 214
0.4ϕ holosensors 215
Dim holograms 215
Polychromatism and resolution 215
Diminishing hologram brightness 216
Background signal from PC-embedded holosensor 216
Polychromatic and cracked surface AAm holosensor 216
Appendix AB: Materials and Equipment 217
Substrates 217
Glass 217
Plastics 217
Silicone elastomers 218
Chemical reagents 218
Gel precursors 218
Substrate modification and bonding 218
Hologram fabrication 219
Saxby developer 219
Formation of Ag^0 nanoparticles (NPs) 219
Holosensor calibration 219
pH buffers 219
Biologics 220
Commercially-available equipment 220
Substrate preparations 220
General 220
Substrate patterning 220
Mould fabrication and injection moulding 220
Surface treatment 220
Gel fabrication 221
UV photo-polymerisation 221
Gel characterisation 221
Holosensor fabrication 221
Holosensor interrogation 222
Holosensor characterisation and validation 222
Biologics 222
Consumables 222
Software 223
REFERENCES 224

List of Figures

Figure 1-1: Schematic diagram of the inner plasma chamber depicting the “ion-dominant” and “neutral-dominant” configuration 8
Figure 1-2: Features of a holographic sensor (holosensor) 11
Figure 1-3: Chemical structures and equilibrium of acidic and basic pH moieties 12
Figure 1-4: Photolysis of DMPA into primary and secondary fragments and radicals 13
Figure 1-5: Oxidisation of hydroquinone to 1,4 benzoquinone (or para-quinone) 13
Figure 1-6: Controlling free radical polymerisation with an inhibitor 14
Figure 1-7: Schematic diagram of the Bragg's condition 16
Figure 1-8: Illustration of trade-off in information output versus HT capability that currently exist for various cell cultivation devices at different scales 17
Figure 1-9: Experimental setup for pulsed laser 21
Figure 2-1: Customised apparatus setup for photo-polymerisation of gel using parallel beam UV @ 365 nm 25
Figure 2-2: Pictures and schematic diagram of customised hologram fabrication apparatus 27
Figure 2-3: Picture and drawings of sample adaptor 28
Figure 2-4: Pictures of the customised holosensor interrogation experimental setup 30
Figure 2-5: Custom-made multi-vial holders 31
Figure 2-6: Sample storage apparatus 31
Figure 2-7: Picture and schematic cross-sectional view diagrams of sample-storage apparatus 32
Figure 2-8: Custom-made spin coater 32
Figure 2-9: Custom-made spectrophotometer enclosure for optical density (OD_{600}) measurements 33
Figure 2-10: Customised hydrophobic-coating apparatus 33
Figure 2-11: Methodology for monitoring *L. casei* cell growth via holosensor pH response 34
Figure 2-12: Holosensor fabrication method flowchart 35
Figure 2-13: Chemical structure of 3-(trimethoxysilyl)propyl methacrylate (Silane A174) 40
Figure 2-14: Chemical structure of Pentaerythritol tetraacrylate (PETTA) 41
Figure 2-15: Calculation for gel precursor proportions in IPA as solvent (for 3.0 mol% EDMA HEMA-co-TFMPA) 43
Figure 2-16: Schematic diagrams for gel fabrication via UV-initiated polymerisation using a tape mask 44
Figure 2-17: Gel fabrication setup 45
Figure 2-18: Hologram fabrication experimental setup 49
Figure 2-19: Devised method of using cleanroom tissue and adjustable iris with protuberance as alignment tool 50
Figure 2-20: Schematic drawing for Delrin® sample adaptor with gel-on-substrate for hologram fabrication 52
Figure 2-21: Picture of laser-cut calibration PMMA block and Illustrations of PDMS chips with 2.0 mm and 4.0 mm diameter chambers 53

Figure 2-22: Conductivity measurements of original and normalised ionic strength 0.1M McIlvaine buffers 55
Figure 2-23: Picture of *L. casei* Shirota streaked on an agar plate after 48h of incubation at 37°C 58
Figure 2-24: Cell count of *Lactobacillus casei (L. casei)* at various measured optical density at 600 nm (OD600) 60
Figure 3-1: Typical gel information of HEMA-co-EDMA (3 mol%)-co-TFMPA (6 mol%) 62
Figure 3-2: Collation of 3.0ϕ HEMA-co-TFMPA holosensor information 67
Figure 3-3: Collation of 3.0ϕ HEMA-co-TFMPA holosensor calibration data 70
Figure 3-4: Generic representation of a sigmoidal curve created by plotting a measured quantity, parameter X, against pH 74
Figure 3-5: Normalised intensity holosensor response, slope of peak wavelength change to pH change, and Modified Henderson-Hasselbalch (H-H) pH calibration curve 75
Figure 3-6: 3.0ϕ HEMA-co-TFMPA holosensor response to different NaCl concentrations 77
Figure 3-7: *Lactobacillus casei (L. casei)* growth curve for 3.0ϕ HEMA-co-TFMPA holosensor 80
Figure 3-8: 3.0ϕ HEMA-co-TFMPA holosensor response *to L.* casei growth 82
Figure 3-9: Standard curve for 3.0ϕ HEMA-co-TFMPA holosensor 83
Figure 3-10: Measured pH versus Predicted pH for 3.0ϕ HEMA-co-TFMPA holosensor 85
Figure 4-1: 0.4ϕ HEMA-co-TFMPA gel profiles 91
Figure 4-2: Schematic diagram for the hologram fabrication setup 93
Figure 4-3: Collation of 0.4ϕ HEMA-co-TFMPA holosensor information 94
Figure 4-4: Video snapshots of the 0.4ϕ HEMA-co-TFMPA holosensor during gel expansion and during N_2 purge 95
Figure 4-5: Collation for the pH calibration information of the 0.4ϕ HEMA-co-TFMPA holosensor 97
Figure 4-6: Normalised intensity holosensor response, slope of peak wavelength change to pH change, and Modified Henderson-Hasselbalch (H-H) pH calibration curve 98
Figure 4-7: 0.4ϕ HEMA-co-TFMPA holosensor response to different NaCl concentrations 100
Figure 4-8: *Lactobacillus casei (L. casei)* growth curve for 0.4ϕ HEMA-co-TFMPA holosensor 101
Figure 4-9: 0.4ϕ HEMA-co-TFMPA holosensor response *to L.* casei growth 102
Figure 4-10: Standard curve for 0.4ϕ HEMA-co-TFMPA holosensor 103
Figure 4-11: Measured pH versus predicted pH for 0.4ϕ HEMA-co-TFMPA holosensor 105
Figure 4-12: Collation of 0.4ϕ HEMA-co-TFMPA holosensor array information 107
Figure 4-13: pH calibration information of the 0.4ϕ HEMA-co-TFMPA holosensor array 109
Figure 4-14: Peak wavelength pH responses of the 0.4ϕ holosensor array spots #1 to #7 and of the whole array during pH calibration 110
Figure 4-15: Pictures of the holosensor array and the individual spots (#1 - #7) in the holosensor array during pH calibration .....Pictures of the holosensor array and the individual spots (#1 - 112
Figure 4-14 Calibration curve for pH characterisation of 0.4ϕ HEMA-co-TFMPA holosensor array 114

Figure 4-15 *L. casei* growth curve for 0.4ϕ HEMA-co-TFMPA holosensor array 115
Figure 4-18: Pictures of the holosensor array and the individual spots (#1 - #7) in the holosensor array during L. casei interrogation 116
Figure 4-16 Calibration curve for pH characterisation of *0.4* HEMA-co-TFMPA holosensor array 118
Figure 4-17 L. casei growth χυρϖε for 0.4 HEMA-co-TFMPA holosensor array..... 119
Figure 4-21: Standard curves of measured pH vs predicted pH for 0.4ϕ holosensor array spots #1 to #7 and of the whole array 120
Figure 4-22: (Ideal case) Measured pH and conductivity (ionic strength) of the batch media (broth) containing live L. casei at increasing OD_{600} values, predicted pH and measured conductivity plotted against increasing OD_{600} of the bacterial media 123
Figure 4-18 Interference pattern from a small scatterer, large scatterer and Picture of a 3.0ϕ HEMA-co-TFMPA hologram with random occurrences of point scatterers 124
Figure 4-19 Schematic diagram of theair-wedge setup, its fringe pattern and Newton's rings setup with its fringe pattern 126
Figure 4-20 Schematic diagram of the Michelson Interferometer 127
Figure 4-21 Intensity distributions for the modes up to the 9th order of the helical and sinusoidal LG mode sets 128
Figure 4-27: Transverse modal field distribution TE_{01}, TE_{02} and TE_{03} for a circular waveguide 128
Figure 5-1: Schematic diagram comparing an ideal flat gel profile and a typical "bat-wing" gel profile 130
Figure 5-2: Concentration profile of photo-polymerised poly-N-isopropylacrylamide (polyNIPAAM) gels 131
Figure 5-3: 3D digital elevation model of the photopolymerised DMAEM gel with 30% power and 60% power 132
Figure 5-4: Swelling of a poly (HEMA) hologram containing 5% (w/w) EDMA as a function of alcohol concentration (vol%) for a range of different alcohols 134
Figure 5-5: Emergence of the flat profile anomaly 137
Figure 5-6: COC cover substrate information 141
Figure 5-7: Schematic diagram for the different types of gel profiles 142
Figure 5-8: Determination of hardness and reduced modulus 143
Figure 5-9: Collation of 0.4ϕ HEMA-co-DMAEM holosensor information 145
Figure 5-10: pH characterisation information of the 0.4ϕ HEMA-co-DMAEM holosensor 147
Figure 5-11: Modified Henderson-Hasselbalch (H-H) pH calibration curve for 0.4ϕ HEMA-co-DMAEM holosensor..... 148
Figure 5-12: Collation of 0.4ϕ HEMA-co-TFMPA holosensor on PC substrate 151
Figure 5-13: Video grab of 0.4ϕ HEMA-co-TFMPA holosensor on PC during gel expansion with pH 6.00 (9.50 mS/cm) McIlvaine buffer 152
Figure 5-14: Spectrophotometric information with peak wavelength, intensity counts, integration time and laser exposure parameters for the samples exposed with 531 nm laser and 411 nm laser 153

List of Tables

Table 2-1: Surface treatment parameters for UV / plasma systems 38
Table 2-2: Parameters for PDMS-glass bonding 54
Table 4-1: Summary of key values for determination of calibration curve, predicted pH and accuracy parameter, χ, for 0.4ϕ HEMA-co-TFMPA holosensor array 122
Table 5-1: Determination of cut-off wavelength below 0.4 mm evaluation length 139
Table 5-2: List of tested crosslinkers depicted with their chemical structures and reaction with PC surfaces 150

Acronyms

(L)	length
(T)	thickness
(W)	width
3D	three-dimensional
AAPH	2,2'-azobis(2-methylpropionamidine) dihydrochloride
abbv.	abbreviated
Acexon	Acexon Technologies Pte Ltd
Ag	silver
$AgClO_4$	silver perchlorate anhydrous or silver (I) perchlorate
$AgClO_4.xH_2O$	silver perchlorate hydrate
AgNPs	silver nanoparticles
Aik Moh	Aik Moh Paints and Chemicals Pte Ltd (distributor for Arcos Organics)
a.k.a.	also known as
APS	ammonium persulphate
APTES	(3-aminopropyl)triethoxysilane
aq.	aqueous
AR	anti-reflection
BQ	benzoquinone
Br	bromide
BSC	biological safety cabinet (or biosafety cabinet)
BSF	Biopolis Shared Facilities (Singapore)
BTU/hr	british thermal units per hour
cfu	colony-forming units
CIE	Commission Internationale de l'Eclairage (International Commission on Illumination)
cmHg	centimetres of mercury at 0 degrees Celsius pressure unit
CMOS	complementary metal-oxide-semiconductor
CNC	computer numeric control
CO_2	carbon dioxide
COC	cyclic olefin copolymer
CPU	central processing unit
Ctrl	control

CW	continuous wave
DC	direct current
DI	de-ionised
DMAEA	2-(dimethylamino) ethyl acrylate
DMAEM	2-(dimethylamino) ethyl methacrylate
DMPA	2-2-dimethoxy-2-phenylacetophenone (a.k.a. Irgacure 651)
DPEPHA	dipentaerythritol penta-/hexa acrylate
DPSS	diode-pumped solid state
EDMA or EDGMA	ethylene glycol dimethacrylate
EMA	ethyl methacrylate
EtOH	ethanol
FDTS	1H-1H-2H-2H-perfluorodecyltrichlorosilane
FOTS	1H-1H-2H-2H-perfluorooctyltrichlorosilane
FEP	fluorinated ethylene propylene
FM	functional moiety
FOV	field-of-view (area of observation captured by camera)
FTIR	fourier transform infra-red
FWHM	full width at half maximum
GDM	glycerol dimethacrylate, mixture of isomers
GPC	gel precursor
HEA	2-hydroxyethyl acrylate
HEMA	2-hydroxyethyl methacrylate
Hg	mercury
H-H	Henderson-Hasselbalch
HMDS	hexamethyldisilazane
Holosensor	holographic sensor
HQ	hydroquinone
ID	inner diameter
IPA	isopropyl alcohol
inHg	inches of mercury at 0 degrees Celsius pressure unit
ISO	International Organization for Standardization
JD-4 (or JARB)	Saxby developer
Kanto	Kanto Kagaku Singapore Pte Ltd
L. casei	*Lactobacillus casei*

LED	light emitting diode
LiBr	lithium bromide
M	molar concentration (number of mols per litre, mol/L, of solvent)
M.R.S.	de Man, Rogosa, Sharpe
M6	ISO Metric screw thread nominal outer diameter 6mm
MAA	methacrylic acid
MeOH	methanol
Metol	4-methylaminophenol sulphate
MFC	mass flow controller
mins	minutes
MMP	Microfluidics Manufacturing Programme
mol%	molar ratio (in %)
ms	milliseconds (typically associated with integration time in this thesis)
mS/cm	millisiemens per centimetre (a unit of electrical conductivity)
MRS media	de Man, Rogosa, Sharpe (M.R.S.) media
Mylar®	trade name for PET (polyethylene terephthalate)
N_2	nitrogen
Na_2CO_3	sodium carbonate
Na_2HPO_4	disodium hydrogen phosphate or sodium phosphate dibasic
$Na_2O_3S_2$	sodium thiosulphate
NaOH	sodium hydroxide
ND	neutral density (a measure of light transmittance)
Ni	nickel
nm	nanometres
NPs	nanoparticles
O_2	oxygen
OD	outer diameter
OD_{600}	optical density @ 600 nanometres (a measure of light absorbance)
opp	opposite to the “weird, wavy” side of COC
PC	polycarbonate
PDMS	poly(dimethylsiloxane)
PEA	2-phenoxyethyl acrylate (ethylene glycol phenyl ether acrylate)
PEG	poly(ethylene glycol)
PEGA	poly(ethylene glycol) acrylate, M_n ~ 375

$PEGDA_{250}$	poly(ethylene glycol) (PEG) diacrylate, average M_n ~ 250
$PEGDA_{575}$	poly(ethylene glycol) (PEG) diacrylate, average M_n ~ 575
PEGPEA	poly(ethylene glycol) phenyl ether acrylate (average M_n ~ 324)
PET	polyethylene terephthalate
PETA	pentaerythritol triacrylate
PETTA	pentaerythritol tetraacrylate
PGMEA	propylene glycol monomethyl ether acetate
pHEMA	poly (HEMA); poly (2-hydroxyethyl methacrylate)
PMMA	poly(methyl methacrylate)
PNIPAAM	poly(N-isopropylacrylamide)
PP	polypropylene
PS	polystyrene
PTFE	polytetrafluoroethylene (better known as its tradename, Teflon™)
PVC	poly (vinyl chloride)
QBS	1,1'-diethyl-2,2'-cyanine iodide (quinaldine blue dye, short)
Quinaldine blue	pinacyanol chloride
ref	reference
RGB	red-green-blue
rpm	revolutions per minute
rms	root mean square
s	seconds
sccm	standard cubic centimeters per minute
s.d.	standard deviation
Sigma	Sigma Aldrich
SIlane A174	3-(trimethoxysilyl)propylmethacrylate (TMPMA)
SIMTech	Singapore Institute of Manufacturing Technology
SLM	single longitudinal mode
SMA	SubMiniature version A
spec	spectrophotometer
t-BAEM	2-(*tert*-butylamino)ethyl methacrylate
Tee Hai	Tee Hai Chem Pte Ltd
TEM_{00}	Transverse Electromagnetic Mode 00
TEMED	tetramethylethylenediamine
TFMPA	2-(trifluoromethyl) propenoic acid / 2-(trifluoromethyl)acrylic acid (TFMA)

T-H	tungsten-halogen / halogen-tungsten
TTEGDA	tetra(ethylene glycol) diacrylate
UK	United Kingdom
UNF	unified screw thread (Fine)
USB	universal serial bus
UV	ultraviolet
UV-VIS	ultraviolet-visible
v/v	volume by volume (volume ratio)
VBG	volume bragg grating
W	watts
w/	with
w/v	weight (in grams) per 100 milliliters (mL) of solvent
ww	“weird-wavy” side of the COC substrate
w/w	weight-to-weight ratio
wrt	with respect to
WD	working distance (between tip of lens to sample surface)
μfd	microfluidic
μm	micrometres

Symbols

ϕ	diameter (in millimetres)
“	inches
λ	wavelength (in nanometres)
Δ	infinitesimal change

Naming conventions

x DMPA	normalised DMPA w/v % (expressed as fraction or multiple "x" of 1.81 w/v % in IPA)
y:1 HQ	DMPA:HQ molar ratio (expressed as an integer multiple, y, of a unit molar quantity of HQ)
α**p**β**m**-**#**γ	UV power (abbv. **p**), UV exposure duration in minutes (abbv. **m**) and seconds (abbv. **s** if any) and UV power equivalence (mW/cm2) described by conversion graphs #1 to #3 in equivalence graph (Appendix J(b)) (expressed in integers by α, β and γ respectively). e.g. 10p5m-#1 means 10% power for 5 minutes, with power intensity 17.11mW/cm2 corresponding to 5% UV power using #1 conversion curve in Appendix J(b) (UV power conversion graph)
COCopp/ww_(χ)+	COC substrate with opp or ww side facing (typically upwards) the UV source, with the substrate size represented with the underscore, and the type of fabrication method expressed in place of χ (**d** for diced and **m** for milled) enclosed with a bracket, followed by substrate identifier "+" e.g. COCopp8x8(d)3a describes a COC substrate with "opp" side which was diced (d) with dimensions 8mm x 8mm and substrate identifier "3a"
$\alpha\Psi\beta\square$	abbreviated manner of summarising the mol% of pH moiety Ψ (T for TFMPA, D for DMAEM and M for MAA) and mol% of crosslinker (typically EDMA) represented by $\square$ described by respective integer values α and β. e.g. 6T3E represents 6 mol% TFMPA with 3 mol% EDMA

1 Chapter 1 Introduction

Recombinant protein therapeutics, primarily produced in mammalian cells, constitute a $108 billion global market [1]. Bioprocesses involving mammalian cell cultures have been evolving rapidly in the biotechnology industry [2]. New biopharmaceutical products and recombinant proteins continually require development for higher throughput [3], lower costs, faster process development [4] and optimization. To develop these new bioprocesses in a cost effective way, researchers perform multiplexed experiments [5] in scaled-down bench-scale bioreactors [6], [7] or microtitre plates [8], [9]. With the advent of nanotechnology, single-cell analysis has also garnered a lot of interest [10], where cell heterogeneity [11], [12] and personalized therapy [13] is more intensively studied. One such platform of studying small volume of cells involves microbioreactors.

1.1 Microbioreactors (MBRs)

Bioreactors provide the necessary controlled environment for an organism to produce a desired biological product with optimal mixing, mass transfer and containment [9]. A microbioreactor may be simply defined as a micro-scale device in which biological reactions such as cell culture are performed [14]. Microbioreactors (and nanobioreactors) involve the monitoring and bioprocessing of microorganisms within microlitre (and nanolitre) sized volumes.

1.1.1 Types of microbioreactors (MBRs)

Since the 1940s, shaken systems have been utilised in bioprocessing to grow antibiotic-producing microbial cultures [8]. Shake-flasks come in various sizes, ranging from 25 mL to 5L, and are made of hydrophilic borosilicate glass or relatively hydrophobic plastic materials [9]. Online measurements of the oxygen transfer rate (OTR), carbon transfer rate (CTR) and the respiratory quotient (RQ) for these systems can be measured by the Respiration Activity Monitoring System (RAMOS). Optical sensor systems also allow the precise online measurement of dissolved O_2 in shake-flasks where the fluorescence quenching or decay time of an oxygen-sensitive dye [1,2-bis(diphenylphosphino)ethane-Pt $\{S_2C_2(CH_2CH_2\text{-}N\text{-}2\text{-}pyridinium)\}][BPh_4]$ is measured [15].

First introduced in 1951, microtitre plates (MTP), or microwell plates, are used as a platform for diagnostic tests and are usually made of plastic, although glass and metal versions exist. The most common method involves shaking the entire MTP on a heated block capable of controlling culture temperature. Control of other experimental parameters such as pH, dissolved oxygen (DO) and oxygen transfer rate (OTR) is difficult for microtitre plates, and special plastic lids are required to prevent

evaporative losses, as compared to parallel experiments in shake flasks. Stopping the shaking device is necessary for parameter sampling, which disturbs the respiration profile of the organism [8].

Shake flasks and microtitre plates (MTP) that rely on surface aeration have k_La values of about 150 h^{-1} to 277 h^{-1}, and 200 h^{-1} respectively [8]. Using the sulphite oxidation method, k_La values of up to 1600 h^{-1} were reported in a 48-well standard geometry MTP with 3 mm orbital throw at 1400 rpm using 300 μL filling volume, which is comparable to conventional stirred tank reactors (STRs) [8].

MBRs are a dramatic improvement over microtitre plates (MTP) [16] and shake flasks [17], which do not provide a sufficiently well controlled environment to monitor accurately the minute metabolic activity of microorganisms and mammalian cells in real-time [18], [19].

1.1.2 Advantages of microbioreactors (MBRs)

Stirred tank bioreactors have online monitoring and control capability of process parameters, but are operationally costly and have low throughput. They also do not make full use of multiplexing and automation that miniaturisation technology provides [20].

The MBR systems generally lead to timeline and/or resource reduction [14]. The entire volume of the bioreactor has to be replaced at every doubling time of the microbes. Compared to the smallest 500 mL stirred tank, a 1 mL microbioreactor easily translates to a 500X cost and volume saving of cell media consumed; a cylindrical microfluidic chamber of 2 mm diameter and 100 μm height, which translates to about 0.314 μL (nanobioreactor), will result in a 1.6 million times cost and volume savings. It is important to note that biological and bioprocess parameters must show good scalable results to the macro scale for the miniaturisation to MBRs to make sense.

It is also worth noting that compared to a large vessel, the flow inside the small channels of microreactors is mostly laminar, which leads to better reproducibility. In the pharmaceutical industry, some batches that do not match specifications has to be thrown away, which are often the accumulation of several months' work. This was one reason why GlaxoSmithKline substantiated the idea of microreactors in the late 1990s, and sought to have a microreactor pumping its product straight into a cell-based assay [21]. Research work has also demonstrated how results obtained with the microbioreactor under well-defined environment were comparable to that of the typical bench-scale bioreactors [22]. Additionally, MBRs are small enough to observe minute differences in the metabolic activity of cells, and can be designed for multiplexing and optimisation.

1.1.3 Commercialised systems

Although there are different systems described in various literature, only a few notable commercialised systems stand out. The Micro-Flask$_{\text{by Duetz}}$ system [23], [24] (Applikon Biotechnology)

involve microtitre plates with specialised closures and clamps with orbital shaker, which minimises evaporation and allows culture times that are weeks long.

BioLector (m2p Labs) [6], [16], [20] is a micro fermentation system based on standard disposable microtitre plate formats with non-invasive optical sensors which enables parallel real time culture monitoring. Inoculums as low as 50 μL were utilised for cultivation volume of 1 mL per well in a 48/96-well MTP.

The Micro24 MicroReactor system from Pall Life Sciences features single-use cassettes with the option of aerobic and anaerobic microbial fermentation, mammalian and insect cell culture capable of running 24 simultaneous bioreactor experiments (7 mL working volume) with independent control. These cassettes are incubated on a shaking platform within a temperature-controlled environmental chamber [14]. A comprehensive characterisation was performed on the single-use-24-well parallel miniature bioreactor system [24], [25]. This system utilises dual referenced optical sensing (PreSens) for pH and DO monitoring [26].

Another single-use microbioreactor, the ambr® (Advanced Microscale Bioreactor System) cell culture system from The Automation Partnership (TAP) is widely used by major pharma and biologics companies, academic and research institutes. For the 24 disposable reactors controlled on a liquid handler, each reactor has a 10 – 15 mL working volume with pH and DO measurement from the base of the reactor using patch sensors [5], [27].

SimCell™ (Seahorse Bioscience) [20] microbioreactors are miniaturised bioreactors of full bench top systems, typically in 600 – 800 μL volume. The use of automation provides central fully automated biopharmaceutical process development. The system also allows for parallelisation, which enables the running of thousands of high throughput experiments simultaneously, up to 1500 independently controlled cell cultivation devices enabling the use of full factorial experimental design method for process optimisation [8]. A gas permeable membrane for surface aeration achieves k_La values of 7 h^{-1}, with its microbioreactor array for cell culture having reactor chambers with 300 – 700 μL working volumes [28]. An array of 180 SimCell mini-scale reactors were reported to optimise 4 process parameters for monoclonal antibody expressing CHO cultivation, with data showing the system performing comparably to the scaled up 3L reactors [5].

1.1.4 Features of MBRs

1.1.4.1 Microbioreactor (MBR) substrates

Polydimethylsiloxane (PDMS) [29]–[35] was chosen as the substrate of most microbioreactors because of its optical transparency for microscopic observation and assays, biocompatibility [36] and gas

permeability for gaseous exchange of oxygen (O_2) and carbon dioxide (CO_2) [37]. The base support of the MBR was made of glass for the rigidity required for optical access [22]. However, PDMS is also permeable to water vapour, and is prone to drying issues. Evaporation of even minute amounts of water can cause a significant change in the osmolarity of the media [38].

Other MBR substrates include, but are not limited to polystyrene [39], [40], poly(methylmethacrylate) (PMMA) [29], [30], [41] , polycarbonate (PC) [33], quartz [42], poly(propylene) (PP) [42], parylene-C [43] and Teflon-AF [43].

1.1.4.2 Volume of MBR chambers

MBRs cover a wide range of bioreactor chamber sizes depending on the smallest feature size or working volume. Their working volumes are typically around 1 mL, while a select few have a working volume of less than 100 μL.

Zanzotto *et al.* revealed methods for in situ measurements of bioluminescence and fluorescence from bacterial cultures grown in 50 μL microbioreactors [32]. The smallest microfluidic housing possible for the screen-printed electrode (SPE) fabricated by McKenzie *et al.* is 23 μL due to the SPE footprint and surface contours [44]. Zanzotto *et al.* (2004) demonstrated 5 -50 μL MBRs for real-time measurements in *Escherichia coli* cell culture and later for global gene expression analysis [22]. The approach to prevent biofilm formation enabled Balagaddé *et al.* to implement a miniaturised bioreactor with a working volume of 16 nL [45].

1.1.4.3 Size of sensors in MBRs

PreSens Precision Sensing GmbH (Regensburg, Germany) manufactures one of the smallest non-invasive pH and DO sensors. Their HP2A sensor foils and PSt3 sensors foils are utilised for pH and DO measurements respectively, and are typically 2 mm in diameter and 150 -220 μm in height [22]. The volume of the sensor itself is about 0.47 μL, assuming a 150 μm height. The PreSens pH and DO sensors [22], [26], [35], [46]–[48] are utilised mainly for microbioreactors around 200 μL in working volume.

1.1.5 Experimental requirements

The main cell types involved in the production of therapeutic products are bacterial and mammalian cells, each of which possess their own benefits and limitations that determine the type of bioreactor suitable for process development. For instance, bacterial cells are not susceptible to shear damage and are generally robust, enabling the use of high agitation rates and highly shearing radial impeller systems such as Rushton turbines. It allows high mass transfer capabilities and high-cell density to be supported. On the other hand, although mammalian cells are typically more shear-susceptible and

requires gentler handling, most cell lines can be grown in stirred tank bioreactors which utilises low-shear axial impellers which gently circulate cells and nutrients [8].

Other than studying mammalian cells (such as human bone marrow cells, hBMCs [37]) and bacterial cells [17], [33] (such as *Escherichia coli* [30]–[32], [39], [43], [47], [49]), yeast [40] (such as *Saccharomyces cerevisiae* [29], [42], [43], [47]), microalgae [34], animal cells (such as CHO cells [20]), as well as cell-based assays [37] have been performed in microbioreactors (MBRs) with defined conditions that are comparable to bench scale bioreactors [31] and offer a high-throughput platform for process development.

1.1.5.1 Oxygen transfer rate (OTR)

In aerobic bioreactors, it is essential for the liquid broth to contain enough oxygen for optimal growth [50]. The volumetric mass transfer coefficient, k_La, is the parameter that characterises the efficiency of the entire bioreactor (and process) in terms of oxygen transfer rate (OTR), usually described by the simple transport law [51]

$$OTR = k_L a(O^* - O)\,, \tag{1.1}$$

where $(O^* - O)$ is the difference in concentration between the liquid-side boundary layer at the gas-liquid interface. k_La can then be determined from the measured OTR (from volume fraction of O_2 and CO_2 in the vent line of the reactor) and known saturation concentration O^*, where dissolved oxygen concentration, O, is controlled to 25% saturation value. Suresh *et al.* describes 10 different methods to determine k_La [52].

1.1.5.2 Biomass and cell growth

There are several methods for quantifying biomass and cell growth. Cell metabolic activity can be quantified by AlamarBlue assay (indicator for cell growth) and cell morphology by multiphoton microscopy quantified by the accumulation of reduced dye with the spectrophotometer [37]. Electrochemical microelectrodes enables the quantitative cell analysis by bio-impedance and respiration activity [53].

Biomass can be determined with cell dry weight (CDW) by centrifugation and drying [16]. It can also be correlated with optical density [33], which is calculated from the absorbance (or more accurately, the scattering) at 600 nm [16], [32]. Light from an orange LED at 600 nm passes through the microbioreactor and is collected by a collimating lens before being sent to a photodetector [22]. The optical density can be calculated by normalising the path length with a multiplication factor as follows:

$$OD = \frac{10{,}000}{L_{path}} \log_{10}\left(\frac{I_0}{I_{signal}}\right), \quad (1.2)$$

where L_{path} is the path length (in μm) through the microbioreactor chamber (essentially the chamber height) to compare with conventional cuvettes with path lengths of 1 cm, I_0 is the control intensity and I_{signal} is the signal intensity.

1.1.5.3 pH and dissolved oxygen (DO)

Commercial DO sensors utilise lifetime detection of fluorescence quenching [20], [32], [54]. An oxygen-sensitive fluorophore, $[Ru(dpp)_3]^{2+}Cl_2$–tris(4,7-diphenyl- 1,10-phenanthroline)ruthenium(II) chloride was also be used as the oxygen indicator by measuring the fluorescence quenching of the fluorophore luminescent intensity in the presence of oxygen [54]. Another kind of dissolved oxygen sensor has been fabricated using platinum(II) octaethylporphine-ketone (PtOEPK) embedded in polystyrene [49].

pH can also be measured using pH sensitive fluorescent dyes [20] such as Phenol red [47], [54] based on ratiometric detection. Electrochemical methods to form Ag/AgCl and IrOx films on Pt electrodes to create quasi-references are utilised for pH and DO measurements [44], as well as ion-selective field effect transistor (ISFET) sensors [39], [40], [55].

It is worth highlighting, however, that fluorescent dyes exhibit phototoxic effects to live cells that result from fluorophore photobleaching. In addition to the decreasing available fluorescence signal with each light exposure, photobleaching generates free radicals and other highly reactive breakdown products [56]. This effect has been even exploited by Jacobson *et al.* for the photoinactivation of proteins in a technique known as chromophore-assisted laser inactivation (CALI) [57]. The pH sensitive dye, phenol red, is a weak estrogen mimic [58], [59] and could affect other cellular functions such as non-estrogenic CFU-f differentiation [60], cytotoxicity in MCF-7 cells [61] and inhibition of renal epithelial cell proliferation [62].

1.1.5.4 Other analytes

Glucose and lactates can be measured amperometrically by biasing the potential vs Ag/AgCl quasi-reference to oxidise the hydrogen peroxide with [44]. To obtain 3D cell embedded cultures, a cell suspension is added to the extracellular matrix (ECM) patterned surface for the cells to interact with it [36].

1.1.5.5 Assays and products of interest

Other than controlling the growth of cells and monitoring analytes, MBRs were utilised for applications ranging from drug and toxicity testing [37], green fluorescent protein (GFP) production [16], biofilm

monitoring of *Candida albicans*, cell-line screening and development of monoclonal antibody processes using CHO cells [24], to long-term monitoring of bacteria by controlling cell density with quorum sensing [63].

1.2 Microfluidics

Microfluidics is a microtechnological field dealing with the precise transport of fluids (liquids or gases) in small amounts (e.g. microliters, nanoliters or even picoliters) [64]. It is a suitable platform for the growth and monitoring of physiological parameters of small populations of living cells (including mammalian and plant cells) in nanobioreactors. Polydimethylsiloxane (PDMS) is one of the most popular silicone elastomers for the use in lab-on-a-chip (LOC) applications [65], [66] due to its temperature stability from -50°C to 200°C, chemical inertness, low cost and simple fabrication [67]. More importantly, it is permeable to gases (such as oxygen), impermeable to liquid water and non-toxic to cells [65], which makes it appropriate for mammalian and plant cell culture. Additionally, microfluidic channels of widths ranging from 10-100 µm can be fabricated onto PDMS through soft lithography, which utilises a mould that can be manufactured using photolithography.

1.2.1 Photolithography

Traditionally, photolithography has been widely employed in the semiconductor and microelectronics industry as a method for selectively crosslinking UV-sensitive photoresists, such as SU-8, to produce silicon integrated circuits. The Whitesides Group has also been adopting the same technology for microfluidics to fabricate polydimethylsiloxane (PDMS) stamps for microcontact printing [68] (or soft lithography) since describing it in 1993. The patterning and etching of photoresists on silicon has also influenced the fabrication of PDMS moulds from silicon masters for rapid prototyping of microfluidic systems [65], including Micro-Electronics-Mechanical-Systems (MEMS).

1.2.2 Oxygen (O_2) plasma treatment

MEMS biosensors have been utilised for purposes such as cell culture monitoring [69] and detection of methicillin resistant Staphylococcus aureus (MRSA) [70]. Many of these devices were fabricated with glass (or quartz) bonded to PDMS, one of the rapid prototyping techniques [65] widely popularised by Whitesides. The glass and PDMS substrates are typically treated with oxygen (O_2) plasma and brought into contact without pressure [71] PDMS consists of repeating units of O-Si $(CH_3)_2$; the CH_3-groups on its surface which get removed and substituted by polar (–OH) groups upon O_2 plasma treatment, rendering its surface hydrophilic. The reactive silanol (Si–OH) groups react with silanol groups on oxidised glass in a condensation reaction [65] to form an irreversible covalent (Si–O–Si) bond.

Various oxygen species are formed in the inner plasma chamber as illustrated in Figure 1-1. At the powered electrode, its surface is bombarded by high-energy ions and electrons (ion-dominant mode). The grounded electrode experiences mainly chemical reactions with reactive oxygen species and radicals (neutral-dominant mode) [72]. PDMS bonds to glass even with the lower power neutral-dominant mode. The PDMS-glass microfluidic chip could then be integrated with various bioassays with automation within a completely contained system to constitute a micro-total-analysis-system (μTAS) [73].

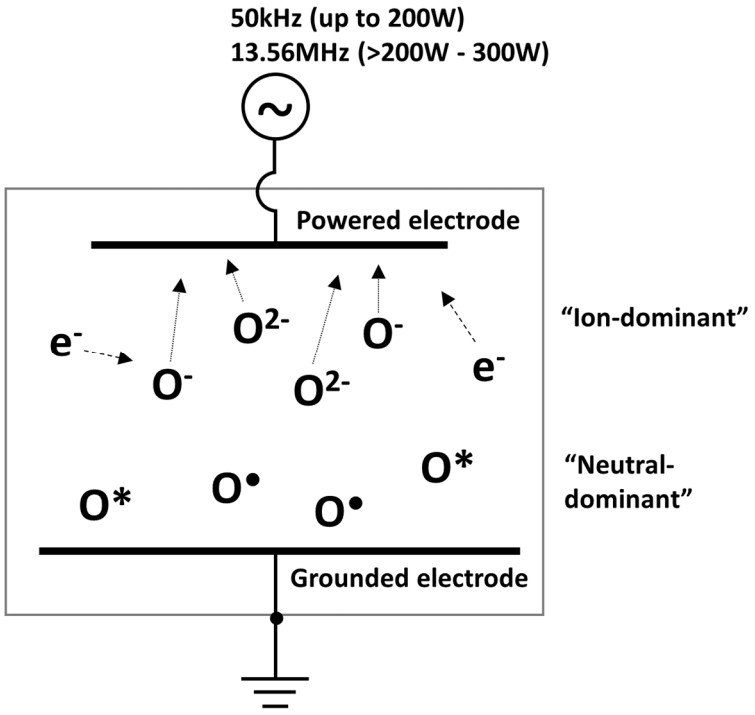

Figure 1-1: Schematic diagram of the inner plasma chamber depicting the "ion-dominant" and "neutral-dominant" configuration.

1.2.3 Fluid dynamics at the micro-scale

At the scale of nanobioreactors, there is a high surface to volume ratio. In a non-intuitive manner, the fluidic dynamics in a microfluidic chip are typically dominated by surface tension, viscosity and capillary forces. The fluid flow in a microchannel tends to be laminar, and is characterised by a Reynolds number (Re) less than 2300 [74], [75]. The Reynolds number is a dimensionless quantity measuring the ratio of inertial to viscous forces involving the density of the fluid, ρ (kg m^{-3}), fluid velocity, υ (m s^{-1}), characteristic length ℓ (m) (e.g. the diameter of a channel), and the kinematic viscosity, μ (N s m^{-2}) as depicted in Equation 1.3,

$$Re = \frac{\rho \upsilon \ell}{\mu}. \tag{1.3}$$

A Re higher than 2300 constitutes turbulent flow. Comparatively, the flow in a microfluidic channel is usually less than 10 or even less than unity. Another consequence to the high surface to volume ratio is the ease of heating and cooling a microchannel. There is therefore a need to introduce temperature control systems to avoid fluctuations [19]. A more comprehensive guide for microfluidics physics and phenomena could be found elsewhere [76].

Microfluidic (Lab-on-chip) LOC devices possess the dimensions and volume handling capacities to manipulate and sample single cells; however, the small absolute amount and low concentrations of the cellular species of interest present significant challenges for detection [77].

1.3 Holographic sensors (holosensors)

To monitor these parameters, the biosensor must be able to detect small concentration changes within a small volume in the nanobioreactor without significantly consuming the analyte that will affect the accuracy of detection.

A biosensor is a chemical sensor that utilises a biochemical mechanism as the recognition system. It typically consists of a chemical (molecular) recognition element (receptor) which translates information from the biochemical domain, such as analyte concentration, into an output signal, and a physiochemical transducer, which converts the signal from the recognition system to a user quantifiable domain [78]. To put it simply, a biosensor converts an unknown analyte concentration to a corresponding signal quantity.

Reflection holograms have been utilised to create holographic (bio) sensors (holosensors) which are responsive to an extensive range of analytes. The analytes that have been studied with holosensors range from pH [79] [80], ionic strength [81], glucose [82]–[84], metabolites [85] (such as urea, penicillin [85] and L-lactate [86], [87]), proteases in stool samples [88], [89], hIgG antibodies [90], water in solvents [91], and alcohol concentrations [92], to metal ion (Li^+, Na^+ and K^+) [93] and divalent metal ion (Ca^{2+}, Mg^{2+}, Ni^{2+}, Co^{2+} and Zn^{2+}) [94] concentrations, hydrocarbon gases and other volatile organic compounds [95].

1.3.1 Alternative technologies

Other biosensing mechanisms include electrochemical measurement methods such as amperometry [19], [96], [97], cyclic voltammetry [98] and field-effect transistor sensing [55], [97], which have been traditionally utilised for measuring important physiological parameters such as carbon dioxide, pH, glucose and dissolved oxygen concentrations in a bioreactor. Fluorescence intensity [99] and phase modulation lifetime fluorimetry [55] are also useful in sensing trivalent metal ions, glucose, dissolved oxygen and pH. Other more expensive and bulky instruments involving spectroscopy, such as mid-

infrared spectroscopy and Raman spectroscopy [100] have also been utilised to measure the concentration of carbon dioxide, glucose and trace gases respectively. However, the aforementioned sensors are expensive, bulky, require extensive analysis and specialised knowledge, or consume the analytes to provide a measurement reading.

The analyte consumption can be neglected in most cases, but poses a problem on the nanolitre scale. Minute metabolic activity gets quickly quenched or consumed by the transducer to obtain a reading. In other words, there are many established techniques available for one-time measurement or as a diagnostic tool for downstream analysis. Real-time monitoring, on the other hand, requires that the sensor is integrated into the system for a more representative non-destructive measurement of the cellular environment.

Nanobiosensors produced using top-down fabrication (miniaturisation) of the electrochemical biosensors are not easily (and inexpensively) scaled up to commercial manufacturing levels (with necessary reproducilibilty and yield). Although they are typically sensitive, there are issues with scalability and reproducibility such as sensing components with consistent electrical behaviour [101].

Holographic (bio) sensors (holosensors) on the other hand, are equilibrative (non analyte consumptive) sensors which are inexpensive, customisable and straightforward (do not require a transducer to convert an analyte signal to a visually interpretable display). Consequently, it is foreseeable to integrate the miniaturised holosensor into a nanobioreactor. The nanolitre volume holographic sensors embedded within a microfluidic chip constitute a nanobioreactor. These sensors can be interrogated using white light to detect minute changes in metabolic analyte concentrations colourimetrically within the nanobioreactor.

1.3.2 Constitutents of a holosensor

A holosensor typically consists of a (plane mirror) reflection hologram recorded within the volume of a thin (~20 μm thick) hydrogel film. Embedded in the hydrogel polymer matrix are ligands or functional moieties that reversibly bind with specific analytes. Under the influence of different analyte concentrations, the hydrogel swells or contracts depending on the osmotic pressure caused by the change in chemical equilibrium charges within the gel matrix. Accordingly, the change in hydrogel thickness results in a corresponding change of the hologram replay wavelength. In other words, the colour of the hologram reversibly changes with different analyte concentrations.

If pH were to be the analyte of interest, embedded functional pH moieties will act as the biological (pH) recognition element, the hydrogel (referred to as “gel” in this thesis) will function as the

transducer, and the resulting hologram colour will display the corresponding blue/red-shift according to the pH change. A pictorial representation of the holosensor features is shown in Figure 1-2.

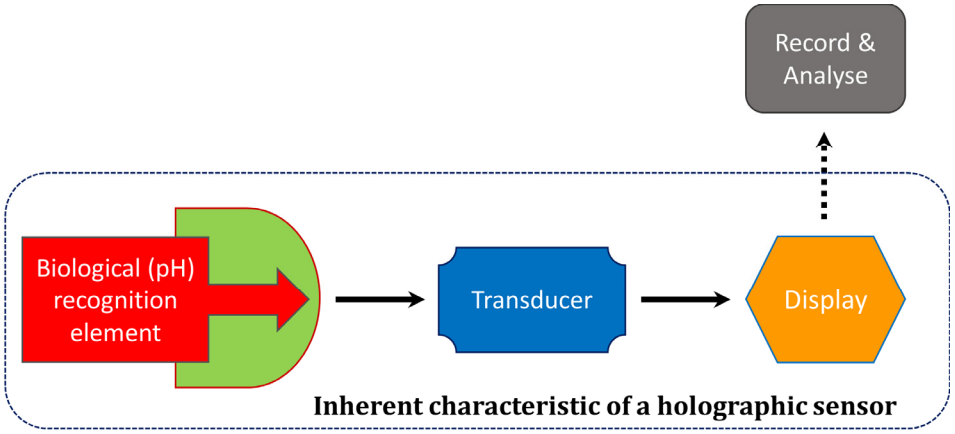

Figure 1-2: Features of a holographic sensor (holosensor)

1.3.2.1 pH (biological) recognition element

pH moieties are broadly categorised into two types: acidic and basic functionalities. Acidic pH moieties generally give up protons from the (–COOH) group above their pK_a and maintain a charged ($–COO^-$) configuration, while the basic pH moiety gains a proton below their pK_a to maintain a positively charged ($–NH_4^+$) configuration as shown in Figure 1-3. The maximum buffering capacity of the moieties is about ± 1 pH unit from their corresponding pK_a, while it still buffers (though not as well) beyond the ± 1 pH unit to ± 2 pH units.

At pH $\gg pK_a$, almost all the acidic moieties are charged. The net charge and their counterions of the pH moieties within the hydrogel (gel) results in an osmotic potential, which imbibes water, expanding the gel [102]. Conversely, water flows out of the gel as pH decreases, contracting it. Since the basic moieties have completely opposite configurations at either ends of the pH scale, it would reason that the net charge within the gel at low pH (below its pK_a) would expand the gel while contracting it at high pH above its pK_a.

Acidic pH moieties			**Basic pH moieties**	
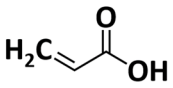	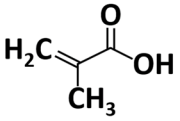	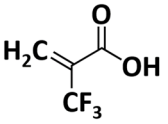	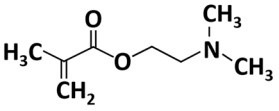	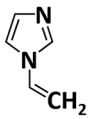
Acrylic acid **(AA)**	Methacrylic acid **(MAA)**	2-Trifluoromethyl propenoic acid **(TFMPA)**	2-Dimethylaminoethyl methacrylate **(DMAEM)**	1-Vinylimidazole **(VI)**
pK_a = 4.22 (monomer) pK_a = **4.58** (apparent)	pK_a = 4.50 (monomer) pK_a = **6.01** (apparent)	pK_a = 3.00 (monomer) pK_a = **4.45** (apparent)	pK_a = 8.40 (monomer) pK_a = **6.93** (apparent)	pK_a = 5.74 (monomer) pK_a = **4.56** (apparent)
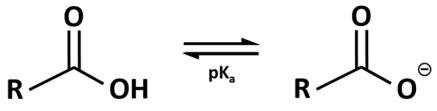			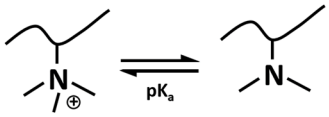	

Figure 1-3: Chemical structures and equilibrium of acidic and basic pH moieties. The monomer and apparent pK_a values were obtained from ref. [80].

1.3.2.2 Transducer

Stimuli-responsive hydrogels that undergo reversible volume phase transitions or sol-gel phase transitions upon minute changes in the environment are termed 'smart' hydrogels. This 'smart' hydrogel (gel) is the transducer for the holosensor [103]. The pH-sensitive gel is formed when a gel precursor solution is dispensed onto a glass substrate and illuminated with UV at 365 nm. This solution contains a monomer, 2-hydroxyethyl methacrylate (HEMA), a cross-linker, ethylene glycol dimethacrylate (EDMA), a pH moiety, 2-(trifluoromethyl) propenoic acid (TFMPA), and isopropyl alcohol (IPA) solvent (for gel porosity and as a chain transfer agent to control gel molecular weight), a free radical initiator, 2-2-dimethoxy-2-phenylacetophenone (DMPA), and an inhibitor, hydroquinone (HQ).

Upon UV exposure, DMPA undergoes photolysis [104] that forms primary benzoyl and acetal free radicals, for which the acetal fragment will further break down to methyl benzoate and a methyl radical [105] as shown in Figure 1-4. These radicals react with the (C=C) bonds in the methacrylates, which triggers chain reactions and initialises polymerisation and formation of the gel matrix. From Appendix A-1(b), it can be seen that 10% (w/v) DMPA in IPA absorbs UV up until about 385 nm. None of the other constituents of the gel precursor solution should also have their absorbance over that range, which was evidenced in Appendix A-1(a), which would otherwise compete with the initiator for the available UV, decreasing the initiator efficiency. The chemical structures of the other ligands, cross-linkers and monomers were also displayed on the same graph.

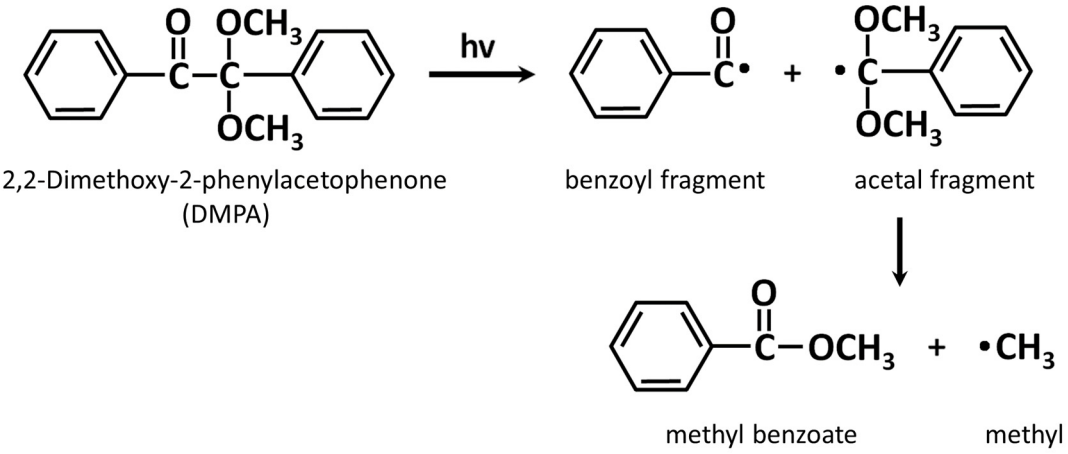

Figure 1-4: Photolysis of DMPA into primary and secondary fragments and radicals

On the other hand, hydroquinone (HQ) works as an inhibitor to quench the radicals produced during free radical polymerisation by donating protons and electrons [106] as shown in Figure 1-5.

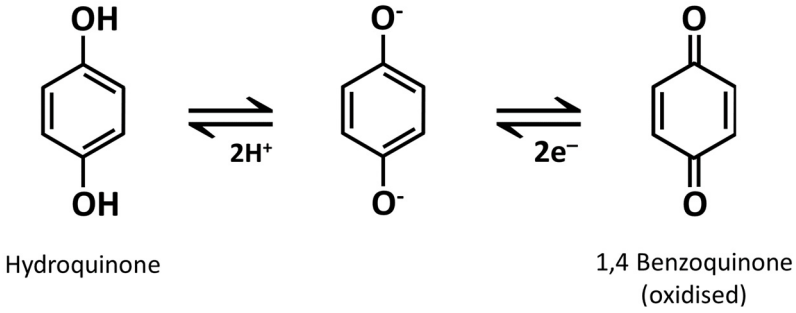

Figure 1-5: Oxidisation of hydroquinone to 1,4 benzoquinone (or para-quinone)

When a photomask is utilised, the UV-exposed region is quickly depleted of the inhibitor due to the overwhelmingly high number of radicals from the UV activation of the initiator and propagation of the radicals during the polymerisation process. At the unexposed region, however, the only radicals that can be found there are those that diffuse out of the exposed region, which could be taken care of by the inhibitor. Figure 1-6 illustrates the formation of polymers within the exposed blue region while the inhibitor helps control polymerisation by quenching radicals that diffuse into the unexposed region.

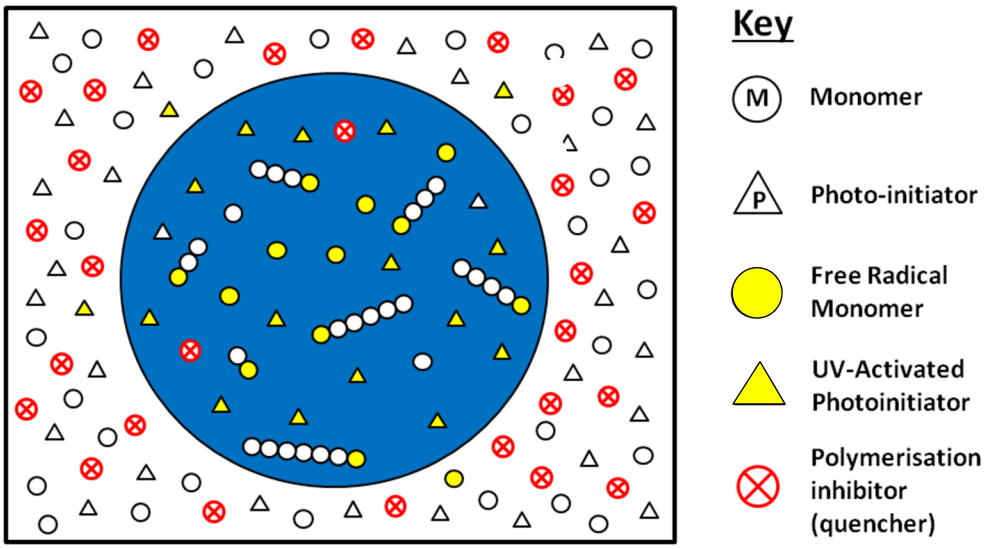

Figure 1-6: Controlling free radical polymerisation with an inhibitor (such as hydroquinone). The blue area represents the UV-exposure region.

1.3.2.3 Display (holographic)

The critical component of the holosensor is the display for the pH change. While the 'smart' hydrogel expands or contracts with pH variation, the volume phase transition has to be reported as a quantifiable measurand. A white light reflection hologram that changes colour and tracks the gel volumetric change can be recorded within the gel matrix.

A hologram is produced by the interference of two monochromatic light beams: the reference beam and object beam. The beams interfere and form standing waves within the gel matrix loaded with photosensitive AgBr formed by utilising a diffusion method [107]. The standing wave results in regions of constructive interference where the beam intensities add up, and regions of destructive interference where they cancel each other out.

1.3.2.3.1 Brief history of holography

In the 1890s, Gabriel Lippmann utilised the principle of interference to produce colour photographic images, for which he was awarded a Nobel Prize in Physics in 1908. Black-and-white photographs had typically been utilised to measure the difference in light amplitude incident onto the exposed photographic film. By utilising interference, the object's phase information can be recorded on the film emulsion as well [108], [109].

It was not until 1948 that Denis Gabor came up with the idea of holography while trying to improve the resolution of the electron microscope [110]. The term 'hologram' was coined by Gabor, the prefix 'holo' meaning 'whole' and the syllable 'gram' signifying a visual representation (or picture) in Greek. He carried out experiments with visible light from a filtered mercury arc, which had limited coherence,

but did produce his first hologram, which bore an image containing names of famous scientists such as Newton, Huygens, Young and Fresnel. For that, he was awarded the 1971 Nobel Prize in Physics for the discovery of the principle of holography. However, only after the first practical ruby laser was built in 1960 by Theodore Maiman that the holography of three-dimensional objects became possible due to the laser's significantly longer coherence length.

The theoretical aspects of Gabor's methods were refined by Emett Leith and Juris Upatnieks when they showed off-axis holograms in 1962 [111]. When Gabor's hologram was illuminated with the original collimated beam, it produced two diffracted waves, one reconstructing an object image in its original location and another with the same amplitude but the opposite phase, forming a second conjugate image. The original image was degraded and superimposed with the conjugate image and by scattered light, which caused a poor quality of the constructed image (holographic signal). The image problem was resolved by ensuring the reference wave was incident on the photographic plate at a large enough angle from the object beam. This offset technique was the breakthrough in the practical application of holography.

At the same time, without knowledge of Gabor's or Leith's work, Yuri Denisyuk drew inspiration from Lippmann's process of producing photographs in natural colours and experimented on an optical configuration different from Gabor's. The reference and object beams were incident on the photographic emulsion from opposite directions, and resulted in interference planes that were parallel to the emulsion surface rather than perpendicular to it, as Gabor's and Leith's were.

1.3.2.3.2 Latent image

Described by the Gurney-Mott mechanism, when a photon impinges onto an AgBr crystal, a photoelectron is liberated to a shallow electron trap site, which attracts interstitial Ag^+ ions and neutralises its charge ($Ag^+ + e^- \rightarrow Ag^0$). The accumulation of Ag^0 forms an aggregate at the electron trap zone, where the photolytic silver clusters (specks) constitute a latent image. This image is later amplified when the gel is developed to form a visible image [112].

1.3.2.3.3 Reflection hologram

When the reference beam and object beam interferes from different sides of the gel containing photosensitive AgBr crystals, the resulting reflection hologram can be viewed with the reflection of white light.

The hologram functions as a display by selectively reflecting a narrow band of light from an illumination white light source via reflection planes formed with the latent images derived from the constructive interference of standing laser waves as mentioned earlier in this section. Post exposure

superadditive development and fixing amplify the latent images and eliminates the unreacted AgBr (and non-reduced Ag^+ ions) to leave reflection planes within the gel matrix which let all other wavelengths pass right through except for a narrow band of light, functioning like a dielectric mirror.

1.3.2.3.4 Bragg's condition

A holographic sensor (holosensor) typically utilises a mirror as the object, to confer monochromatic and planar properties for accurate spectrophotometric measurements. The resulting periodic Bragg reflection planes (or fringes), resembling the slats of a venetian blind, adhere to the Bragg condition. The optical path length difference ($2\eta d\cos\theta$) is equal to an integer multiple, m, of the constructively interfered wavelength of light, λ, as described by Equation 1.4,

$$m\lambda = 2\eta d\cos\theta \,, \tag{1.4}$$

where η is the average refractive index of the gel, d is the fringe spacing between the reflection planes, and θ is the angle of the illumination light source with respect to the normal of the reflection plane. Some textbooks use $\sin\theta$ instead due to a different defined reference plane (parallel to the fringes instead of normal to it), and is actually conceptually the same.

1.3.2.3.5 Holographic signal offset

In view of Snell's law of reflection, the orientation of the embedded gel reflection planes (Ag^0 fringes) has to be offset by an angle, α, in order to separate the holographic signal from the reflection of the illumination light source from the glass substrate surface as shown in Figure 1-7.

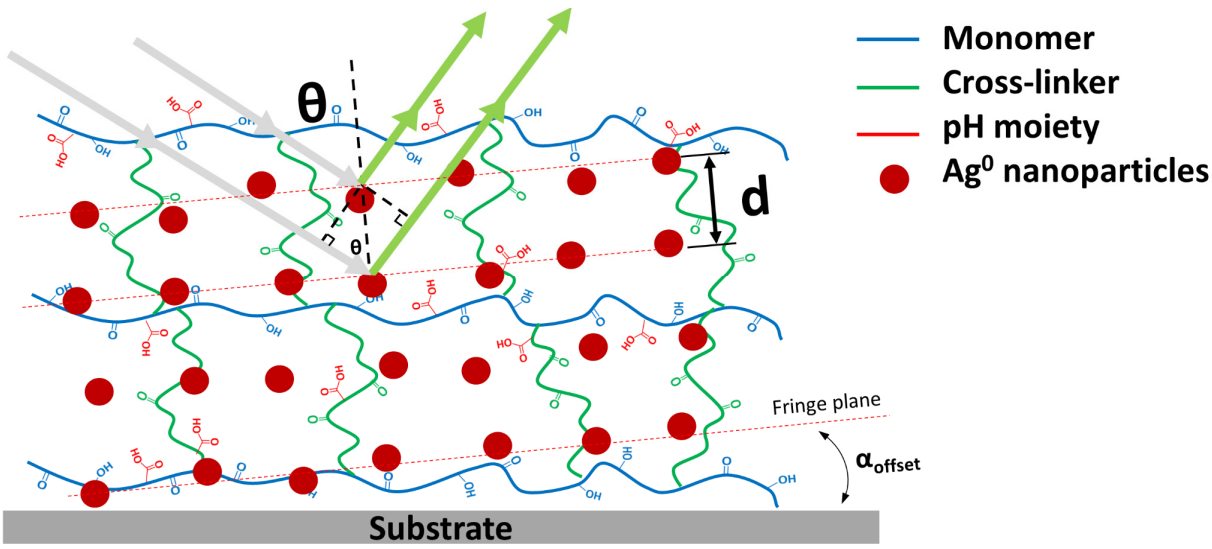

Figure 1-7: Schematic diagram of the Bragg's condition

The distance, d, between the fringe reflection planes, changes according to the expansion or contraction of the gel, which shifts the band of wavelength that reflects off the (Ag^0 fringes) reflection planes (after constructive interference) as the holographic signal.

1.3.2.3.6 Holographic signal interrogation

The holographic signal can be collected through fibre optic cables to a spectrophotometer in order to find out the peak wavelength response. Digital information of the hologram colour can also be collected as RGB values, and converted to the CIE xyY colour space using a transformation matrix (detailed in Appendix B). The xyY values can then be plotted on the CIE 1931 chromaticity diagram with the change in pH following a certain path (or locus) on the diagram.

1.4 Miniaturisation challenges and technology gaps

1.4.1 Process information available at miniaturised scale

Typically, micro-scale cultures reduce cost by reducing usage of media. Yet, with the volume reduction, it directly affects sampling time and minimum sampling volume negatively. For example, a typical 50 µL sample volume for high-performance liquid chromatography (HPLC) taken from a 100 nL nanobioreactor requires 500 turnovers of the chip volume. With a 1 h^{-1} bacterial growth rate, a single sample can take 500h, which results in only end-point measurements [33]. It suggests that there is no environmental control and monitoring existing at the scale below that of microplates.

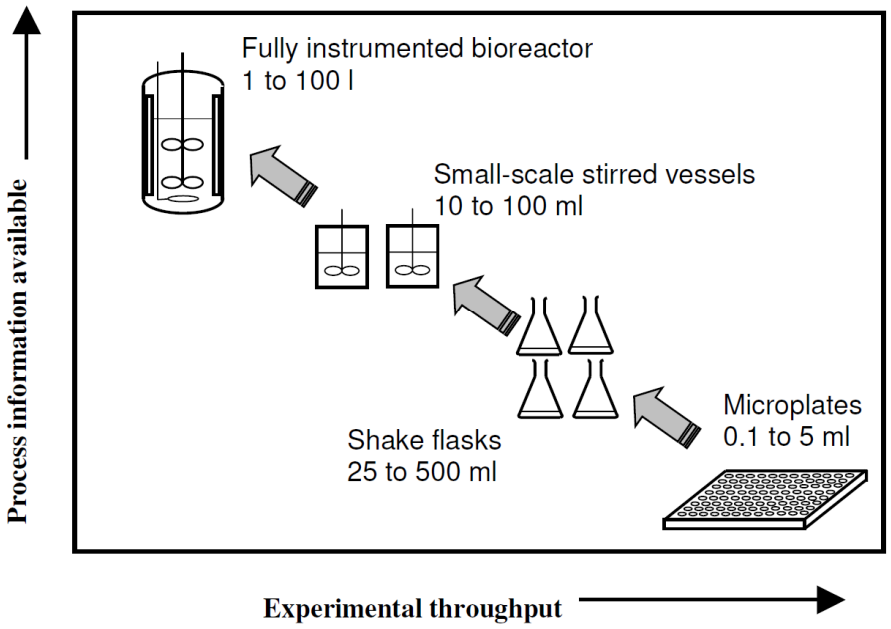

Figure 1-8: Illustration of trade-off in information output versus HT capability that currently exist for various cell cultivation devices at different scales. This figure shows that as bioreactors increase in scale, typically more process information is available due to improved monitoring and control systems. Reproduced from Open Access article ref. [8] *distributed under the terms of the* Creative Commons Attribution License.

Consequently, there is a fundamental requirement for millilitre or microliter scale bioreactors (and definitely including nanobioreactors) to obtain OD, pH and DO data in real time to avoid the need for sample removal and sampling [113]. Various sensing techniques, i.e., electrochemical sensors, fluorescence sensors, quorum sensing, and bioluminescence sensors were utilised to obtain control over different cell culture parameters as mentioned in §1.1.5. There seemed to be a limit to how small the sensors can be miniaturised to, as evident by the smallest working microbioreactor (MBR) volume mentioned in §1.1.4.2. There is thus a need to address this bottleneck before sensors can be integrated into a nanobioreactor of volumes smaller than 100 nL.

1.4.2 Detectable limit of holograms

In order to detect the holographic signals and use the RGB values of the holosensor for analysis, the photodiode has to be sensitive enough to distinguish the background noise from the signal. Especially if the holosensor were to be miniaturised, the difficulty of detecting the signal will increase by a multiple of the ratio of their characteristic length squared. For instance, a 5.0ϕ holosensor would be $\frac{5^2}{3^2} = 2.78X$ brighter than a 3.0ϕ holosensor, but will be $\frac{5^2}{0.5^2} = 100X$ brighter than a 0.5ϕ holosensor even though it is only 10X larger. This means that the hologram fabrication technique cannot be scaled down with the same photodiode interrogating the holosensor. Either the photodiode has to be made 100X more sensitive, or the hologram has to be made 100X brighter.

The angular intolerance of the holographic signal also makes it challenging to detect. The contrast between the hologram and the background has to be high in order to distinguish the actual signal from noise. Additionally, the (optimal) light brown colour of the gel depending on the size of Ag^0 nanoparticles, which originates from the scattering of light off the reduced Ag^0 planes, is a constant source of noise that will interfere with weak holographic signals at every interrogation angle.

1.4.3 Buffering capacity of the holosensor

Although holographic sensors are equilibrative (non-consumptive) and do not consume the analyte it is measuring, it still has to be in equilibrium with a small volume of analyte. This buffering capacity has been taken into account and its effects will be minimised (to 1% error) if the nanobioreactor chamber in the microfluidic chip is larger than a calculated volume ratio with the hydrogel volume. Accordingly, the gel height will have to be below 40 μm (examples of calculation with 1% and 5% buffering capacity effect for 0.46 mm ϕ and 3.27 mm ϕ gels were detailed in Appendix L) for the buffering capacity to be safely neglected.

1.4.4 Dimensional control of gel

As the buffering capacity differs with gel volume, the control of both the gel diameter and height are important, particularly its diameter. By taking partial derivatives and summing for the total derivative of gel volume, V (assuming the gel is cylindrical),

$$\frac{\Delta V}{V} = \frac{2\Delta D}{D} + \frac{\Delta h}{h}, \tag{1.5}$$

where D is the gel diameter and h is the gel height. Equation 1.5 illustrates that a small change in D has a 2X larger effect on volume (and hence its buffering capacity) than the same margin of change in gel height.

As a general guideline, the height of the gel (emulsion film) should be at least 10 wavelengths thick [114] for the fringes (or Bragg planes) to select the appropriate band of wavelengths to reconstruct the holographic image. When using a 532 nm laser for hologram fabrication, that translates to a little over 5.32 μm in gel height.

1.4.5 Effect of ionic strength on pH holosensors

Since pH holosensors rely on the charges on the pH moieties inside the gel matrix to elicit a corresponding pH response via their expansion/contraction mechanism, any other charges would also interfere with the pH response and provide inaccurate readings. A change in ion concentration such as that of Na^+ or K^+ will also affect the osmotic pressure of the gel, modifying the pH holosensor response even when pH remains the same.

1.4.6 Unbleached vs bleached holosensor

Current holographic sensors have volumes in the range of microlitres (~20 μL) and the hydrogel is deposited onto the traditional glass substrate. Appendix C-1(ai – aiii) illustrates a typical holosensor pictured with its hologram when illuminated at an angle. Other than the gel height variability along the substrate, there is also a difference in gel colour due to different levels of Ag reduction within the gel matrix. The problem can be resolved by bleaching the hologram to introduce a halogen such as iodine to form transparent silver iodide, which makes the gel transparent (Appendix C-1(aiv & av)). The colour uniformity is resolved but the photosensitivity of bleached holosensors will cause gradual darkening and unpredictable degradation of the sensor signal.

1.4.7 Tape mask fabrication method

A tape with a hole punched out can be utilised as a mask during hologram fabrication selectively to isolate the hologram where the hole was. Since the gel coated the whole slide, and the diffusion of

the silver and bromide salts is anisotropic through the gel, the resulting gel on the substrate looks messy as illustrated in Appendix C-1(bi & bii). The mask applied only during laser exposure (Appendix C-1(biii & biv)) made it even more difficult to detect the hologram itself.

Pressure-sensitive adhesive tapes generally fit into two categories, those with acrylic-based adhesives and those with silicone-based adhesives.

1.4.7.1 Acrylic-based adhesive tape

The greatest advantage of acrylic-based adhesive tapes is that they could be made thin, down to even 10 μm in thickness, which is the ideal thickness for holosensors. However, the acrylic-based adhesives dissolve easily in alcohols, which make them unsuitable to be used with the IPA-based gel precursor solution. 'Flash', a thin layer of undesired photo-polymerised gel, sometimes forms just outside the masked region (due to the diffusion of the initiator out of the photomask UV transparent window) during UV exposure. The 'flash' is covalently bonded to the rest of the gel, which ruptures the gel when the cover substrate is peeled off after UV photo-polymerisation. Additionally, the tape leaves a residue at its outer edges when peeled off, as indicated by the white arrow in Appendix C-1(d). It is thought that the acrylic-adhesive residue could have been implanted into the gel matrix itself during polymerisation, causing the gel to be tacky.

1.4.7.2 Silicone-based adhesive tape

PTFE and silicone-based adhesives such as the heat resistant polyimide Kapton tape are mostly non-reactive to organic solvents, although some silicones like PDMS swell with solvents. However, the thinnest silicone-based adhesives are 50 μm thick, much thicker than desired. Nevertheless, silicone adhesive tapes can be cut with CO_2 laser to their desired shape (Appendix C-1(e)), and the gel precursor solution dispensed into the well for photo-polymerisation, with the corresponding gels shown in Appendix C-1(f).

1.4.7.3 5.0ϕ HEMA-co-MAA holosensor

Using the punch and tape method, the holographic sensor can be reduced to about 1 μL, with appreciable dimensional uncertainty. Preliminary work on a 5.0ϕ HEMA-co-MAA pH holosensor utilising the tape-mask method, including pH characterisation using known pH buffers, is presented in Appendix C-2.

1.4.8 Other methods of gel fabrication

Prior to this work, holographic sensors were fabricated using a pulsed 350 mJ 532 nm laser. Either a 10 ns pulse for the traditional photochemical method [80], [83], [85]–[87], [92], [94], [115]–[119] or 6 ns pulse for the ablation method [120]–[123] was utilised to produce the hologram. The former

involves an adapted technique from photography development while the latter encompasses the formation of a holographic element within the gel matrix by ablating the larger developed Ag^0 grains into small ones. Both use the experimental setup described in Figure 1-9.

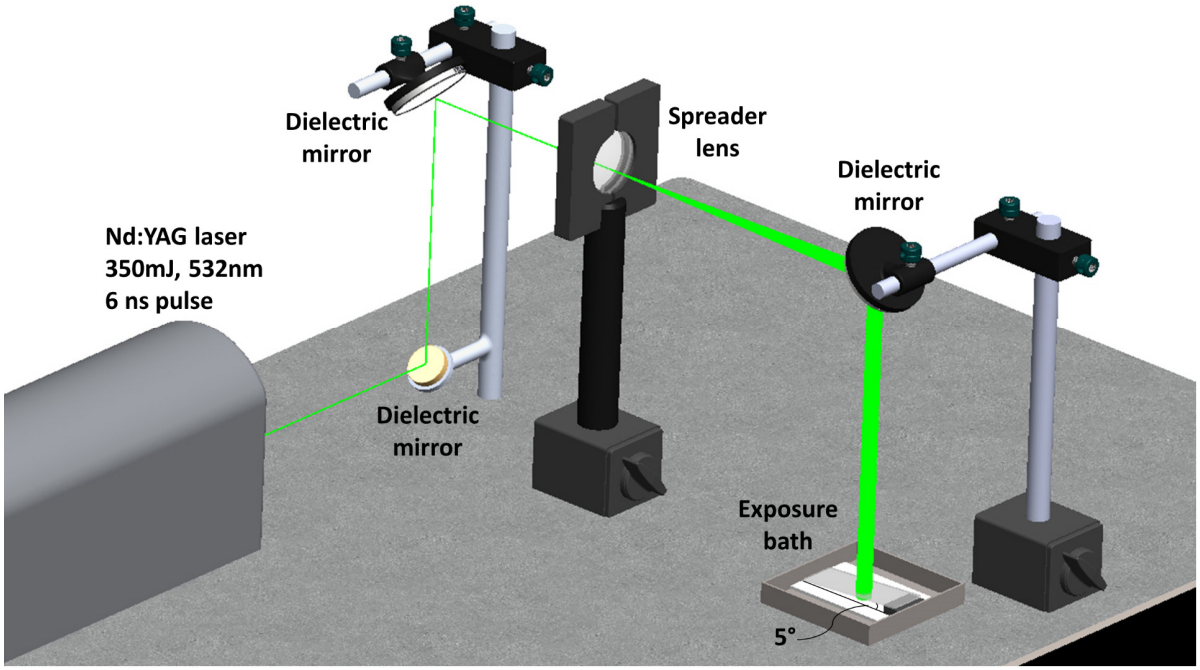

Figure 1-9: Experimental setup for pulsed laser. Reprinted from ref. [123] *with permission of The Royal Society of Chemistry. Copyright© 2014.*

Flake holograms under 1 μL in volume have also been fabricated [124], but they can only be fabricated in suspensions or as a random coating on a substrate. Heat-activated polymerisation with ammonium persulphate and tetramethylethylenediamine (APS-TEMED) introduces a heat gradient, which causes undesired polymerisation where there is heat diffusion.

1.5 Holographic pH sensor in nanobioreactors

Monitoring pH is critical in numerous industrial processes such as biopharmaceutical manufacturing, as pH control is vital for the optimisation of key parameters such as yield and product quality [125]. Marshall *et al.* produced the first pH sensitive holographic sensor in 2003. A variety of different hydrogel compositions containing pendant ionisable pH functional groups were synthesised as thin films ~ 10 μm thick and utilised as pH sensitive reflection holograms. The poly-HEMA-co-MAA (6 mol%) holographic sensor was able to measure pH over a linear range (pK_a ± 1) with a sensitivity of ~165 nm/pH unit, equivalent to a pH resolution of 0.006 units [80]. Lowe *et al.* in 2004 suggested that an array of 3 mm "spot" holographic sensors could be produced using a contact-printing process whereby a fluorinated ethylene-polypropylene polymer (FEP) mask is used to produce the holographic support medium. The FEP, which is oxygen rich, inhibited polymerisation occurring in the masked regions, allowing the development of the holographic spots where there were no inhibition [118].

In 2011, Bell utilised the tape method to fabricate a spot holosensor with an area of about 1 cm^2 (10 μL, 11.3 mm diameter, 100 μm height) and incorporated it into a microfluidic chip to monitor the growth of *Lactobacillus casei* [79]. Three optically interrogated microfluidic devices for biological use were presented: an encapsulated pH sensitive holosensor, an expanded holosensor device with ethanol / internal calibration, and a hydrodynamic trapping array for use with fluorescent photo-activation localisation microscopy (FPALM). The reported maximum sensitivity of the pH MAA (6 mol%) and TFMPA (6 mol%) holosensor at its peak response ($pK_a \pm 0.5$) were ~41 nm/pH unit and 115 nm/pH unit, equivalent to a pH resolution of 0.024 and 0.009 units respectively.

In order to utilise a holographic sensor (holosensor) in a nanobioreactor, the holosensor has to be miniaturised to below 0.8 mm in diameter (assuming 20 μm gel height) to be below 10 nL in volume. In order to validate the miniaturisation method and demonstrate the utility of the holosensor for cell culture monitoring, a pH holosensor can be integrated into a nanobioreactor to monitor the change in pH during cellular growth. Due to the small size of the required holosensor spots, an optical method coupled with collimated UV source and addition of an inhibitor could be utilised to ensure photomask fidelity.

1.6 pH monitoring of *Lactobacillus casei (L. casei)*

A 'model' microorganism is required to ensure the holosensor measured only the change in pH, that is, the microorganism should not have complex metabolism that changes significantly according to its cellular environment, such that an alternative "gold standard" method cannot be utilised simultaneously to track the efficiency of the holosensor. In other words, for a pH sensor, the 'model' microorganism is one that exhibits a consistent pH change throughout its growth that can be monitored with another parameter, such as optical density or actual cell count, for sensor validation.

Lactobacillus casei (L. casei) is a Gram-positive non-spore-forming homolactic fermentative bacterium, producing two lactic acid molecules from every glucose molecule. Only the L-enantiomer of lactic acid is formed. It is a facultative anaerobe – preferentially non-aerobic, but aerotolerant, acid-tolerant and strictly fermentative. The *L. casei* strain Shirota cells extracted from Yakult are rod-shaped and are 0.4-0.6ϕ x 2-3 μm in size. The strain is able to grow between 27°C and 43°C with an optimum at 37°C. It can grow at 15°C, but not at 45°C, and can grow at a pH as low as 3.5, though its optimal pH is 6.5 [126]. They are safe to handle, inexpensive and metabolically consistent compared to a more popular and extensively studied bacterium, *Escherichia coli* (*E. coli*).

1.7 Research scope

The market for recombinant therapeutic proteins, and how microbioreactors could aid in the development of high product yields, has been described above. The potential of multiplexed, well-controlled and cost-effective parallel experiments performed with embedded biosensors is analysed and could be facilitated by microfluidics. A review of conventional sensors was discussed together with their drawbacks, while the non-consumptive holographic sensor (holosensor) as the ideal nanobiosensor for nanobioreactors, and how it could be integrated into a microfluidic chip for cell monitoring, are suggested. *Lactobacillus casei (L. casei)* has been chosen as the model microorganism to demonstrate such a capability, with plans to extrapolate the cell monitoring application to mammalian cell culture.

1.8 Aims and objectives

Previous work has been done for pH holographic sensors [80], flake holograms [124] and (~20 μL) gel volume holosensors [79]. The next step forward would be to further miniaturise the pH holographic sensor (holosensor) to below 10 nL in volume in a < 100 nL microfluidic chamber for monitoring the growth of microorganisms, which constitutes a nanobioreactor. In this regard, the objectives of the project are to:

- Realise a method for the production of holographic sensors (holosensors) bright enough to detect the holographic signal at 30X magnification at the 1.05 ms integration time limit of the spectrophotometer with a resolvable signal-to-noise ratio.
- Develop a method to miniaturise the pH holosensor in a replicable manner for use in a PDMS-glass nanobioreactor to monitor the growth of *Lactobacillus casei* (*L. casei*) while accounting for any ionic strength variations.
- Demonstrate proof-of-concept of a miniaturised pH holosensor array capable of independent pH measurements.
- Investigate the utility of employing a miniaturised pH holosensor for cell culture.

2 Chapter 2 Materials and Methods

2.1 Materials

The sources for substrates (glass, plastics, and silicone elastomers) and chemical reagents (gel precursors, substrate modification and bonding, holosensor fabrication and calibration can be found in Appendix AB.

2.2 Laboratory equipment and apparatus

The sources for the commercially available equipment utilised for the work done in this thesis (involved with substrate preparation, gel fabrication and characterisation, holosensor fabrication, interrogation and validation) can be found in Appendix AB.

2.2.1 Custom-made commercial apparatus

2.2.1.1 Customised gel fabrication apparatus

Figure 2-1 illustrates the schematic diagram for the customised apparatus setup. It consists of the film photomask (base or top photomask with pattern), glass-chrome photomask (with pattern), silicone spacers, poly (methyl methacrylate) (PMMA) spacers and cyclic olefin copolymer (COC) and sample glass substrate (though it could be PMMA, PC, PS or PET as well). The parallel UV (365 nm) beam was produced by UV-LED smart.

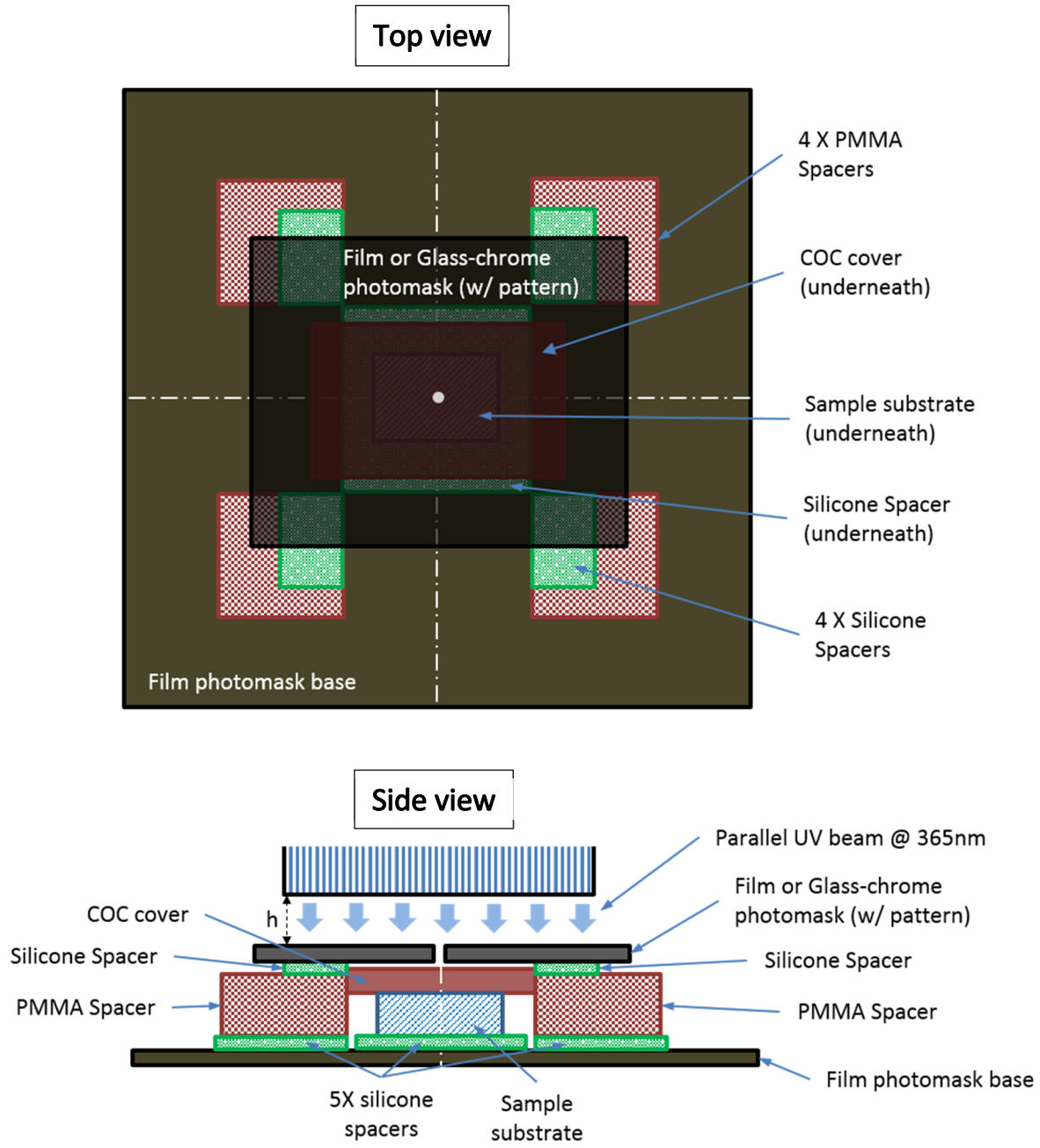

Figure 2-1: Customised apparatus setup (Top & side view) for photo-polymerisation of gel using parallel beam UV @ 365 nm.

2.2.1.2 Customised hologram fabrication apparatus

The fabrication requirements were designed and customised based on identified requirements - a continuous-wave (CW) laser, half-wave plate and adjustable tilt-yaw mirror mount were chosen and included into the experimental setup over the conventional pulsed laser system [80], [83], [85]–[87], [92], [94], [115]–[119] for their respective intensity, polarisation and alignment control.

The components of the customised setup for hologram fabrication were purchased from Acexon Technologies Pte Ltd, Singapore. The customised system consists of a 532 nm single longitudinal mode (SLM) TEM_{00} DPSS (diode pumped solid-state) 50 mW 532L-2B MatchBox2™ (Integrated Optics UAB) CW Class 3b green laser, a 405 nm continuous wave (CW) SLM TEM_{00} VBG (volume Bragg Grating) diode 40 mW 405L-21A MatchBox2™ (Integrated Optics UAB) CW Class 3b violet laser, fabricated platforms for mounting the two lasers at a designated height (see Figure 2-2(a)), AM-H1 air-cooled heatsinks with attached 40 mm fan for each of the two lasers, two half waveplate AR (anti-reflection) coated 990-0071-400H variable laser power attenuators (one for the 532 nm laser and the other for the 405 nm laser) housed in 840-0197 rotating holders (for low dispersion), 7T173-20-50 adjustable 50 mm travel linear stage with a mounted 5BM131-1-2SM Standa protected silver mirror, a 1-PCV-2-A127 Altechna plano-concave lens, two custom-made manual shutters (one for each laser), a 10IBS10-5-0.5-AR iris diaphragm (0.5 – 5 mm aperture) and an adjustable tilt-yaw post (3APC-12-32 adjustable angle post clamps with 2SR32-20 200 mm silent rod) mounted with another protected silver mirror (@ 45°). All of the components were enclosed in a customised PMMA box (front side transparent and all other sides were black and opaque) fixed onto a vibration-isolation optical table as shown in Figure 2-2(b). The A-02-D12-BBF-USB laser power meter (up to 200 mW, for wavelength 190 nm – 25,000 nm) from Laserpoint was also purchased from Acexon. A 54082 ND filter (circular 0 – 0.4 OD) obtained from Edmund Optics Singapore Pte Ltd was used in place of the attenuator for the 405 nm CW laser.

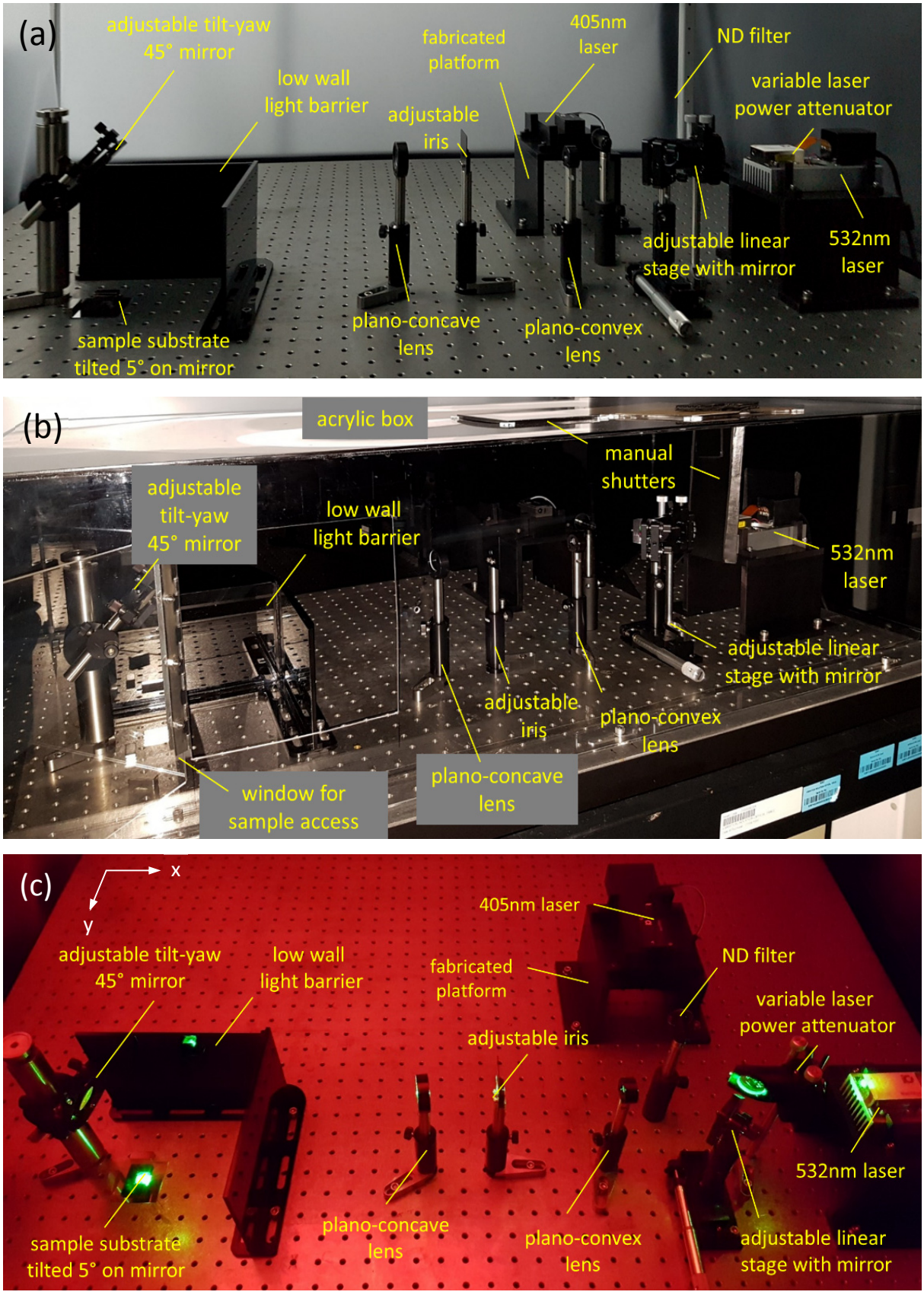

Figure 2-2: Pictures and schematic diagram of customised hologram fabrication apparatus. **(a)** Front view of experimental setup without acrylic box, featuring the low wall light barrier and adjustable tilt-yaw mirror. **(b)** Isometric view of experimental setup featuring the acrylic box with manual shutters. **(c)** Top view of experimental setup with 532 nm laser operating under red-safe light.

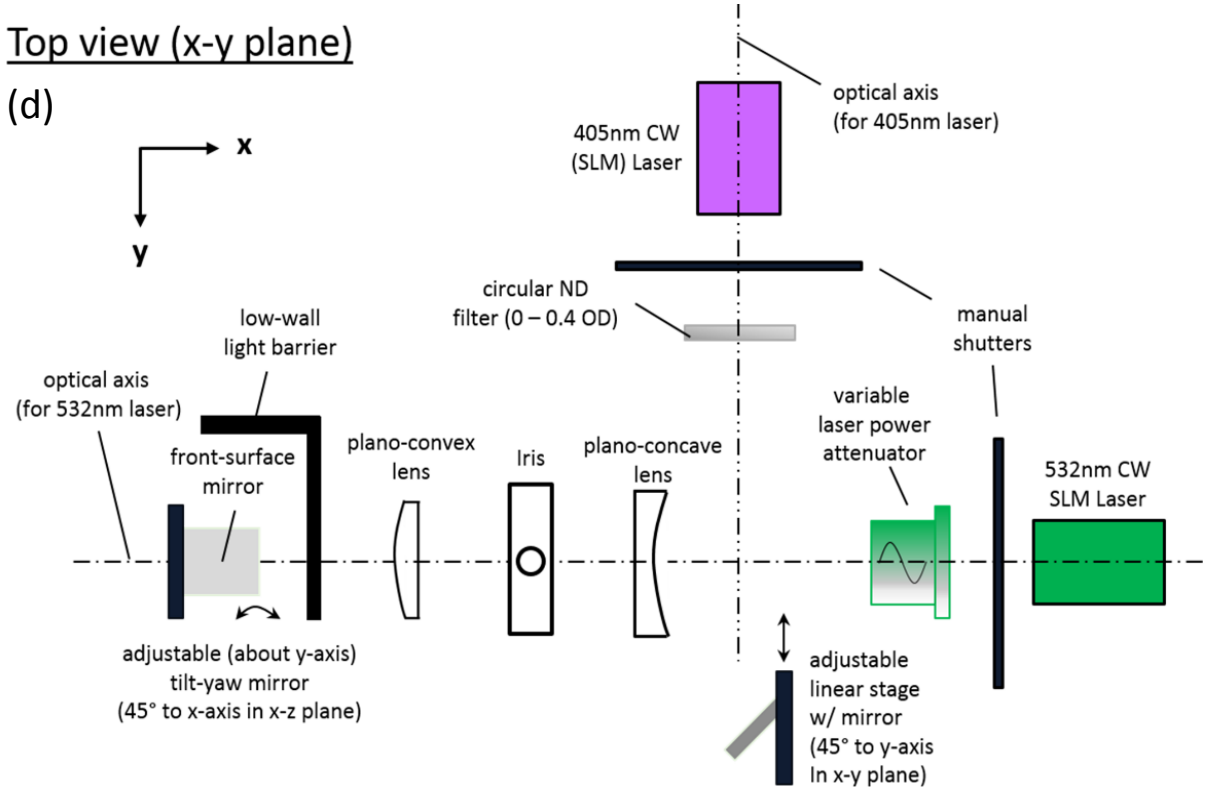

Figure 2-2 (contd.): **(d)** Schematic diagram (top view) of experimental setup labelled with all parts.

The sample substrate was kept at a constant offset design angle of 7.16° by placing it on a sample adaptor milled from Delrin® by Status P-E Pte Ltd as shown in Figure 2-3.

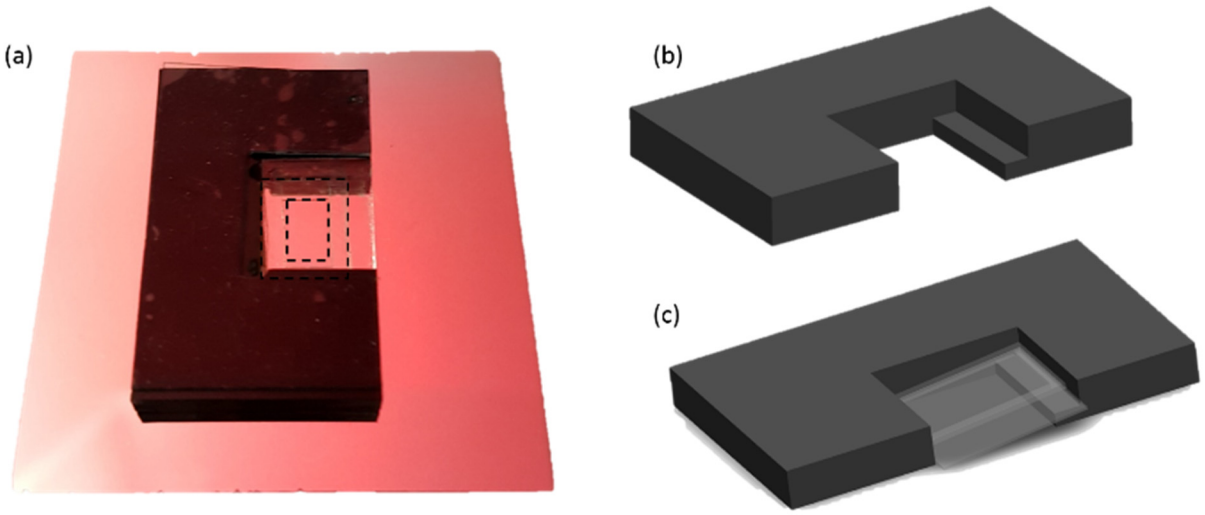

Figure 2-3: Picture and drawings of sample adaptor. ***(a)*** *Actual picture of sample adaptor with cover substrate and PDMS spacer (location highlighted by dotted lines) placed within the open chamber. The adaptor was pictured stuck to a 50 mm x 50 mm front surface mirror under red-safe lighting with a 0.25 mm thick interfacial PDMS layer laser-cut to the same "C-shape.* ***(b)*** *Drawing of Delrin® sample adaptor with step to convey a hologram-recording angle of 7.16°.* ***(c)*** *Drawing of sample adaptor with cover substrate and circumferential PDMS spacer (illustrated in lighter grey).*

2.2.1.3 Customised holographic sensor interrogation apparatus

A customised holographic sensor (holosensor) interrogation apparatus was procured from CRS Engineering Pte Ltd after defining the requirements and designing the assembly of the components in the setup. Additionally laser-cut parts were added for improved functionality, especially for the sample module.

The (optics) interrogation module (depicted red in Figure 2-4(a)) consists of the colour camera and connected 1-50486 12X zoom lens (12 mm fine focus), 1-6030 2X-adapter and 1-6010 C-mount coupler with attached 1-50013 0.75X lens attachment (for longer WD) mounted on a customised ZWG Z-stage from Mitsumi South East Asia Pte Ltd. The coupler, adapter, zoom lens and lens attachment were obtained from Navitar Inc. The colour camera coupler adaptor can be interchanged with the fibre optic cable leading to the spectrophotometer with attached (SMA connection) ATTN-DA-HAL-KP attenuator with iris range 0.00 – 12 mm via a 200 μm diameter core fibre optic cable (with collimator adaptor having external UNF 3/8-24 screw thread).

The lighting module (labelled blue in Figure 2-4) comprised of a fibre optic cable connected to the Avalight-Hal-S (Halogen-Tungsten), 6500K Prixmatic LED or Xenon light source (mounted on a KSP-606MR manual 65 mm rotary stage (obtained from OptoSigma Corporation, USA) fixed onto a customised TADC-652WS25-M6 manual 2-axis XY positioning stage (65 mm size, 25 mm travel), and integrated with a ZWG140 Z-stage from Mitsumi.

The sample module (depicted green in Figure 2-4) consists of a GFSG40-60 manual axis 40 x 40 mm goniometer mounted on an OEM x-y stage with 5OM61 Standa high stability optics mount (also from Acexon). A laser-cut customised adaptor was designed and fabricated to hold the inlet and outlet modified SH18-B-9018G (0.050” OD, 0.036” ID) blunt needle tips (procured from San-EI Tech Asia Pte Ltd) with interference-fit 95609-30 (0.113” OD, 0.0449” ID) and ND-100-80 (0.02” OD, 0.06” ID) Tygon® tubing from Cole Parmer. 0.25 mm thick PDMS spacers were laser-cut and utilised as spacers and leak-free contact for the interrogated microfluidic chip samples. The modified OBC-3045-M6 system base plate with M6 internal thread array and attached grips, measured (L) 300 mm x (W) 450 mm x (H), and was procured from OptoSigma.

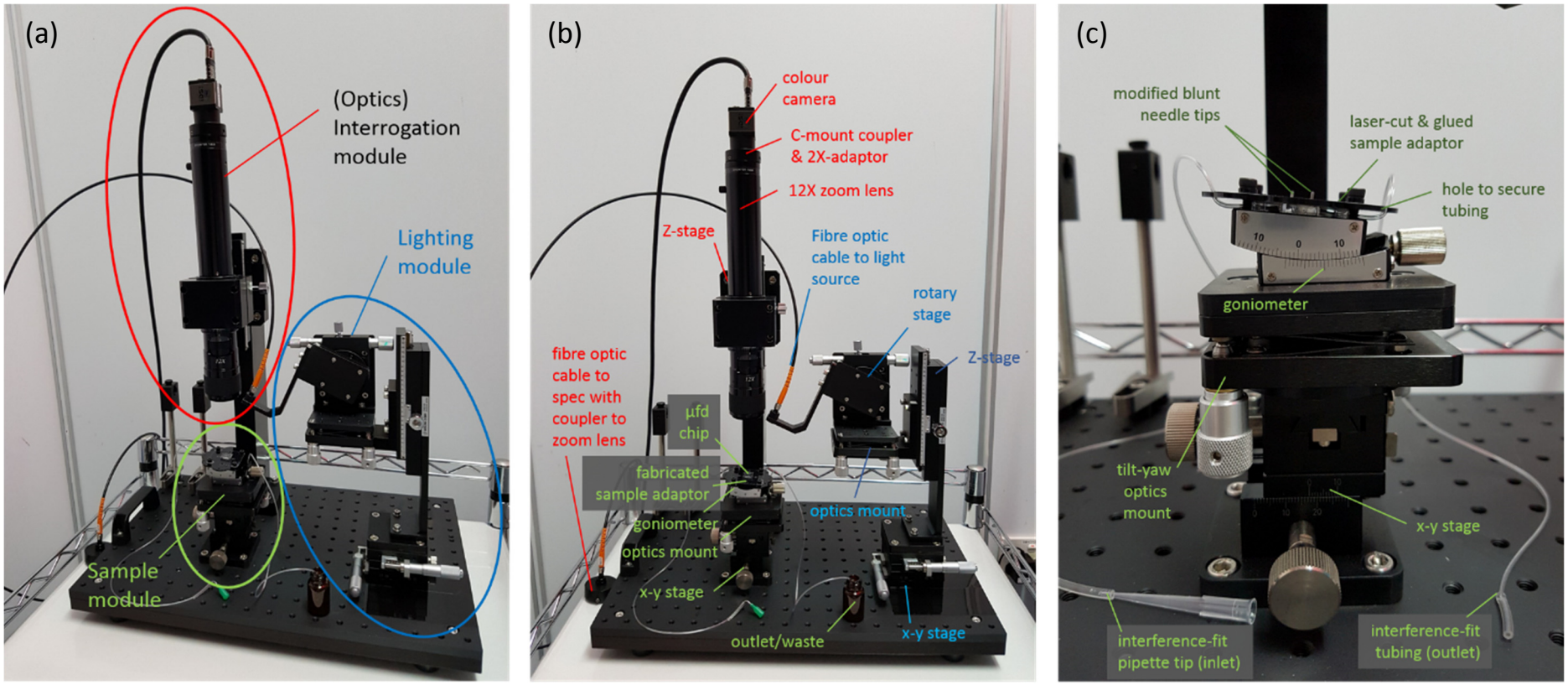

Figure 2-4: Pictures of the customised holosensor interrogation experimental setup. ***(a)*** *Various modules of the hologram interrogation system* ***(b)*** *Parts of each module (front view).* ***(c)*** *Close-up of the sample module and its constituent parts*

2.2.2 Laboratory-developed devices

2.2.2.1 Customised sample holders

2.2.2.1.1 Gel precursor solution vial holder

The customised 2 mL amber vial holder was made up of 60mm and 90 mm (diameter) polystyrene (PS) petri dishes, 5 mm thick poly (methyl methacrylate) (PMMA) and a 0.25 mm thick silicone (PDMS) films that were laser-cut to their desired designs. The PMMA and PDMS made up the internal pocket, which provides an anti-slip alignment feature for the vials. Parafilm "M" laboratory film was utilised to wrap around the holder cover in position.

Figure 2-5: Custom-made multi-vial holders (pictured with vials) – capacity: 8 and 22 for the 60mm and 90mm Greiner petri dishes respectively

2.2.2.2 Customised sample-storage apparatus

The customised apparatus, pictured and illustrated in Figure *2-6*(a) and Figure *2-6*(b) respectively, consisted of a 4" square petri dish, 0.25 mm thick laser-cut silicone PDMS film and laser-cut 1mm thick poly (methyl methacrylate) (PMMA). It was used to store the small (12.5 mm x 9.4 mm) cut silanised glass substrates. The semi-sticky silicone surface protected the sample surfaces, while the aluminium foil that was wrapped around the petri dish prevent light-inactivation of the silanised glass surface. It could be used to store two times more silanised glass substrates when a 2 mm high laser-cut PMMA shelf was fabricated and placed on top of the first layer without touching the substrates below.

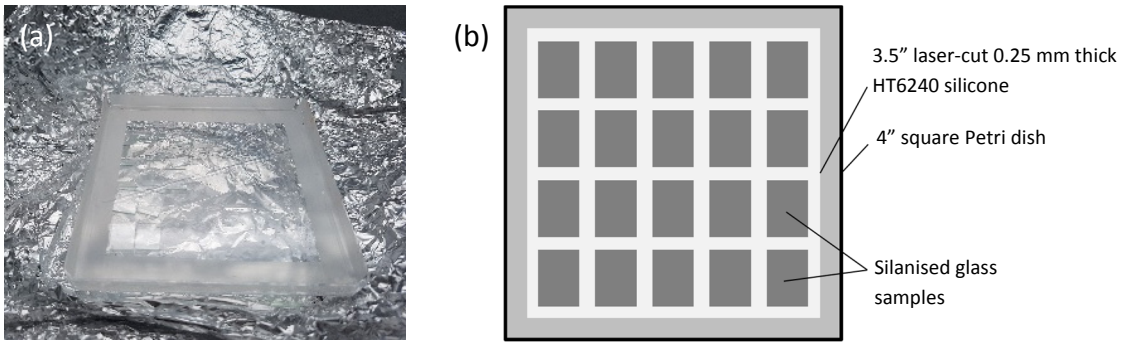

*Figure 2-6: **(a)** Sample storage apparatus pictured with aluminium foil opened up. **(b)** Schematic top view diagram of silanised glass sample storage apparatus*

Once the gels were cured, the photo-polymerised gels and holosensors on the substrates were stored between 2 pieces of silicone films backed with Mylar® film surfaces as shown in Figure 2-7. This protected the gels and substrates from scratches and dirt, and was easily customisable for better organisation and handling.

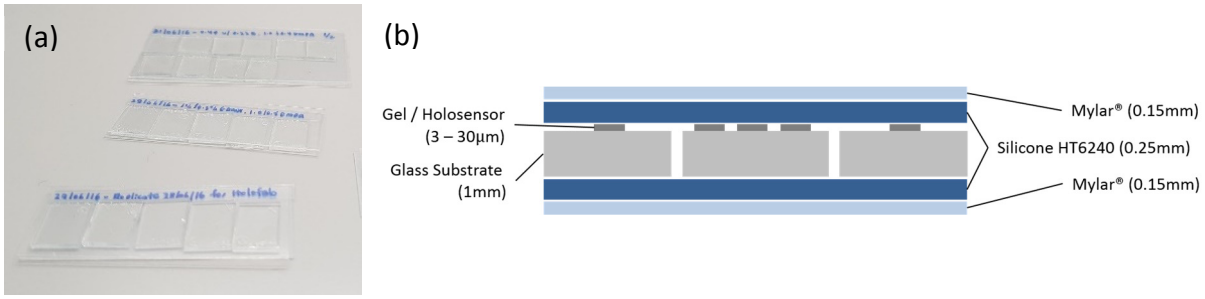

Figure 2-7: ***(a & b)*** *Picture and schematic cross-sectional view diagrams of sample-storage apparatus respectively*

2.2.2.3 Custom-made spin coater

The custom-made spin coater (shown in Figure 2-8) consisted of a 12V DC brushless CPU fan purchased from Maplin UK, a power supply unit obtained from RS Scientific UK, and crocodile clips purchased from Amazon, UK. The speed (rpm) of the CPU fan was controlled by varying the voltage from the power supply. The revolutions per minute (rpm) was measured and calibrated to the voltage with a digital DUSIEC non-contact tachometer, which was also procured from Amazon, UK. A tubular spirit level was utilised to ensure the fan was on a flat surface. The sample was mounted onto the CPU fan with double-sided foam tape on the 30 mm circular central portion of the fan. To prevent the coating solution from splashing all over, a 5L beaker was inverted and placed over the customised spin coater.

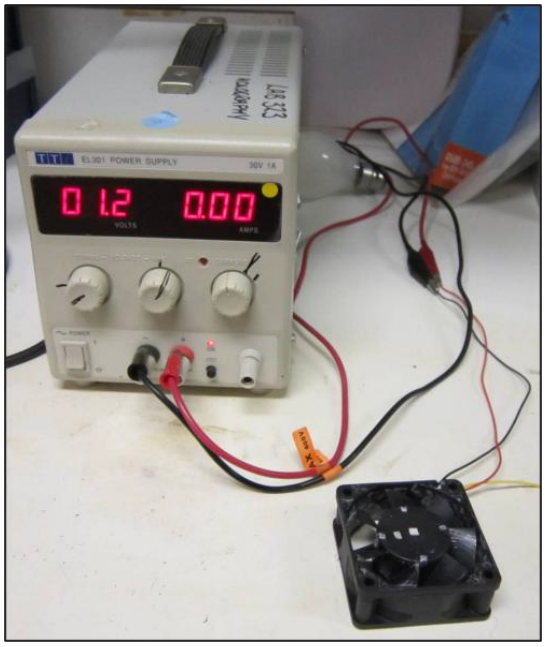

Figure 2-8: Custom-made spin coater

2.2.2.4 *Custom-made spectrophotometer enclosure*

An existing Shimadzu cell module shown in Figure 2-9(b) was modified for optical density (OD_{600}) measurements, but was recalled due to the machine shifting to another facility downtown. Transparent 5 mm thick poly (methyl methacrylate) (PMMA) sheets were cut according to desired design, and utilised for the customised insert on the cell module. Due to the lab shift, a custom-made spectrophotometer enclosure (Figure 2-9(a)) was designed and fabricated (via CO_2 laser cutting) with 5mm thick (matt spray-painted) PMMA for connection to the monochromator, and the other side to the spectrophotometer.

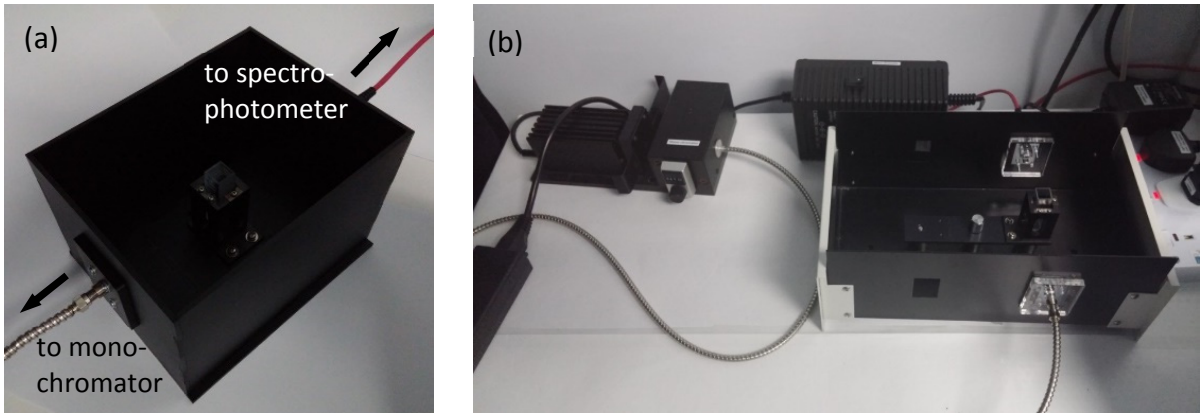

Figure 2-9: ***(a)*** *Custom-made spectrophotometer enclosure for optical density (OD_{600}) measurements and* ***(b)*** *modified Shimadzu cuvette cell module with monochromator and connected spectrophotometer respectively.*

2.2.2.5 *Customised hydrophobic-coating apparatus*

The customised apparatus (Figure 2-10) was put together by Ms Alicia Toh from SIMTech, MMP. It consisted of a Model 280A Isotemp® vacuum oven and an AV3 Edwards vacuum pump with oil filter, both of which were purchased from Fisher Scientific Pte Ltd.

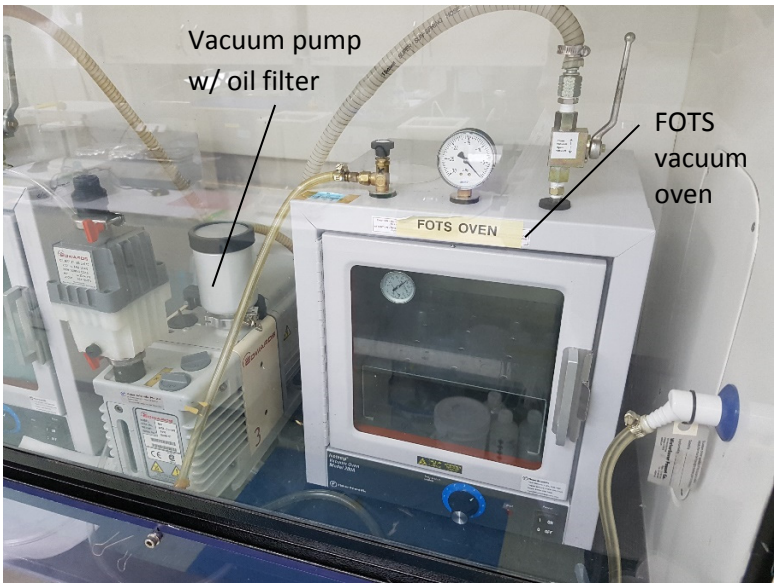

Figure 2-10: Customised hydrophobic-coating apparatus

2.3 Laboratory ware

The sources for the laboratory consumables and software utilised can be found in Appendix AB.

2.4 Methods

The outcome for monitoring *Lactobacillus casei* cell growth via a holosensor pH response was achieved using the following methodology:

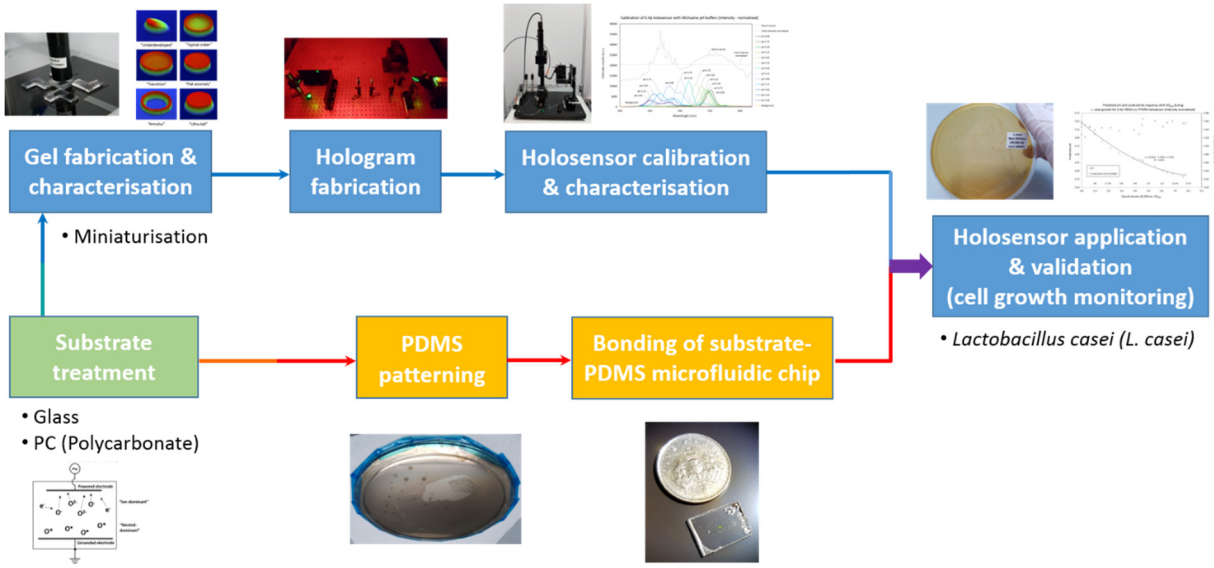

Figure 2-11: Methodology for monitoring L. casei cell growth via holosensor pH response. The research challenges were segregated and undertaken based on the process of holosensor miniaturisation and substrate-PDMS microfluidic chip fabrication.

The process starts with the surface treatment of the substrate for promotion of gel adhesion. UV photopolymerisation is utilised to form the gel on the substrate (§2.4.2.4), followed by the fabrication of an off-axis reflection hologram within the gel volume (§2.4.2.8). A polydimethylsiloxane (PDMS) cover with microfluidic channels and chamber is formed with soft lithography utilising a Ni mould (§2.4.1.1.3). The gel substrate is then aligned and bonded with the PDMS cover to form a PDMS-glass microfluidic chip (§2.4.3.1). pH buffers and cell culture media is introduced through pre-punched inlet/outlet fluidic holes. The corresponding pH responses of the holosensors are collected, characterised and calibrated. Finally, the holosensor-on-chip is then ready for validation by bacterial growth monitoring (§2.4.4).

Each step of the miniaturised holosensor fabrication and integration of the sensor into the microfluidic chip presents unique research challenges. Referring to Figure 2-11, the microfluidic chip fabrication (depicted in yellow) involved adhesion issues between gel and polymer substrates, as well as polymer and PDMS bonding. The issues involved in the miniaturised holosensor fabrication (illustrated blue in Figure 2-11) included (but were not limited to) realising gel profile uniformity and replicability,

acquiring inordinately bright holograms and monochromatic diffraction, detecting the diminutive sensor signal with off-axis illumination and interrogation, and minimising and/or deconvoluting possibly conflicting sensor responses and noise such as ionic strength during cell growth monitoring.

The production of a working holographic sensor can be further broken down into the following stages (elaborated in Figure 2-12):

1) Substrate preparation
2) Gel fabrication
3) Hologram fabrication
4) Holosensor interrogation and calibration
5) Holosensor application

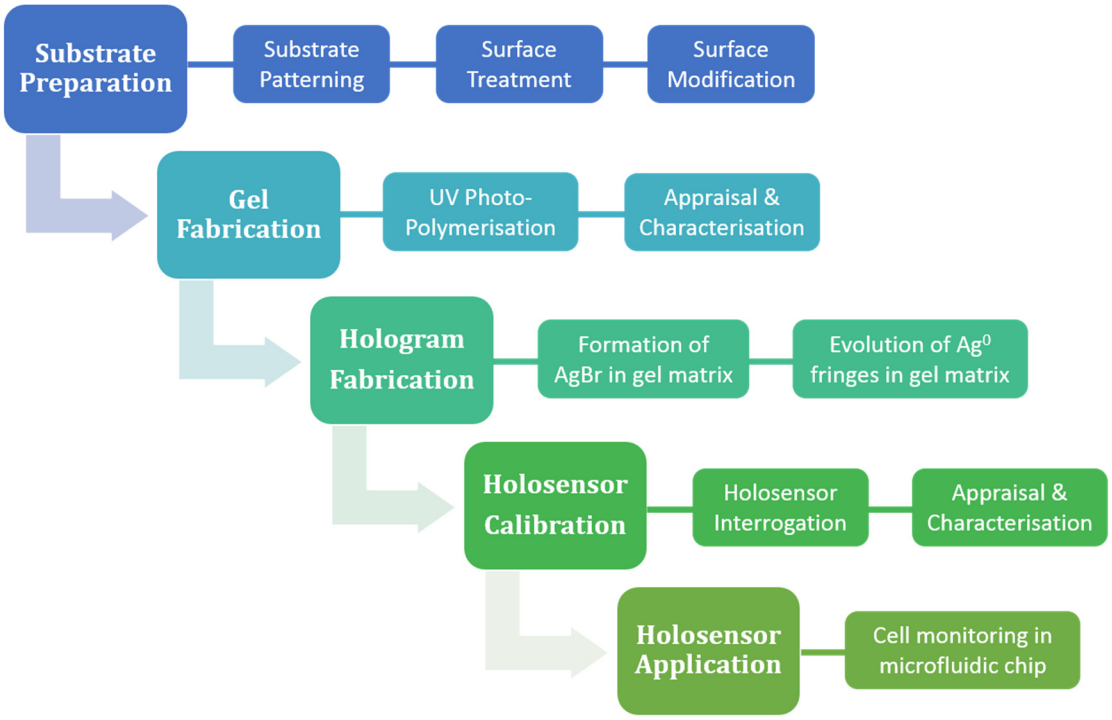

*Figure 2-12: Holosensor fabrication method flowchart – The production of a working holosensor (hologram within gel with analyte-sensitive ligands). Main processes are **(1)** substrate preparation, **(2)** gel fabrication, **(3)** hologram fabrication, **(4)** holosensor calibration, and **(5)** holosensor application*

Typically, a holosensor is fabricated by recording a holographic image using an ordered array of reduced silver nanoparticles (Ag^0 NPs) produced by standing laser waves within a photo-polymerised polyHEMA (pHEMA) gel on a glass substrate. Here, fabrication methods to produce miniaturised holosensors on a polymer substrate were investigated and employed.

2.4.1 Substrate preparation

2.4.1.1 Substrate patterning

The typical glass sample size is (L) 12.5 mm x (W) 9.4 mm x (T) 1 mm. This size was designated because it was 1/16th of a standard 76 mm x 25 mm x 1mm microscope glass slide – small enough to not waste material, yet just an appropriate size to handle and accommodate to the largest tested gel size of 3 mm in diameter. Glass was typically cut using the scribe-and-snap method (for gel-on-glass samples), or diced to the desired sizes with a diamond-tip dicing saw.

Injection-moulded PC and COC come in the form of discs, due to existing moulds. They are thin enough to be cut out with scissors, albeit not as flat and smoothed-edge as those that are micro-milled or diced.

2.4.1.1.1 Through-cut

Poly (methylmethacrylate) (PMMA), polystyrene (PS) petri dishes, poly(dimethylsiloxane) (PDMS), and various kinds of double-sided and single-sided tapes were cut to desired shapes and sizes with the CO_2 laser cutting machine (cutting recipes shown in Appendix A). 0.25 μm and 0.50 μm thick silicone elastomer (abbv. PDMS) sheets were cut to size with a pair of scissors or laser-cut with the laser cutting machine.

The plain injection moulded discs were fabricated with the help of Mr Han Yat Siew (SIMTech). The injection-moulded polycarbonate (PC) discs were cut to 8 mm x 8 mm (0.60 mm thickness) size with scissors to test for proof-of-concept PC-gel adhesion with alcohol-resistant properties.

1.0 mm thick polycarbonate (PC) sheets and 0.60 mm thick injection-moulded cyclic olefin copolymer (COC) substrates were cut to 12 mm x 8mm and 8mm x 8mm size with the milling machine attached with a 900 BTU/hr cold air gun from Vortec, USA. A 1600.0394.120 ϕ1 carbide end mill from Kyocera Asia-Pacific was typically utilised with 6000 rpm, 50-60 mm/min feed rate and 30 – 40 mm/min approach velocity for the 1 mm PC substrate. 6000 rpm, 40 mm/min and 20 mm/min approach velocity was used for cutting the brittle 0.6 mm thick injection-moulded COC. The micro milling was performed with the help of Mr Rahmad Bin Selamat (SIMTech). It is noteworthy that the CO_2 laser machine should not be used to cut PC. The polymer at the heat-affected zone will turn yellowish, the edges will deform, and toxic fumes will be produced. The fumes are not only hazardous to the user's health; they will also damage the optics of the machine.

Injection-moulded cyclic olefin copolymer (COC) discs were cut to 8 mm x 8 mm (0.64 mm thickness) size using the dicing saw machine with a diamond-tipped blade at 24,000 rpm and 1.2 mm/s feedrate

with the help of Mr Mohaime Bin Mohahidin (SIMTech). The cut samples were then used as a cover substrate during the gel photo-polymerisation procedure.

2.4.1.1.2 Scribe-and-snap method

To obtain the 1 mm thick microscope glass of typical sample dimensions 12.5 mm x 9.4 mm, the scribe-and-snap technique was used. The surface-treated and modified standard microscope glass slides were scribed along the centre of each slide with a diamond tipped scriber, and an elevated platform in the form of a glued toothpick on a cutting mat was used to align with the scribe line to snap the slide in two. For PC and PMMA substrates, the scribe line was aligned with the edge of a hard, thick PMMA and snapped by applying a large, sudden force downwards on the overhanging portion. The process of scribing and snapping in two was repeated until the desired sample size was achieved.

2.4.1.1.3 PDMS patterning via mould casting

Poly (dimethyl siloxane) (PDMS) with microchannel features for a microfluidic chip was realised by casting over a fabricated mould and allowing to cure at room temperature or in an oven. Part A (base) and part B (hardener or curing agent) Sylgard 184 elastomer (a.k.a. PDMS) was mixed at 9:1 w/w using the weighing balance. The mixture was further homogenised, degassed, and stabilised by spinning the cup containing the mixture at 1000 rpm for 80s, followed by 1900 rpm for 60s, and then 200 rpm for 60s respectively with the Thinky® mixer. It was then cast by carefully pouring the degassed mixture onto an electroplated nickel mould with the microfluidic channel features. The thickness of the PDMS was controlled by a 2 mm thick poly (methyl methacrylate) PMMA spacer (with 127 μm thick 3M tape) that was cut to shape and circumscribed to the mould area for PDMS casting within the mould. The edge of a cast polycarbonate sheet was used as a trowel to level the surface with respect to the top surface of the PMMA spacer. The mould with PDMS was then put into the vacuum packing machine for 5 cycles, or until there are few or small bubbles that do not disappear with subsequent vacuum cycles, whichever was more. Thereafter, it was cured by leaving it on an optical table overnight to allow the PDMS to flow and cure slowly. To accelerate the curing process, the mould with PDMS was placed in an 80°C oven for 2h. The cast PDMS was then slowly peeled off after cutting the edges along the inside of the circumscribed PMMA spacer.

The moulds were fabricated using with two different patterning methods. In the UK, an SU-8-2025 glass mould was used while a nickel-plated glass mould was utilised in Singapore. Details of the fabrication can be found in Appendix E.

2.4.1.2 Surface treatment

The surfaces of glass and polymers are chemically different to that of the gel utilised in the experiments. As such, the substrate surfaces were treated with UV ozone or oxygen plasma to make it favourable for substrate-gel adhesion by rendering the polymeric surfaces hydrophilic and reactive for dissimilar material adhesion. The parameters for using such systems are summarised in Table 2-1.

Table 2-1: Surface treatment parameters for UV / plasma systems

UV / Plasma System	Parameters	Purpose	Recipe No. & Source
Diener Femto Plasma System	**Power:** 50% power (50W) **Duration:** 60s **Flowrate:** 40% MFC (mass flow controller) - 18 sccm **Pressure:** 0.68 mbars (5.1 x 10^{-1} Torr)	Surface Treatment (for gel adhesion – PMMA-pHEMA & PMMA/PC-PDMS)	**Recipe #1**; Adapted from Sunkara *et al., 2011* [127]
Syngene UV transilluminator	**Wavelength:** 254 nm (400 μW/cm² @15 cm) **Exposure duration:** 20 min **Distance:** 7.5 mm (from sample)	Surface Treatment (for PC-pHEMA gel adhesion & PMMA-PDMS)	**Recipe #2**; Experimentally determined
Clear View dual wavelength (254/365nm) UV transilluminator	**Wavelength:** 254 nm (~2.4mW/cm²) **Exposure duration:** 15 min Treatment-side faced down covered with aluminised polyester sheet	Surface Treatment (for gel adhesion to PMMA/PC)	**Recipe #3**; Experimentally determined
	Power: 50W **Duration:** 60s **Flowrate:** 19 sccm O_2 **Pressure:** 2.5 x 10^{-1} Torr (base pressure); 1.89 – 2.0 x 10^{-1} Torr (operating pressure)	Surface Treatment (ion dominant; for PC-pHEMA gel adhesion & PC-PDMS)	**Recipe #4**; Adapted from Sunkara *et al., 2011* [127]
	Power: 400W **Duration:** 3 min **Flowrate:** 100 sccm O_2, 120 sccm Ar **Pressure:** 4 x 10^{-1} Torr	Surface Treatment (for hologram fabrication – "high power plasma")	**Recipe #5**; Adopted from discussion with Ms Ng Shupei (SIMTech)
	Power: 150W **Duration:** 40s **Flowrate:** 100% O_2; ~78 – 85 sccm **Pressure:** 6 X 10^{-1} Torr	Surface Treatment (neutral-dominant; for gel adhesion of Glass-PDMS)	**Recipe #6**; Adopted from discussion with machine supplier
	Power: 60W **Duration:** 60s **Flowrate:** 50 sccm **Pressure:** 4 X 10^{-1} Torr	Surface Treatment (ion-dominant; for gel adhesion – PMMA-PDMS)	**Recipe #7**; Adapted from Sunkara *et al., 2011* [127]
	Power: 60W **Duration:** 60s **Flowrate:** 19 sccm **Pressure:** 2 x 10^{-1} Torr	Surface Treatment (ion dominant; for gel adhesion to PC / PP / PET & PC-PDMS)	**Recipe #8**; Experimentally determined
	Power: 250W **Duration:** 3 min **Flowrate:** 45% O_2, 55% Ar; ~30 sccm & 36 sccm **Pressure:** 4 x 10^{-1} Torr	Surface Treatment (ion dominant; for hologram fabrication and pre-treatment for glass silanisation)	**Recipe #9**; Adapted from discussion with Ms Ng Shupei (SIMTech) and machine supplier

For gel-substrate adhesion, the substrates were typically cleaned with 99% (v/v) ethanol or isopropyl alcohol (IPA) before plasma-treated with the various different recipes. The exposure of the cleaned surface to UV (254 nm) or O_2 plasma further breaks contaminant molecular bonds on the substrate surface [128]. The increased hydrophilicity of the treated surface facilitates the formation of a covalently bonded intermediate layer, which favours adhesion of another substrate with a different surface chemistry to that of the pristine untreated substrate surface.

Substrates to be plasma treated were preferably, with the exception of the PDMS-glass bonding process, placed on the powered electrode so that the surface will react mostly with charged ionic species (hence "ion-dominant"). Substrates placed on the non-powered electrode will mostly be chemically reacted with oxygen radicals or uncharged/neutral molecules (thus "neutral-dominant"). Where the powered electrode was the upper electrode, as in the case of the COVANCE 2MPR plasma system, the substrates were stuck to the powered electrode using double-sided tape.

UV treatment at 254 nm requires that the treated surface be facing the UV source, as most polymers and even glass does not transmit UV at that wavelength. Where ozone is present, either introduced to the treatment chamber or formed in the presence of UV @ 185 nm, the treatment time to clean the surface becomes significantly shorter, faster than 2 min [128].

Silanised glass substrates have diminished adhesion to polyHEMA gels after just 2 months of being exposed to light. They should be stored in a dark, dry place until just before use, or its container wrapped with aluminium foil. Alternatively, they could be "revived" by undergoing an ion-dominant high-power O_2 plasma treatment (recipe #9 of Table 2-1) followed by the silanisation procedure as if they were pristine glass slides.

2.4.1.3 Surface modification

2.4.1.3.1 Silanisation of glass slides

The microscope glass slides were taken out from a newly opened box of microscope glass slides. The slides were then wiped using cleanroom wipes with ethanol and blown dry with a nitrogen air. After surface treatment by O_2 plasma (ion-dominant mode) as described in Table 2-1 (recipe #9), the glass slides were placed treated-side up within the confines of a metal tray. While plasma treatment was not crucial for glass-gel adhesion (previous work with other holographic sensors use a silanisation process without prior cleaning or treatment with good effect), it was experimentally determined that the glass-gel adhesion was stronger and lasted longer with surface treatment.

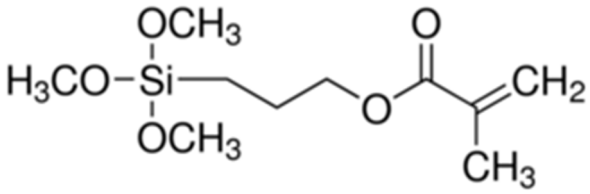

Figure 2-13: Chemical structure of 3-(trimethoxysilyl)propyl methacrylate (Silane A174)

Performed inside a fume hood, 2 mL of 3-(trimethoxysilyl)propyl methacrylate (Silane A174) was added to 40 mL of acetone in a measuring cylinder. Acetone was utilised as a solvent to wet evenly and coat uniformly a thin coat of silane on the glass slides. The hydroxyl groups on the glass surface displaces the methoxy group of Silane A174, enabling the silane to covalently bond to glass via the Si-O-Si bond [129]. The 2 mL of Silane A174 was introduced via a glass syringe as acetone dissolves polystyrene. The solution was then carefully poured on top of all the slides and the solution slowly swished about the tray to ensure even coverage, before disposing of the solution into a waste glass beaker, leaving some residue on the slides. The tray was then cautiously wrapped with aluminium foil, ensuring it did not touch the slides. It was then stored in a cool, dark place overnight. It had to be equilibrated in the dark to ensure the methacrylate functional groups do not react with each other instead of with the gel in a downstream step. After 12 h, the aluminium foil was removed, and each glass slide wiped and cleaned with ethanol and Kimwipes or cleanroom wipes. It was not recommended to leave glass slides with the residue for more than a day after to prevent permanent stains from forming.

The cleaned slides were then stored in customised sample storage apparatus (§2.2.2.2) with the silanised surface facing up, and wrapped with aluminium foil to protect the samples from light degradation. The slides were subsequently cut to size (~ 12.5 mm x 9.4 mm) with a glass scriber, ruler and cutting mat before use, and the unused substrates stored in a cool, dark place. Even under UV-filtered lighting, light exposure of more than 3 months can revert the silanised glass substrate to its original pre-silanised state. In the event where the silanised layer became passivated, such as after prolonged exposure to light, the glass substrate could be retreated with the same O_2 plasma treatment recipe and silanisation process aforementioned to regain its adhesion potential to the gel.

2.4.1.4 Surface modification of polymers

2.4.1.4.1 Surface modification of polycarbonate (PC)

Polycarbonate (PC) substrates were wiped with ethanol and cleanroom wipes before O_2 plasma treated or UV treated with recipe #1, 2, 3, 4, or 8 accordingly from Table 2-1. Just before the cessation of the surface treatment, 1 µL of pentaerythritol tetraacrylate (PETTA) was aspirated using the reverse pipetting technique and then carefully dripped onto an aluminised polyester sheet slightly larger than

the sample substrate. The aluminised polyester sheet was chosen due to its passivity to pHEMA, and it has a flat mirror surface that promotes more uniform PETTA coverage and reflects light back uniformly to spot air bubbles more effectively. It was thought that hydroxyl groups formed on the plasma- or UV-treated PC surface would displace one or more of the alkoxy arms of PETTA (illustrated in Figure 2-14) to covalently form R-O-R' ether bonds.

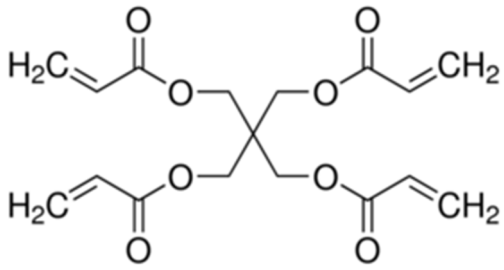

Figure 2-14: Chemical structure of Pentaerythritol tetraacrylate (PETTA)

The PC substrate was then slowly lowered and pressed down using tweezers (to avoid forming large air bubbles) onto the viscous PETTA droplet treated-side down, and left to equilibrate for 5 min. An N_2 air gun was then utilised to "flatten" the area where the gel was designated to form and the sides cleaned with cleanroom wipes moistened with DI water.

2.4.1.4.2 Surface modification of other common polymers

Polystyrene (PS), polyethylene terephthalate (PET) and poly(methyl methacrylate) (PMMA) can be surface treated with recipe #8 in Table 2-1 and gel formed on the treated surface via the photo-polymerisation process. It is important to note though, that a broad range UV source was required (e.g. low pressure mercury vapour lamp in the mask aligner) for successful photo-polymerisation of gel on PMMA surface, i.e. a narrow-band i-line 365 nm UV does not photo-polymerise gels on the PMMA surface.

2.4.2 Gel fabrication

2.4.2.1 Preparation of gel precursors

The gel precursor solution consisted of monomer, crosslinker, functional moiety (FM), free radical initiator, polymerisation inhibitor and solvent. They are 2-hydroxyethyl methacrylate (HEMA), ethylene glycol dimethacrylate (EDMA); 2-(dimethylamino) ethyl methacrylate (DMAEM), 2-(trifluoromethyl) propenoic acid (TFMPA) or methacrylic acid (MAA) – generally abbreviated as functional moiety (FM); 2-2-dimethoxy-2-phenylacetophenone (DMPA), hydroquinone (HQ) and isopropyl alcohol (IPA) respectively. The total amount of HEMA, EDMA and FM was kept at a fixed 8 mmol per 1 mL of IPA. EDMA:FM mol ratio (as opposed to % w/v to IPA) was varied to study the

consequent effects on the gel behaviour. The amount of MAA and DMAEM can be accurately measured with a pipette since they are liquid. However, especially since TFMPA was not significantly soluble in isopropyl alcohol (IPA), TFMPA was prepared by measuring its weight.

The amount of DMPA was normalised to 1.0 at 0.0707 mmol (calculated from the proportion of DMPA of past gel precursor recipes) and varied as a fraction (e.g. 1/18 DMPA or 0.4 DMPA) of this amount for the results of this work to compare against past results. The amount of DMPA was also varied in whole mole ratio numbers with respect to a unit HQ amount (such as 2:1 HQ or 10:1 HQ) to visualise the various precursor interactions more easily. 10% w/v DMPA and 10% w/v HQ were prepared instead of using their powder forms during precursor solution preparation due to the miniscule amount of DMPA and HQ powders required which may lead to significant errors depending on the measurement accuracy during each preparation. This, however, made the calculation for the exact volume of IPA extremely challenging. To simplify and keep the formulation consistent, the % w/v of DMPA and HQ was kept at 10% w/v and the total volume resulting from the dissolved DMPA and HQ was neglected. Referring to the green 500 μL column of Figure 2-15, 389.94 μL of IPA was added to all the solutions added in the upper chunk to give 500 μL of IPA added to a total of 8 mmol of constituents (HEMA, EDMA and FM).

2.4.2.2 Preparation of DMPA and HQ solutions

The gel precursors were stored in 30 mL amber bottles and refrigerated at 4°C (to minimise auto-polymerisation), except for IPA and the 10% w/v DMPA. DMPA tended to precipitate out of solution (as visible white crystals) when 10% w/v DMPA in IPA solution was taken in and out of the fridge regularly, and would not usually dissolve again unless heat was applied. This introduced uncertainty in the DMPA concentration, which will result in an inaccurate volume of DMPA from subsequent aspirations. It was better to store DMPA solution in a cool, dark place.

Quinone (or 1,4 benzoquinone, more commonly known as para-quinone), the oxidised version of HQ, was red in colour, but could still be discerned in an amber vial. When held up against light, an “expired” solution containing quinone would look duller and more opaque. It should thus be checked periodically for signs of oxidation.

The gel precursors were added sequentially via the appropriate pipette with the same method into a 2 mL amber vial. The total volume of 1 mL gel precursor solution in the vial was then mixed by pressing against a vortex mixer for 30s, and then refrigerated (and equilibrated) for at least 2h before use.

01/11/2016 - 1.0 DMPA (2:1 HQ) | For 0.4D gel | 8TH-2 | 6T3E

HEMA-TFMPA - pH sensitive

DMPA	HQ
2	1

*Reciprocal of DMPA fraction

DMPA			Check
1	/	1.000	1.0

Total no. of mmol = 8 mmol (We want 8mmol constituents in 1ml IPA)

		mw (g/mol)	desired mol%	Total amt (mmol)	weight (g)	w/v % made	Density (g/cm3) (g/ml)	vol (ml) (for 1ml) 1	vol (in ul) for 1ml 1000	vol (in ul) for 500ul 500	vol (in ul) for 300ul 300	vol (in ul) for 200ul 200	vol (in ul) for 600ul 1400	For 500
2-Hydoxyethyl methacrylate	HEMA	130.14	91.00%	7.28000	0.94742	100	1.073	0.8830	882.96	441.48	264.89	176.59	529.78	
Ethylene glycol dimethylacrylate	EDMA	198.22	3.00%	0.24000	0.04757	100	1.051	0.0453	45.26	22.63	13.58	9.05	27.16	
2-(Trifluoromethyl) propenoic acid	TFMPA	140.06	6.00%	0.48000	0.06723	99999999	-	0.0000	0.00	0.00	0.00	0.00	0.00	0.03361 g
2,2-Dimethoxy-2-phenylacetophenone	DMPA	256.30	-	0.07070	0.01812	10	-	0.1812	181.20	90.60	54.36	36.24	108.72	
Hydroquinone	HQ	110.11	-	0.03535	0.00389	10	-	0.0389	38.92	19.46	11.68	7.78	23.35	
Total		-	100%	8.000	1.08423	-	-	0.2201	220.13	110.06	66.04	44.03	132.08	
				8.10605										This Row = tot solvent vol (ADD ALL non-100% & non-9999999 vol)
2,2-Dimethoxy-2-phenylacetophenone	DMPA	256.30	66.67%	0.07070	0.01812	10		0.1812	181.20	90.60	54.36	36.24	108.72	
Hydroquinone	HQ	110.11	33.33%	0.03535	0.00389	10		0.0389	38.92	19.46	11.68	7.78	23.35	

Monomers-to-solvent ratio = 1.06222 g/ml

Total reagents-to-solvent ratio = 1.084234 g/ml

IPA (to make it 1ml)	IPA	60.10	-	-	-	-	0.785	0.7799	779.87	389.94	233.96	155.97	467.92	

Figure 2-15: Calculation for gel precursor proportions in IPA as solvent (for 3.0 mol% EDMA HEMA-co-TFMPA)

A detailed rundown of the calculation behind Figure 2-15 is shown in Appendix F.

2.4.2.3 UV-initiated free radical polymerisation with masking tape mask

A 5mm punch was utilised to put a hole through black (opaque) masking tape before sticking the tape onto a silanised glass substrate. 200 µL of the gel precursor solution was dripped onto a metallised (aluminised) polyester sheet and covered by the tape-covered glass slide (tape-side down) to form a hermetically-sealed well for the solution to flow into as shown in Figure 2-16 below.

From past work, the glass substrate with tape mask was pushed downwards against the polyester sheet until the gel precursor solution filled up the well and the excess squeezed out between the tape-polyester sheet interfaces. The ultraviolet (UV) light propagates through the glass substrate and sets off the free radical polymerisation within the gel precursor solution. The aluminised polyester sheet ensured any transmitted UV through the solution was reflected back to the solution to increase the rate of polymerisation.

In order to prevent a change in UV intensity reaching the gel precursor solution when using different substrate materials (such as polymers), another configuration of "Mylar®-on-top" was utilised as depicted in Figure 2-16(b). A change in substrate material will affect UV transmittance to the gel precursor solution. Consequently, the top layer was a PET cover film in anticipation for future substrate changes (polymer instead of glass). Any other films can be utilised in place of PET as long as it can be used consistently for all substrates. Additionally, air bubbles were also less likely to form with this configuration when the gel precursor solution can be dripped directly into the well before covering with the PET film.

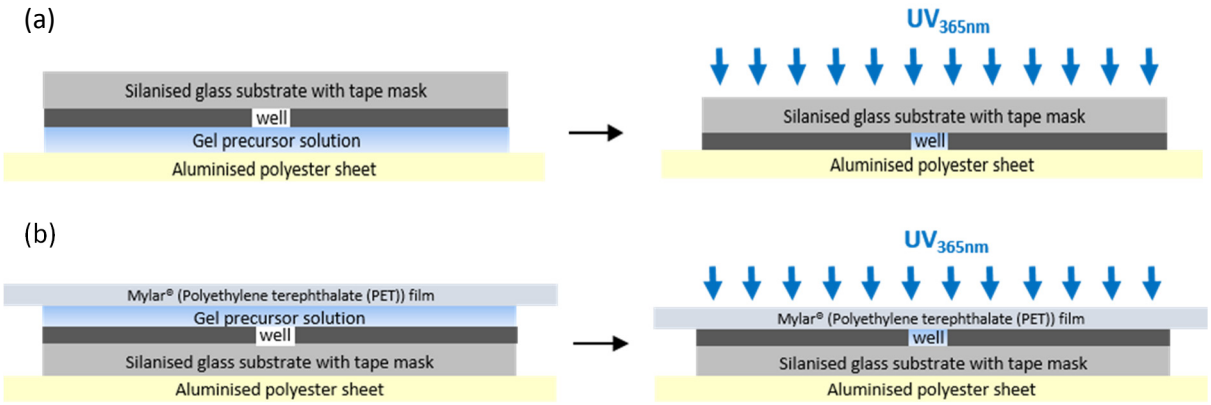

*Figure 2-16: Schematic diagrams for gel fabrication via UV-initiated polymerisation using a tape mask in the **(a)** substrate-on-top and **(b)** cover-on-top configuration*

After the gel was cured via UV photo-polymerisation, the glass substrate was rinsed with copious amounts of DI water to get rid of any unreacted monomers in the solution. The tape was then carefully peeled away to leave the polymerised (covalently bonded) 5 mm diameter gel on the silanised glass substrate.

2.4.2.4 UV-initiated free radical polymerisation with photomask

In order to obtain good mask fidelity, a parallel or collimated UV beam had to be utilised during photo-polymerisation. As the desired gel size (0.4 ϕ) was small, the silanised glass slides (76 mm x 25 mm x 1 mm) were cut into 16 smaller pieces, to utilise fully the substrates, which converted to about (L) 12.5 mm x (W) 9.375 mm.

The sample substrate (glass/PMMA/PC) was first cleaned with isopropyl alcohol (IPA) before being placed onto the silicone spacer, silanised-side up. A Mylar® spacer was placed between the COC cover and sample substrate before a typical 3 µL of gel precursor solution was introduced with an adjustable volume pipette at the interface through the side via capillary action. The Mylar® spacer was then carefully removed and the photomask placed on top of the silicone spacers on the PMMA spacers as illustrated in Figure 2-17. This method prevented air bubbles from forming during the dispensing of the gel precursor solution. Thereafter, the film photomask was adjusted for alignment with the UV LED (@ 365 nm) pen before UV exposure. The UV parameters (power % and duration) were assigned using the smartUV 1.1.1 software. The UV power was periodically (every 3 months) checked for intensity changes with a power meter.

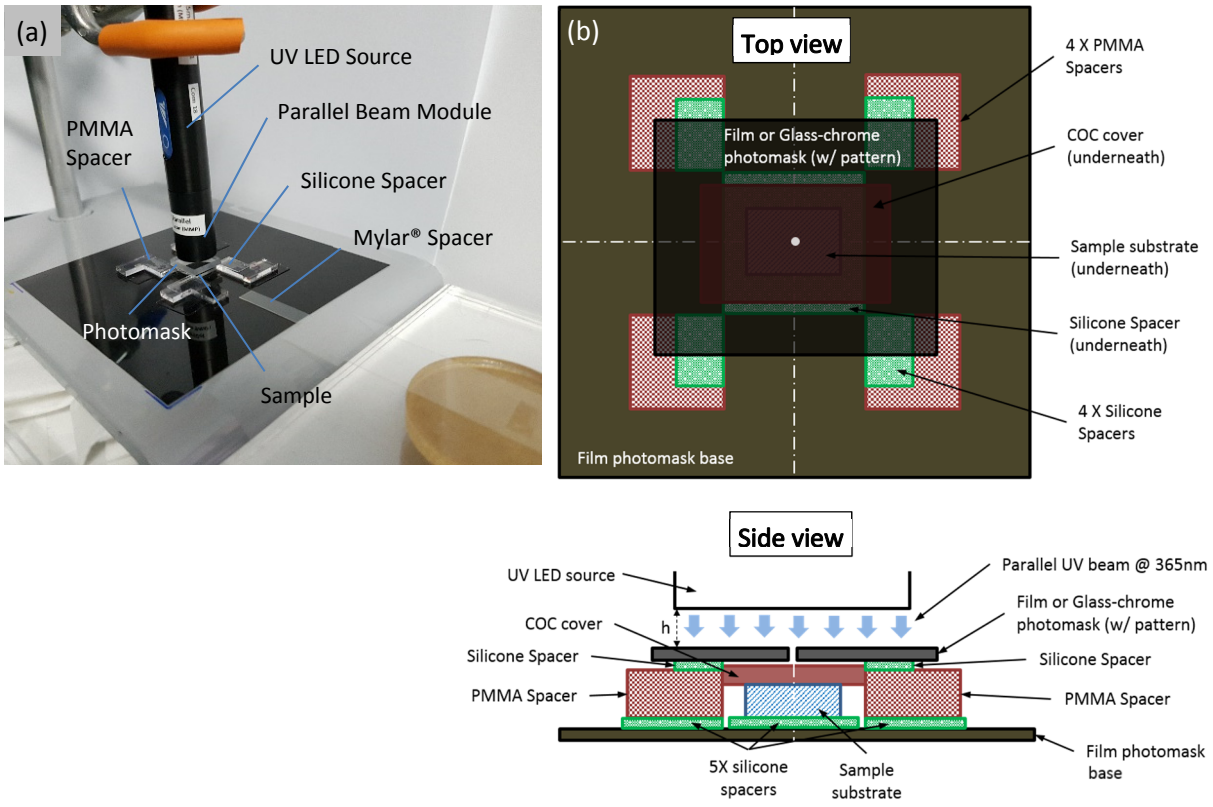

Figure 2-17: Gel fabrication setup. ***(a)*** *Picture and* ***(b)*** *schematic diagram (top view & side view) of the experimental setup. A zoomed-in version of the top and side view from (b) is shown in Figure 2-1.*

2.4.2.5 Glass (quartz)-chrome vs film (acetate) photomask

Where possible, a quartz-chrome mask was utilised for photo-polymerisation. The curvature on an alternatively cheaper acetate mask would cause distortion to the polymerised gel. It is not recommended to press the substrate hard against the acetate mask to reduce the warpage causing the distortion, as the gel precursor solution was liquid. If it were necessary to use an acetate mask, the features should not be too close together on the photomask. There would be undesirable gel polymerisation in between those features, especially where an array was involved. In addition, the heights of the polymerised gel would not be consistent as well. A method to minimise this inconsistency was to plasma-treat the substrate surface in high power ion-dominant mode, i.e. the substrate should be on the powered electrode so that ions would bombard the surface. On top of the plasma treatment, the gel inconsistency can be minimised by leaving the gel without UV exposure for an experimentally optimised amount of time after the actual UV exposure. The diffusing and energetic initiator would continue to polymerise the gel at a lower rate to achieve features that are more consistent. Otherwise, using a quartz-chrome mask would resolve most of these issues.

2.4.2.6 Cover substrate for photo-polymerisation

Employing the same logic for the photomask, a flexible cover substrate is not recommended for controlled polymerisation. Mylar® (PET) films typically exist in a roll format, for example. The use of it as a cover substrate would entail dealing with certain film warpage. With a 3.0ϕ feature photomask, when the form of the PET film was predominantly curving upwards (concave from the top), the polymerised HEMA-co-MAA gel would be of a ring shape > 20 μm tall instead of a cylinder. When the form of the film was predominantly curving downwards (convex from above), the polymerised gel would be a flat disc around 3 μm in height[1].

Although the surface of single-crystal quartz was flat and even, it tended to be difficult to pry it off the gel substrate, which damages the polymerised gel. The gel also tended to form on quartz, glass and PC instead of the gel glass substrate if these alternative substrate materials were utilised as cover substrates. The notable exception was COC.

PolyHEMA gels did not form on PMMA with UV at 365 nm with the PC-embedded holosensor recipe. It required other UV wavelengths for the adhesion to happen. Consequently, it was recommended that the mask aligner or a mercury/Xenon UV source be utilised instead for PMMA-polyHEMA adhesion.

[1] This observation was applicable to the 8 mmol total gel constituents, 1.0 DMPA, 10:1 HQ, 6 mol% MAA, 3 mol% EDMA, 20 mW/cm^2 for 3 min with mask aligner, 3.0ϕ, 5 μL gel precursor solution on Mylar® film recipe

2.4.2.7 Gel characterisation

After UV photo-polymerisation, the substrates containing the cured gels were sprayed with isopropyl alcohol (IPA) and air-dried with a nitrogen (N_2) gun before a 12 min 70% (v/v) ethanol (EtOH) immersion after UV photo-polymerisation. It was noteworthy that the gels had to be rinsed with IPA or 100% EtOH instead of DI water or tap water as any residual free radical initiator (DMPA) and/or polymerisation inhibitor (HQ) may precipitate out as a white precipitate or cause downstream problems during hologram fabrication. Under certain circumstances, the gel will delaminate from its substrate. The 12 min 70% (v/v) EtOH immersion test served to provide an indication of the gel-substrate adhesion strength since polyHEMA gels typically expand the most around 70% (v/v) EtOH [92], and 12 min was the typical duration for the equilibration of the gel during the hologram fabrication process.

The gel dimensional and roughness profiles were obtained with the white light profiler. Structural properties of the gel such as reduced modulus and hardness were determined with the nanoindentation system.

Nanoindentation is a destructive testing method. Its destructive nature of the indentation process lies mainly with the use of cyanoacrylate glue to stick the sample onto an aluminium block to ensure the sample does not move due to the elastic nature of other non-permanent adhesive methods. Consequently, the sample would be grinded away for the next indentation run. The damage can be mitigated by letting the sample protrude out of the aluminium block perimeter, with the gel close to the edge. Snapping the sample out would cause certain sample damage, but a few redundant samples of the same parameters could circumvent this problem. Alternatively, all of the holosensor characterisation and effectiveness studies can be done first while leaving the nanoindentation process to the last. Either way, a few redundant samples would help to characterise the holosensor and still be able to be utilised after that.

2.4.2.8 Hologram fabrication

2.4.2.8.1 Experimental setup

A darkroom within a Class 10k cleanroom with UV-filtered and red-safe lighting was set up for gel fabrication and holographic sensor (holosensor) fabrication respectively. Thick opaque curtains with VELCRO® were put up to entirely surround the light-sensitive hologram fabrication equipment and keep the area light tight. Fluorescent tapes were placed at strategic locations in the darkroom to locate switches and avoid barriers during the movement of samples from one area to another. The laser hologram-recording system was placed on a vibration-isolated optical table and covered with a

custom-made acrylic enclosure for safety redundancy, better temperature stability and airflow restriction. The air-conditioning was disabled within the darkroom with the curtains drawn to enclose the optical table area, and to mitigate the effects of draughts and temperature variations from outside of the darkroom.

The optomechanical parts were set up as shown in Figure 2-18. The parallelism of the laser beam path was fulfilled by using an adjustable iris as an alignment tool for every component. The lenses were also adjusted such that the beam went through its centre and reflected back to the laser source. A small offset was required. It was critical, however, that the beam was retroreflected back to its source but not exactly back down the same path. In other words, the reflected beam had to be offset. Additionally, reflecting the beam exactly back down its original path will distort the wavefront of the incoming beam, changing the incoming beam properties. The half waveplate variable laser power attenuator and plano-convex lens were slightly rotated to offset the beam to the left or right of the original beam path. As for the plano-concave lens, the protuberance of the adjustable iris was used to determine the minimum offset of the beam (i.e. the reflected beam had to be in the “umbra region” on the protuberance as depicted by the blue arrow in Figure 2-18(b)).

2.4.2.8.2 Sample alignment

With the sample substrate secured on the front surface mirror with 0.25 mm PDMS, the light beam was first adjusted such that when the pinhole was closed to the minimum (0.5 mm diameter), it does not go through the gel, though the rest of the beam does when the iris was opened to the maximum (5 mm diameter). Figure 2-19(a) and Figure 2-19(b) depict the centre of the beam just barely outside the circumference of the retroreflected gel images for the gels with diameters 0.4 mm and 3.0 mm respectively. The sample was fixed in place using rectangular neodymium magnets on the optical table. Finer adjustments were performed using the adjustable tilt-yaw 45° mirror such that the downstream interference were concentric (illustrated in Figure 2-19(c) with the red arrow) when the iris was closed to its minimum. The bright and dimmer spots were most visible when the centre of the beam did not go through the gel on the sample substrate. Presumably, the gel would have distorted the beam and prevented the dimmer beam from being noticed. When done correctly, the retroreflected beam would be a beam spot just slightly above the central beam spot (shown in Figure 2-19(d) as almost being resolved to a single point; the picture did not clearly elucidate it, but could be seen with the eye).

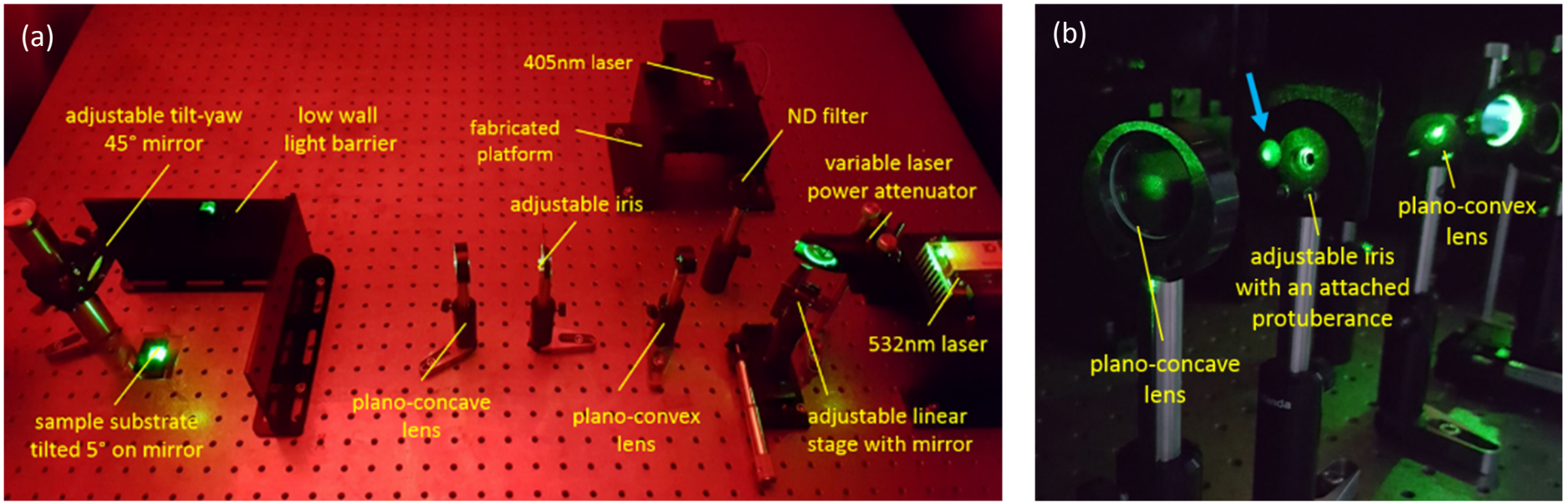

Figure 2-18: Hologram fabrication experimental setup. ***(a)*** *Picture of setup for hologram fabrication (shown without acrylic enclosure).* ***(b)*** *Picture illustrating the offset retroreflection from the slightly rotated plano-concave lens to the umbra on the attached protuberance of the adjustable iris indicated by the blue arrow.*

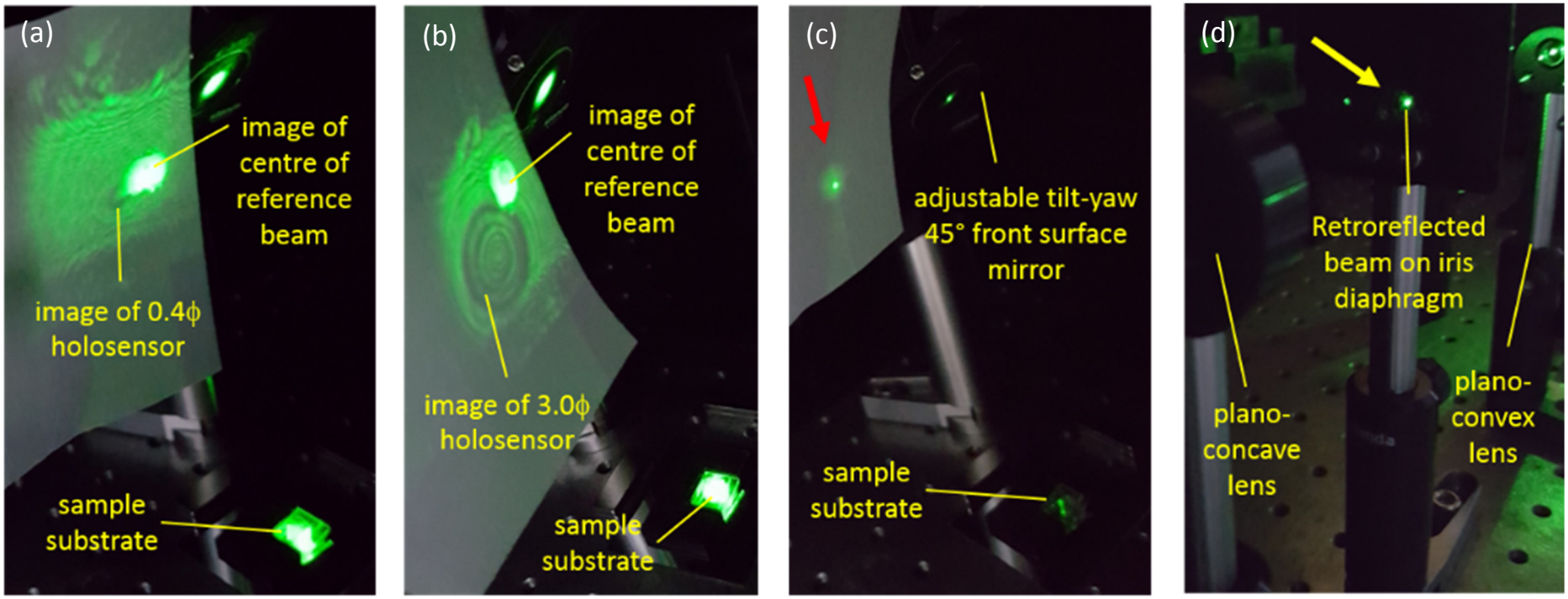

Figure 2-19: Devised method of using cleanroom tissue and adjustable iris with protuberance as alignment tool. ***(a)*** *Picture showing the images of the 0.4ϕ holosensor with the centre of the reference beam on a cleanroom tissue held just beside the tilt-yaw front surface mirror diagonally above the sample substrate when iris was opened to its maximum of 5 mm diameter.* ***(b)*** *Picture similar to (a) except that the sample was 3.0ϕ.* ***(c)*** *Picture illustrating an adjustable tilt-yaw mirror where the central bright spot was concentric with the outer dimmer spot, as emphasised by the red arrow when the iris was closed to its minimum.* ***(d)*** *Picture depicting the retroreflections of the beam almost coinciding and almost resolved as a single spot, pointed out by the yellow arrow. The dimmer spot on the left of the retroreflected beams are the offset beams reflecting off the surfaces of the plano-concave lenses.*

2.4.2.8.3 Preparation of developer

JD-4 (or JARB) developer, referred to, as the Saxby developer in this thesis, was prepared as two separate solutions for longer shelf life – Saxby A and Saxby B. The constituents of the Saxby Developer were filtered with a 0.22 μm (pore size) syringe filter and separately prepared in two different bottles – reductants and alkaline buffer labelled Saxby A and Saxby B respectively - which were mixed in equal proportions only just before use. The filtration prevented suspended Metol from adsorbing onto the gel surface during development, which could cloud the holographic signal. When the alkaline buffer (Saxby B) was stored separately from the reductants (Saxby A), the developer could be used for 2 weeks before Metol started to precipitate out of solution; but after being mixed, will last at most a day.

Saxby A consists of 0.6% w/v 4-methylaminophenol sulphate (Metol) and 4.0% w/v L-Ascorbic Acid. 0.3g of Metol was mixed with 50 mL of DI water first as it is only sparingly soluble in water. After stirring with magnetic stirrer for 10 min, 2g of L-ascorbic acid was added and further stirred for another 10 min. Saxby B consists of 10% w/v sodium carbonate (Na_2CO_3) anhydrous and 3.0% w/v sodium hydroxide (NaOH). 5g of Na_2CO_3 and 1.5g of NaOH was added to 50 mL of DI water and stirred with a magnetic stirrer for 10 min. It should be noted that the preparation should be done with appropriate gloves and eye protection as the solution is caustic.

To ensure that the Saxby developer (Saxby A mixed with Saxby B in equal volume proportion) was functional, solution A and B should be below pH 2.5 and above pH 13.5 respectively. Optimally when mixed, its pH should be more than pH 12.8. Any values lower than pH 11.5 would be considered “spoilt” – in comparison, Saxby developer left overnight was pH 11.28.

2.4.2.8.4 Fabrication procedure

Previous holographic sensor (holosensor) fabrication procedures utilising a pulsed laser with the photochemical [119] or ablation [122] method was adapted for the fabrication of the miniaturised holosensors. The difference with current holosensor fabrication techniques involves the use of a continuous wave (CW) laser and specialised optomechnical components for process control that is more precise and replicable.

The gel-on-glass substrate in the laser-cut sample adaptor was placed and aligned as illustrated in Figure 2-3. Thin strips (2 mm width) of double-sided tape were placed on the inner sides of the adaptor to minimise movement after sample placement. An optional step of plasma treating the gel made the surface more hydrophilic and easier for subsequent chemicals to diffuse into the gel during the hologram fabrication process. The treatment also mitigated the problem of premature darkening of

the gel by the reduced Ag^0 and/or cogulation of insoluble DMPA or HQ within the gel matrix. This step was later supplanted with the immersion of the gel with 70% (v/v) EtOH for 1 min and successive drying with N_2 gun.

The gel was placed face-up and covered with 80 μL of 0.5M $AgClO_4$ in DI water for 1 min. IPA was not used in the Ag solution due to overdevelopment and poorer hologram quality. The slide containing the gel was then dried with an N_2 gun for 5s before being immersed into bromide solution (made by mixing 20 mL of 3% w/v LiBr in 3:2 (v/v) MeOH/DI with 1 mL of 0.1% w/v QBS dye in MeOH) for 1 min. The substrate was picked up, tilted on a cleanroom tissue and knocked a few times onto the tissue to minimise the amount of bromide solution left on the slide approximately 5s before the 1 min was up,. Thereafter, the substrate was quickly immersed in 70% (v/v) EtOH for 1 min while holding onto the substrate and swirling it around to dissolve away as much unreacted reagents which could contribute to noise. After that, the gel was sprayed onto a few times with 70% (v/v) EtOH and then rinsed thoroughly with DI water for 30s. The substrate was then blown dry with N_2 for 10s before 20 μL of L-ascorbic acid of around pH 4.50 (adjusted with NaOH) was dripped onto the 0.25 mm thick PC cover within the (laser-cut) 0.25 mm thick PDMS (around 5.5 mm x 8.5 mm) chamber.

The gel substrate was then pressed onto the 0.25 mm thick PDMS spacer and against the sides with the double-sided tape strips (shown in Figure 2-20) to ensure it replicated previously calibrated alignment and minimised possible movement during laser exposure. The side with markings (scraped using a diamond tip pen) was placed on the step of the sample adaptor, which was also the direction from which light was illuminated to view the hologram. In relation to the experimental set up, the sample adaptor was orientated to the same x-y plane configuration as described in Figure 2-2(d).

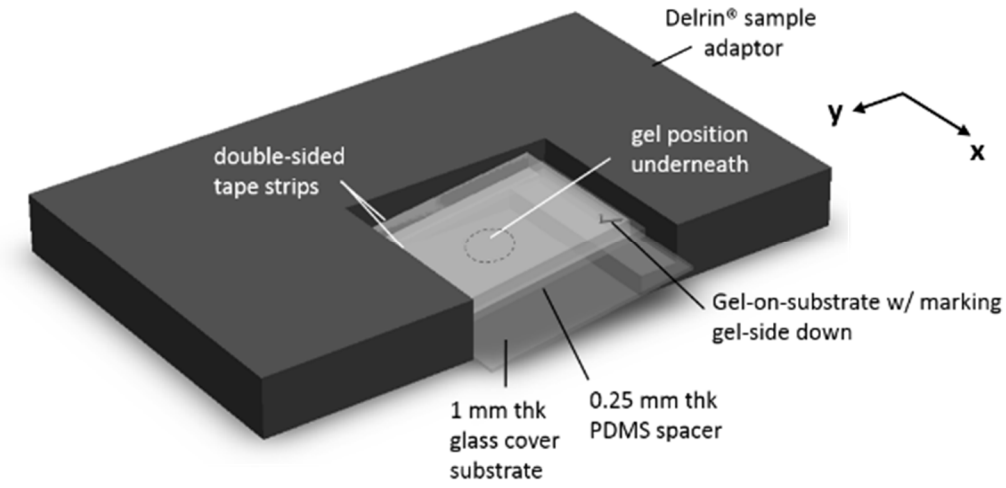

Figure 2-20: Schematic drawing for Delrin® sample adaptor with gel-on-substrate for hologram fabrication

The equilibration duration was 12 min - for the gel to equilibrate with the solution and reach thermal equilibrium. A manual shutter was carefully lifted up a little (without exposing the gel) for 15s before exposing the gel to the 532 nm laser for 3s at 0.290 mW power intensity (beam size at sample – 9 mm diameter). The gel substrate was then immersed and jiggled inside the Saxby developer for 18s before being immersed and shaken in 5% (v/v) acetic acid (STOP bath) for 20s. After thorough DI rinsing, the holosensor was tested with pH 6.0 McIlvaine buffer. The hologram typically takes about 30s to appear fully after buffer application. Once confirmed that it worked, the substrate was immersed in 100% IPA for 1 min followed by another 1 min into 10% (aq.) (v/v) sodium thiosulphate ($Na_2S_2O_3$), followed by immersion in 6.7% (v/v) $Na_2S_2O_3$ in 33% EtOH (prepared by mixing 1.5 mL each of DI water, 20% (v/v) $Na_2S_2O_3$ and 99.8% (v/v) EtOH).

2.4.3 Holosensor calibration

2.4.3.1 Microfluidic chip fabrication

A Ni mould with the desired channel features was used to cast poly (dimethylsiloxane) (PDMS). In order to verify that the inlet and outlet holes of the PC-PDMS microfluidic chip was aligned with the position of the plug-and-flow design of the sample adaptor, a laser-cut calibration PMMA block (illustrated in Figure 2-21(a)) was utilised as a guide for cutting and punching. The perimeter of the block mirrored the size of the glass/PC substrate (12.5 mm x 9.4 mm) and was placed on top of the PDMS slab and cut to size with a surgical knife accordingly, with inlet and outlet holes punched *in situ*. The central circle represented the field of view (FOV) of the camera.

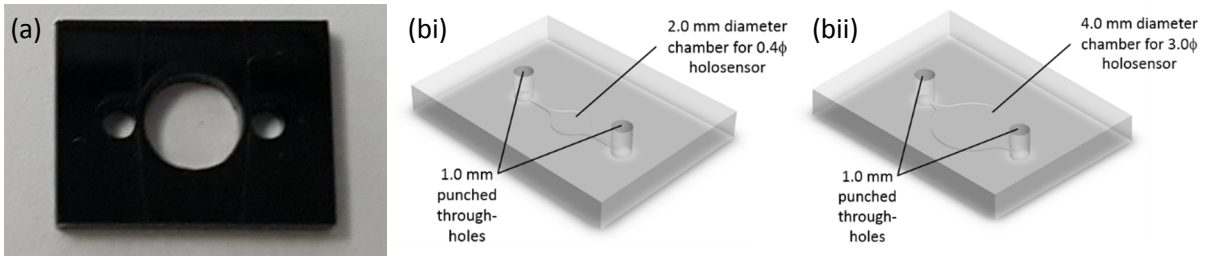

*Figure 2-21: **(a)** Picture of laser-cut calibration PMMA block as a cutting and punching gauge. **(b)** Illustrations of PDMS chips with 2.0 mm and 4.0 mm diameter chambers for **(i)** 0.4ϕ and **(ii)** 3.0ϕ holosensors respectively punched with 1.0 mm through-holes as fluidic inlet and outlet.*

The cut out PDMS slabs (shown in Figure 2-21(b)) were bonded with the gel-on-glass substrate samples after hologram fabrication using O_2 plasma. The parameters for the plasma used for PDMS-glass bonding was described in Table 2-2. The glass was carefully cleaned with IPA while dust and particles on the cast PDMS were removed using 3M tape before the bonding procedure. The bonding surfaces were aligned and lightly pressed for 30s following plasma activation to ensure a quality bond.

To bond polycarbonate (PC) to poly(dimethylsiloxane) (PDMS), a simple room temperature bonding method adapted from Sunkara *et al.* [127] was utilised. The same aforementioned recipes #1, 2, 3, 4 and 8 in Table 2-1 can be used for O_2 plasma treatment before a 20 min 1% (v/v) (aq.) (3-aminopropyl)triethoxysilane (APTES) immersion of both the treated PC and PDMS surface. They were then dried with an N_2 gun before undergoing the same plasma treatment recipe. Upon completion of the latest treatment, the two treated surfaces were carefully brought together and pressed against each other for about 3 min. Care was made to ensure that the PDMS chamber cover does not adhere with the gel, which would cause irreversible structural damage to the gel.

Table 2-2: Parameters for PDMS-glass bonding

UV / Plasma System	Parameters	Purpose
CONVANCE 2MPR Plasma System	**Power:** 150W **Duration:** 40s **Flowrate:** 100% O_2; ~ 78 – 85 sccm **Pressure:** 6 x 10^{-1} Torr	PDMS-Glass Bonding (for holosensor calibration)

2.4.3.2 Preparation of ionic-strength balanced McIlvaine buffer

The McIlvaine buffer was chosen because of the multiple pK_a values of citrate and phosphate across a large range of the pH scale (3.0 – 9.0), which makes it the ideal universal pH buffer. The buffer was prepared by mixing 9.5 mS/cm ionic strength balanced (adjusted with 3M NaCl) 0.1M citric acid with 0.1M disodium hydrogen phosphate (Na_2HPO_4) in various proportions into 50 mL skirted tubes to obtain pH solutions of 0.25 pH unit increments from pH 3.00 to pH 9.00. The pH buffers were calibrated with the Mettler Toledo conductivity meter and pH meter with a Pro-ISM electrode. The conductivity and pH electrodes were calibrated using standard 12.88 mS/cm conductivity solutions and three standard pH buffers at pH 4.01, pH 7.0 and pH 9.21 respectively. Total volumes of about 40 mL McIlvaine buffers of different pH were concocted based on an experimentally determined recipe as shown in Appendix H. The average and standard deviation of the final conductivity of the buffers were 9.507 mS/cm and 0.035 mS/cm respectively.

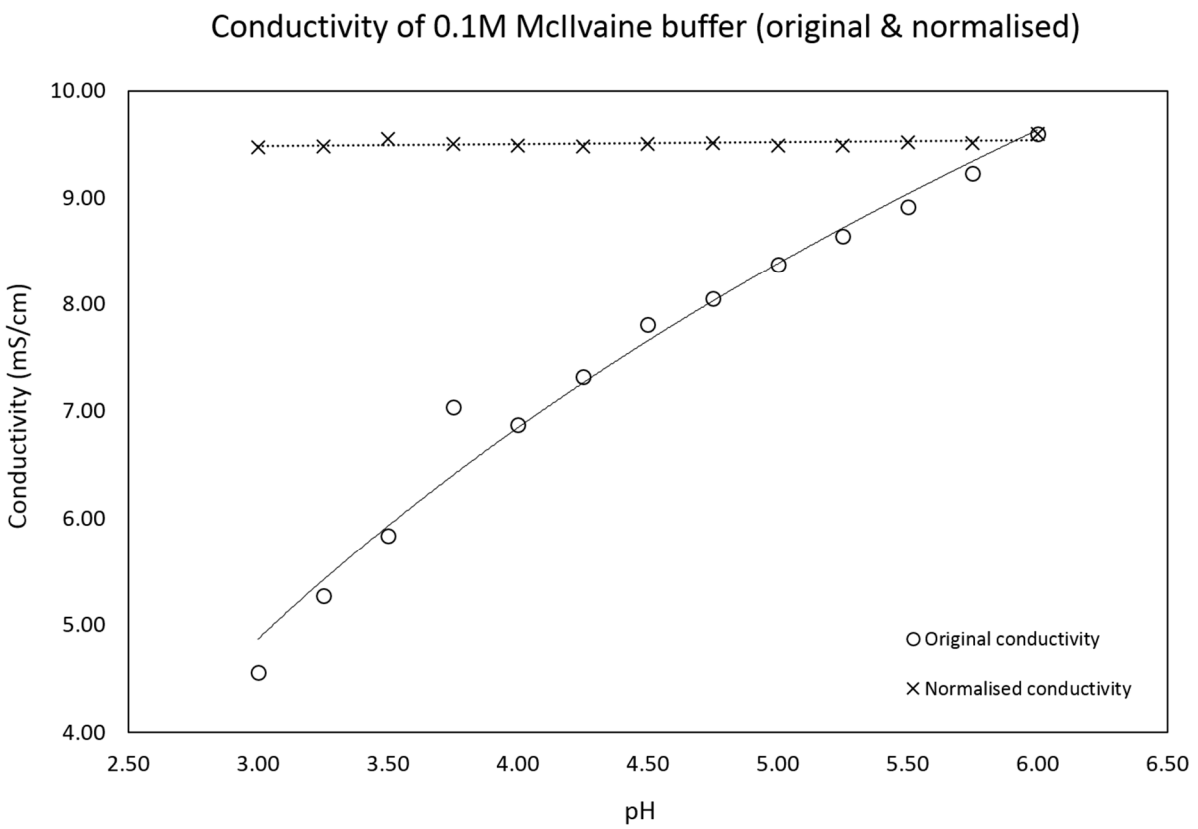

Figure 2-22: Conductivity measurements of original and normalised ionic strength 0.1M McIlvaine buffers from pH 3.00 to 6.00 in increments of 0.25 pH units.

2.4.3.3 pH characterisation of holosensors

After the gel-on-substrate was bonded with the cover PDMS chip having channel features mentioned in Figure 2-21(b), the bonded microfluidic chip was push-fit (via the inlet/outlet fluidic ports) into the modified blunt tip on the sample module indicated in Figure 2-4(c). Ionic-strength balanced pH 6.0 McIlvaine buffer was flushed through the chip via the inlet before the lighting and sample module shown in Figure 2-4(a) was adjusted for maximum sensor (hologram brightness) signal. While the intensity of the signal was visually assessed via the colour camera of the (optics) interrogation module, the distance of the illumination source from the sample, zoom of the lens (0.58X – 7X) and exposure settings on the camera could be modified to prevent overexposure or underexposure. Typically, tungsten-halogen illumination was utilised for hologram interrogation and calibration. However, as a high powered light source was required to gather as much signal as possible from the miniaturised holosensor, a 150W Xenon lamp (for HEMA-co-TFMPA) and 6500K White LED (for HEMA-co-DMAEM) sources were utilised.

There was a signal from the holosensor only at a narrow angular window as the ingoing illumination constructively interferes and reflects via the laser-recorded holographic fringes at a specific angle. Once a signal was obtained at pH 6.0, the buffer was pneumatically flushed out of the chip, followed

by sequential holographic signal detection with pH 4.5 and pH 3.0 buffers. Where the signal was not visible or uniform throughout the gel, the tilt and yaw of the lighting and/or sample module were adjusted for the optimal signal responses with the three different pH buffers.

Thereafter, the microfluidic chip was again flushed with the "starting buffer"[2] of pH 6.0 McIlvaine buffer and left to equilibrate for 15 min. The holosensor picture was taken, followed by a switch to the fibre optic cable for spectrophotometric data acquisition. This procedure was repeated with 50 μL of the solutions for the various pH buffers at decreasing 0.25 pH units intervals until pH 3.0. An adjustable pipette (20 – 200 μL) with 200 μL pipette tips were directly plugged into the tubing to control the fluidic plug within the tubing and chip. The pipette tip could be taken out and pushed back in with any initial volume setting to push or pull the fluid plug away from or back to the inlet. This method allowed for easy fluidic manipulation throughout the inlet tubing, within the microfluidic chip, and along the outlet tubing to the waste bottle. In the event of trapped air bubbles especially inside the microfluidic chamber, the fluidic plug could be pneumatically oscillated to dislodge the bubbles, or induce better mixing by introducing vortices within the chip.

For subsequent runs (i.e. from pH 6.0 to 3.0), the microfluidic chip was thoroughly flushed with a continuous 3 mL flow of DI water via a 5 mL syringe followed by extended pneumatic purging (which dehydrated the gel) before introducing the "starting buffer" for the 2nd and 3rd runs. The average and standard deviation of the spectrophotometric data obtained served as the calibration standard for the holosensor. For better calibration, especially for newly fabricated holosensors, the first run was treated as a "warm-up"[3] run, with the average and standard deviation of the data from the 2nd to 4th runs serving as the calibration standard.

RGB values from the holosensor picture was collected, linearised and transformed to the xyY colour space with the transformation equations described in Appendix B. The x-y coordinates were then plotted on a CIE 1931 chromaticity diagram. The change in pH follows a path, or locus, which could be utilised as a guide for the measured pH.

[2] The "starting buffer" was so named as it aimed to mimic *L. casei* metabolism from its starting pH of 6.0 to about pH 3.8

[3] The "warm-up" helped to mitigate hysteresis effects by initialising the gel elasticity and also for the experimenter to know the duration of a stabilised pH response for more accurate data acquisition

2.4.4 Holosensor validation and application

Lactobacillus casei (L. casei) was exploited as a model for monitoring bacterial growth by examining its lactic acid fermentation metabolism via the corresponding extracellular pH drop from pH 6.0 (with MRS broth) to about pH 3.8.

2.4.4.1 Preparation of MRS media (agar and broth)

de Man, Rogosa, Sharpe (MRS) broth and agar were prepared in Schott glass bottles according to manufacturer's instructions at concentrations of 52 g/L and 61.73 g/L respectively. A glass bottle typically filled with 600 mL of prepared media (agar or broth) was heated using a hot plate, or by placing them into the microwave at full power (600W) for about 1 min without boiling. In the case of MRS broth, it was also filtered using a 0.22 μm (pore size) syringe filter to minimise bacteria contamination and ensure the broth remained particle free for optimal OD_{600} measurements. Thereafter, the media was further segregated into smaller 80 mL aliquots (via a 50 mL syringe), where they were lightly capped and autoclaved at 121°C for about 20 min (up to around 0.22 MPa or 2.2 bar) followed by 30 min of drying.

For MRS agar, it was heated up to a point where the agar becomes liquid and poured into five separate 90 mm Petri dishes in a biological safety cabinet (BSC). They were then stored upside-down in the refrigerator to preserve and isolate moisture from contaminating the agar. It was to be noted that other bacteriological agars were discouraged from being utilised as it could contain constituents that particularly inhibited the growth of *L. casei*.

MRS broth and agar were typically autoclaved within 2h of preparation to prevent the growth of unknown fungi, mould or bacteria already present in the broth and agar powder, which would cloud the media even with autoclaving. It was also important to note that media (broth and agar) typically expires in about 2 weeks, and *L. casei* do not grow properly in these expired media.

2.4.4.2 Culturing of Lactobacillus casei (L. casei)

2.4.4.2.1 *L. casei* cell culture

The *L. casei* bacteria was extracted from Yakult by dipping a disposable sterile plastic wire loop into the liquid (flicking off any excess) and streaking across the MRS agar plate using the standard streaking technique in the biological safety cabinet (BSC). After 48h of incubation at 37°C, the agar should look as depicted in Figure 2-23. A colony forming unit (cfu) was carefully extracted (without touching other colonies on the agar) using a disposable sterile plastic wire loop. It was then inoculated into an autoclaved (sterile) 70 mL bottle of MRS broth (after 10 mL of sterile broth was transferred into a

sterile 20 mL container to be utilised as control) inside the BSC before placing it into the 37°C incubator, lightly capped. This enabled carbon dioxide (CO_2) produced during the bacterial metabolic activity to displace oxygen (O_2) out of the bottle for optimal anaerobic growth. The bacteria grew more unpredictably and slowly with aerobic metabolism.

Figure 2-23: Picture of L. casei Shirota streaked on an agar plate after 48h of incubation at 37°C

2.4.4.2.2 Preparation of *L. casei* batches

After 12h of incubation, the optical density with monochromatic red light at 600 nm (OD_{600}) was monitored using a customised spectrophotometer (with 200 μL quartz cuvette) from 12 - 18h of incubation. OD_{600} was specifically, the extent of scattering resulting from corresponding cell density (cfu/mL) changes, quantified by absorbance measurements. Batches of samples with OD_{600} of 0.93, 1.16 and 1.30 were taken after respective 13.75h, 14.5h and 15.25h of incubation. Each batch went through a series of steps as follows:

(1) The sample was split into fourteen aliquots of 1 mL each in 1.5 mL Eppendorf tubes and centrifuged at 10,000 rpm for 10 min
(2) The supernatant was poured away before 500 μL of 20% (v/v) (aq.) glycerol was added and re-suspended using a vortex mixer
(3) After re-suspension, the solution was immediately put and stored in a -20°C freezer

This procedure ensured that all subsequent experiments were performed with bacteria of the same batch from the exponential growth phase. It is worth highlighting that OD measurements are only linear around OD 1.0 and below. Above that, the culture broth was diluted until the readings were below 1.0 and the actual measurement will be a multiple of the dilution factor. For example, where an OD reading was 2.0, it was diluted 5X to 0.4. However, due to the non-linearity, the actual reading after the 5X dilution will be around say, 0.3. The actual OD reading will thus be a factor (dilution) 5X of 0.3, which is 1.5.

2.4.4.2.3 Cell count of *L. casei* against OD_{600}

The cell count of *L. casei* was typically measured at regular time intervals from OD_{600} = 0.25 (12.25h after inoculation) to OD_{600} = 2.97 (20.25h after inoculation) using an adapted serial dilution method. Seven 1.5 mL eppendorf tubes were prepared with 900 μL of filtered (with 0.25 μm pore size) sterile MRS broth. For each OD_{600} reading, a 100 μL aliquot was taken from culture broth and serially-diluted from 10^{-1} to 10^{-7}. 100 μL aliquots were then separately taken from the eppendorf tubes labelled 10^{-5}, 10^{-6} and 10^{-7} respectively below OD_{600} = 2.5, and 10^{-6} to 10^{-8} for $OD_{600} \geq 2.5$. These aliquots were then spread on separate sterile MRS agar for the counting of colony forming units (cfu). The cfu spots were enumerated 48h later and only the ones having a count of 30 to 300 were counted [130]. Lesser than 30 would be too vague an estimation while more than 300 would constitute as too dense, as the colony forming units would coagulate and be difficult to justify its counts.

The actual cfu for a particular OD_{600} reading was back calculated based on its dilution factor. For instance, the cell count from an agar sample taken from the 10^{-5} aliquot would be multiplied by 10^5 (cfu/100 μL) x 10 (cfu/mL). The graph of cell count with their corresponding OD_{600} and inoculation duration were shown in Figure 2-24.

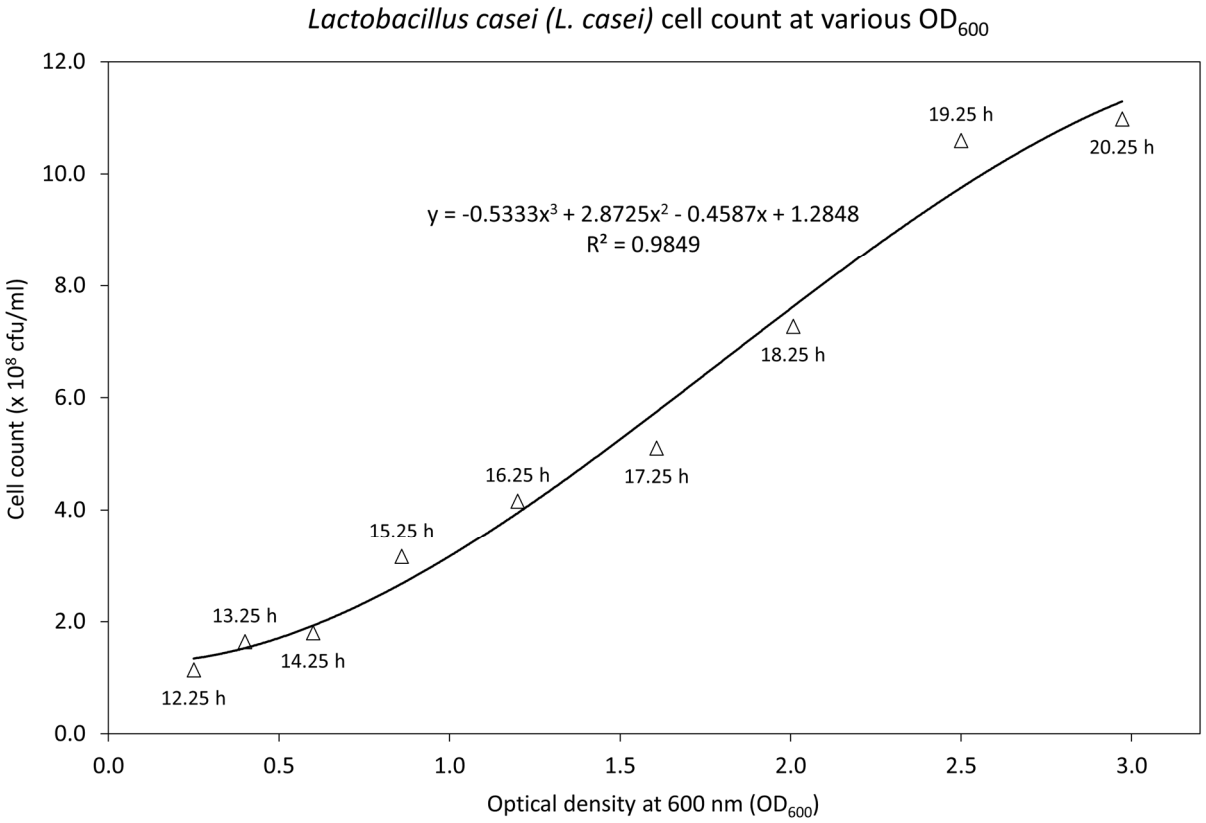

Figure 2-24: Cell count of Lactobacillus casei (L. casei) at various measured optical density at 600 nm (OD_{600})

2.4.4.2.4 Inoculation of *L. casei*

For each experimental run, 200 μL (out of the 500 μL) of the frozen sample, slightly thawed by agitating and stirring the slush, was aspirated and inoculated into sterile 70 mL MRS broth (after 10 mL was transferred out from the 80 mL MRS broth bottle as OD_{600} control) inside the BSC. Subsequently, the inoculated broth was placed in a 37°C incubator, loosely capped.

After 13h of incubation, the shaken 70 mL sample was aseptically separated into eight sterile containers containing 8 mL of the solution in the BSC, with any remaining inoculated broth discarded. The containers labelled t0 to t7 were then immediately put back into the 37°C incubator, loosely capped. The pH, ionic strength, OD_{600}, holosensor signal (micrograph) and holosensor peak wavelength derived from the *L. casei* inoculated media were examined from then every hour with a pH electrode, conductivity electrode, customised spectrophotometer, high resolution (with 12X zoom) colour camera and spectrophotometer in the listed order respectively.

The various data obtained from the same tests were then analysed and compared accordingly with each other, which would be presented in the following chapters.

3 Chapter 3 Integrated pH holosensor in a microfluidic system

An adapted method for controlling the holosensor gel diameter and integrating it into a microfluidic system for holographic signal interrogation is described in this chapter. To validate the practicality of the pH holosensor, the calibrated sensor was utilised to monitor the growth of *Lactobacillus casei (L. casei)*. The importance of controlling gel diameter and improving hologram brightness as the main objectives necessitated the addition of a polymerisation inhibitor and use of a continuous wave laser source. The designated 3.0 mm gel diameter maintained a standard deviation lower than 0.2 mm, and the hologram registered an intensity count of more than 10,000 with the spectrophotometer when interrogating the holosensor at its pK_a with 20 ms integration time at 12X magnification. The effectiveness of the sensor was also compared and evaluated against that of the pH meter.

3.1 Controlled polymerisation

Instead of using a physical mask [131] to polymerise the gel for hologram fabrication, photolithography was utilised together with a polymerisation inhibitor, hydroquinone (HQ), to control the rate of polymerisation by neutralising free radicals. It was suggested that a polymerisation inhibitor (or terminator) such as hydroquinone (HQ) and ascorbic acid could scavenge free radicals [132] and control the uniformity of photopolymerised microgels [133]. Areas exposed to UV undergo rapid polymerisation from the homolytic fragmentation of the free radical initiator 2-2-dimethoxy-2-phenylacetophenone (DMPA). The active (initiating) benzoyl radical fragment [134], [135] and secondary methyl fragment [136] creates reactive species with the methacrylate C=C groups of the gel precursors. The radicalised methacrylate groups of the monomers, crosslinkers and pH moieties, together with the UV induced decomposition radical fragments of DMPA made it highly likely for HQ to be quickly expended. The relative inactivity of DMPA in the unexposed regions and hence the unreacted gel precursors were however, restricted by the presence of HQ. Using the recipe described later in §3.2, the experimental parameters were varied to obtain consistent gel diameters comparable to industry standards. According to DIN ISO 2768-1, the permissible deviations broken edges (external radii and chamfer heights) of fine tolerance class for “0.5 mm up to 3 mm” was ± 0.2 mm [137].

3.2 Typical 3.0ϕ HEMA-co-TFMPA gel profiles

2-(trifluoromethyl) propenoic acid (TFMPA) has an apparent pK_a of about pH 4.45 in a block co-polymer of HEMA-co-EDMA (3 mol%)-co-TFMPA (6 mol%) [80]. This made it ideal for monitoring *L. casei* since optimal growth for the bacteria was around pH 4.5 to 5.0 – well within the range where TFMPA would result in the largest holographic peak wavelength shift.

An arbitrary 3.0 mm diameter gel (3.0ϕ) was designated for the proof-of-concept of this adapted method since that size would be small enough for a typical microfluidic chip. Figure 3-1 shows the typical profile, micrographs and schematics of 3.0ϕ gels. The standard deviations (s.d.) for the minimum (ϕ_{min}) and maximum diameters (ϕ_{max}) were both 0.06 mm (Figure 3-1(c)).

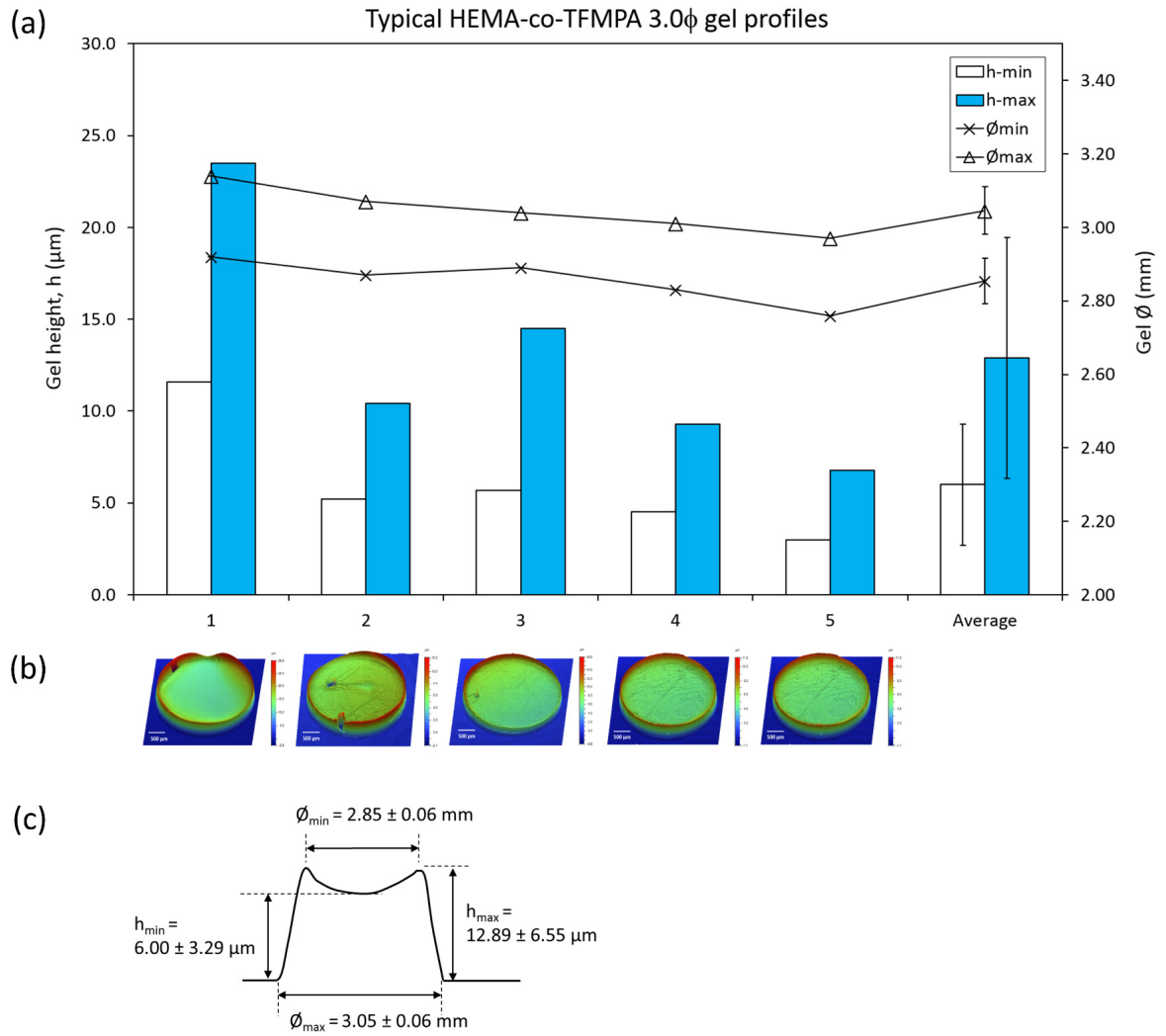

Figure 3-1: Typical gel information of HEMA-co-EDMA (3 mol%)-co-TFMPA (6 mol%). ***(a)*** *Graph depicting the gel heights (µm) and diameters (ϕ in mm) of 5 samples and their average, the error bars for the average was ± 1 standard deviation (s.d.).* ***(b)*** *Micrographs of the gel profiles obtained from the white light profiler.* ***(c)*** *Schematic diagram of the average gel profile with 1 s.d. as the tolerance.*

The gel precursor was introduced on a glass substrate and photocured with a parallel beam 365 nm narrow band UV LED source as described in §2.4.2.4. A number of parameters such as amount of free radical initiator (DMPA), inhibitor (HQ), crosslinking (EDMA) and monomer (HEMA) were varied to obtain the current recipe for fabricating 3.0ϕ gels. The proportion of pH moiety (TFMPA), 6 mol%, was not varied and was adopted from an earlier work on pH holosensors [79]. For a more straightforward comparison and optimisation with different recipe batches, the total number of moles for the gel

precursors were fixed at 8 mmol per 1 mL of solvent (IPA). The amount (in mol%) of DMPA was normalised to the regular DMPA recipes from previous work in the Lowe Group, and the amount of HQ was pegged as a molar ratio to DMPA. Naming conventions to describe the recipes were detailed in Appendix F.

For the 3.0ϕ gel, the recipe was 8 mmol gel precursors with HEMA:EDMA:TFMPA 91:3:6 mol% (8TH-2, 6T3E), 3.93 x 10^{-3} mmol DMPA (1/18 DMPA), 1.96 x 10^{-3} mmol HQ (2:1 HQ) in 1 mL IPA, 29.64 mW/cm^2 (9% power) UV@365 nm exposure for 4 min (9p4m) using a diced, 8 mm x 8mm cyclic olefin copolymer cover substrate (identifier: 3a) with a particular Newton rings configuration (COCopp8x8d3a). The injection molded cover substrate was chosen due to its hydrophobicity compared to glass, as well as its UV transparency and monorefringence. The distance from the UV LED source was kept at a constant 5 mm away from the gel sample during photo-polymerisation.

3.3 Holosensor brightness optimisation

Instead of using the conventional pulsed laser for hologram fabrication, a continuous wave (CW) laser was proposed as a means to achieve significantly brighter holograms. Crucially, intricate control of the laser power intensity and beam quality were thought to improve the Bragg planes' diffraction efficiency, and hence the resultant hologram brightness. Additionally, Q-switched operation releases high output power during a short duration. This could result in high intensity reciprocity failure (HIRF), where there is not enough time for the mobile silver ions to neutralise the trapped photoelectrons. Electrostatic repulsion would cause the subsequent photoelectron to be trapped at a different site. There may also be higher rate of holes recombining with the electrons, rendering latent image formation redundant [138]. Beam divergence can also be more accurately and easily manipulated with a CW laser. As most CW lasers possess significantly lower power intensities compared to their pulsed laser counterparts, a much longer laser exposure was required. Where it took only a few nanoseconds for a pulsed laser exposure, the CW laser requires seconds.

3.3.1 Effect of vibrations and temperature variations on hologram brightness

The biggest disadvantage of using CW lasers for hologram fabrication was the issue of movement during the recording of the hologram. In the extremely short time required for pulsed lasers to illuminate and record its interference within the gel volume, movement during that duration would be negligible. Holograms, such as those of living persons or animals, are recorded using a diverged pulsed laser beam.

On the other hand, vibrations from nearby tables or draughts from air-conditioners and ducts, or the expansion/contraction of the optomechanical components due to temperature fluctuations - even

down to a quarter of a wavelength - would disperse the interference pattern recorded by the standing waves during the laser exposure. The overlap of these “multiple exposures” occuring due to the infinitesimal movement of any part of the experimental setup could result in a fuzzy or dim hologram. Thermal instability could also lead to low intensity reciprocity failure (LIRF) [138]. When an isolated silver atom is not stabilised by combining with another silver atom within its lifetime (~2s), it decomposes back to an electron and silver ion [138].

However, with the introduction of a vibration-isolation table and inclusion of an acrylic enclosure around the setup, vibrations and temperature fluctuations were kept to a minimum. Thin (2 mm width) double sided tape was utilised to stick the gel sample securely onto the adaptor during the hologram fabrication process. Thick, darkroom curtains also encircled the experiment area to further isolate vibrations and the influence of nearby air-conditioning ducts from the experimental setup.

3.3.2 Effect of polarisation on hologram brightness

Polarisation is a property of light which specifies the orientation of the electric vector (and hence the orthogonal magnetic vector) of the propagating transverse electromagnetic wave. While most of the light we see in our daily lives are randomly polarised, such as sunlight, the formation of coherent interference within the gel volume depends heavily on a non-orientation changing wave.

A noteworthy polarisation phenomenon is that light can become perfectly polarised in a plane orthogonal to the plane of incidence upon reflection. When a light beam is radiated onto a surface at a particular angle of incidence, known as the Brewster angle, the reflected beam is s-polarised while the transmitted beam is p-polarised. In relation to the plane of incidence, the s-polarised light is vertically polarised while the p-polarised light is horizontally polarised. It was also reported that if a narrow width of the diffraction efficiency was required for volume reflection holograms, one should exploit the p-polarisation [139]. However, as front surface mirrors were essential for recording high reflection plane holograms – taking into account that reflective surfaces change the polarisation orientation – there was not much that could be done to further optimise the setup in terms of selecting the perfect polarisation orientation.

In the experimental setup, a rotatable quartz half-wave plate was placed in front of the beam together with a thin film Brewster type polariser that reflects s-polarised light and transmits p-polarised light. This configuration allows the adjustment of the beam power intensity by simply rotating the half waveplate while preserving the original linear polarisation of the laser.

3.3.3 Effect of orientation of optomechanical components

Many gels exhibited undesirable hologram quality such as those shown in Appendix Y-1. Before the optimal experimental setup for hologram fabrication was put in place, gels developed either without a hologram, with only a dim hologram, a hologram only at a small specific spot (or area) within the gel, a polychromatic hologram, a holosensor damaged in the microfluidic chip after gel expansion, or appearance of bubbles which compromised the holographic signal. The parameter which resulted in the most efficient method for producing significantly brighter holograms involved two counterintuitive measures.

First, it was found that there was a much higher success rate of producing holograms when the laser power intensity was adjusted to about 0.290 mW at 9 mm beam diameter, as opposed to 3.5 mW which worked with few issues while in Cambridge, even with a battery operated CW laser. It appeared that some sort of laser scattering or zero order interference, could have prevented the formation of a hologram within the gel volume, as was mostly the case with numerous hologram fabrication trials. Through careful observation of various parameters, a rather perculiar commonality between successful samples was observed. Critically, it was noticed that whenever the retroreflection of the return beam was slightly offset by a certain angle, it became a lot more likely for the gel to exhibit a bright hologram.

The kinematic mirror mount that housed the front (or first) surface mirror provided positional accuracy unlike with screw type fasteners. Initially, the beam was sent back along the same path but would almost never produce a hologram. It was only when the half waveplate was rotated to a different laser intensity did it work better sometimes. The breakthrough moment came when an adjustable iris with a protuberance was used to locate the (retroreflected) return beam spot. It was later concluded that for every section of the light path between adjacent optomechanical components, any back reflections would have to be reflected away or purposely angled away. Described with more detail in §2.4.2.8.1, this essential offset needed to be applied to every optomechanical component of the setup, especially that of the downstream plano-convex lens. It also necessitates an offset of the centre of the laser beam (validated by minimising the iris diameter) from illuminating within the diameter of the gel.

3.4 Integration of the 3.0ϕ HEMA-co-TFMPA holosensor into a microfluidic chip

The PDMS-glass microfluidic chip has been widely used since the introduction of soft lithography for rapid prototyping of microfluidic systems [66] and microbioreactors [31], [140]. The PDMS acts as a semi-permeable membrane for oxygen exchange while glass has traditionally been utilised as the substrate of choice for holosensor gels due to its stability, UV transparency and ease of silanisation. The fabrication method for PDMS-glass microfluidics was directly adopted without any modifications since the holosensor gel was robust and could still function after undergoing the requirement of high-powered oxygen (O_2) plasma treatment for instant bonding of the holosensor embedded glass to the PDMS.

The desired channel features were designed and translated to a mould for soft lithography. PDMS was poured into the mould, degassed and crosslinked in an 80°C oven for an hour. After taking the crosslinked PDMS out, the mould could be reused repeatedly as long as it was hydrophobised with 1H,1H,2H,2H-perfluorooctyltriethoxysilane (FOTS) or 1H,1H,2H,2H-perfluorodecyltriethoxysilane (FDTS) every 30 moulding cycles using a procedure described in Appendix E. 1 mm diameter inlet and outlet holes were created with a biopsy punch before cleaning the surfaces with isopropyl alcohol (IPA). Tape was then utilised to extract any hydrophobic stains on the PDMS, before recipe #6 from Table 2-1 was utilised to form the microfluidic chip.

Blunt angled syringe tips were modified for fluidic interfacial connection to soft tubings leading to the inlet and out of the outlet to a waste container. This setup was then mounted on an in-house designed and fabricated sample adaptor as illustrated in Figure 2-4(c). All the fluidic connections were interference fit to prevent leakages.

In addition to the mounting of the microfluidic chip onto the sample interrogation stage, a precise method of adjusting light illumination angle was required. A rotary stage with angular markings integrated with an optics mount for tilt-yaw and an x, y and z axis stage was integrated with an adaptor to secure the fibre optic cable (Figure 2-4(b)).

Finally, the most critical component was the eyes of the microfludic system. Field of view and working distance were the 2 interconnected parameters where a compromise must be found to optimise the system. For the best field of view to interrogate a small area, the working distance should be short. For a long working distance, in order to accommodate for illumination adjustment, the large field of view would make it difficult to see clearly any features and/or colour variations of the hologram.

3.5 3.0ϕ HEMA-co-TFMPA holosensor

As the emphasis was on hologram brightness and uniformity, a number of bright holograms could not be utilised due to their polychromatism or existence of a double peak when interrogated by the spectrophotometer. The profile of typical 3.0ϕ gels were mostly even, unlike the holosensor depicted in Figure 3-2, which was chosen based solely on its exceptional brightness and difficulty of obtaining a bright, uniform holographic signal for the 3.0ϕ gel. For simplicity, assuming linear intensity difference at every magnification multiple, and normalising the intensity counts to a typical hologram, the brightness of this holosensor (measured with 1.05 ms integration time at 11,000 out of 65,000 saturation counts) was about 18.3X brighter than a typical 'bright' hologram (measured with 50 ms integration time at 30,000 counts).

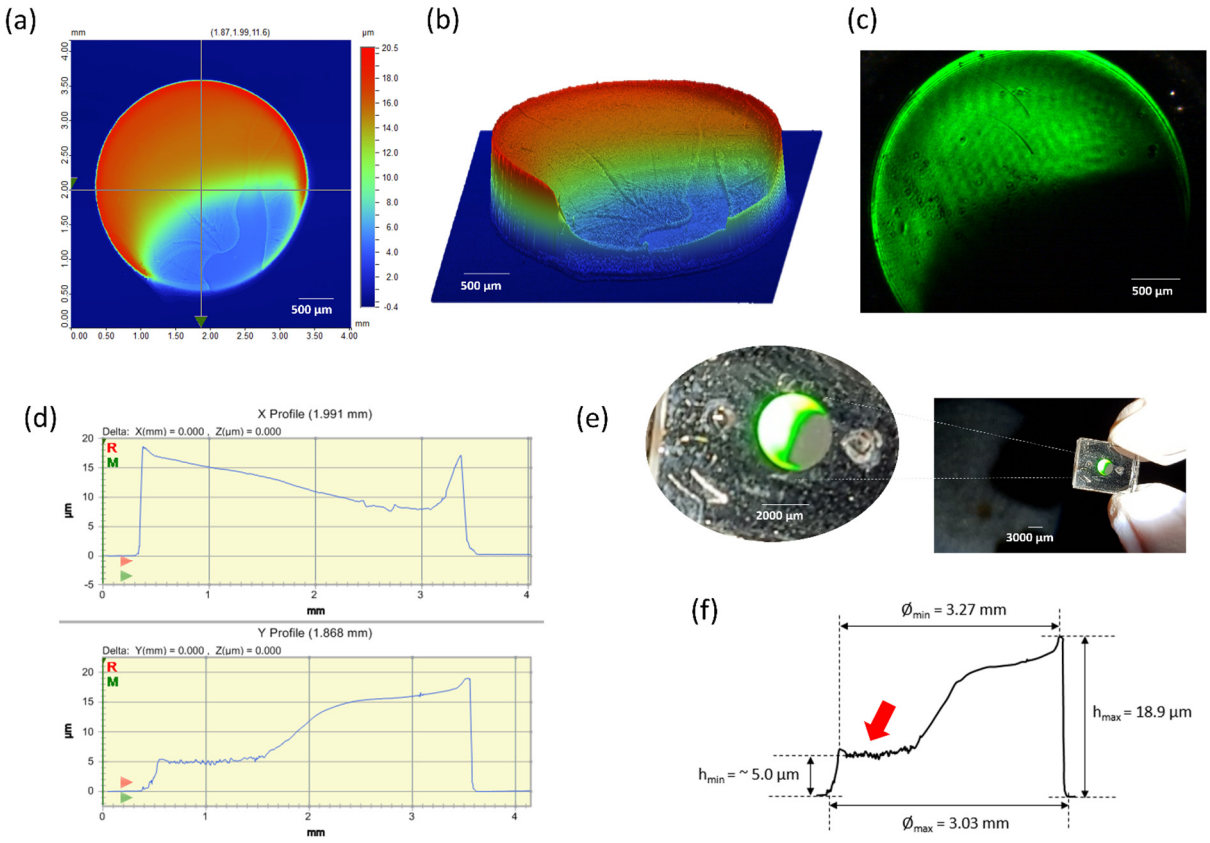

Figure 3-2: Collation of 3.0ϕ HEMA-co-TFMPA holosensor information. ***(a & b)*** *2D and 3D digital elevation model of the chosen 3.0ϕ holosensor after hologram fabrication respectively.* ***(c)*** *Picture of the hologram taken by the high-resolution camera at 6.96X zoom setting while the 3.0ϕ microfluidic chip-embedded holosensor was immersed in pH 6.0 McIlvaine buffer.* ***(d)*** *Cross-sectional x and y profile of the 3.0ϕ holosensor along the crosshair depicted by the 2D digital elevation model.* ***(e)*** *Picture of the hologram taken with a Samsung S7 mobile phone with pH 6.0 McIlvaine buffer inside the microfluidic chip.* ***(f)*** *Reproduced y profile of the 3.0ϕ gel with measured white light profiler data. The red arrow points out a particularly rough portion of the gel, which coincided with a lack of holographic signal at that region.*

3.5.1 Gold standard in hologram brightness

A portion of the gel was probably peeled off after gel fabrication, but the remaining portion displayed a monochromatic hologram that far exceeded any regular holograms in brightness. To put it in perspective, the "gold standard" for holography was the gelatin hologram. Its proteinaceous and hydrophilic functional groups make it much easier to trap Ag atoms during the laser exposure phase. They were also generally thicker and contained more fringes, which would improve its diffraction efficiency. Under tungsten-halogen (T-H) light illumination, the gelatin hologram would saturate the detector at 1.05 ms integration time with more than 65,000 counts. This gelatin hologram was fabricated (in Cambridge) with the same experimental setup and used as an alignment tool for subsequent HEMA-based holograms. The bright gelatin hologram was previously utilised to detect proteases [88] and water in solvents [91], but possessed complex sensory behaviour due also in part to its rich proteinaceous gel matrix, which severely restricts application to other biochemical analytes. Comparatively, when a regular hologram was illuminated with the same T-H light source, it typically averages about 30,000 counts for a 50 – 100 ms integration time. The maximum intensity count for saturation was 65,000 – and this count will be scaled according to the chosen integration time in ms). An example of a hologram displaying an acceptable holographic signal at 30 ms integration time can be found in Appendix C-2(d).

3.5.2 Comparison of holosensor to gold standard

Even though the 150W Xenon light source currently utilised for holosensor interrogation was much brighter (at least by virtue of its power) than the 10W tungsten-halogen lamp, it is worth noting that the holographic signal from the 3.0ϕ holosensor was also saturated beyond the maximum of 65,000 counts at 1.05 ms integration time with a pH 4.50 McIlvaine buffer. In addition, the 3.0ϕ holosensor was interrogated at a 12X zoom setting, which significantly reduced the holographic signal intensity per unit area. For the next step beyond the scope of this thesis, a like-for-like comparison will be made between a commercial hologram and our in-house fabricated hologram for a more accurate holosensor brightness evaluation.

3.6 Holosensor pH calibration

3.6.1 Choice of pH calibration buffer

For precise work, the pH meter was calibrated with 12.88 mS/cm ionic strength buffer followed by a 3-point calibration with standard pH buffers at pH 4.01, pH 7.00 and pH 9.21 before being utilised for holosensor calibration itself. 0.1M McIlvaine (citrate-phosphate) buffers were prepared from pH 3.00 to pH 6.00 in steps of 0.25 pH units and their pH values measured with the pH meter. This was the

only “universal” pH buffer, which buffers well across the designated pH range. The universality of the buffer was likely due to the combination of the triprotic citric acid and conjugate base of the triprotic phosphoric acid. In order to minimise the convolution of the buffers’ different ionic strengths at different pH, 3M NaCl was added accordingly to the prepared McIIvaine buffer to balance the ionic strength (measured by a conductivity electrode connected to the dual pH/conductivity meter). As described in §2.4.3.2, the McIIvaine buffers were normalised to the buffer with the highest original ionic strength 9.50 mS/cm (pH 6.00 buffer).

3.6.2 Calibration technique

Typically, the microfluidic chamber was rinsed thoroughly with DI water before introducing the next pH buffer for sensor appraisal. However, to minimise any possible hysteresis effect when the pH returned to the holosensor’s own pK_a during a thorough DI water rinse, pneumatic N_2 gas drying was utilised between each tested pH buffer. The N_2 gas was pumped into the system via the same fluidic connection to purge, dry and clean up the fluidic path and microfluidic chamber before the next pH buffer was introduced. Each time, 50 μL of the pH buffer was injected into a flexible tube leading to the 0.942 μL microfluidic chamber (2 mm in radius, 75 μm height) with an adjustable pipette.

With the overpipetting technique, the pH buffer fluid column could be easily manipulated to move forward, backward or even oscillate with just an adjustable pipette. The first introduction of pH buffer was to prime the holosensor with the new buffer by rocking the fluidic column to and fro and then purging it with N_2 gas, followed by introducing a new batch of the pH buffer for sensor interrogation. In this manner, residue from the previous buffer can be washed away while preparing the holosensor for the new buffer without drastically changing its pH environment, ionic strength or concentration of buffer experienced by the holosensor within the microfluidic chip. The buffers were also introduced step-wise from pH 6.00 down to pH 3.00, the same expected pH shift direction for the growth monitoring of *Lactobacillus casei.*

After the “dummy” 1st round, the approximate duration required for the stabilisation of the holographic signal was obtained. It took around 5 min to equilibrate to a stable peak wavelength, and would quickly settle to a new steady value within 1 min for subsequent measurements. This further demonstrated that the gel required priming before the actual calibration or experimental run. The priming requirement could be due to the wettability of the gel during continuous buffer calibration compared to when it was stored in a dry environment. Each pH buffer was typically left for 5 min to equilibrate before the pictorial, spectrophometric and peak wavelength response of the hologram was recorded. To prolong the lifespan of the holosensor, the intense Xenon light was blocked until readings were taken. Unreacted residual photosensitive AgBr would eventually darken and affect the intensity

of the holographic signal. The calibration cycle was repeated 3 times to ensure calibration accuracy. The results obtained from one of the calibration cycles is summarised in Figure 3-3.

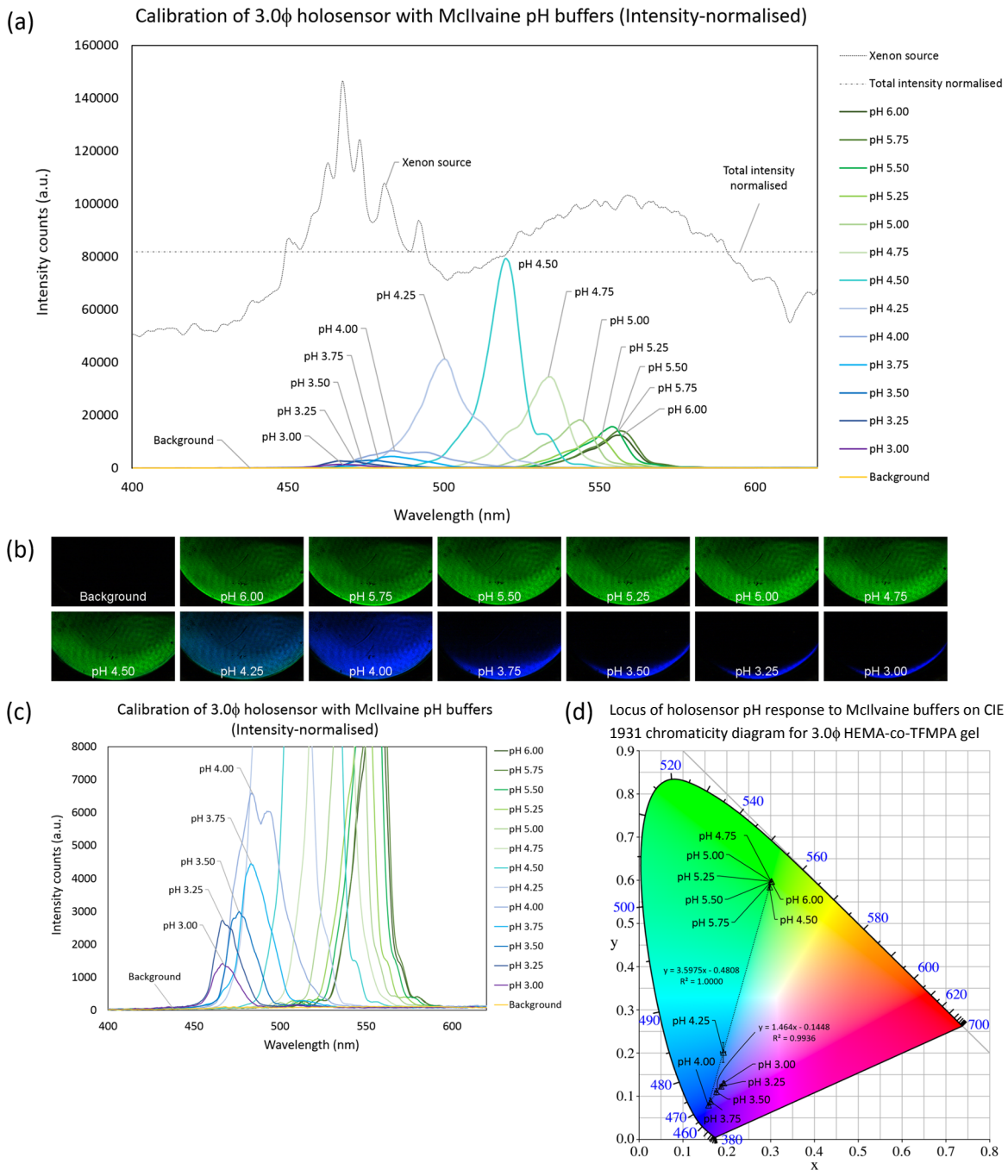

Figure 3-3: Collation of 3.0ϕ HEMA-co-TFMPA holosensor calibration data. ***(a)*** *Total intensity-normalised peak wavelength holosensor pH responses obtained from pH 6.00 down to pH 3.00. The height of the peaks represents the corresponding spectral intensity recorded by the spectrophotometer.* ***(b)*** *Picture montage of holograms captured by the high-resolution camera at 12X zoom setting when immersed in correspondingly decreasing pH starting from pH 6.00 to pH 3.00 just before the spectrophotometric data of (a) was collected.* ***(c)*** *A zoomed-in version of (a) to more clearly discern the signal-to-(background) noise ratio.* ***(d)*** *Visualisation of colour change with locus of holosensor pH response corresponding to RGB-xyY transformed values from (b) plotted onto the CIE 1931 chromaticity diagram.*

Background data (picture from Figure 3-3(b)) was obtained at the beginning of the experiment after the microfluidic system was flushed with the starting pH 6.00 buffer and purged away with N_2 gas.

3.6.3 Holosensor reliability

To ensure that the reliability and repeatability of the holosensor, data from the first run of pH 6.00 to 3.00 was neglected. This protocol was introduced, as first runs were anomalous (due to the newly introduced buffers), which undermined the real accuracy of the holosensor. Furthermore, the pristine sensor required a warm-up run for the gel matrix to consolidate its expansion and contraction states. Accordingly, it would also filter out the unreliable holosensors that lose their brightness or elasticity, as discussed in Appendix AA (§Diminishing hologram brightness).

3.6.4 Normalisation of holographic signal

The emission spectrum shape of the Xenon light source was arbitrarily superimposed on the peak wavelength graph to juxtapose with the relative illumination intensity of the holographic peak wavelength signals. To recapitulate the mechanism of obtaining the holographic signal – the holosensor works by selecting a particular band of wavelengths (from the illumination source) for reflection depending on the arrangement of the Ag^0 fringes within the gel matrix while transmitting the rest. Where there was a pronounced drop or increase in illumination intensity over a certain wavelength range, the holographic signal would be attenuated or heightened accordingly. This would mean that the intensities obtained from the peak wavelength graph depended on the spectral intensity of the illumination source.

To mitigate this undesirable influence, the varying intensities of the light source across the evaluation wavelength range were normalised to a constant value. The area under the curve of the light source spectrum (using the trapezium rule method) was divided by the wavelength range to arrive at a total intensity normalised value. The relative intensity ratio between the original and normalised intensity value of the Xenon light source was used to correct for the intensities of the peak wavelength curves at that particular wavelength. The result was a peak wavelength curve that behaved as if the illumination source had a uniform intensity throughout the evaluation wavelength range.

3.6.5 Holosensor interrogation angle

It was observed that the hologram became thinner after being blue shifted (contracted) as illustrated in Figure 3-3(b). Upon investigation of this phenomenon, it was realised that the gel could have changed shape or orientation during contraction, which would display the hologram at a different angle. This was verified at the lower pH values. There are two schools of thought with regard to this occurrence. One would continually search for the maximum intensity hologram at every pH value

regardless of the interrogation angle, while the other would stick to a particular interrogation angle throughout the entire evaluation pH range. The rationale for the former was that the finding of the maximum intensity would convey consistency in terms of the uniformity of the holographic signal. The latter would argue that based on the Bragg's condition, a change in interrogation angle would result in a spurious peak wavelength reading because the action of changing the angle itself would result in a corresponding wavelength shift. Even with the same pH buffer, changing the interrogation angle would shift the wavelength peak. Unless there were an automated system where it constantly searches for the maximum intensity, it would seem unwise to change the interrogation angle. The latter method of maintaining the same interrogation angle was thus employed. This scheme would also be more suitable for commercialisation since it would not require constant automation.

3.6.6 RGB to xyY colour space

The purpose of taking hologram pictures with the high-resolution camera was to observe not only features on the gel and discern its brightness visually, it was also meant to evaluate an alternative method for visualising the colour change corresponding to pH change from the raw hologram pictures. RGB values were obtained from a MATLAB® programme, with the algorithm coded by Dr Gita Moghaddam, using a self-designated evaluation region of the hologram picture file. They were then normalised to [0.0, 1.0], linearised (or inverse sRGB companded [141]), and transformed to the XYZ colour space [142]. The transformation matrix takes into account D65 as the reference white.

The conversion of XYZ values to the xyY colour space enabled the plotting of the converted RGB values on a CIE 1931 chromaticity diagram. With the data points and locus of the pH change, one may be able to predict the pH by plotting the transformed RGB values onto the calibrated pH locus diagram in Figure 3-3(d). A drawback to this chromaticity diagram (or colour space) was its non-linearity, and we can only estimate the pH to its nearest data point. For example, a mid-point between the pH 4.00 and 4.25 does not necessarily mean that the unknown sample was pH 4.125.

3.6.7 Holosensor at its pK_a

It was noticed that the peaks were a lot broader at the two ends of the evaluated pH range. This was in line with the prediction of sensitivity for a pH holosensor with apparent pK_a around 4.45. Within ± 1 pH unit of its pK_a, the change in gel elevation with respect to pH change would be the largest due to the appreciable charge difference of the TFMPA pH moiety close to its pK_a.

Just by looking at the intensity-normalised peak wavelength graph, a certain symmetry was observed about pH 4.50. The pK_a, which was the pH value whereby half the TFMPA moieties were charged (or

neutralised), could be inferred to be around pH 4.50 because the sensitivity to pH changes was maximum there.

Referring to the Henderson-Hasselbalch (H-H) Equation 3.1 as follows:

$$pH = pK_a + \log_{10}\frac{[A^-]}{[HA]} \tag{3.1}$$

At the pK_a, pH = pK_a, and the ratio between the acid HA and its conjugate base A^- was 1. The availability of both these species at equal proportions allowed for buffering at both sides of its pK_a, making it highly sensitive to pH changes.

The pK_a can typically be determined by measuring a certain parameter, parameter X, as a function of pH, which typically describes a sigmoidal curve (Figure 3-4). The pK_a could then be established at the inflection point where parameter X = 0.5. Assuming the working pH range (pH 3.00 to 6.00) of the holosensor included the entire buffering capacity of the TFMPA moiety, parameter X can represent the degree of dissociation of the acid (TFMPA). Zero ("0") would therefore coincide with only the non-dissociated acid configuration (at λ_{min}), while one ("1") would denote the condition where only the fully dissociated acid configuration (at λ_{max}) was present in solution. The degree of dissociation, α, for acids is defined as:

$$\alpha = \frac{[A^-]}{[HA] + [A^-]} \tag{3.2}$$

α can also be expressed as the following:

$$\alpha = \frac{\lambda - \lambda_{min}}{\lambda_{max} - \lambda_{min}} \ , \tag{3.3}$$

where λ is the wavelength coinciding with a particular degree of dissociation.

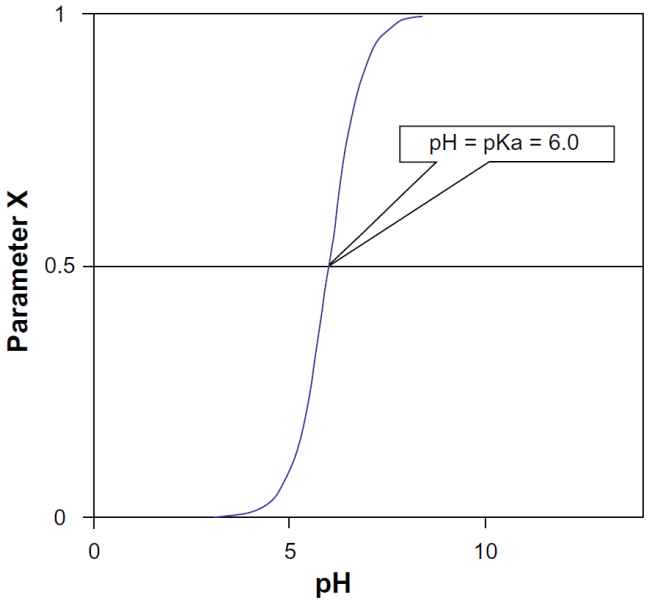

Source: Reijenga, J., van Hoof, A., van Loon, A. & Teunissen, B. Development of methods for the determination of pK$_a$ values. Anal. Chem. Insights 8, 53–71 (2013).

Figure 3-4: Generic representation of a sigmoidal curve created by plotting a measured quantity, parameter X, against pH (in this particular example, the pK$_a$ was 6.0 where parameter X=0.5).

3.6.8 Modified Henderson-Hasselbalch (H-H) calibration curve

Combining Equations 3.1, 3.2 and 3.3, while making λ the subject, the modified H-H equation becomes

$$\lambda = \frac{\lambda_{max} \cdot (10^{pH - pK_a}) + \lambda_{min}}{1 + 10^{pH - pK_a}} \tag{3.4}$$

The derivative of λ with respect to pH was determined by applying the quotient rule (details shown in Equations I.12 to I.14 of Appendix I) and its expression was as follows:

$$\frac{d\lambda}{dpH} = \frac{(10^{pH - pK_a} \cdot \ln 10)(\lambda_{max} - \lambda_{min})}{(1 + 10^{pH - pK_a})^2} \tag{3.5}$$

The slope of the curve ($\frac{d\lambda}{dpH}$) was calculated at every pH test point, and plotted together with a normalised average (avg) intensity curve in Figure 3-5(a). The normalised average intensity curve was determined by normalising the intensity counts to 1.2X of the maximum intensity counts. This was to ensure the error bars would not exceed 1.0.

Equation 3.4 was used to plot a calibration curve on the same graph as the raw data values. The pK$_a$ was initially estimated by choosing the nearest 0.05 pH unit to the maximum slope. During each iteration, it was varied together with λ_{max} and λ_{min} , which were also tweaked by up to 5 nm for a better curve fit as the actual holosensor buffering capacity (~ pH 4.40 ± 2 pH units for this particular example) do extend slightly beyond the pH evaluation range (pH 3.00 to 6.00). The resultant best fit curve with the raw data points were plotted and shown in Figure 3-5(b).

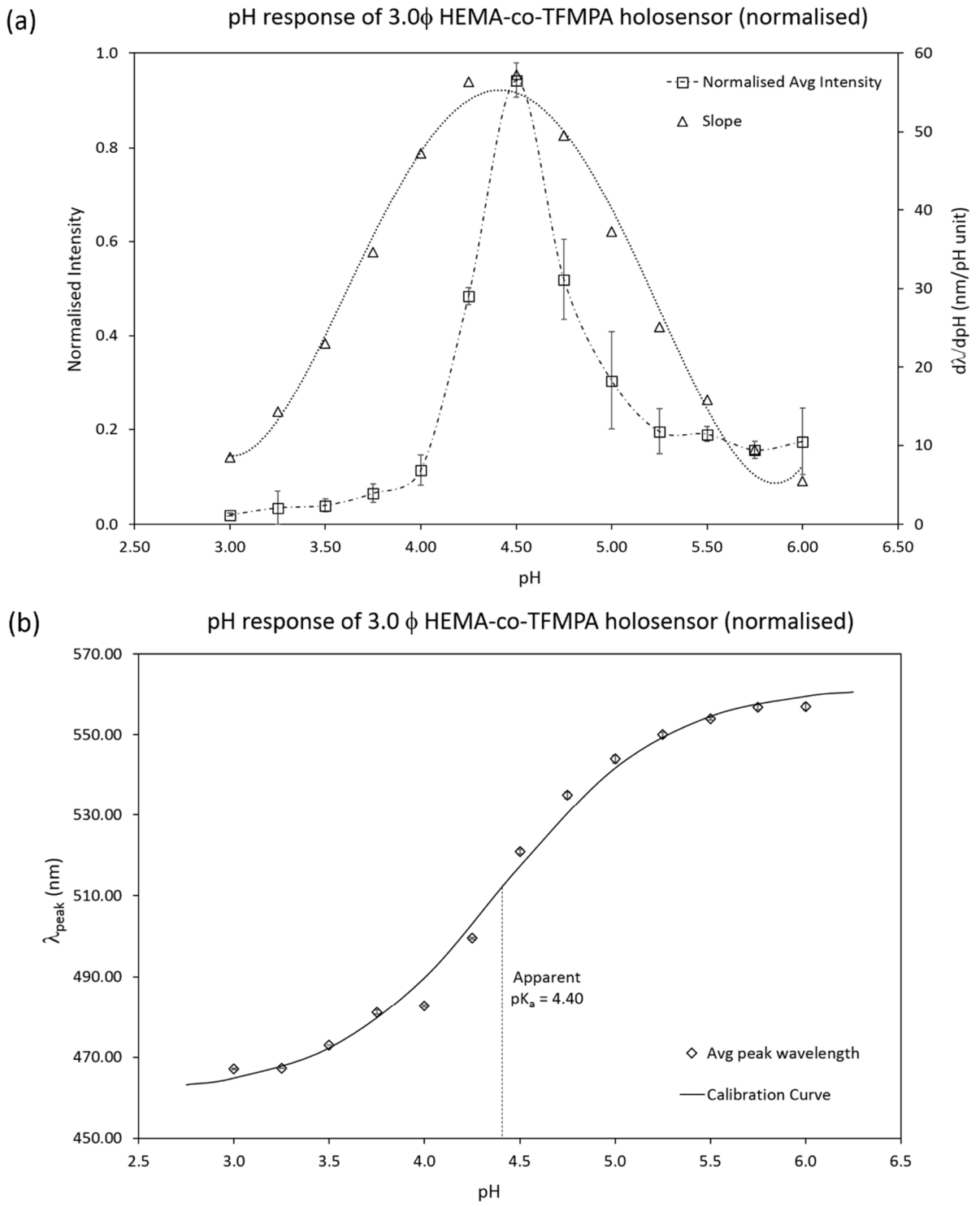

Figure 3-5: ***(a)*** *Normalised intensity holosensor response at varying pH values between pH 3.00 and 6.00 with ± 1 s.d. as the error bars, and slope of peak wavelength change to pH change ($\frac{d\lambda_{peak}}{dpH}$).* ***(b)*** *Modified Henderson-Hasselbalch (H-H) pH calibration curve with the average of three runs (from pH 6.00 to pH 3.00), and ± 1 s.d. assigned as error bars. The apparent pK_a of the holosensor was pH 4.40.*

The slope and normalised average intensity curves appear to peak closely to the apparent pK_a. This observation was consistent with earlier deductions and definitions in §3.6.7 – the sensitivity of the holosensor was highest at its pK_a and that the pK_a was defined to be near to the maximum slope.

3.7 Difference in pK_a between solution and gel matrix-bound TFMPA

The apparent pK_a for the 3.0ϕ holosensor was 4.40 for a concentration of 6 mol% TFMPA within the gel matrix, which was close to the previously reported 4.45 [80]. It was to be noted that the pK_a of the free-bound TFMPA monomer was 3.0 and was upshifted by +1.45 units. This upshift of matrix-bound TFMPA was due to the influence of its polymeric microenvironment, which changes its apparent tendency to dissociate. The charged configuration of the acidic group were destabilised due in part to the relative hydrophobicity of HEMA and unfavourable electrostatic interactions.

3.8 Effect of ionic strength on the calibrated holosensor

The holosensor gel expands or contracts at various pH levels due to the presence of charged TFMPA moieties within the gel matrix. The change in the Donnan equilibrium results in an osmotic pressure differential that causes water together with counterions to flow in or out of the gel matrix. Consider a scenario where the pH remained the same but substantial amount of 3M NaCl was added to the solution. The Na^+ ionic charge, being much stronger than the dipole-dipole interaction of TFMPA with water molecules competes for the $–COO^–$ charge. Water would thus be forced out of the gel matrix, which would result in gel contraction.

The ionic strength holosensor response corroborates with the obtained peak wavelength data from Figure 3-6(a) – the holosensor contracts at high ionic strength and expands at lower ionic strength. The intensity data coincided with the pictures shown in Figure 3-6(b). Even when the intensity of the 150 mM NaCl hologram in Figure 3-6(b) only visually reduces by a little, there was a drastic drop in the recorded peak wavelength. For future experiments, NaCl concentrations more than 120 mM could be omitted, which would allow a different interrogation angle to provide a uniform and brighter holographic signals throughout the ionic strength test range. Additionally, it was also evident from the chromaticity diagram (Figure 3-6(c)) that there were 2 different loci, for which 1 would be eliminated when only concentrations of 120 mM NaCl and below were utilised.

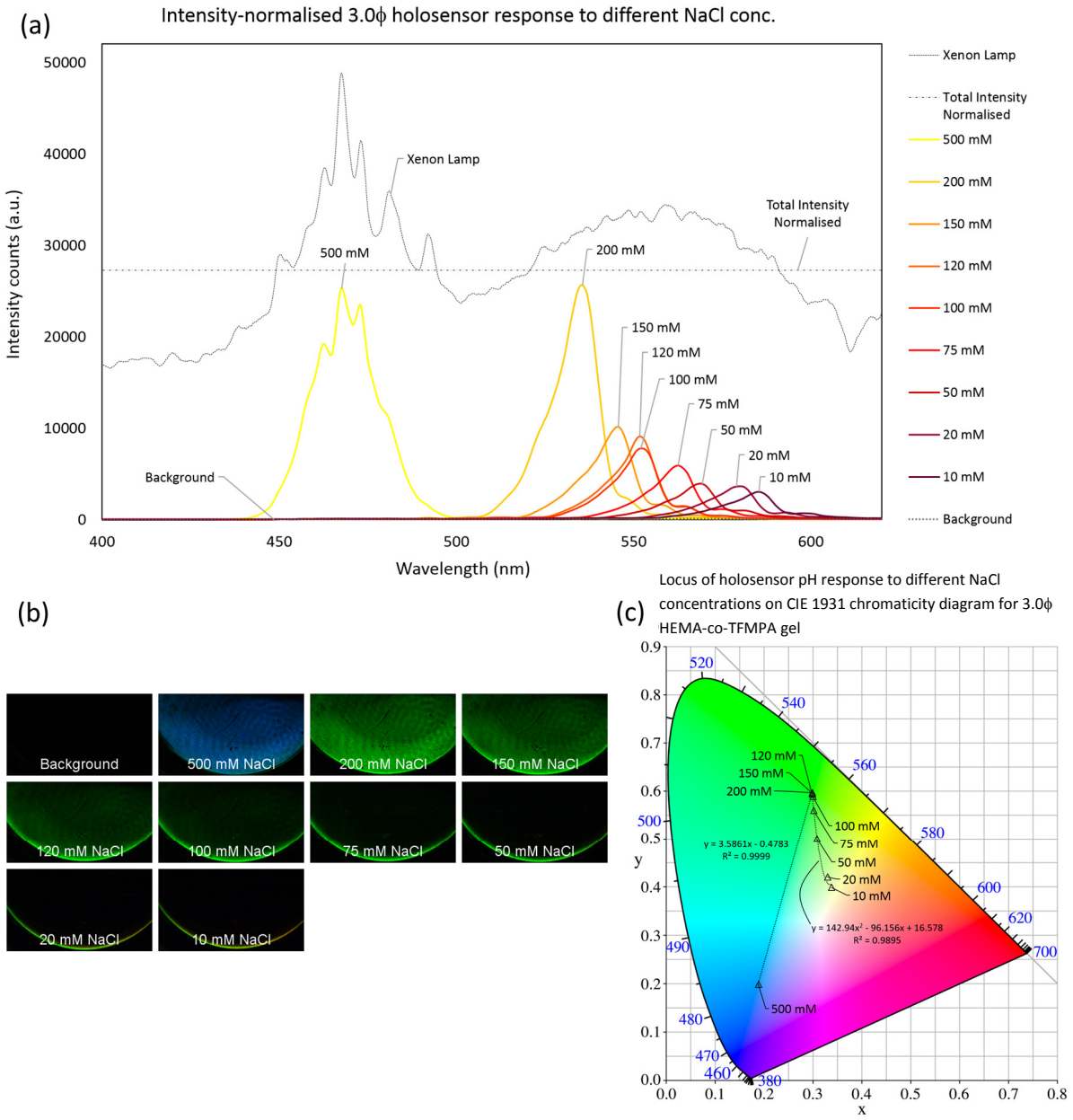

Figure 3-6: 3.0ϕ HEMA-co-TFMPA holosensor response to different NaCl concentrations. ***(a)*** *Total intensity-normalised peak wavelength holosensor ionic strength response obtained from 500 mM NaCl down to 10 mM NaCl.* ***(b)*** *A picture montage of holograms taken with the high-resolution camera at 12X zoom setting corresponding to the NaCl concentrations the holosensor was immersed in.* ***(c)*** *Visualisation of colour change with loci in diagram corresponding to the holosensor response to different NaCl concentrations. RGB-xyY transformed values from (b) were plotted onto the CIE 1931 chromaticity diagram.*

3.9 Monitoring of bacteria growth

3.9.1 Morphology and growth characteristics

Lactobacillus casei (L. casei) is a homofermentative acid, facultative anaerobe bacterium. The Shirota strain cells harvested from Yakult were rod-shaped (0.4-0.6ϕ x 2-3 μm), and occur singly, in pairs, or in short chains comprising 3-4 cells. It produces two lactic acid molecules for every glucose molecule, although small amounts of acetate, ethanol and diacetyl are produced as well. It typically takes 48h at 37°C for colonies on MRS agar to reach 2-3 mm in diameter, beige, smooth and circular edges under anaerobic conditions [126].

3.9.2 Experimental parameters

When a non-anaerobic environment was utilised, the colonies took about 52h to reach their desired sizes after streaking on MRS agar. A clean colony was then chosen and inoculated with 70 mL of filtered (with 0.25 μm syringe filter) sterile MRS broth. To be more exact, 10 mL of the sterile broth was aliquoted for negative control before inoculation. Upon reaching various different optical densities at 600 nm (OD_{600}), 15 mL aliquots of broth containing live *L. casei* cells were centrifuged, its supernatant removed, sterile 20% v/v glycerol added, cells re-suspended, and frozen at -20°C in 14 different eppendorf tubes as a collective batch. In all, 3 different batches with OD_{600} of 0.93, 1.16 and 1.30 were prepared. For comparison, the cell count at OD_{600}=1.2 was about 4.16 x 10^8 cfu/mL. Details for frozen batch preparation and cell count are described in §2.4.4.2.2 and §2.4.4.2.3 respectively. The OD_{600}=1.16 batch was utilised for the 3.0ϕ holosensor. A 200 μL aliquot of frozen sample from each eppendorf tube was utilised each time for inoculation into MRS broth for holosensor interrogation experiments.

3.9.3 Repeatability of inoculation duration to reach OD_{600}=1.0

The inoculation duration required to reach a certain optical density for *L. casei* Shirota was dependent on three main parameters. They were: (1) the volume of MRS broth utilised, (2) how loosely capped the glass bottle containing the MRS broth with inoculated bacteria colony was, and (3) volume of frozen OD_{600}=1.16 sample inoculated into the MRS broth. The volume of broth and frozen bacterial sample (assuming the survival rate of all frozen samples were equal) directly affects the cell density after a certain inoculation duration. The more noteworthy observation was when the glass bottle was tightly capped, the growth rate was exceptionally slow – it could take 2 days just to reach OD_{600}=1.0. This was likely due to the bacteria's preference for an anaerobic environment. With the glass bottle

loosely capped, the denser[4] and more soluble (solubilities of CO_2 and O_2 in 100 g of water at 293K are 0.169 g/100g and 0.0043 g/100g H_2O respectively [143]) CO_2 produced during their fermentative metabolism would displace the lighter and less water soluble O_2 from the loosely-capped bottle.

To achieve consistency, the 70 mL MRS broth was carefully measured, filtered and autoclaved; the glass bottle was always loosely capped just to the point where the lid barely holds the bottle after inoculation, and the frozen bacteria sample was agitated and stirred with the pipette tip before carefully extracting the 200 μL aliquot for inoculation. There were still some variations in the inoculation duration even when utilising the same batch. The survival rate of the frozen aliquots, as well as the frequency of mixing the bulk media during pH, conductivity and peak wavelength measurements do result in discrepancies in the inoculation duration required to reach OD_{600}=1.0. To minimise the increasing possibility of contamination during every experimental run, and mitigate the occurrence of mixing and disturbing the *L. casei* growth; it was mixed only once after 14h of inoculation and aliquoted into eight separate loosely capped sterile containers of 7 mL broth. At stipulated inoculation durations, the pH, conductivity and OD_{600} readings were taken followed by the collection of peak wavelength and hologram pictorial data. Figure 3-7 depicts the *L. casei* growth characteristics, pH and OD_{600}, measured with a pH meter and spectrophotometer respectively, for growth monitoring with the 3.0ϕ holosensor.

[4] One mole of ideal gas at standard temperature (0°C) and standard pressure (1 atm) has a volume of 22.4 litres. The densities (molecular weight divided by 22.4) of CO_2 and O_2 are thus 1.965 g/L and 1.428 g/L respectively.

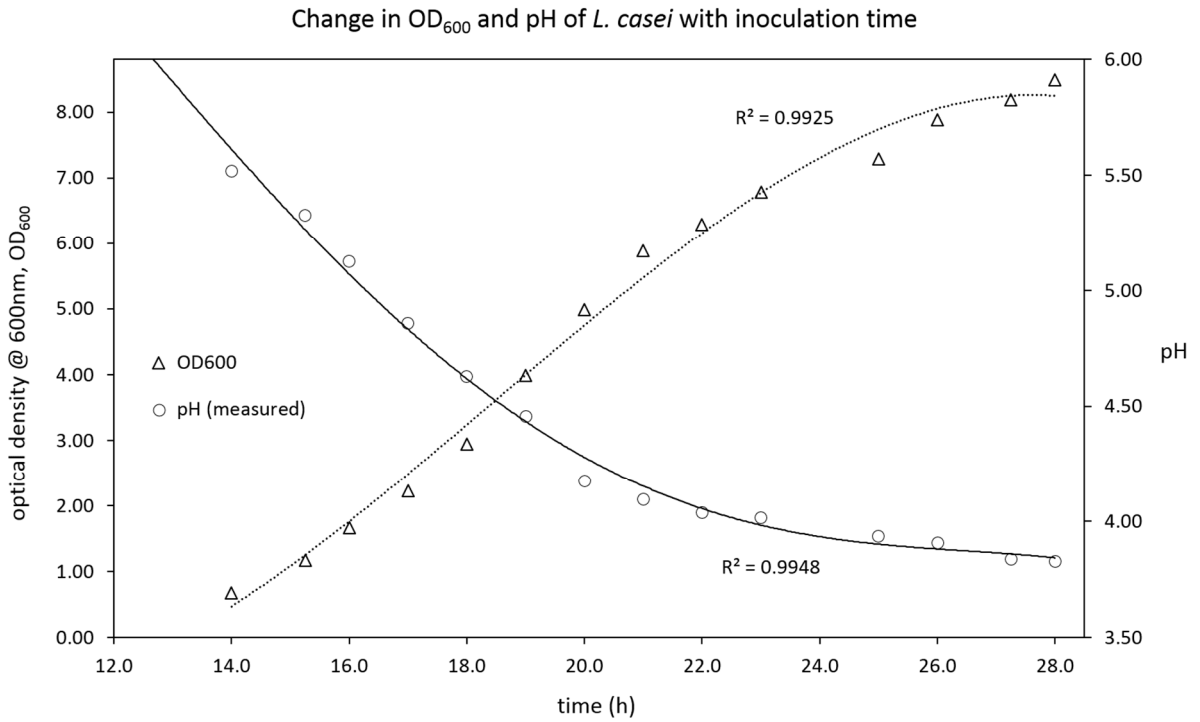

Figure 3-7: Lactobacillus casei (L. casei) growth curve for 3.0ϕ HEMA-co-TFMPA holosensor. The optical density at 600 nm (OD_{600}) and pH of the media was measured with a pH meter at approximately 1h intervals starting at t=14.0h from MRS broth inoculation.

The graph from Figure 3-7 agreed with the effect of increasing cell count (and hence its density in the broth) and decreasing pH from its lactic acid producing metabolism with time. As different batches have different pH at the same prescribed time intervals due to batch-to-batch variation, it was more meaningful to capture only the actual run of the tested batch for analysis (instead of considering the average and standard deviation of the pH variation across a few batches) and comparison to a gold standard (pH meter) measurement method. A higher cell density translated to more scattering, which led to a higher OD_{600} reading. Without introduction of fresh broth, the lactic acid and carbon dioxide produced as waste products gradually brought the pH of the broth down. Due to gradually depleting resources and nutrients, the bacterial growth rate slowed down, and resulted in the OD_{600} and pH curve starting to plateau after about 22h.

3.10 *L. casei* 3.0ϕ HEMA-co-TFMPA holosensor interrogation

Similar to the pH characterisation procedure, the holosensor was first primed with the negative control broth. At regular intervals, the live cells-containing broth was introduced into the microfluidic chamber containing the holosensor. During the 5 min equilibrations, pH, conductivity, and OD_{600} measurements were taken from the container. Thereafter, pictorial and spectrophotometric data were collected with the high-resolution camera and spectrophotometer respectively. N_2 gas purged and dried the chamber between every run. Figure 3-8 illustrates the collected data.

3.10.1 Difference between measured and predicted pH

At first glance, the total-intensity normalised peak wavelength curves from Figure 3-8(a) would suggest that there was a different intensity distribution compared to that of the characterisation curve in Figure 3-3(a). As a reference, the measured pH at 15.25h, 16.00h, 17.00h, 18.00h, 19.00h 20.00h and 22.00h were 5.33, 5.13, 4.86, 4.63, 4.26, 4.18 and 4.04 respectively (from Figure 3-7). Comparing their relative peak wavelength intensity counts, the significant difference was the pH value where there was a maximum peak intensity count (pH 4.26) while the maximum peak for the calibration curve was at pH 4.50. The expected maximum peak (at pH 4.50 from Figure 3-3(a)) was likely to be between t=18.00h and t=19.00h (Figure 3-8(a)), which corresponded to pH 4.63 and pH 4.26 respectively.

Looking at Figure 3-8(b), it could suggest, by intuition, a discrepancy in the uniformity of the hologram throughout the evaluation area of the holosensor. Recall that the hologram started to thin and only display at the edges of the holosensor due to a shift in the optimal interrogation angle for the maximum hologram intensity. *L. casei* typically exhibits a slower growth rate and reaches the stationary growth phase with the pH hovering around 3.5 to 3.8 after about 28h of inoculation. The pH had not reached the point of "diminishing hologram" (at pH 3.75) as illustrated in Figure 3-3(b).

With the backdrop of a perceived apparent discrepancy, Figure 3-8(c) also appeared to show significant difference between the curved-like locus of pH reduction on the CIE chromaticity diagram as compared to that of the linear locus depicted in Figure 3-3(c). As briefly mentioned in §3.6.6, the xyY was a non-linear colour space, and any difference could appear to vary dramatically. Furthermore, the locus was only meant as a qualitative visualisation of colour change.

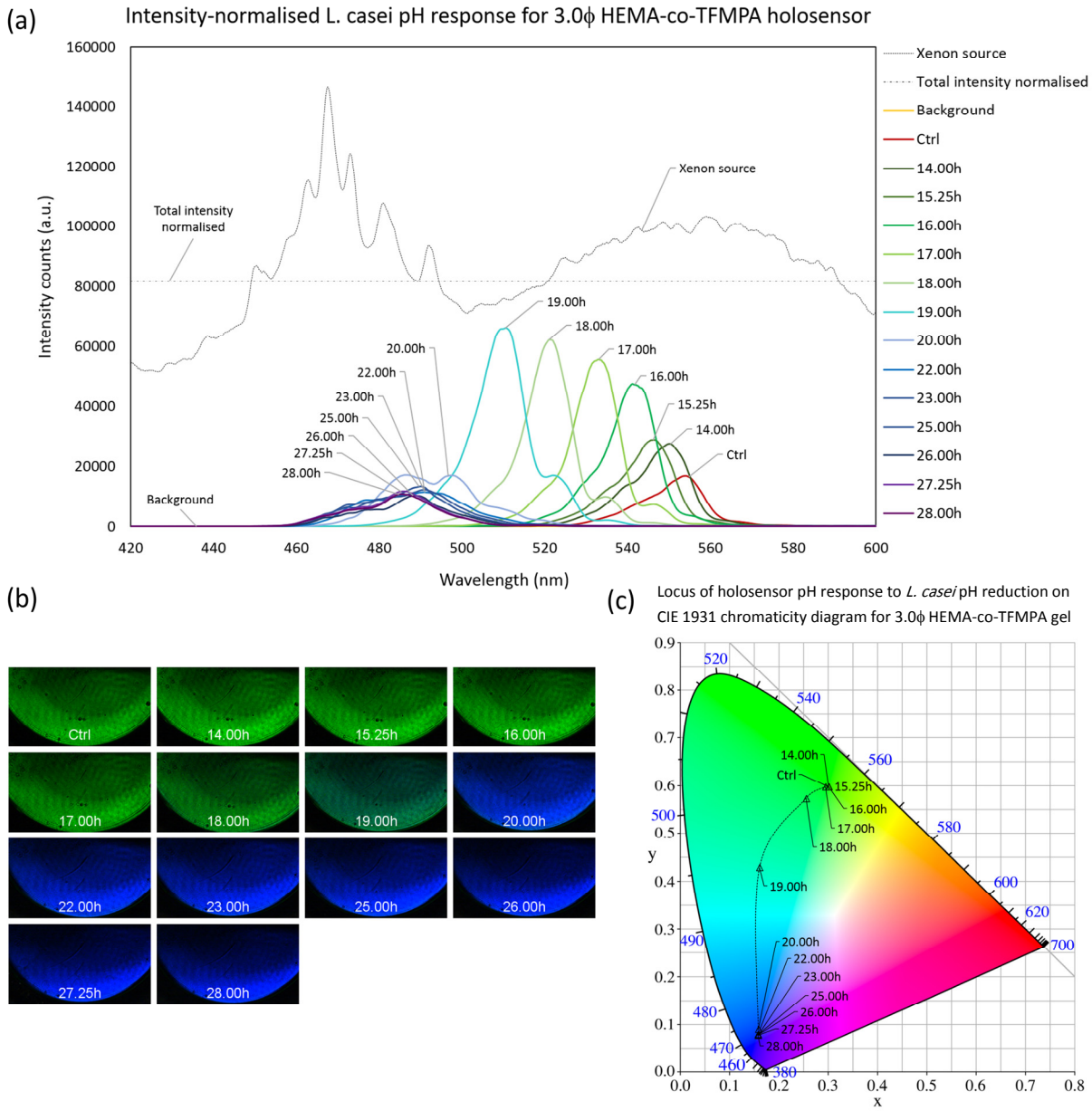

Figure 3-8: 3.0ϕ HEMA-co-TFMPA holosensor response to L. casei growth. ***(a)*** *Total intensity-normalised peak wavelength holosensor Lactobacillus casei (L. casei) pH response obtained from batch process interrogation from t=14.00h to t=28.00h.* ***(b)*** *A picture montage of holograms taken with the high-resolution camera at 12X zoom setting corresponding to the batch sample introduced into the microfluidic chip at corresponding inoculation durations from t=14.00h to t=28.00h.* ***(c)*** *Visualisation of colour change with locus of holosensor response at corresponding inoculation durations from t=14.00h to t=28.00h. RGB-xyY transformed values from (b) were plotted onto the CIE 1931 chromaticity diagram.*

3.11 Standard curve for the 3.0ϕ HEMA-co-TFMPA holosensor

After the holosensor was calibrated with the ionic-strength normalised McIlvaine pH buffer, the best-fit calibration curve was utilised to predict the pH derived from its total intensity-normalised peak wavelength pH response. The best-fit calibration curve provided the information on the apparent pK_a, maximum wavelength (λ_{max}) and minimum wavelength (λ_{min}) values. Referring back to Equation 3.4,

the expression can be expanded with the inverse log of (pH – pK_a) made the subject, followed by taking the logarithm on both sides of the equation. The resulting expression for the predicted pH would be as follows:

$$pH = \log_{10}\left(\frac{\lambda - \lambda_{min}}{\lambda_{max} - \lambda}\right) + pK_a \tag{3.6}$$

Equation 3.4 was used to calculate the predicted wavelength response from the holosensor, and the information from the calibration curves aforementioned were inserted into Equation 3.6 to find out the holosensor predicted pH. The measured pH and predicted pH values were then plotted as shown in Figure 3-9. The R^2 of 0.98 illustrated correlation between the measured and predicted pH. The non-unity slope and y-intercept of the best-fit line explains why the measured pH does not map directly to the same predicted pH value.

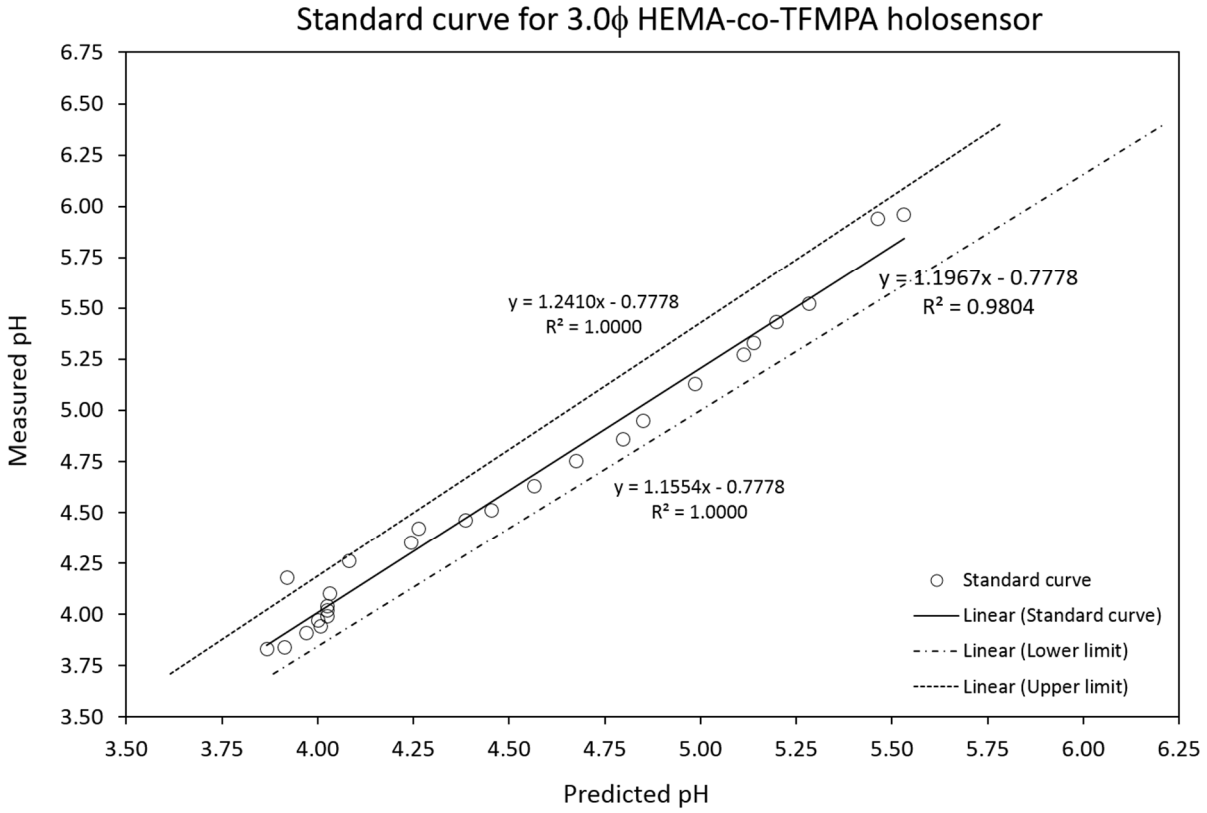

Figure 3-9: Standard curve for 3.0ϕ HEMA-co-TFMPA holosensor illustrating the correlation between the measured and predicted pH. The upper and lower limits were determined by the zero point of the pH meter at pH 7.00 ± 0.25 (3.57% allowable uncertainty)

3.11.1 Effectiveness of holosensor

Conventional pH meters measure the concentration of hydronium ions (pH) in a solution by comparing the difference in electrical potential between its measuring electrode and a reference electrode. The Mettler Toledo SevenGO-SG23-ELK pH meter with InLab Expert Pro-ISM pH electrode with automatic temperature compensation was utilised for holosensor calibration throughout the interrogating pH range of the holosensor, i.e. from pH 6.00 down to pH 3.00. Its zero point of pH 7.00 ± 0.25 (values obtained from the pH electrode specifications brochure) indicates an uncertainty of 3.57%, and this value was utilised as the upper and lower limit of the standard curve to illustrate the corresponding uncertainty of the holosensor readings.

3.11.1.1 Allowable error

The upper and lower limit curves were determined by assigning a +3.57% and -3.57% value for a particular predicted pH value, which correspond to 2 measured pH values based on the best-fit line equation. The corresponding values then make up the upper and lower limit lines, which provides a visualisation of the accuracy and effectiveness of the holosensor at a glance.

Most of the data points lie within the upper and lower limit of the given uncertainty, or allowable error corresponding to the given specifications of the pH meter itself, illustrating a high accuracy commensurate to the pH meter.

3.11.1.2 R^2 ratio

Another way of evaluating the holosensor effectiveness was to compare the coefficient of determination (R^2) of the graph when the measured or predicted pH values were plotted against the parameter, OD_{600}, which tracks the growth of *L. casei*. The higher the correlation, the better that method. Since the pH meter itself was utilised to calibrate the holosensor, it would definitely show a higher correlation. Nonetheless, the R^2 value related to the pH meter could serve as the theoretical maximum or ideal case for the prediction of pH for *L. casei*. As illustrated in Figure 3-10(a) and Figure 3-10(b), the R^2 values were close to unity. A ratio of the holosensor predicted pH R^2 (0.9807) over the pH meter measured pH R^2 (0.9907) provides a representative accuracy parameter, depicted in Equation 3.7 for which the holosensor effectiveness could be evaluated. In this case, the holosensor accuracy was 98.99%.

$$\chi = \frac{R^2_{predicted}}{R^2_{ideal}} \times 100\% \tag{3.7}$$

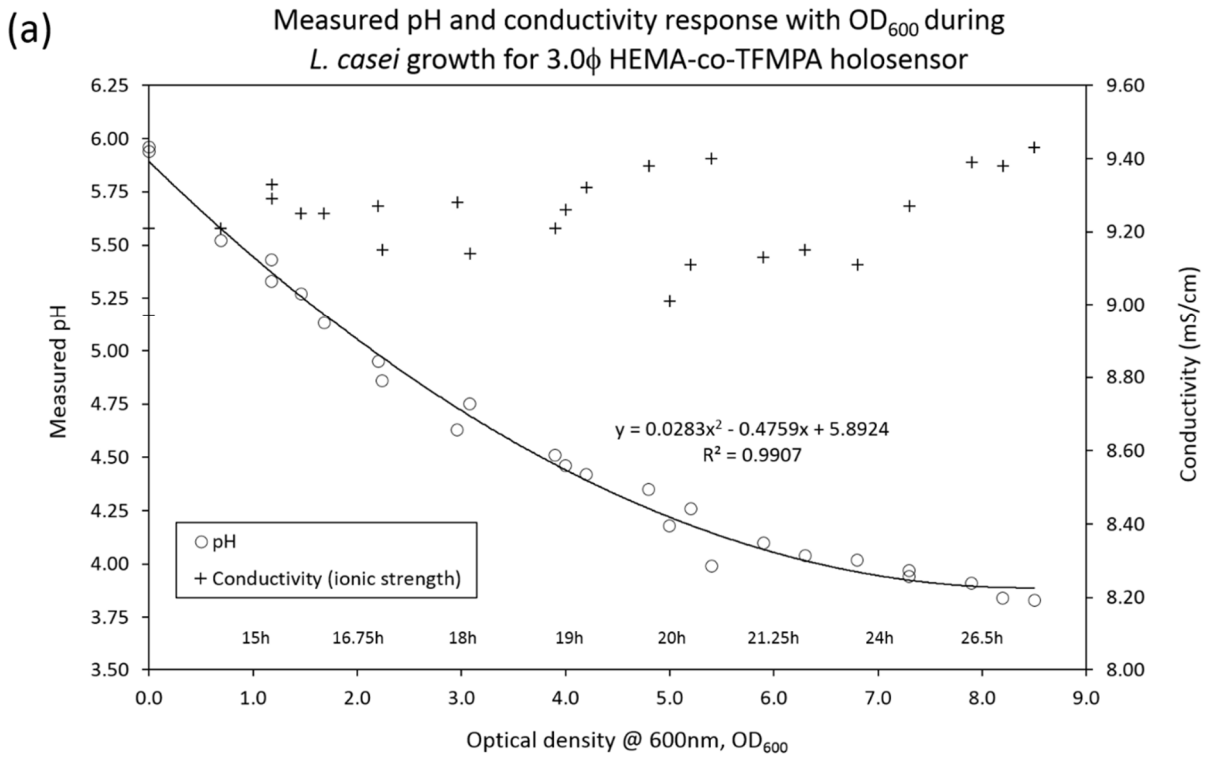

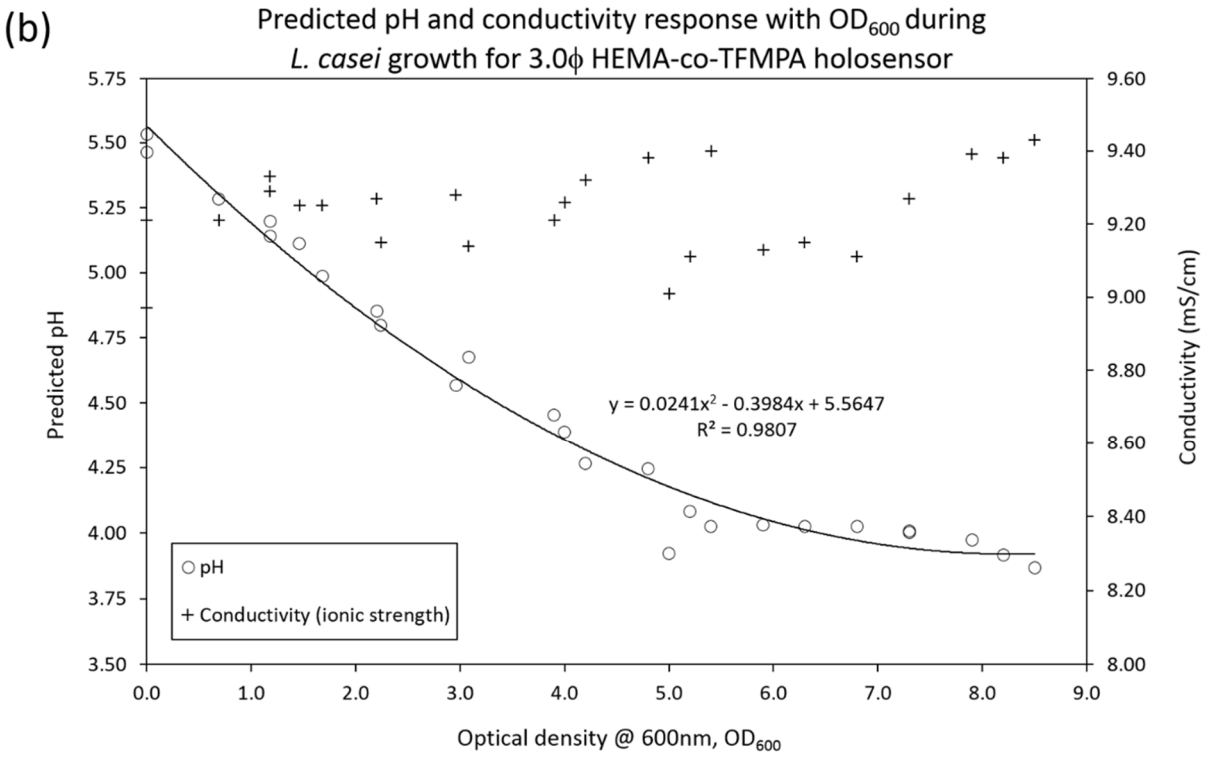

Figure 3-10: ***(a)*** *Measured pH and conductivity (ionic strength) of the batch media (broth) containing live Lactobacillus casei (L. casei) from inoculation duration t=14.00h to t=28.00h at increasing OD_{600} values, versus* ***(b)*** *Predicted pH (from the calibration curve in Figure 3-5(b)) and measured conductivity plotted against increasing OD_{600} of the bacterial media (broth)*

3.12 Ionic-strength correction for the 3.0ϕ HEMA-co-TFMPA holosensor

Ionic strength (conductivity) values superimposed on the graphs of Figure 3-10 were not constant throughout the holosensor interrogation of the *Lactobacillus casei (L. casei)* containing broth. The values appeared to vary randomly between 9.00 mS/cm and 9.50 mS/cm.

Noting that an ionic strength difference (expansion and contraction with lower and higher ionic strength respectively) could affect pH readings, a series of calculations were done and graphs plotted to correct for the fluctuations in ionic strength. The average holosensor total intensity normalised peak wavelength ionic strength response was plotted together with average conductivities of the various tested NaCl concentrations in the range of 8.7 mS/cm to 10.2 mS/cm Appendix K(a & b). This evaluation range included that of the randomly varying ionic strength of the *L. casei* at different inoculation durations. Since the McIlvaine pH characterisation buffers were ionic-strength balanced at 9.50 mS/cm, this same value was used to normalise the peak wavelength response at various conductivity measurements (Appendix K(c)). With the best-fit line equation, the peak wavelength response of the holosensor was corrected by adding or subtracting the corrected differences from the assigned 9.50 mS/cm response. This corrected wavelength was then inserted back into the predicted pH Equation 3.6 as described in §3.11 to derive an ionic-strength corrected predicted pH value and a new predicted pH against OD_{600} graph was plotted (Appendix K(d)). The correction did not make any significant difference, since the total ionic strength fluctuation range was really only about 5% of the ionic strength value of 9.50 mS/cm. It was noteworthy to point out that the accuracy parameter based on the R^2 ratio discussed in §3.11.1 did increase by 0.09% to 99.08%.

3.13 Conclusions

Both the measured diameter parameters (ϕ_{max} and ϕ_{min}) of the 3.0ϕ holosenor had standard deviations of 0.06 mm, which was 30% more precise than the specified tolerance from DIN ISO 2768-1. An average holographic signal brightness was about 30,000 counts for a 50-100 ms integration time while a good one exhibits approximately the same number of intensity counts (30,000) in the range of 30 ms integration time. The gold standard was a hologram fabricated with gelatin as the monomer (instead of HEMA), which saturated the detector at 1.05 ms integration time. At 12X magnification, the fabricated 3.0ϕ holosensor saturated the detector at 1.05ms integration time. pH calibration using ionic-strength balanced McIlvaine buffers set the apparent pK_a of TFMPA to 4.40, close to the previously reported 4.45 value. This included intensity-normalisation of the holosensor response (peak wavelength) to isolate the influence of illumination spectral intensity on the holographic peak wavelength signal. The 3.0ϕ holosensor was also utilised for the monitoring of pH with a lactic acid bacterium, *Lactobacillus casei*, and its effectiveness was compared against that of the pH meter used for calibration. An evaluation R^2 ratio parameter prescribed the accuracy of the holosensor to 99.0% of the pH meter zero point uncertainty (obtained from the specifications brochure of the supplier). Finally, a further ionic strength correction method was employed to normalise the small variation of ionic strength between different measurements of the bacterial broth and found to be of insignificant difference.

4 Chapter 4 Miniaturised pH holosensor array

Holographic sensors (holosensors) integrate the sensing element, transducer and display into a single device by recording a hologram in a stimuli-responsive hydrogel (or "smart hydrogels"). The equilibrative nature of the holosensor makes it an attractive candidate for integration into a microfluidics system.

In this chapter, the utility of such a sensor is extended by miniaturisation to less than 5 nanolitres (nL) in volume to monitor a small number of cells. In chapter 3 (§3.9), a 3.0ϕ holosensor was integrated into a microfluidic system for *Lactobacillus casei* (*L. casei)* pH monitoring. Here, a miniaturised 0.4ϕ holosensor (~ 3 nL in volume) is fabricated to demonstrate the feasibility of obtaining the holographic signal for the same application. To go one step further, pH reduction from the *L. casei* metabolism is also interrogated with an array of miniaturised 0.4ϕ pH holosensors.

4.1 Buffering capacity of the holosensor

The pH moiety (TFMPA) of a holosensor takes part in a chemical equilibrium involving protons (H^+) with its surrounding solution to impart the pH-responsive capability by expanding or contracting the gel based on the corresponding charge configuration of the TFMPA embedded in the gel matrix. The appropriation and restoration ("borrowing" for operation) of these H^+ ions (into and out of the gel matrix), although insignificant for a large sample, is cause for concern when the holosensor is miniaturised.

The buffering capacity of the holosensor, or amount of H^+ required before being able to provide an accurate pH measurement, was calculated in Appendix L for both the (a) 0.46ϕ and (b) 3.27ϕ holosensor (generally referred to as 0.4ϕ and 3.0ϕ holosensors). The gel volume was first calculated by overestimating it as a cylinder with gel height, h_{max}. The %mol and actual proportion of TFMPA in the gel precursor solution, and correspondingly within the gel matrix after photopolymerisation, were calculated to find out the amount (number of moles) of L-lactic acid which will be "borrowed" for operation. A 5% utilisation (for the 3.0ϕ holosensor) and a 1% utilisation (for the 0.4ϕ holosensor) was assigned to designate only 5% and 1% (respectively) of the available H^+ ions (in the microfluidic chamber) to be temporarily utilised for sensing within the gel. Depending on the production rate of L-lactic acid by *L. casei*, and assigning a 75 μm chamber height (to ensure a typical 20 μm high holosensor had space to expand into), a minimum chamber diameter was determined. Together with an assumed 80 g/L of L-lactic acid production (Senedese *et al.*) [144] by the bacteria, the minimum chamber

diameter for the 0.4ϕ and 3.0ϕ holosensor (to reduce the buffering capacity effect to 1% and 5% respectively) are 1.69 mm and 5.40 mm. Appendix L shows the detailed calculations and minimum chamber diameter values corresponding to varying microfluidic chamber heights, designated buffering capacity utilisation % and *L. casei* L-lactic acid production rates.

4.2 Typical 0.4ϕ HEMA-co-TFMPA gel profiles

4.2.1 Effect of solvent in gel precursor solution

4.2.1.1 Cage effect and gel porogen

A solvent dissolves solutes to form solutions. The solvent-solute mixture exists as a single phase with all solute molecules occurring as solvates (solvent-solute complexes). Molecules of the solvent arrange around the solute molecules, like a cage, interacting and mixing with each other at the molecular level. Referring to Appendix M, almost half of the gel precursor solution (by weight) was the IPA solvent, with slightly more than half accounted for by the HEMA monomer. The free radical initiator, DMPA occupied only about 1% in the case of 1.0 DMPA (for the 0.4ϕ holosensor), and 0.05% for the 1/18 DMPA recipe (for the 3.0ϕ holosensor). The amount of solvent in the precursor solution can affect the polymerisation kinetics, since only radicals that escape the cage can initiate free radical polymerisation [145]. Experimentally, the gel precursors polymerised faster with only some IPA, just enough to dissolve the initiator (DMPA) and inhibitor (HQ).

Other alcohols such as benzyl alcohol and ethanol have been utilised as a porogen for polyHEMA [146] and a hybrid EMA-HEA hydrogel [147] respectively. Similarly, different IPA concentrations could also lead to different gel porosities.

4.2.1.2 Chain transfer agent

Elementary reactions occurring during free radical polymerisation are initiation, propagation, chain transfer to monomer or small molecules, and termination [148]. IPA is commonly used as a chain transfer agent to control molecular weight control during polymerisation [149], [150]. A hydrogen atom is abstracted from a solvent molecule to form a radical on the solvent molecule, which will not propagate further. A polymer with a predetermined molecular weight can be obtained this way based on the type and concentration of alcohol or solvent utilised.

4.2.1.3 Dielectric constant

Generally, the rate of reaction involving dipolar molecules is dependent on the dielectric constant of the medium, which is approximately equal to the dielectric constant of the solvent in dilute solutions. Equation 4.1 relates the rate of reaction, k, to the dielectric constant, ε, of the solvent with the rate

constant in a medium of infinite dielectric constant, $In\ k_{\varepsilon=\infty}$, Avogadro's constant N, distance between ions $r^{\ddagger}$, charges of interacting ions z_A and z_B, the unit of electric charge e, molar gas constant R, and absolute temperature T [151].

$$\ln k = \ln k_{\varepsilon=\infty} - \frac{N z_A z_B e^2}{RTr^{\ddagger}} \frac{1}{\varepsilon} \tag{4.1}$$

By choosing different solvents, the rate of reaction and hence polymerisation will change. If the ion charges involved are the same, the slope of $\ln k$ vs $\frac{1}{\varepsilon}$ should yield a straight line with negative slope. An increase in dielectric constant would thus result in an increase in the rate of the reaction.

4.2.2 Photoinitiator (DMPA) concentration

4.2.2.1 1/18 DMPA for 3.0ϕ HEMA-co-TFMPA holosensor

The 3.0ϕ holosensor from the previous chapter was fabricated with a photoinitiator (DMPA) concentration 1/18th to that of previous work with pH holosensors. This extremely low concentration was utilised because residual water-insoluble DMPA and polymerisation inhibitor HQ could precipitate out and compromise gel transparency, affecting hologram diffraction efficiency. The hydrophobic DMPA and HQ could also have made the gel more hydrophobic during photo-polymerisation by incorporating into the matrix and causing the hydrogel to become less soluble and less transparent, which would compromise gel transparency and affect the hologram quality. With the 1/18 DMPA recipe, the probability of DMPA being radicalised by UV exposure under the photomask was already low for the 3.0ϕ gel. Where the gel precursor solution would cover the entire glass substrate (9.38 mm x 12.5 mm) during photo-polymerisation, the surface area of the 3.0ϕ photomask only occupied 6.03% of the substrate. In a unit area, the relative "molecular area" for DMPA is 0.05% (Appendix M(b)). The probability parameter of finding a 0.05% DMPA molecule in the 6.03% UV-illuminated area would be 3.015 x 10^{-5}.

4.2.2.2 1.0 DMPA for 0.4ϕ HEMA-co-TFMPA holosensor

With miniaturisation, the same 1/18 DMPA concentration could not be utilised for photo-polymerisation of smaller diameter gels. Experimentally, either photo-polymerisation did not take place, or the gels were simply just severely underdeveloped even with all other experimental parameters kept constant. To put it into perspective, the surface area of the 0.4ϕ photomask (0.126 mm^2) was 56.1X smaller than the 3.27ϕ photomask (7.07 mm^2), or 0.11% of the glass substrate. The probability parameter of finding a 0.05% DMPA molecule in the 0.11% UV-illuminated area would be 5.500 x 10^{-7}. Conversely, with 1.0 DMPA, the relative "molecular volume" for DMPA would be 0.97% (Appendix M(a)), which translates to a much closer probability parameter of 1.067 x 10^{-5}. The linear

conversion to determine the probability parameter was meant as a rough approximation for comparison, while the actual probability would require Monte Carlo simulation for a more accurate representation. Regardless, graphs (c) and (d) from Appendix M do paint an accurate depiction of the relative space (or "molecular volume") taken up by the gel precursors in solution.

4.2.3 0.4ϕ HEMA-co-TFMPA gel recipe

For the 0.4ϕ HEMA-co-TFMPA gels, the fabrication recipe was 8 mmol gel precursors with HEMA:EDMA:TFMPA 91:3:6 mol% (8TH-2, 6T3E), 7.07 x 10^{-2} mmol DMPA (1.0 DMPA), 3.54 x 10^{-2} mmols HQ (2:1 HQ) in 1 mL IPA, 29.64 mW/cm^2 (9% power) UV@365 nm exposure for 4 min (9p4m) using a diced, 8 mm x 8mm cyclic olefin copolymer cover substrate (identifier: 2b) with a particular Newton rings configuration (COCopp8x8d2b).

After the gel parameters were measured with the white light profiler, a graph was plotted as shown in Figure 4-1 for 5 samples together with their average and 1 standard deviation (s.d.) as error bars.

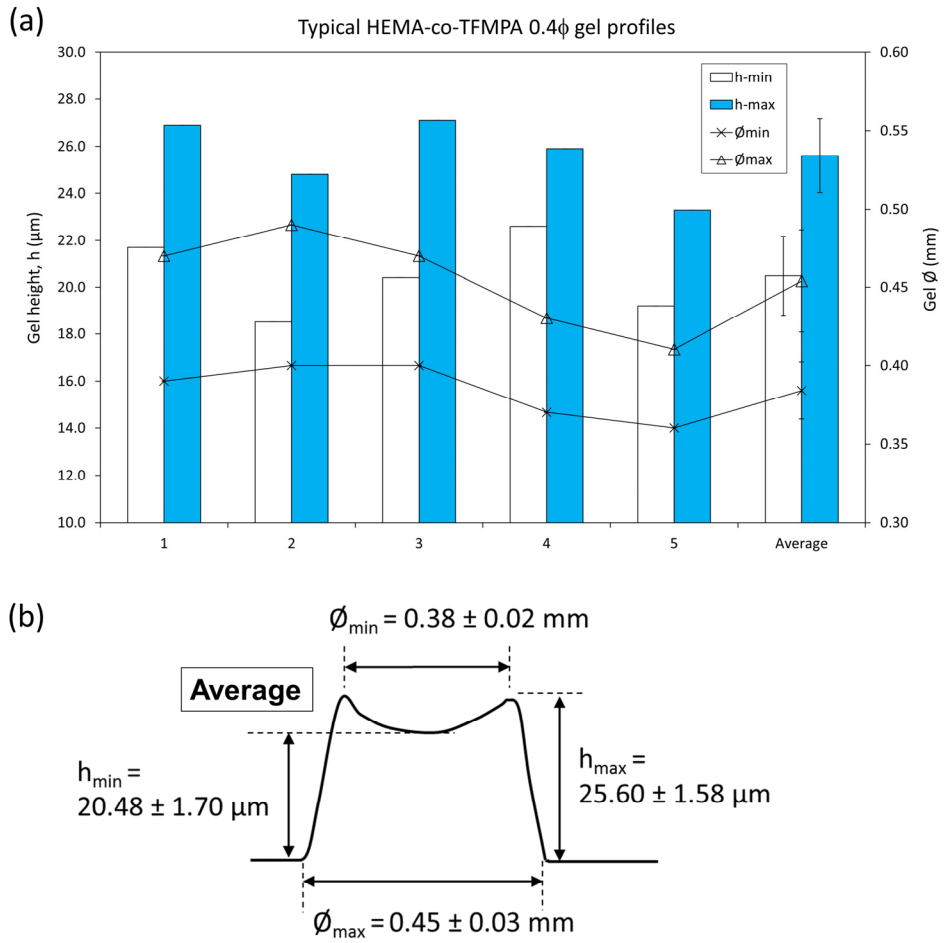

Figure 4-1: ***(a)*** *Collation of five typical 0.4ϕ HEMA-co-TFMPA gel profiles and their associated dimensions, presented with their averages having error bars of ± 1 s.d.* ***(b)*** *Schematic diagram of a typical 0.4ϕ gel with their dimensional averages with ± 1 s.d.*

A tolerance requirement was needed to qualify the gel dimensions for consistency and quality assuarance. However, there are no official standards relating to external radii smaller than 0.5 mm. According to DIN ISO 2768-1, the permissible deviations broken edges (external radii and chamfer heights) of fine tolerance class for "0.5 mm up to 3 mm" was ± 0.2 mm [137]. Using 0.2 mm as the allowable tolerance, the allowable uncertainty could range from 6.67% to 40% depending on whether 0.5 mm or 3 mm was used in the percentage calculation. Even with the minimum allowable uncertainty of 6.67%, the standard deviation of the gel diameters would be, if expressed in percentages, 5.26% and 6.67% for ϕ_{min} and ϕ_{max} respectively.

4.3 0.4ϕ HEMA-co-TFMPA holosensor

4.3.1 Gel miniaturisation

Miniaturisation of the holosensor to 0.4ϕ required a more stringent requirement for gel fabrication. It was observed that the UV source would have to be collimated, or at least be focussed at the plane of gel photo-polymerisation. Prior experiments utilising UV transilluminators or flood lamps tend to result in asymmetrical gel profiles. For instance, the gel would appear oval even when the photomask was a perfectly circular one. Directionality of the UV light was hence an important parameter to control. UV exposure duration was also important in ensuring good mask fidelity. Even with a collimated UV source, the gel would polymerise beyond the photomask-designated area if the gel were not removed from the UV source at the same duration for different samples.

4.3.2 Determination of hologram fabrication offset angle

An offset angle was required for hologram fabrication to isolate the reflected illumination light from the reflected holographic signal. If it were too small, the angular isolation would be insufficient, but if it were too large, the quality of holographic signal would be compromised due to the glancing angle.

Light refracts when it propagates into another medium. This refraction is described by Snell's Law, which states that the ratio of the sines of angle of incidence (θ_1) and refraction (θ_2) of a wave propagating between two media is equivalent to the ratio of phase velocities (v_1 and v_2) or the reciprocal of the ratio of their indices of refraction, (η_2 and η_1 correspondingly):

$$\frac{\sin\theta_1}{\sin\theta_2} = \frac{v_1}{v_2} = \frac{\eta_2}{\eta_1} \tag{4.2}$$

Snell's Law was applied at every interface from when the laser impinges on the top layer of the glass substrate, through the gel, exposure bath, glass cover, air wedge and then reflected back through all the layers again. It was found that in order for the gel to have a 5° offset fringe plane, the incident beam, α (as illustrated in Figure 4-2) would have to be 7.16°. Any lesser angle would put the

illumination light reflection plane too close to the holographic signal reflection plane. Another noteworthy observation from the calculations was, for parallel fringe planes to form within the volume of the gel, the fluid above the top glass substrate (with gel) and below the bottom glass cover must be the same, i.e. either the whole setup was submerged in the exposure bath or kept dry (η_{water}= η_{bath} = 1.33 and η_{air} =1.0 respectively). The symmetry would minimise the formation of interference artifacts formed from the non-parallel retroreflected beam and incident-propagating beam interfering at different angles. From the calculated 7.16° requirement, a mechanical Delrin® spacer was designed specifically to satisfy that offset requirement. The 0.25 mm thick PDMS spacer maintains a fixed distance between the 2 glass substrates and prevents the exposure bath solution from evaporating or moving during exposure.

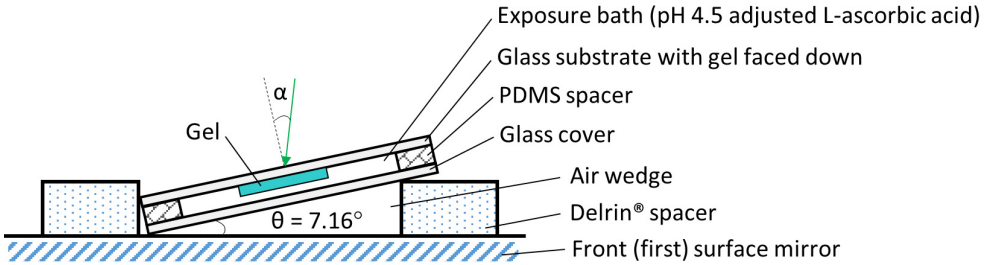

Figure 4-2: Schematic diagram for the hologram fabrication setup

4.3.3 Hologram fabrication for 0.4ϕ HEMA-co-TFMPA gels

Hologram fabrication of the 0.4ϕ gels was expected to present even more difficulties since the surface area of the 0.4ϕ gel was 56X smaller than that of the 3.0ϕ gel. Interestingly, the success rate of obtaining a bright monochromatic hologram for the 0.4ϕ gel was, unexpectedly, significantly higher than that of the 3.0ϕ gel. It was likely due to the higher probability and available sites related to the hologram fabrication alignment method described in Figure 2-19. Achieving the required brightness and monochromatism were challenging, especially when there were no existing optical systems in place to visualise clearly the hologram because of the angular intolerance of the holographic signal. Regardless, when the experimental parametric nuances were figured out for the production of a significantly bright hologram, it appeared that smaller gels would produce consistently bright and monochromatic holograms, albeit not always brighter than the 3.0ϕ ones.

This propitious occurrence was likely due to the beam-offset requirement discussed earlier in §3.3.3. There were simply more ways of aligning the centre of the beam outside of the gel diameter with a 9 mm diameter beam for the 0.4ϕ gel than with the 3.0ϕ gel.

Figure 4-3 summarises, not in the reported order: a chosen 0.4ϕ gel profile (cross sectional x and y profile, 2D, 3D and schematic diagram) and hologram pictures (with pH 6.0 McIlvaine buffer) taken by a Samsung S7 mobile phone, and high-resolution camera at 36X.

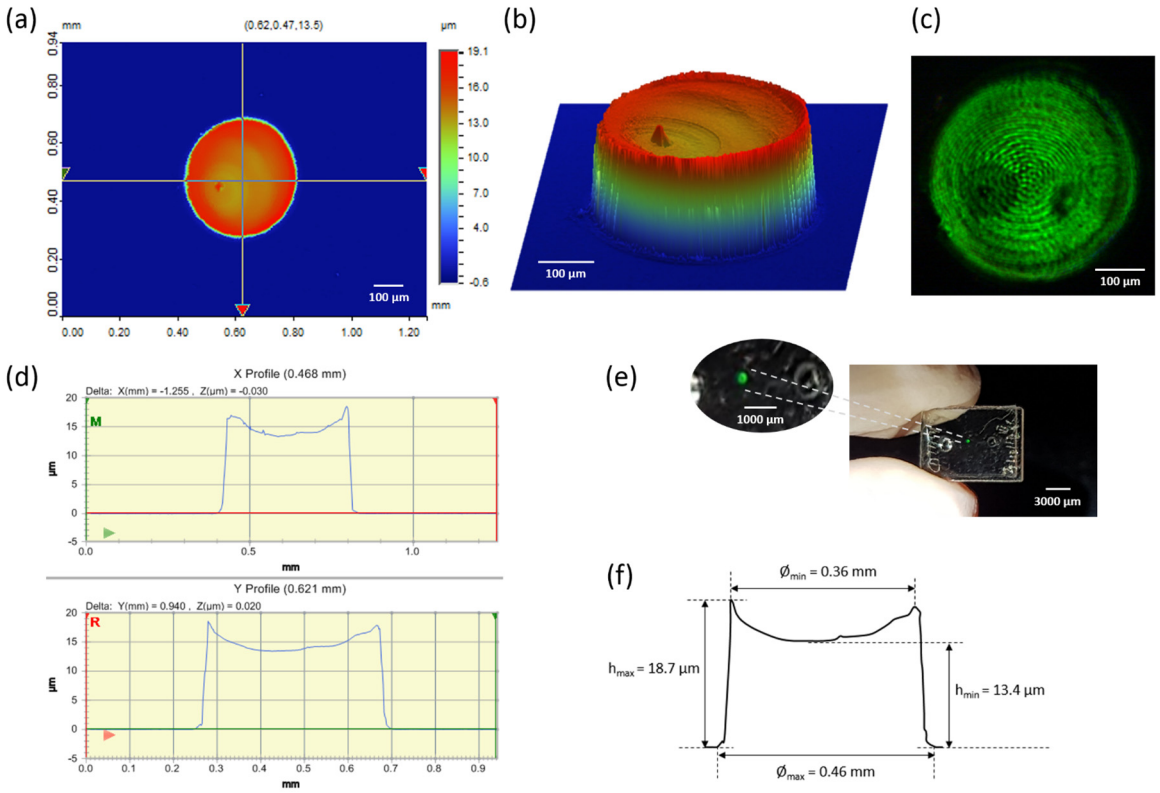

Figure 4-3: Collation of 0.4ϕ HEMA-co-TFMPA holosensor information. ***(a & b)*** *2D and 3D digital elevation model of the chosen 0.4ϕ holosensor after hologram fabrication respectively.* ***(c)*** *Picture of the hologram taken by the high-resolution camera at 36X magnification while the 0.4ϕ microfluidic chip embedded holosensor was immersed in pH 6.0 McIlvaine buffer. Its orientation was modified to match that of the digital elevation model from (b).* ***(d)*** *Cross-sectional x and y profile of the 0.4ϕ holosensor along the crosshair depicted by the 2D digital elevation model.* ***(e)*** *Picture of the LED illuminated hologram taken by a Samsung S7 mobile phone with pH 6.0 McIlvaine buffer inside the microfluidic chip.* ***(f)*** *Reproduced y profile of the 0.4ϕ gel with measured white light profiler data.*

4.4 0.4ϕ HEMA-co-TFMPA holosensor observations

After the polymerisation inhibitor has been used up during UV photopolymerisation, the diffusing consitutents of the gel precursor solution quickly polymerises at the edge of the illuminated area (defined by the photomask pattern). As most of the gel precursor constituents are unable to reach the centre of the UV illuminated region, it results in a build-up of newly polymerised material at the edges as depicted in Figure 4-3. The gel matrix could have different morphology or rigidity across the gel diameter. Consequently, the edges would likely be more cross-linked as the edge region had a constant supply of monomer diffusing from the non-illuminated regions, which do not have the

chance to diffuse to the centre of the gel after all the monomer in the illuminated region have been used up. Because of the way the gel was formed on the substrate, the edges would have more space sideways to expand to while the middle portion would be pushing upwards and outward. A combination of these two factors would cause the gel to expand upwards and radially outwards, with the edges expanding the fastest (which would retard the expansion from the middle) before the centre portion starts to push outwards. The momentum of the eventual expansion from the middle would cause the edge to expand outward again before making a correction to reach kinetic equilibrium. Figure 4-4 illustrates video snapshots (with time stamps) of the (a) expanding 0.4ϕ TFMPA holosensor and (b) of the microfluidic chamber purging with N_2.

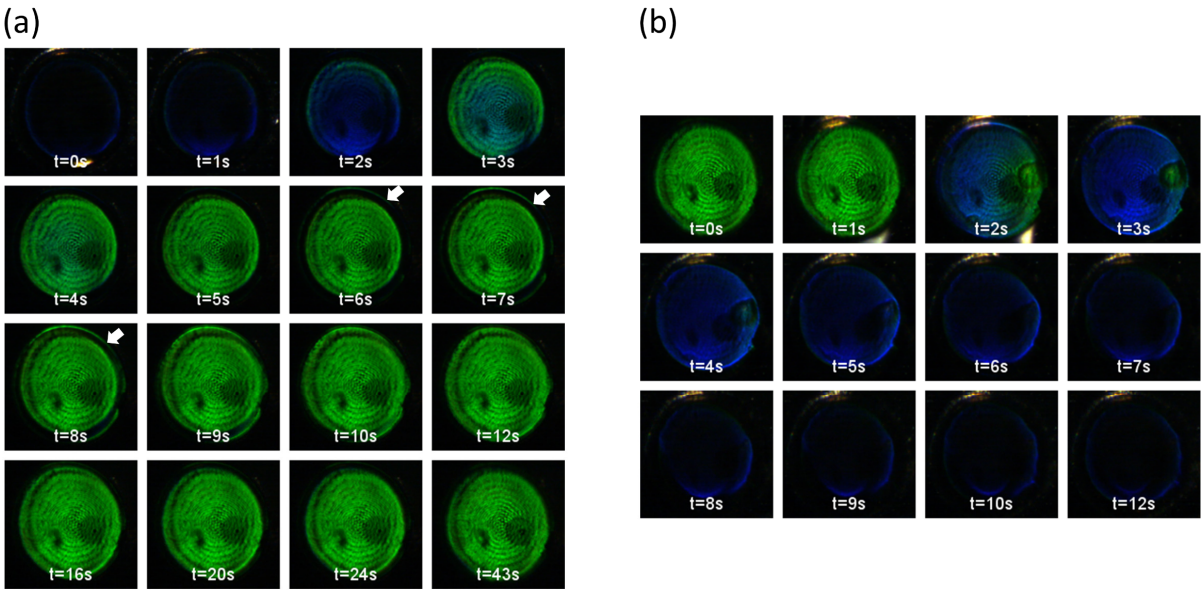

*Figure 4-4: Video snapshots of the 0.4ϕ HEMA-co-TFMPA holosensor **(a)** during gel expansion when pH 6.00 McIlvaine buffer was introduced, and **(b)** during N_2 purge of the buffer from the microfluidic chamber. The white arrows depict the boundary of the green hologram that showed an expansion to that point before slowly receding.*

4.4.1 Gel expansion

Although the background signal (at t=0s) was negligible compared to the holographic signal, there was an observable faint blue ring at the edges. Assuming that the rest of the gel was much more contracted, as there was almost no water within the gel matrix, the blue ring would indicate that the edges could have been more rigid, which limited its elasticity and did not further contract compared to the rest of the gel. It could also suggest that there were distorted Bragg reflection planes at the steep gel edges, or insufficient fringes to display effectively an accurate holographic signal.

At t=3s, there was an obvious colour difference between the centre and the outer regions of the gel, which was consistent with the explanation that the outer regions expanded first and the fastest. At t=6s, a thin and bright ring was observed at the edge of the holosensor. The outward expanding edge

appears to have expanded upwards, red-shifted and reached the fringe spacing for green colour. The middle portion then pushed outwards due to the elastic recovery from the initial squeezing from the edges. Relieved of the lateral compression, the middle portion could now expand upwards, which manifested itself as the spreading out of the green colour from t=6s to t=9s. Once again, the outward expansion would cause the edges to move outwards and expand beyond the green or it could have distorted the angle of the Bragg plane at the edges. This push and pull kinetics (due to its elasticity continued until the gel reached equilibrium, where in the case of Figure 4-4(a), the green colour receded a little towards the centre. It was likely that the edges had a distorted Bragg reflection plane.

4.4.2 Gel contraction during purging

Figure 4-4(b) shows that the holosensor contracted quickly compared to the expansion as the air flow instantly expelled the water from the gel matrix, which caused an immediate collapse of the gel to its contracted (blue) Bragg plane spacing. It was analogous to a demolition team taking out a building's critical load-bearing columns with thermite (a compound utilised for controlled demolition) and bringing it down in seconds. It should be noted that gel contraction due to a new pH buffer would take longer due to the gel elasticity kinetics similar to that of its expansion.

4.4.3 Maximum holographic signal

At pH 4.50, where the hologram was recorded, the gel was expected to be the brightest because the fringes at the edges would have slightly contracted inwards a little compared to when it was immersed in pH 6.0 buffer, which would be the configuration where the fringes were parallel across the whole diameter. This observation was consistent with the reported 3.0ϕ and 0.4ϕ holosensors.

4.5 0.4ϕ HEMA-co-TFMPA holosensor pH calibration

Similar to the 3.0ϕ, the miniaturised 0.4ϕ holosensor was calibrated to the ionic strength corrected (9.50 mS/cm) McIlvaine pH buffers. The spectrophotometric and high-resolution picture data were captured and presented in Figure 4-5(a) & (b) together with the RGB-derived xyY colour space data plotted on the CIE chromaticity diagram (Figure 4-5(c)).

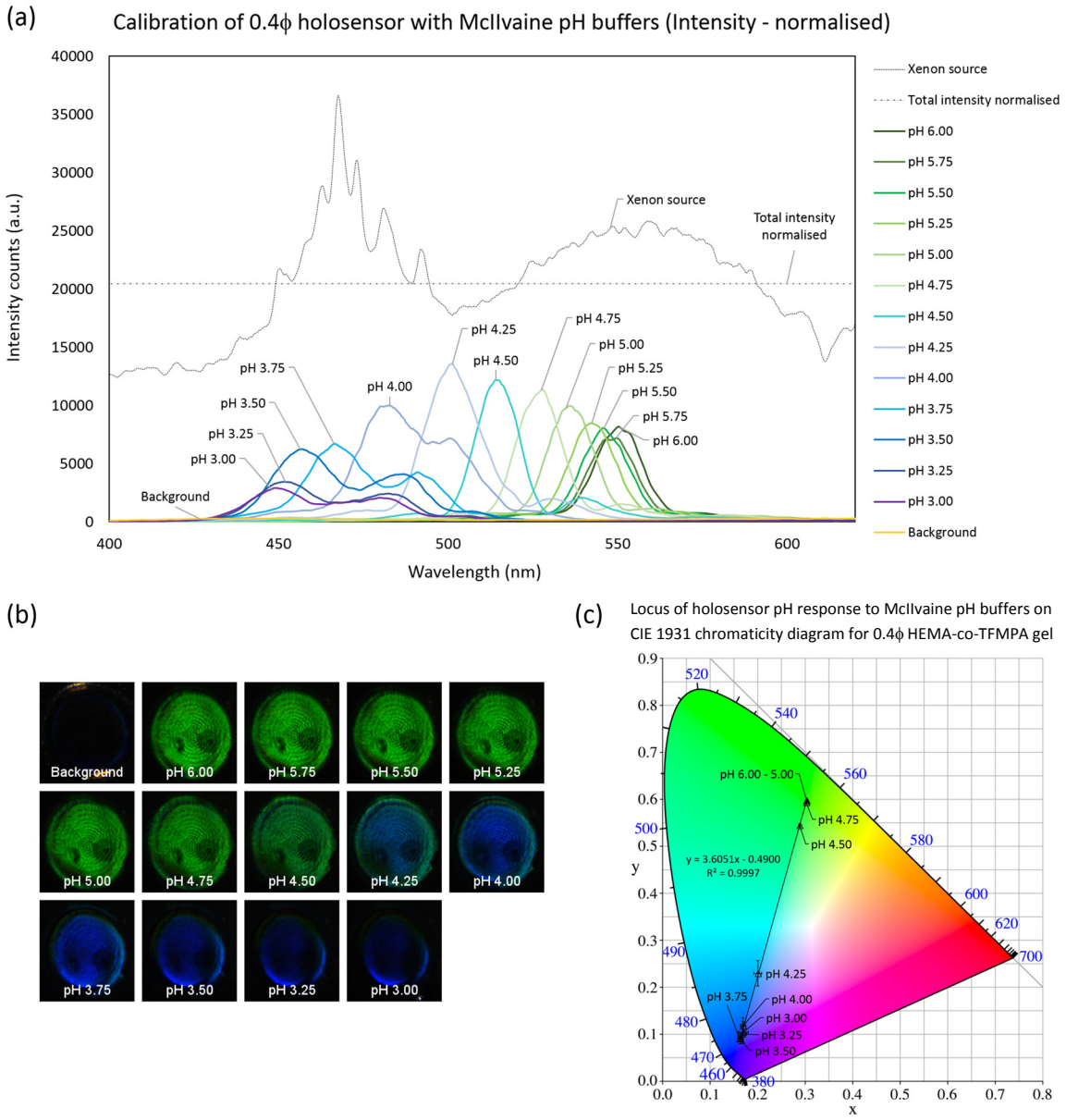

Figure 4-5: Collation for the pH calibration information of the 0.4ϕ HEMA-co-TFMPA holosensor. ***(a)*** *Total intensity-normalised peak wavelength holosensor pH responses obtained from pH 6.00 to pH 3.00. The height of the peaks represents the corresponding spectral intensity recorded by the spectrophotometer.* ***(b)*** *Picture montage of holograms captured by the high-resolution camera at 36X magnification when immersed in correspondingly decreasing pH starting from pH 6.00 to pH 3.00 just before the spectrophotometric data of (a) was collected.* ***(c)*** *Visualisation of colour change with locus of holosensor pH response corresponding to RGB-xyY transformed values from (b) plotted onto the CIE 1931 chromaticity diagram.*

Once again, to mitigate the influence of the illumination light intensity on the recorded holographic signal intensity, the peak-wavelength pH response of the holosensor was normalised to the total intensity value, and corrected based on the intensity ratios at a particular wavelength. From Figure 4-5(a) and Figure 4-6(a), it can be deduced that the holosensor was most sensitive at around pH 4.25, or its apparent pK_a. The RGB values of the hologram from Figure 4-5(b) were transformed to the xyY colour space and plotted on the CIE 1931 chromaticity diagram in Figure 4-5(c). The locus that

connected pH 6.00 all the way down to pH 3.00 can be utilised as another tool for estimating the actual pH.

4.6 Calibration curve for 0.4ϕ HEMA-co-TFMPA holosensor

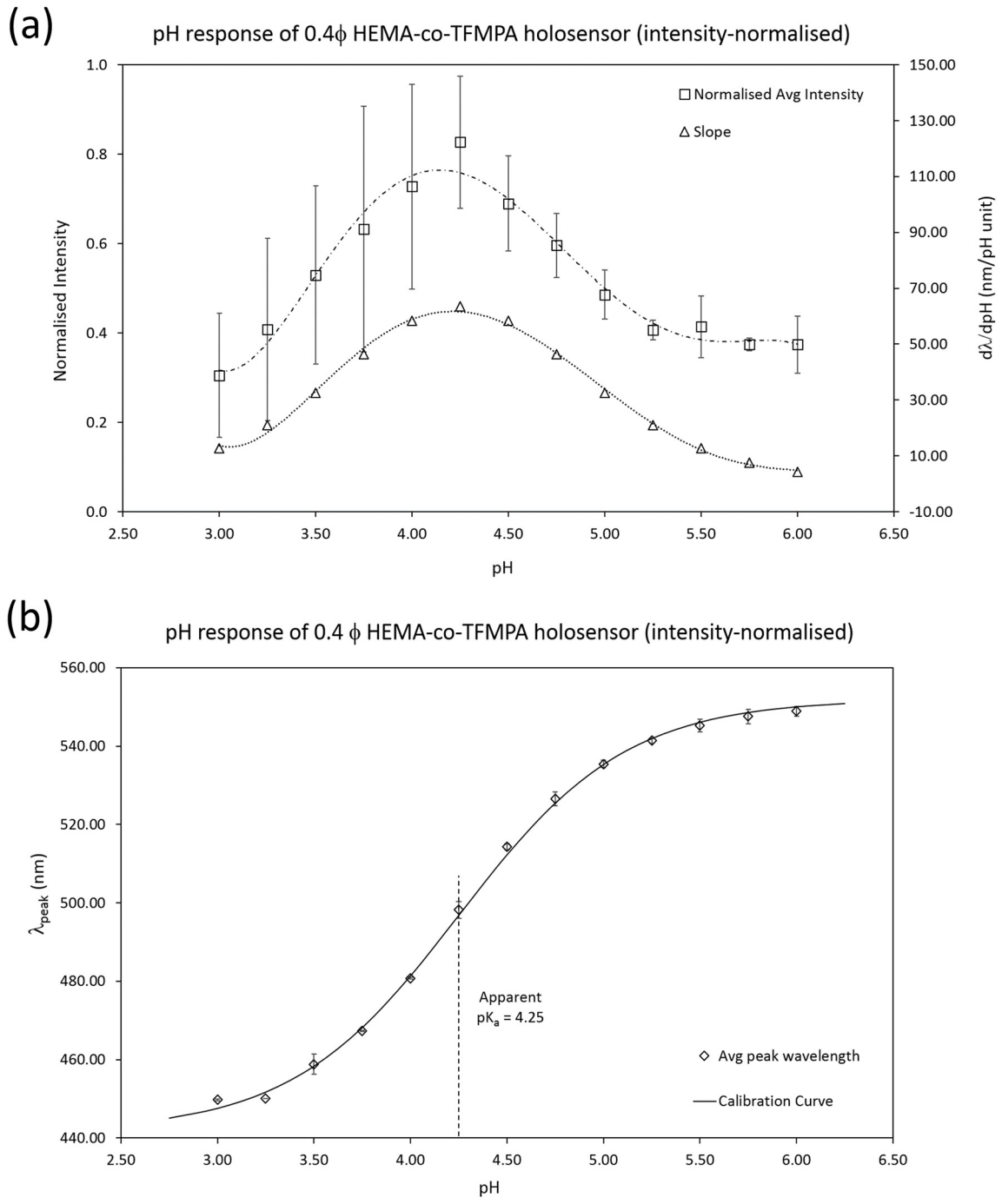

Figure 4-6: ***(a)*** *Normalised intensity holosensor response at varying pH values between pH 3.00 and 6.00 with ± 1 s.d. as the error bars, and slope of peak wavelength change to pH change ($\frac{d\lambda_{peak}}{dpH}$).* ***(b)*** *Modified Henderson-Hasselbalch (H-H) pH calibration curve with the average of 3 runs (from pH 6.00 to pH 3.00), and error bars with ± 1 s.d. The apparent pK_a of the holosensor was pH 4.25.*

Three runs from pH 6.00 down to pH 3.00 were performed and the average taken with 1 standard deviation as the error bars. The estimated pK_a of 4.25, λ_{min} and λ_{max} values from the raw data were substituted into Equation 4.3 to obtain the modified H-H calibration curve. The substituted values were then tweaked, where necessary, to provide the best-fit curve for the data points.

$$\lambda = \frac{\lambda_{max} \cdot (10^{pH - pK_a}) + \lambda_{min}}{1 + 10^{pH - pK_a}} \tag{4.3}$$

It was observed that the maximum intensity and slope (derivative of Equation 4.3, $\frac{d\lambda_{peak}}{dpH}$) lies close to the apparent pK_a of the holosensor as shown in Figure *4-6*(a) and mentioned in §4.4.3.

4.7 Effect of ionic strength on 0.4ϕ HEMA-co-TFMPA holosensor

The effect of ionic strength on the 0.4ϕ holosensor was also studied. The influence of the varying intensity of the illuminating Xenon light source was minimised by normalising the total intensity across the evaluation wavelength (as described in §3.6.4).

Referring to the peak wavelength response of the 0.4ϕ holosensor to ionic strength changes in Figure 4-7(a), the hologram displayed significant peak wavelength shift (about 100 nm) from 500 mM down to 10 mM NaCl As the ionic strength decreases, the 0.4ϕ holosensor expands. With fewer Na^+ ions to compete for the negative charges in the gel matrix, more water flows into the gel together with their counterions, expanding it.

4.7.1 RGB to xyY colour space

RGB values of the holosensor were obtained from Figure 4-7(b) and transformed to the CIExyY colour space using the MATLAB® programme mentioned in §3.6.6 (details of the transformation in Appendix B). Two loci were inscribed within the CIE 1931 chromaticity diagram from the obtained xyY coordinates in Figure 4-7(c) for: (1) between 100 mM and 500 mM and (2) from 10 mM to 120 mM.

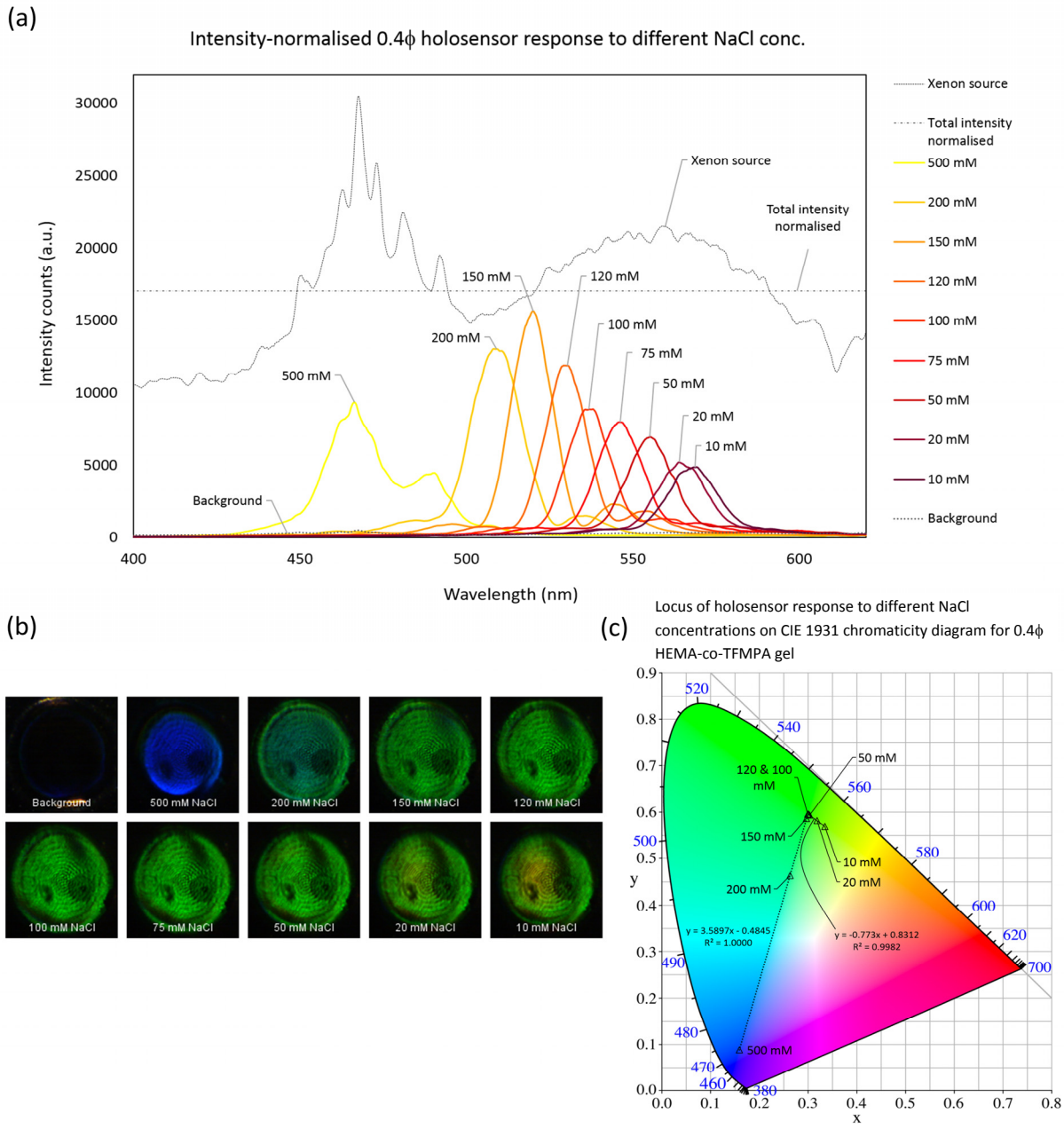

Figure 4-7: 0.4ϕ HEMA-co-TFMPA holosensor response to different NaCl concentrations. ***(a)*** *Total intensity-normalised peak wavelength holosensor ionic strength response obtained from 500 mM NaCl down to 10 mM NaCl.* ***(b)*** *A picture montage of holograms taken with the high-resolution camera at 12X zoom setting corresponding to the NaCl concentration the holosensor was immersed in.* ***(c)*** *Visualisation of colour change with loci of holosensor responses to the corresponding NaCl concentrations. RGB-xyY transformed values from (b) were plotted onto the CIE 1931 chromaticity diagram.*

4.8 Monitoring *L. casei* with 0.4ϕ HEMA-co-TFMPA holosensor

A frozen batch of *L. casei* when its OD_{600} was 1.16 was inoculated into MRS broth and its growth curve monitored as reported in Figure 4-8. OD_{600} readings were taken together with pH from t =13.5h to t=26.0h of inoculation. The growth curve suggested that the bacterial growth started to plateau after around 23h, which coincided with pH 4.10. This was expected, since the optimal pH for *L. casei* growth was around pH 5.0. While it can grow at a pH as low as pH 3.0, the broth does not typically go below pH 3.70 [126].

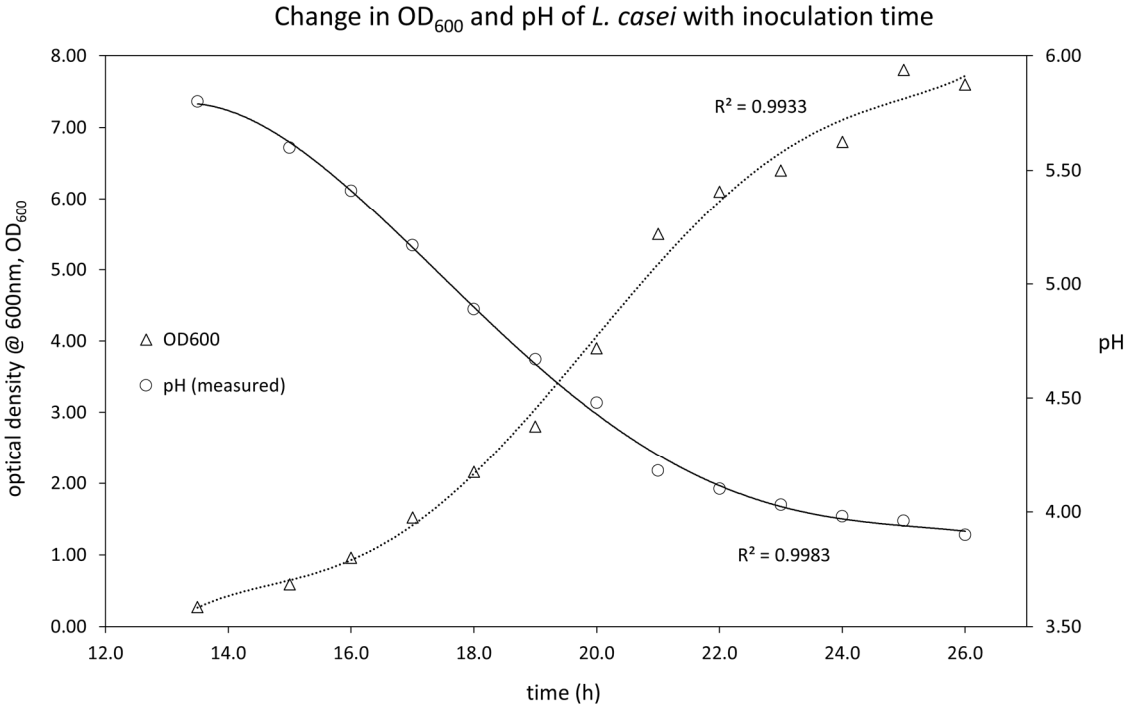

Figure 4-8: Lactobacillus casei (L. casei) growth curve for 0.4ϕ HEMA-co-TFMPA holosensor. The optical density at 600 nm (OD_{600}) and pH of the media was measured with a pH meter at approximately 1h intervals starting at t=13.5h from M.R.S. broth inoculation.

4.9 *L. casei* 0.4ϕ HEMA-co-TFMPA holosensor interrogation

From t=13.5h of inoculation, a sample of the *L. casei* was monitored for its peak wavelength pH response and a picture taken of the hologram at that particular pH with a high-resolution camera every hour as depicted in Figure 4-9(a) and Figure 4-9(b) respectively.

As with the pH characterisation procedure, the pH response (peak wavelength) of the holosensor was normalised to the total intensity normalised value. The negative control was a 7 mL aliquot of sterile, filtered MRS broth that the microfluidic system was primed with before *L. casei* was interrogated. It was worth highlighting that the pH response (peak wavelength) was interrogated with the lowest 1.05

ms integration time setting. The locus for the pH reduction from t=13.5h to t=26.0h inscribed a straight line in the CIE 1931 chromaticity diagram as shown in Figure 4-9(c). The xyY colour coordinates were obtained from the RGB transformation described in Appendix B.

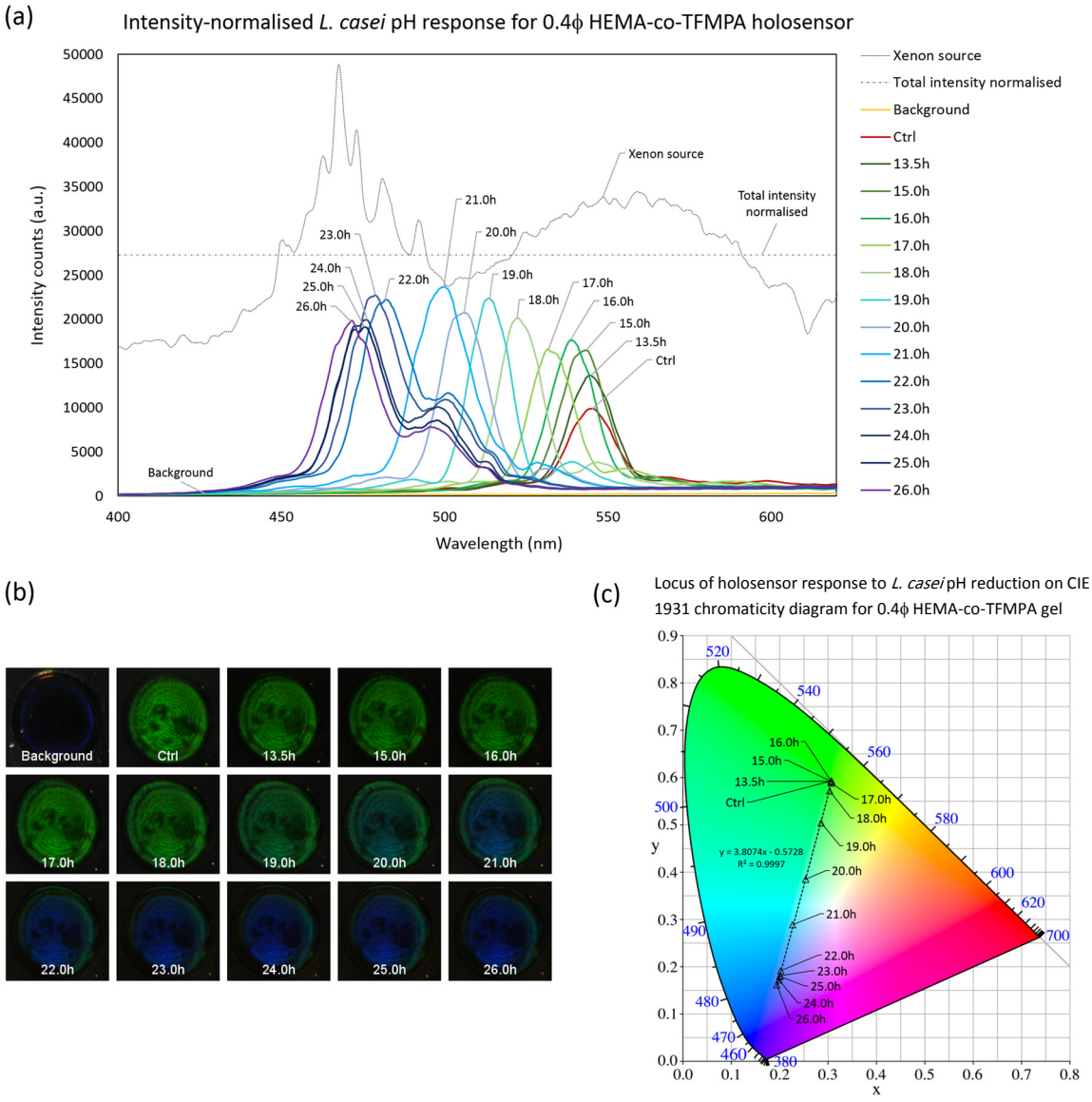

Figure 4-9: 0.4ϕ HEMA-co-TFMPA holosensor response to L. casei growth. ***(a)*** *Total intensity-normalised peak wavelength holosensor Lactobacillus casei (L. casei) pH response obtained from batch process interrogation from t=13.50h to t=26.00h.* ***(b)*** *A picture montage of holograms taken with the high-resolution camera at 36X magnification corresponding to the batch sample introduced into the microfluidic chip at corresponding inoculation durations from t=13.50h to t=26.00h.* ***(c)*** *Visualisation of colour change with locus of holosensor response at corresponding inoculation durations from t=13.50h to t=26.00h. RGB-xyY transformed values from (b) were plotted onto the CIE 1931 chromaticity diagram.*

4.10 Standard curve for 0.4ϕ HEMA-co-TFMPA holosensor

In order to obtain the standard curve, the apparent pK_a, maximum wavelength (λ_{max}) and minimum wavelength (λ_{min}) values were extracted from the determination of best fit for the pH calibration curve and inserted into the derived modified H-H Equation 4.3.

$$pH = \log_{10}\left(\frac{\lambda - \lambda_{min}}{\lambda_{max} - \lambda}\right) + pK_a \tag{4.4}$$

Equation 4.4 was utilised to determine the predicted pH corresponding to the measured pH. The resulting graph was plotted as illustrated in Figure 4-10. Upper and lower limit lines were graphed based on the zero point uncertainty (obtained from the specification brochure of the supplier) of the pH meter (pH 7.00 ± 0.25) which converted to a 3.57% allowable error. This error provided 2 points per predicted-pH point to be mapped onto their corresponding measured pH based on the standard curve line equation (y=1.2369x – 0.9065).

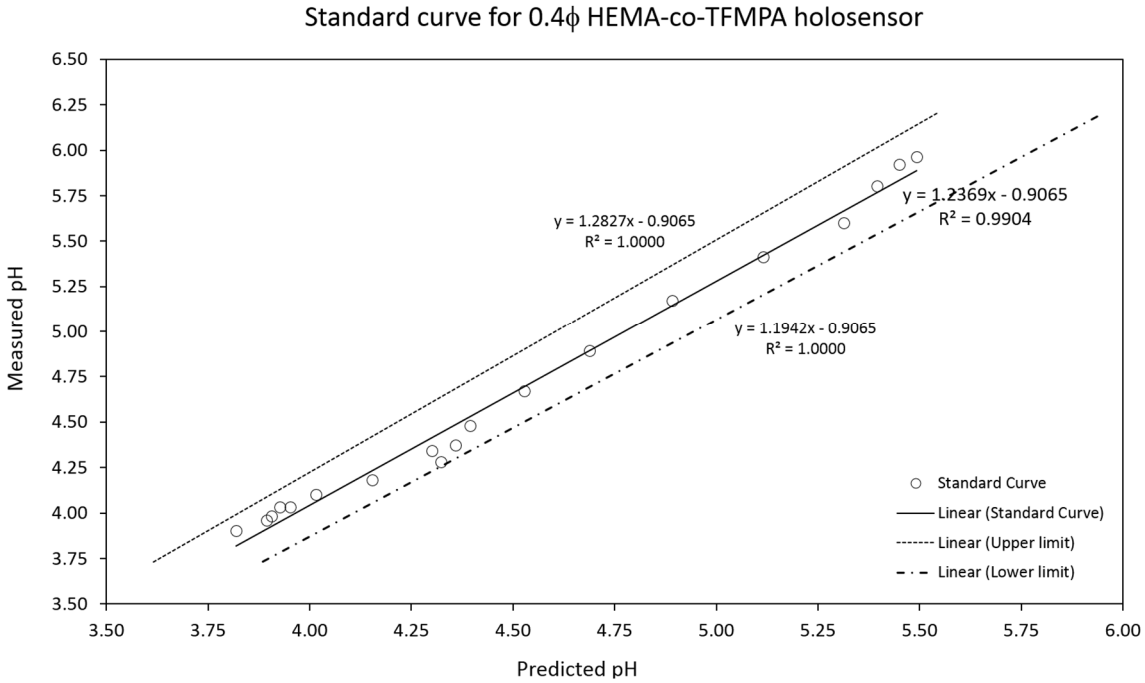

Figure 4-10: Standard curve for 0.4ϕ HEMA-co-TFMPA holosensor illustrating the correlation between the measured pH and predicted pH. The upper and lower limits were determined by the zero point of the pH meter at pH 7.00 ± 0.25 (3.57% allowable uncertainty)

Accordingly, data points that stayed within the upper and lower limit bands were designated as accurate measurements. From the plot of Figure 4-10, it was apparent that all the data points were well within the limits. Additionally, the 0.4ϕ holosensor exhibited better accuracy than the 3.0ϕ holosensor. Therefore, it can be presumed that the 0.4ϕ holosensor was as accurate as the pH meter in tracking the growth of *L. casei* by pH reduction monitoring.

4.11 Predicted pH vs measured pH (0.4ϕ HEMA-co-TFMPA holosensor)

Another method of determining the accuracy of the 0.4ϕ holosensor was by comparing the corresponding OD_{600} changes (which have been the established way of estimating bacterial cell density) to the measured and predicted pH. A devised accuracy parameter, χ, defined as the percentage ratio of R^2 derived from the measured pH and predicted pH graphs could be utilised as a gauge for accuracy compared to an ideal benchmark, depicted in Equation 4.5.

$$\chi = \frac{R^2_{predicted}}{R^2_{ideal}} \times 100\% \tag{4.5}$$

Since the 0.4ϕ holosensor was calibrated with the pH meter itself, the extent of correlation (R^2) between the measured pH and its corresponding OD_{600} was used as the ideal benchmark of accuracy.

Plotted in Figure 4-11(a) and Figure 4-11(b), the R^2 for the respective measured and predicted pH against OD_{600} graphs were 0.9959 and 0.9911 respectively. The accuracy parameter, χ was thus 99.52%.

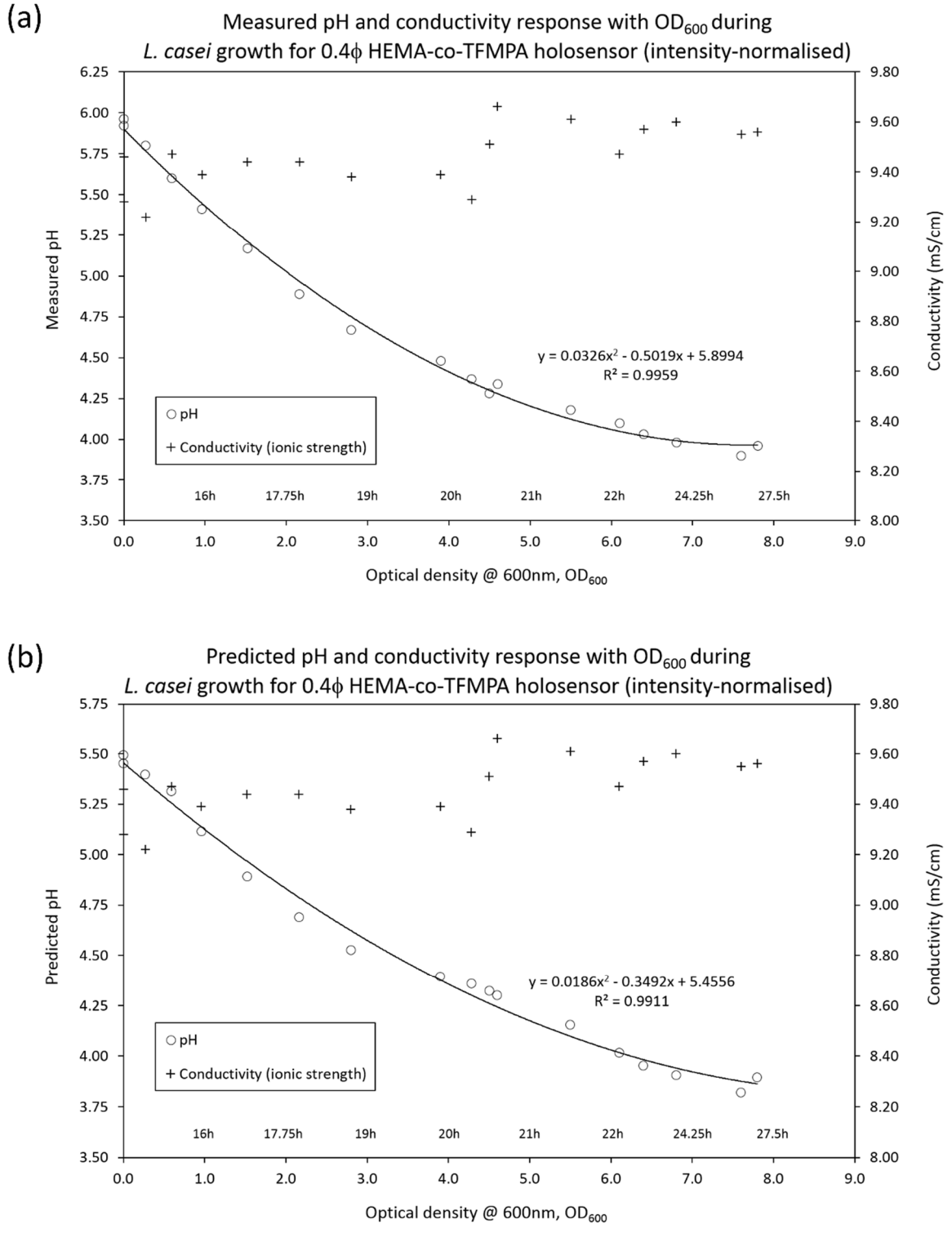

Figure 4-11: ***(a)*** *Measured pH and conductivity (ionic strength) of the batch media (broth) containing live L. casei from inoculation duration t=14.00h to t=28.00h at increasing OD_{600} values, versus* ***(b)*** *predicted pH (from Equation 4.4) and measured conductivity plotted against increasing OD_{600} of the bacterial media (broth)*

4.12 Ionic strength correction for the 0.4ϕ HEMA-co-TFMPA holosensor

Throughout the growth of *L. casei*, the measured ionic strength (by measuring conductivity) varied randomly within a range approximately ± 0.30 mS/cm from the ionic strength normalised value of 9.50 mS/cm (Figure 4-11) that was utilised for the ionic strength normalisation of the McIlvaine pH buffers used for characterisation of the 0.4ϕ holosensor.

As described in §3.12, the ionic strength values were corrected from the graphs of ionic strength to conductivity and peak wavelength response by introducing a correction factor based on the difference in peak wavelength response compared to if the conductivity were constant at 9.50 mS/cm. The associated corresponding ionic strength correction graphs for the 0.4ϕ holosensor were illustrated in Appendix N, which reported an R^2 value of 0.9897 for the ionic strength corrected predicted pH against OD_{600} curve. Although the correction did not exhibit significant differences, the accuracy parameter χ did fall a little from 99.52% to 99.38%.

4.13 0.4ϕ HEMA-co-TFMPA holosensor array

Following the successful integration of the 3.0ϕ and miniaturised 0.4ϕ holosensors in the microfluidic system, an array of seven 0.4ϕ holosensors was fabricated to provide a proof-of-concept for the feasibility of using an array of miniaturised holosensors in a microfluidic system. Only the results from the array (when considered as a whole) will be reported in this chapter, while the graphs associated with the other individual 0.4ϕ holosensor array spots are reported in Appendices P and Q for reference.

The same fabrication method as the 3.0ϕ and 0.4ϕ holosensor was employed to fabricate the 0.4ϕ miniaturised holosensor array. For optimal results, the spacing between the holosensor spots in the array were kept at 2.0 mm (edge-to-edge) distance from each other to prevent undesirable "cross-talk" photo-polymerisation of gels (experimentally observed for those < 2.0 mm distance to each other) in the (photomask) non-exposed regions, which would affect the consistency and aesthetics of the holosensors. The quality of the holographic signal would also be reduced and convoluted otherwise. Furthermore, a quartz-chrome photomask, instead of an acetate mask, was required to produce holosensors spots of comparable dimensions. Deviations from the recommended guidelines would not guarantee the quality of the fabricated holosensors. The white light profiler data, high-resolution holosensor array pictures, average gel dimensions and (camera) phone-taken pictures were illustrated in Figure 4-12.

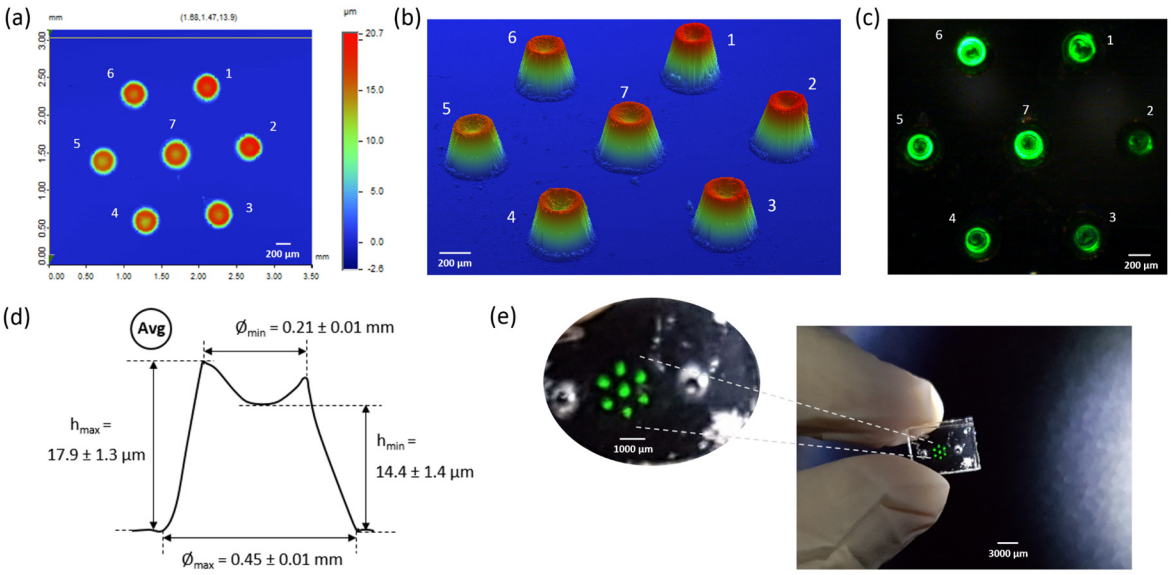

Figure 4-12: Collation of 0.4ϕ HEMA-co-TFMPA holosensor array information. ***(a & b)*** *2D and 3D digital elevation model of a 0.4ϕ holosensor array after hologram fabrication respectively. The different holosensors in the array were labelled accordingly for later comparison* ***(c)*** *Picture of the hologram taken by the high-resolution camera at 6.96X magnification while the 0.4ϕ microfluidic chip-embedded holosensor array was immersed in pH 6.0 McIlvaine buffer.* ***(d)*** *Average dimensional profiles (with standard deviation) of the seven 0.4ϕ holosensors in the array.* ***(e)*** *Picture of the hologram taken with a Samsung S7 mobile phone in the presence of pH 6.0 McIlvaine buffer inside the microfluidic chip.*

The standard deviations of the average gel diameters (ϕ_{min} and ϕ_{max}) for the 0.4ϕ holosensors in the array were 4.76% and 2.22% respectively when expressed as percentages of their averages. These values were comfortably within the minimum allowable error of 6.67% as discussed in §4.2.3.

4.14 pH characterisation for 0.4ϕ HEMA-co-TFMPA holosensor array

pH characterisation was performed for the 0.4ϕ HEMA-co-TFMPA holosensor array by considering 7+1 configurations of the array – 7 individual holosensor spots and the whole array as a collective unit. Ionic strength balanced (to 9.50 mS/cm) McIlvaine pH buffers were utilised. The spectrophotometric peak wavelength pH response and hologram pictures recorded by a high-resolution camera were illustrated in Figure 4-13.

The pH response (peak wavelength) was normalised to a total-intensity normalised value to eliminate the influence of the varying illumination intensity. Only by looking at the maximum intensity from Figure 4-13(a), it appeared that the pK_a of the whole array was around pH 4.75, though it later turned out to be pH 4.45. The intensity of the peak wavelength holographic signal, although useful as a quick initial prediction, could not be used as a definitive method of determining the pK_a of the calibrated holosensor.

A notable observation was the non-uniform hologram brightness across the array (Figure 4-13(b)). However, it was not due to problems with the individual holosensors. When the illumination angle was changed, the holograms that appeared dimmer previously would light up. Either the illumination angle was different due to the relative positions of the holosensor, or the individual holosensor was expanding/contracting at a slightly different angle. The peak wavelength graphs and pH calibration pictures of other individual 0.4ϕ holosensor array spots can be found in Figure 4-14 (or Appendix Q-1) and Figure 4-15 (or Appendix O-1) respectively. The intensities of the other holosensor spots in the array (Appendix Q-1) were almost constant throughout the pH range, which further showed that a best-fit calibration curve was required for determining its pK_a.

According to the RGB-transformed values (to xyY), the corresponding pH values tracked a certain path in the CIE 1931 chromaticity diagram (Figure 4-13(c)). This path could not be described by a curve or line. When the pH range was 3.75 to 6.00, the pH values follow a straight line as described in Figure 4-13(d). The other pH characterisation curves in the CIExyY chart included only up to pH 3.75. There was a good straight-line fit, and *L. casei* growth does not typically go below pH 3.75. However, it is important to note that the CIE chromaticity space is non-linear, and can only serve as a visual representation of a colour change.

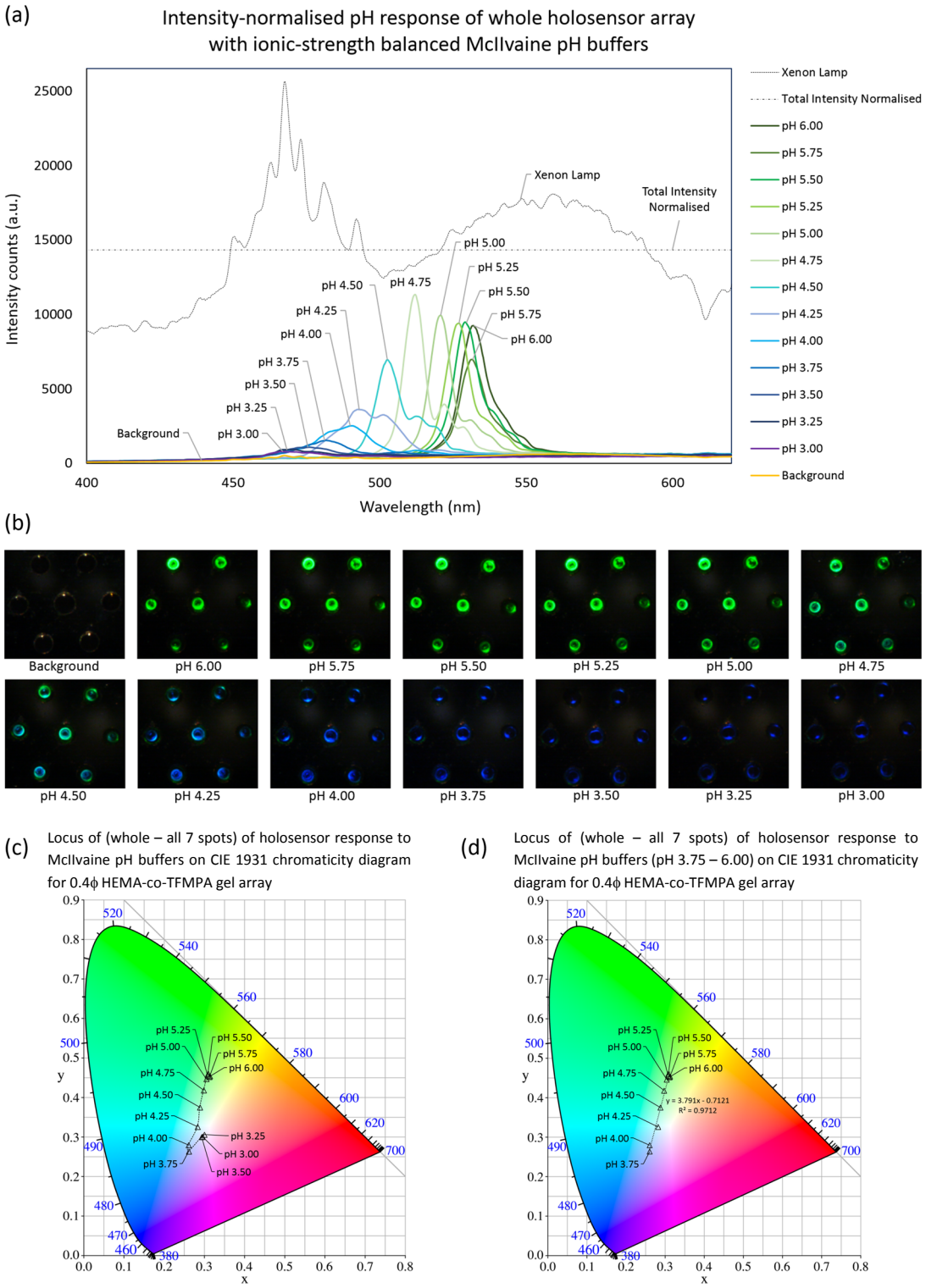

Figure 4-13: pH calibration information of the 0.4ϕ HEMA-co-TFMPA holosensor array. ***(a)*** *Total intensity-normalised peak wavelength holosensor pH responses obtained from pH 6.00 down to pH 3.00. The height of the peaks represents the corresponding spectral intensity recorded by the spectrophotometer.* ***(b)*** *Picture montage of hologram array captured by the high-resolution camera at 6.96X magnification when immersed in correspondingly decreasing pH starting from pH 6.00 to pH 3.00 just before the spectrophotometric data of (a) was collected.* ***(c & d)*** *Visualisation of the holosensor array response with loci at various pH corresponding to (b) for pH range of [3.00, 6.00] and [3.75, 6.00] respectively. RGB-xyY transformed values from (b) were plotted onto the CIE 1931 chromaticity diagram.*

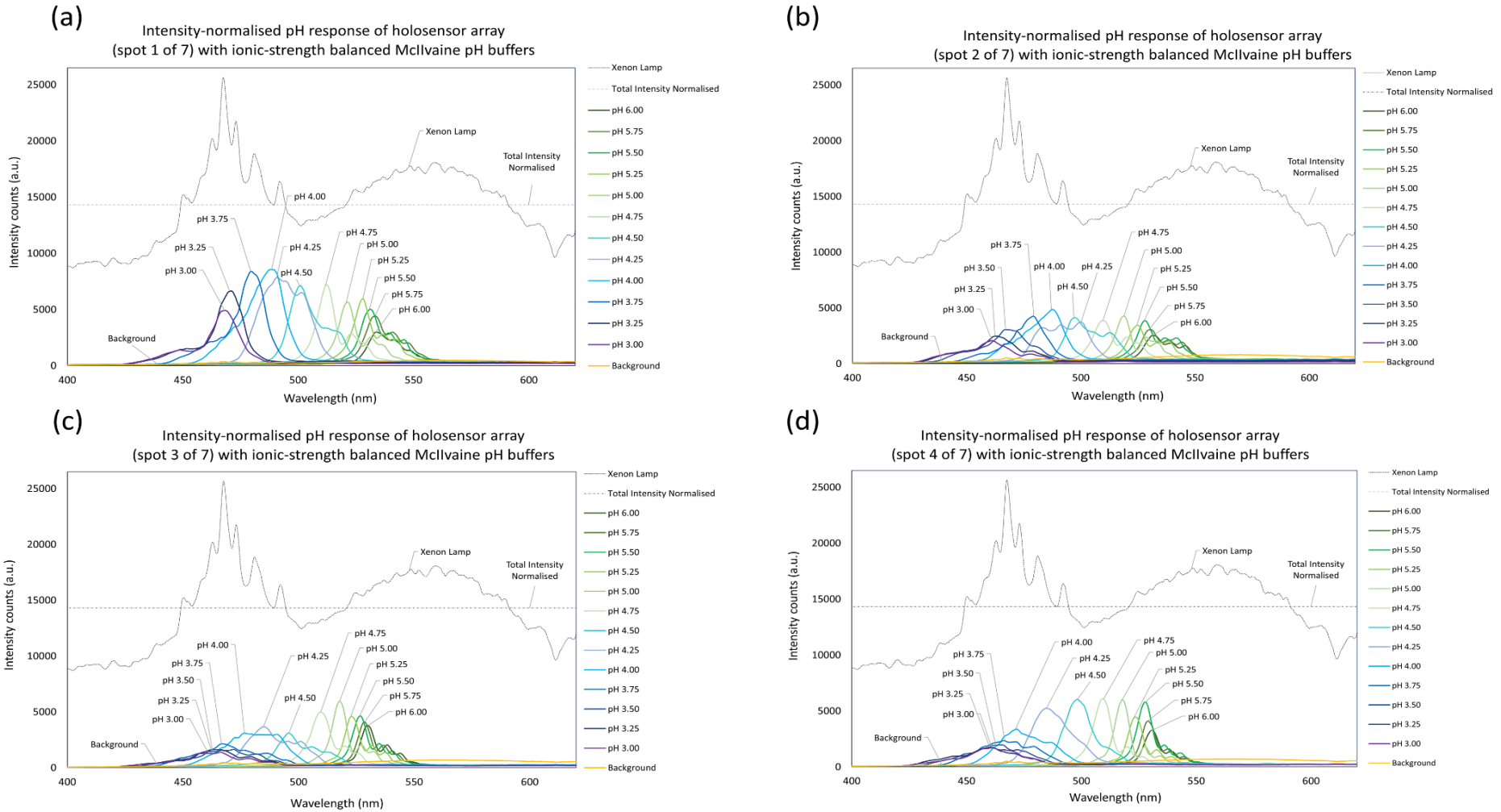

Figure 4-14: (a) Peak wavelength pH responses of the 0.4ϕ holosensor array ***(a – d)*** *spots #1 to #4 respectively during pH calibration*

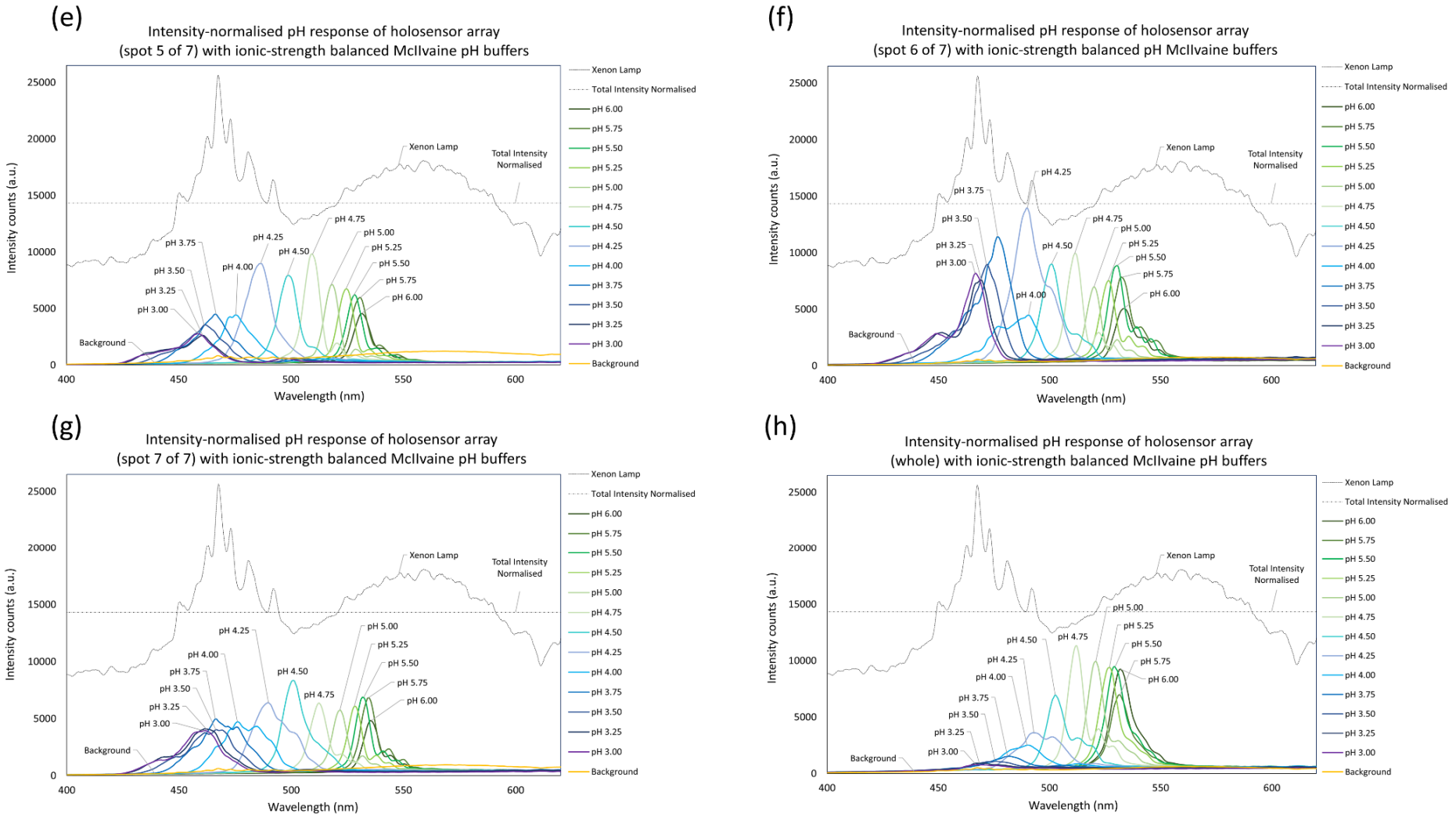

Figure 4-14*: **(b)** Peak wavelength pH responses of the 0.4ϕ holosensor array **(e – g)** spots #5 to #7 and of the whole array (h) respectively during pH calibration*

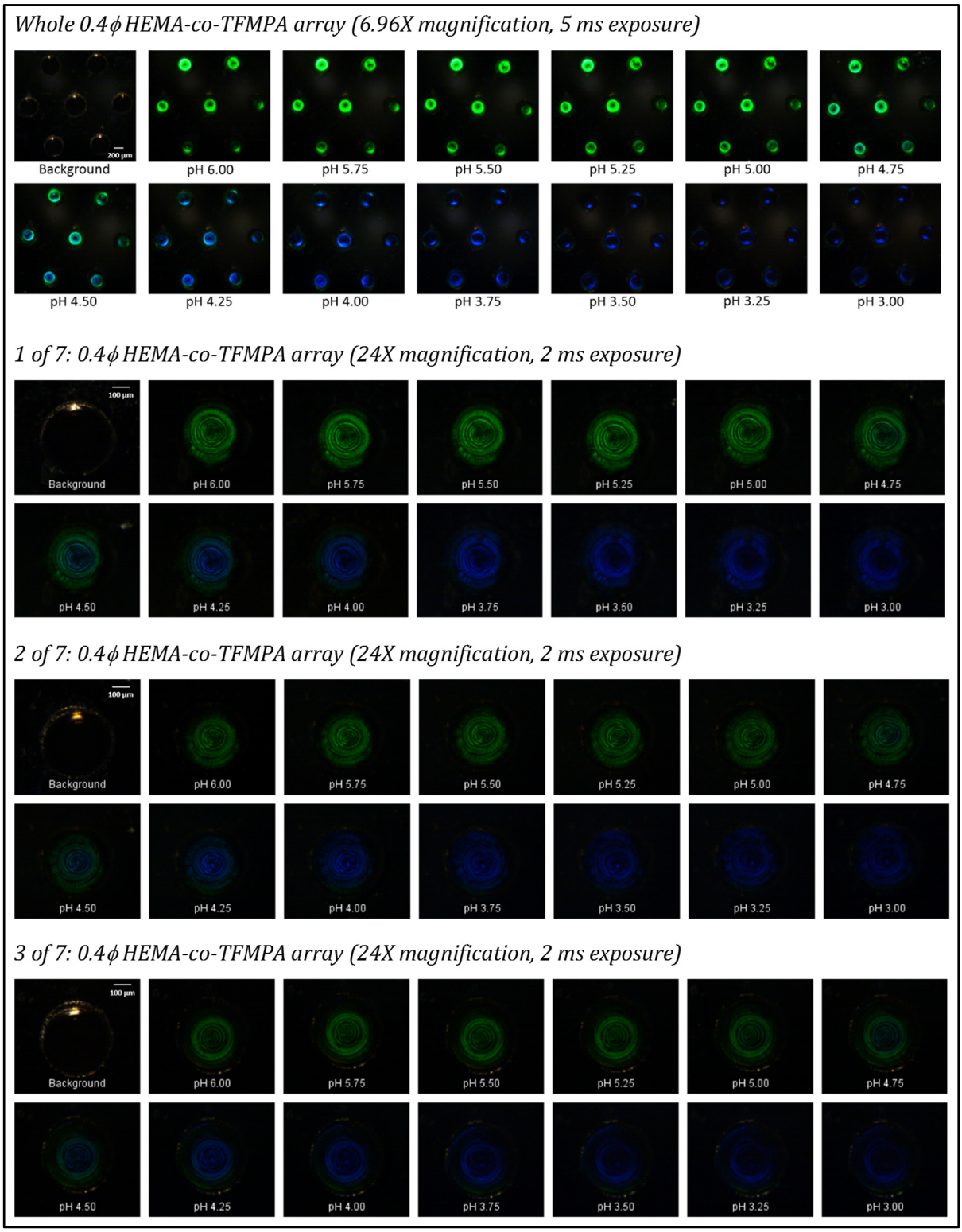

Figure 4-15: ***(a)*** *Pictures of the holosensor array and the individual spots (#1 - #3) of the array during pH calibration,*

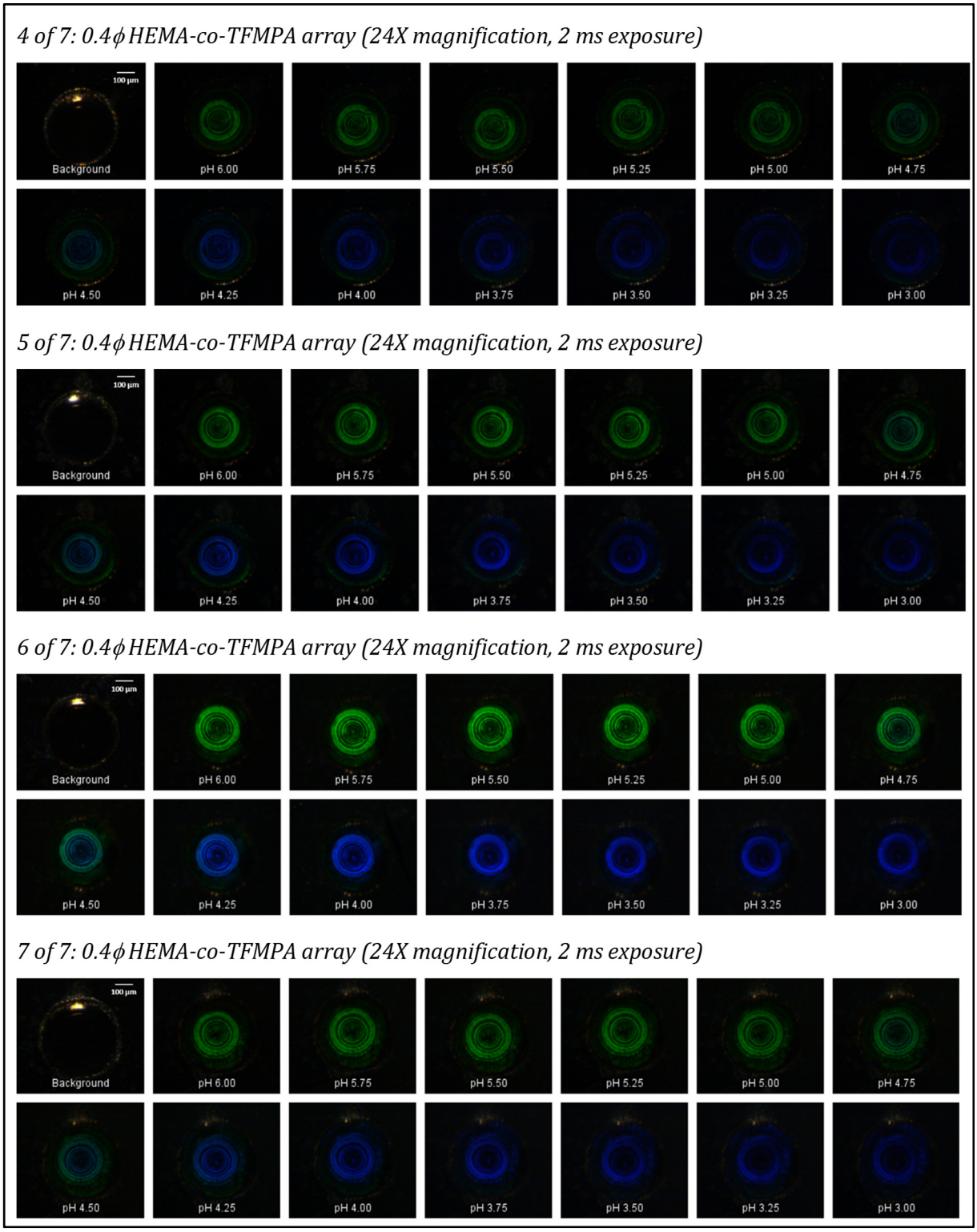

Figure 4-15: ***(b)*** *Pictures of individual spots (#4 - #7) in the holosensor array during pH calibration*

4.15 Calibration curve for 0.4ϕ HEMA-co-TFMPA holosensor array

The average of three runs for the intensity-normalised pH responses (peak wavelength) of the whole array was plotted with error bars of ± 1 s.d. (Figure 4-16(a)). Using Equation 4.3, the assumed pK_a, λ_{min} and λ_{max} values were extracted from the raw data and slightly tweaked to the best-fit graph for the calibration curve (Figure 4-16). The individual characterisation curves (using the modified H-H equation) for the other 0.4ϕ holosensor array spots were collated in Appendix Q-3.

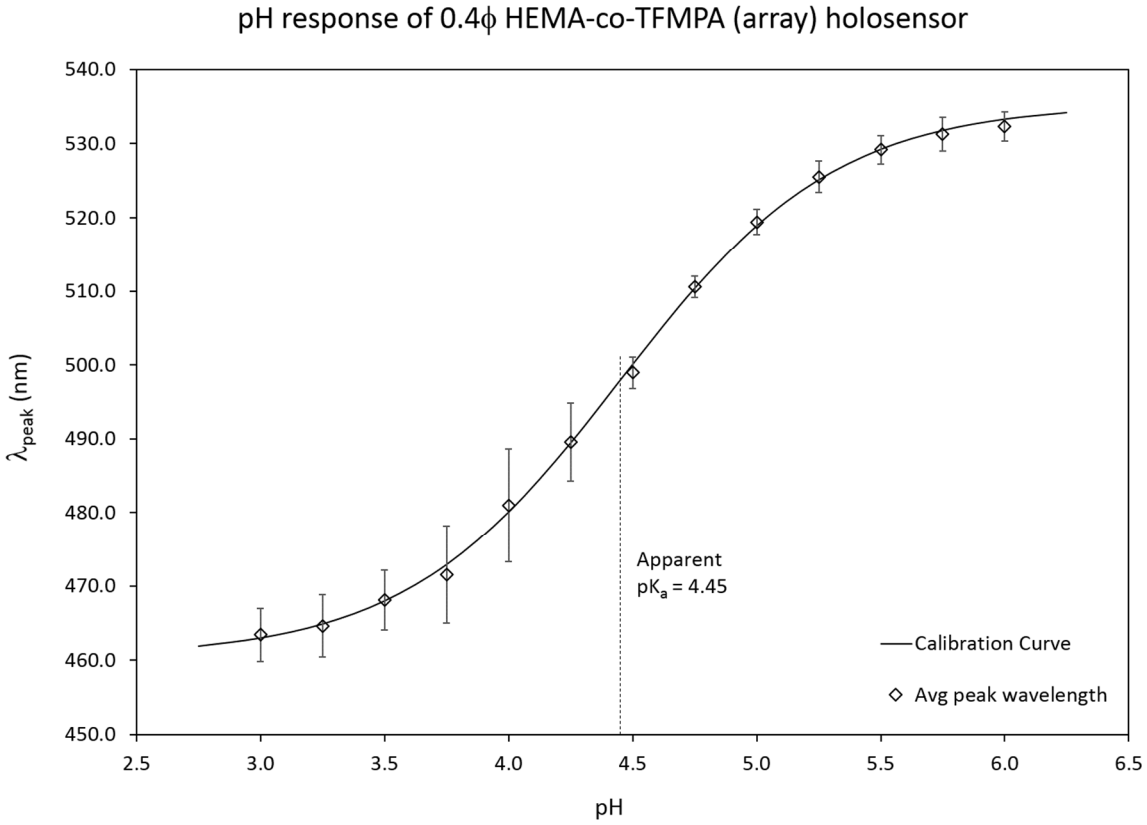

Figure 4-16: Calibration curve for pH characterisation of 0.4ϕ HEMA-co-TFMPA holosensor array. Error bars represent 1 s.d.

4.16 *L. casei* growth curve for 0.4ϕ HEMA-co-TFMPA holosensor array

L. casei was inoculated with the frozen OD_{600}=0.93 batch with the growth curve characteristics illustrated in Figure 4-17.

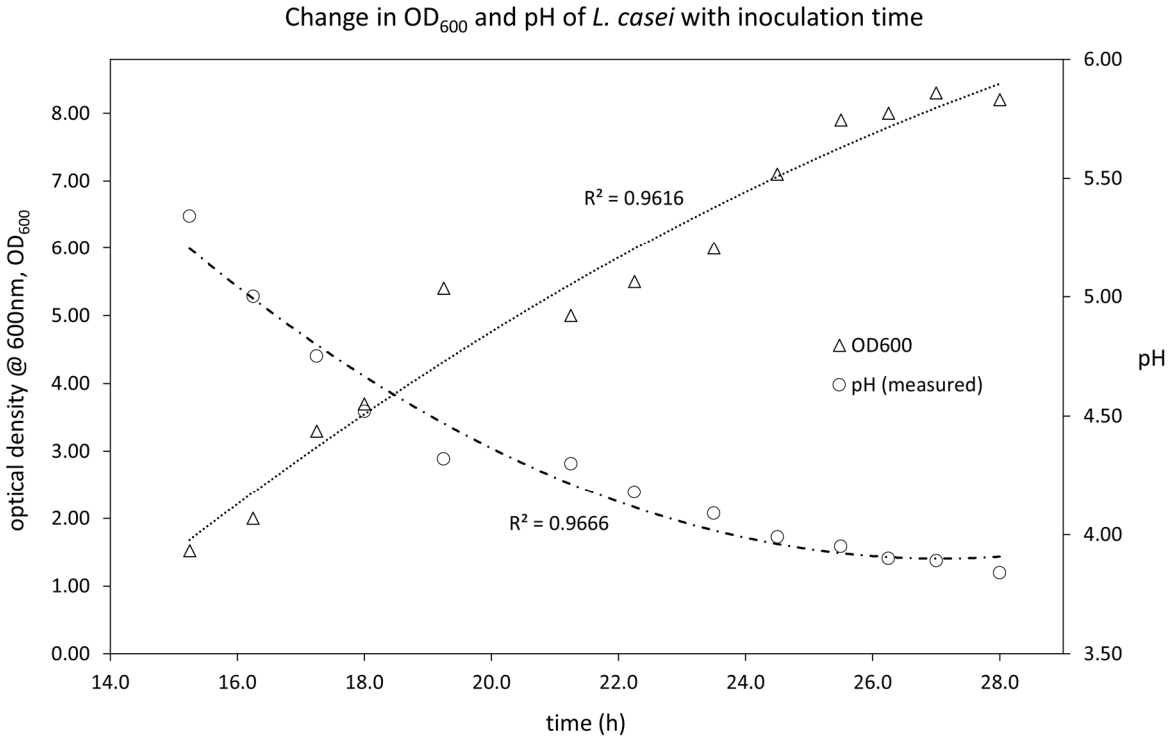

Figure 4-17: L. casei growth curve for 0.4ϕ HEMA-co-TFMPA holosensor array

4.17 *L. casei* interrogation with 0.4ϕ HEMA-co-TFMPA holosensor array

L. casei was monitored from 15.25h to 28.00h of inoculation. The spectrophotometric data and hologram pictures taken with the high-resolution camera, together with the RGB-transformed xyY values of the whole array constituted Figure 4-19. During the interrogation of *L. casei*, there was slight damage to spot #6 as illustrated in Figure 4-19(b). Close-up pictures of the individual holosensor spots are depicted in Figure 4-18 (or Appendix O-2). The gel appeared to have stuck permanently to the other side of the microfluidic chip since deliberate reciprocating flow and continual DI water rinses could not restore the hologram to its original consistency.

Despite the discrepancy, the average RGB values for the 7 spots (considered as a whole) that was transformed to the xyY colour space and plotted on the CIE chromaticity diagram and formed a straight line as shown in Figure 4-19(c). Even though all the points fit into a straight line, since the growth never went below pH 3.75 anyway, the data points were not of chronological order on the line. This could be attributed to a few possibilities. The hologram pictures taken during *L. casei* interrogation were of a higher magnification and exposure (integration time), which could have

altered the field of view and white balance. It was not likely though, as spots #1 and #2 (as labelled in Figure 4-12(a–c)) did not exhibit any issues.

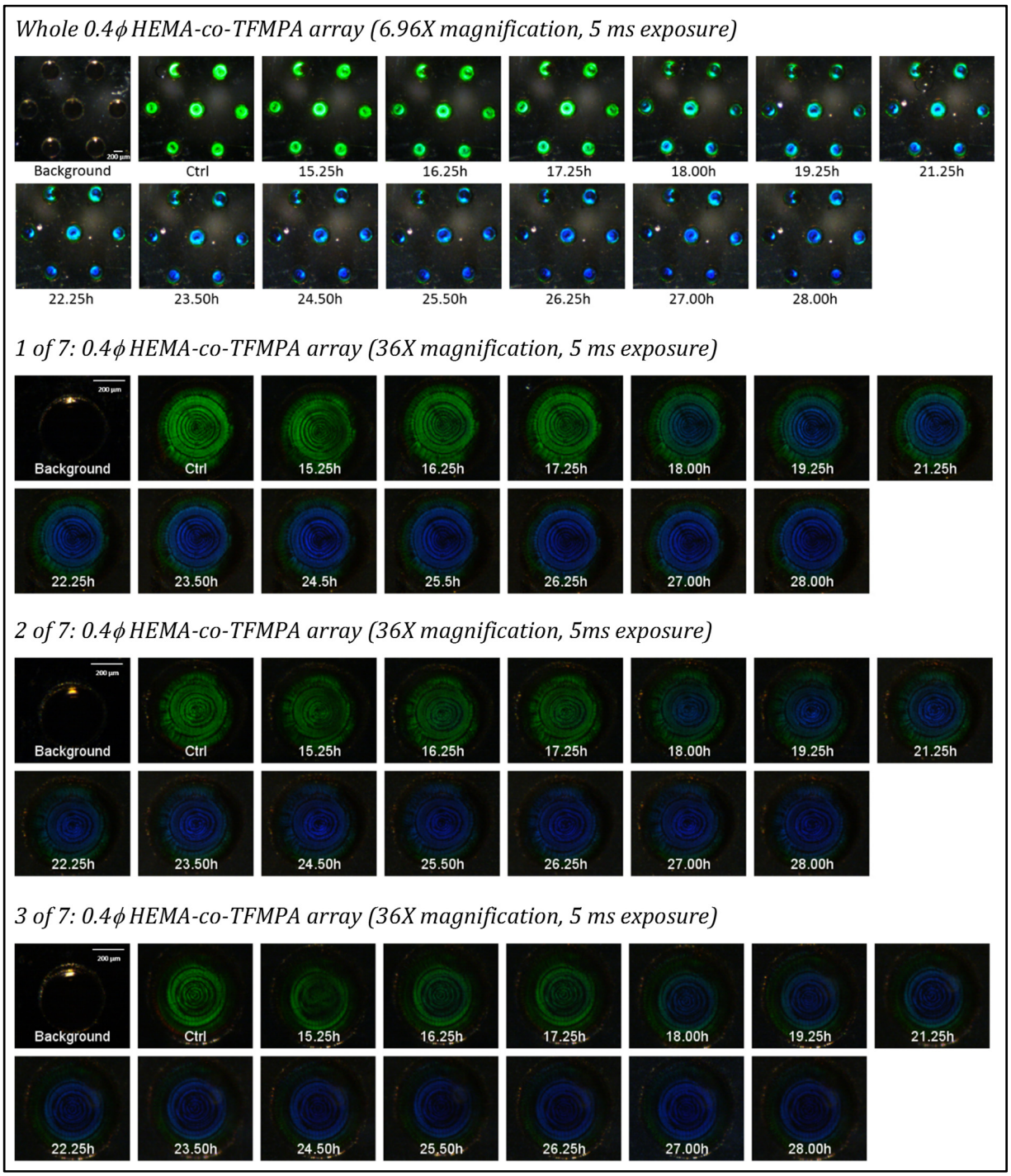

Figure 4-18: ***(a)*** *Pictures of the holosensor array and the individual spots (#1 - #3) of the array during L. casei interrogation,*

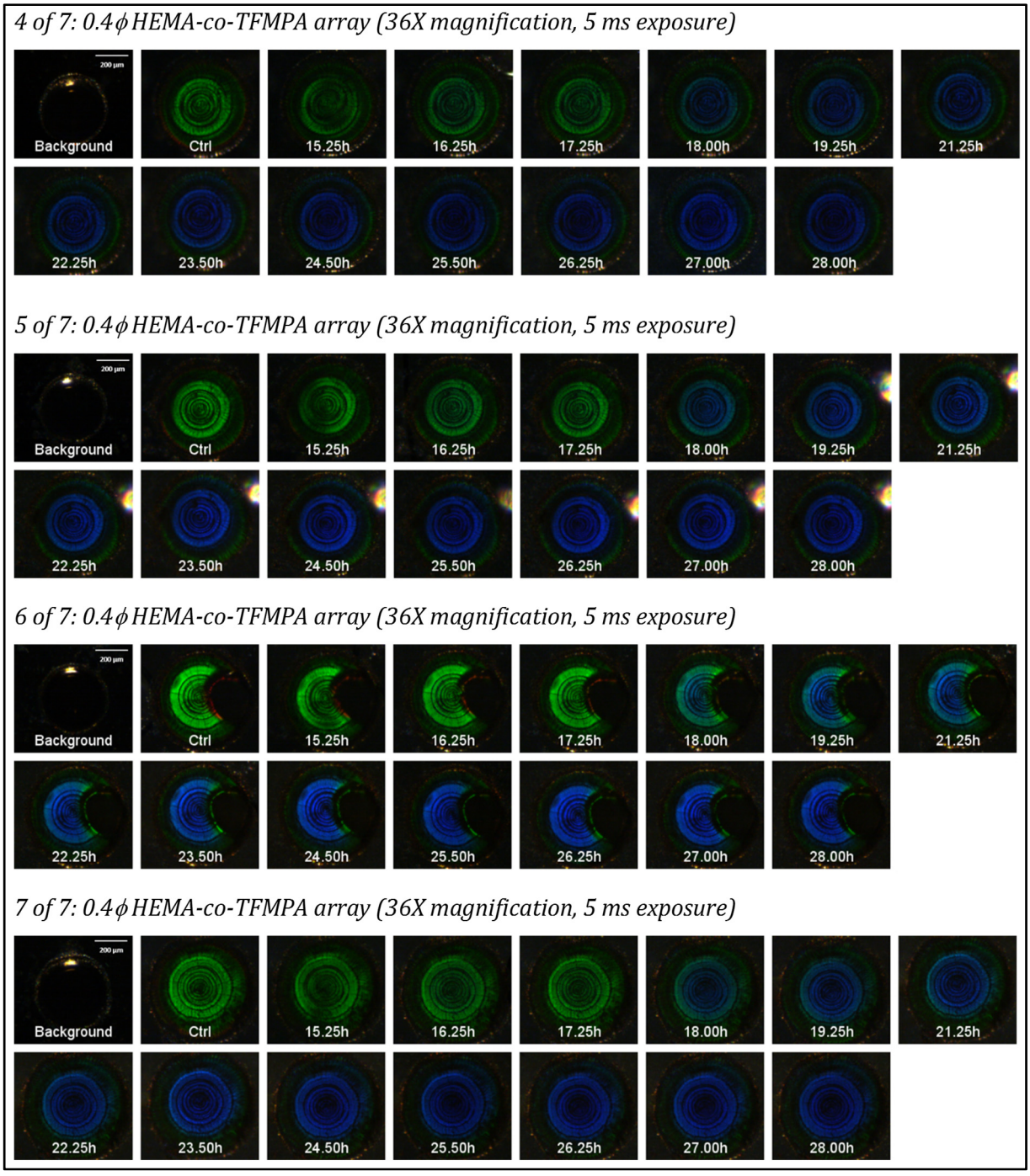

Figure 4-18: ***(b)*** *Pictures of individual spots (#4 - #7) in the holosensor array during L. casei interrogation*

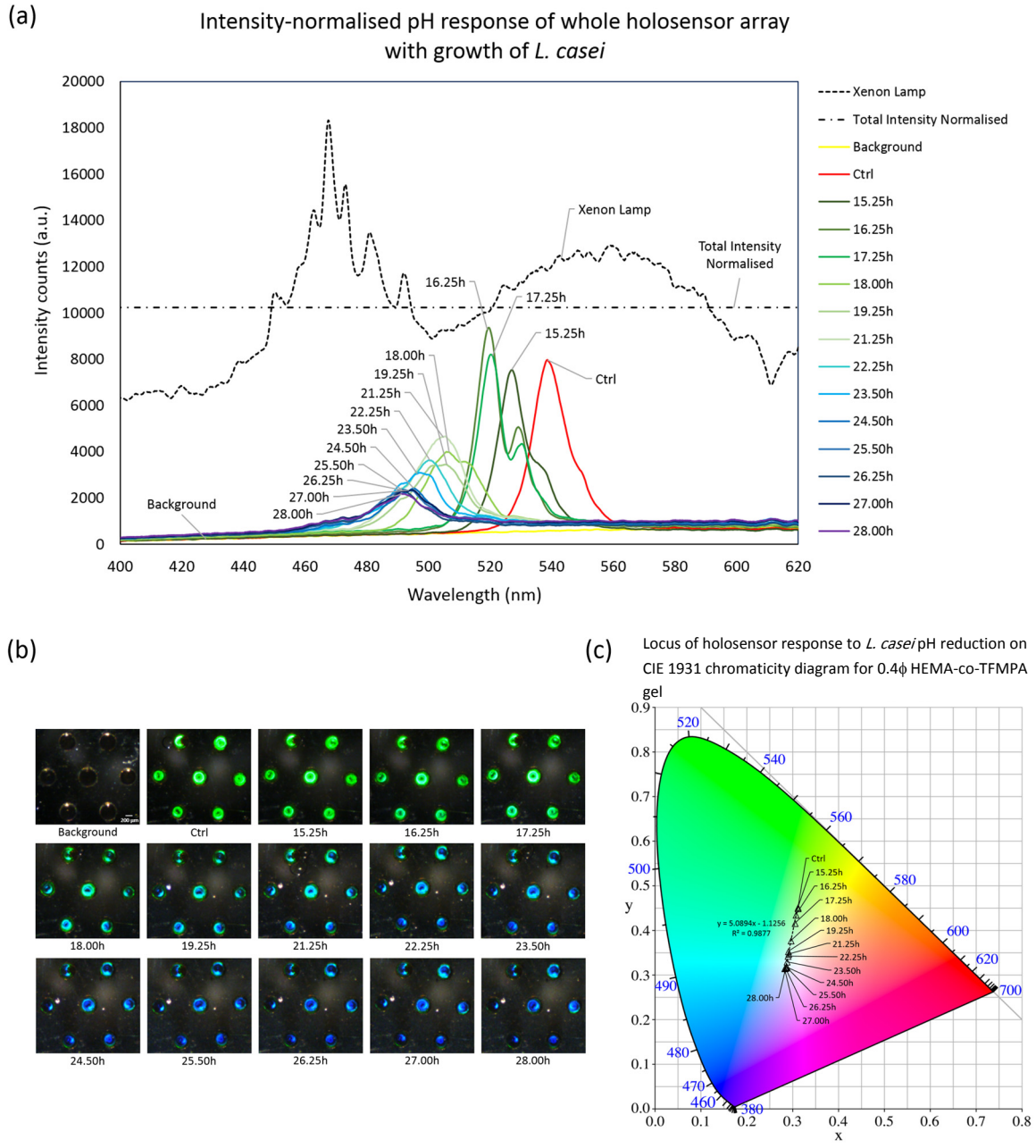

Figure 4-19: 0.4ϕ HEMA-co-TFMPA holosensor array response to L. casei growth. ***(a)*** *Total intensity-normalised peak wavelength holosensor Lactobacillus casei (L. casei) pH response obtained from batch process interrogation from t=15.25h to t=28.00h.* ***(b)*** *A picture montage of holograms taken with the high-resolution camera at 6.96X magnification corresponding to the batch sample introduced into the microfluidic chip at corresponding inoculation durations from t=15.25h to t=28.00h.* ***(c)*** *Visualisation of colour change with locus of holosensor response at corresponding inoculation durations from t=15.25h to t=28.00h. RGB-xyY transformed values from (b) were plotted onto the CIE 1931 chromaticity diagram.*

4.18 Standard curve for 0.4ϕ HEMA-co-TFMPA holosensor array (whole array)

The standard curve was obtained by plotting the measured pH against the corresponding predicted pH by using the derived equations discussed earlier in the chapter (§4.10). The calibration curve information from §4.15 was utilised to calculate the slope of the calibration curve, $\frac{d\lambda}{dpH}$, which was obtained by differentiating Equation 4.3 with respect to pH using the quotient rule and substituting the calibration values accordingly. The predicted pH was then calculated with the rearrangement of Equation 4.3 into Equation 4.4, from which the standard curve could be plotted with the measured pH against the predicted pH as shown in Figure 4-20.

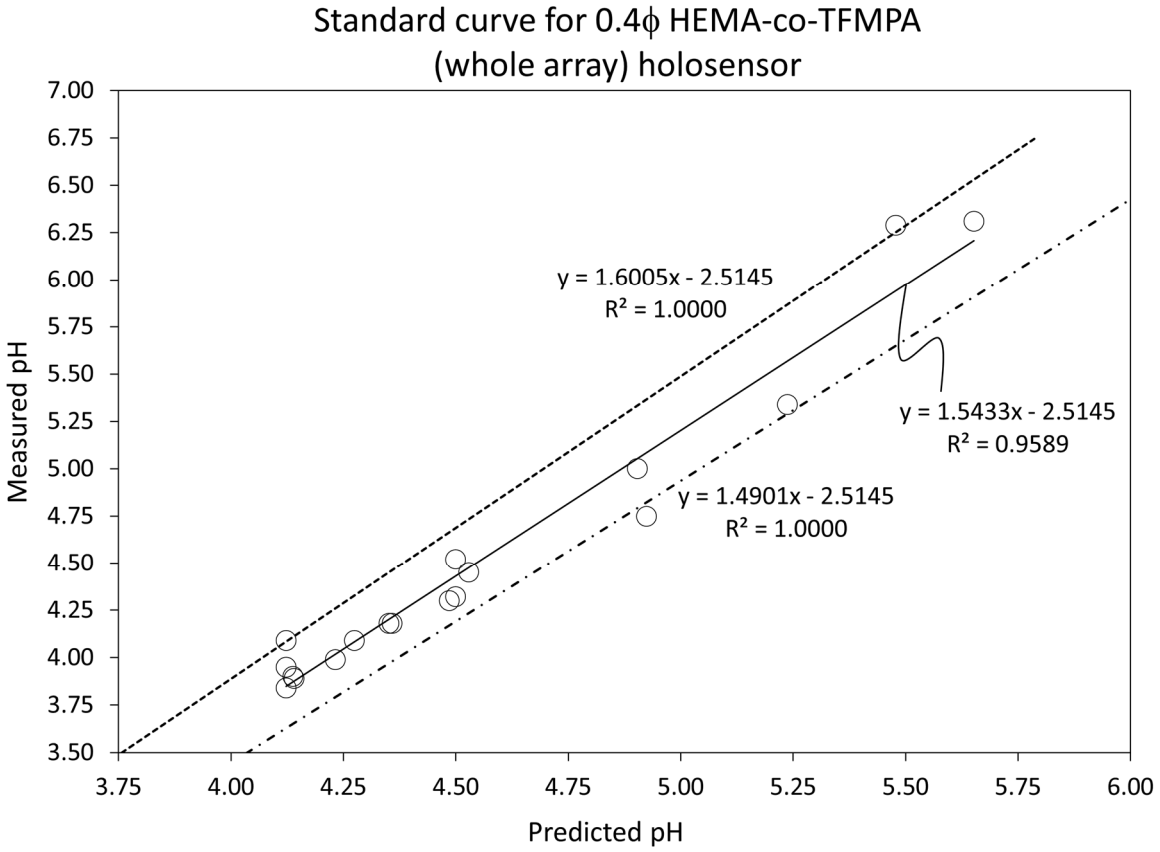

Figure 4-20: Standard curve for 0.4ϕ HEMA-co-TFMPA holosensor array illustrating the correlation between the measured and predicted pH. The upper and lower limits were determined by the zero point of the pH meter at pH 7.00 ± 0.25 (3.57% allowable uncertainty)

The upper and lower limits were defined by the zero point of the pH meter (pH 7.00 ± 0.25), which translated to an allowable error of 3.57%. Visually, the accuracy of the holosensor could be assessed by looking at the distribution of readings within the limits. The standard curves with upper and lower limits for the individually interrogated holosensor spots are shown in Figure 4-21 (or Appendix Q-4).

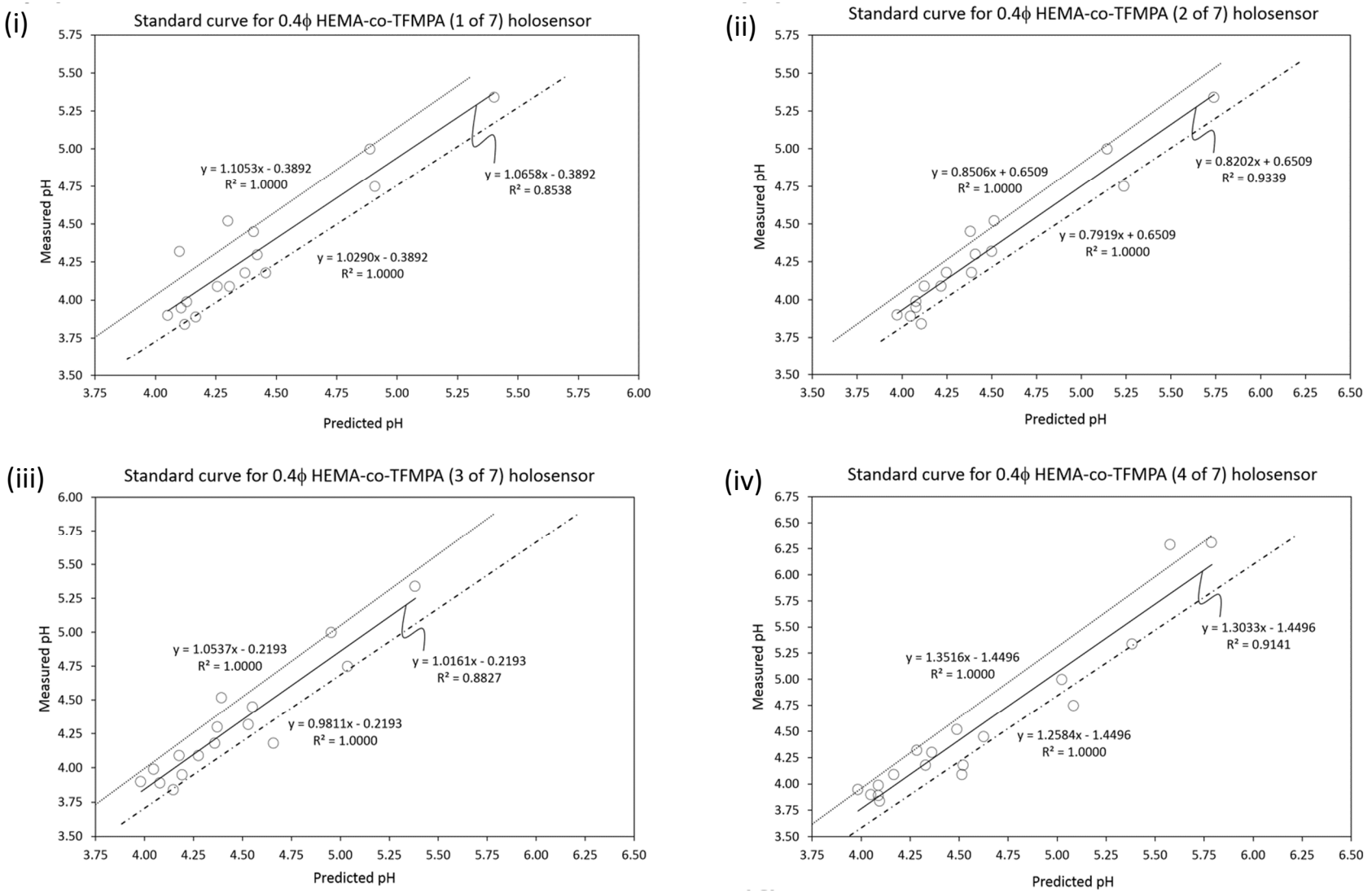

Figure 4-21: ***(a)*** *Standard curves of measured pH vs predicted pH for* ***(i – iv)*** *0.4ϕ holosensor array spots #1 to #4 respectively*

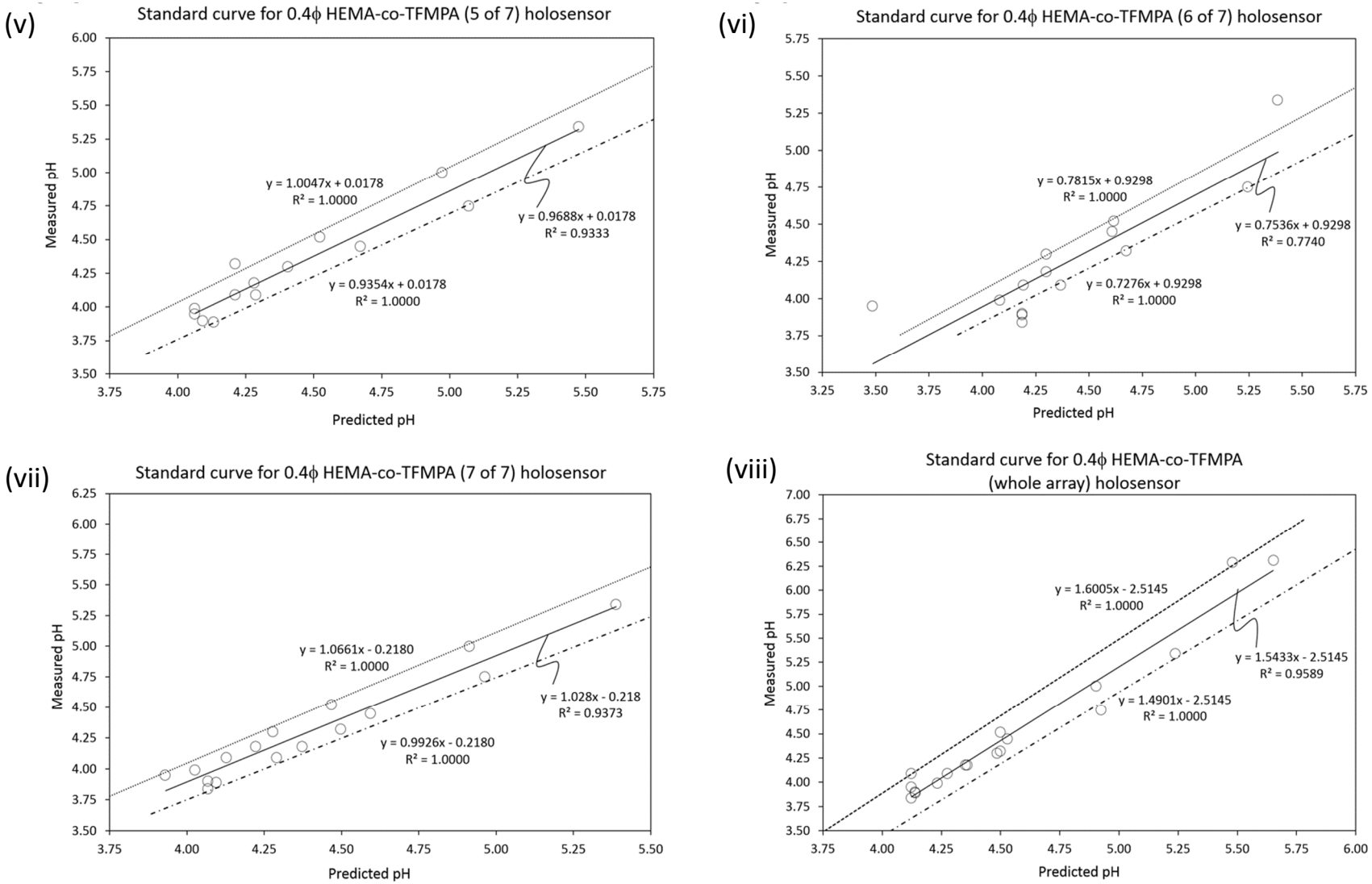

Figure 4-21*: **(b)** Standard curves of measured pH vs predicted pH for (v – viii) 0.4ϕ holosensor array spots #5 to #7 and of the whole array respectively*

To obtain a quantifiable performance indicator, an accuracy parameter χ (as discussed in §4.11) was devised to compare the accuracy of the holosensor array to that of the pH meter. The R^2 of the ideal pH meter benchmark (illustrated in Figure 4-22(a) or Appendix Q-5) was 0.9874, and the R^2 of the predicted pH based on the 0.4ϕ holosensor array when considered as a whole (Figure 4-22(b) or Appendix Q-6(h)) was 0.9654. The accuracy parameter, χ was 97.77% accordingly.

To summarise the key values required for appraising the 0.4ϕ holosensor array, Table 4-1 details the key derived parameters for the determination of the calibration curve, predicted pH and accuracy parameter, χ. As the 0.4ϕ holosensor array spot #6 was damaged, the averages and their corresponding standard deviations were calculated with and without spot #6. The accuracy parameter of spot #6 itself was 74.72%. Using the devised accuracy parameter χ, the accuracy of the miniaturised 0.4ϕ holosensor array was 91.53% ± 3.96% without spot #6, and 89.13% ± 7.31% with spot #6 included.

Table 4-1: Summary of key values for determination of calibration curve, predicted pH and accuracy parameter, χ, for 0.4ϕ HEMA-co-TFMPA holosensor array

	Assumed pK_a	$\frac{d\lambda}{dpH}$	λ_{max}	λ_{min}	std curve R^2	R^2 (measured pH)	R^2 (predicted pH)	Accuracy χ (%)
WHOLE	4.35	40.3	535.0	465.0	0.9589	0.9874	0.9654	97.77%
1	4.35	39.31	533.7	465.4	0.8538	0.9874	0.8460	85.68%
2	4.35	43.26	533.4	458.3	0.9339	0.9874	0.8687	87.98%
3	4.40	41.40	532.0	460.1	0.8827	0.9874	0.9116	92.32%
4	4.45	44.26	533.6	456.7	0.9141	0.9874	0.9326	94.45%
5	4.40	45.89	533.4	453.7	0.9333	0.9874	0.9145	92.62%
6	4.40	41.44	535.7	463.7	0.774	0.9874	0.7378	74.72%
7	4.40	47.81	538.3	455.3	0.9373	0.9874	0.9492	96.13%
Average (1 – 7)	4.39	43.34	534.30	459.03	0.8899	0.9874	0.8801	89.13%
Std. dev. (1 - 7)	0.03	2.91	2.07	4.32	0.0598	0.0000	0.0722	7.31%
Average (w/o 6)	4.39	43.66	534.07	458.25	0.9092	0.9874	0.9038	91.53%
Std. dev. (w/o 6)	0.04	3.06	2.16	4.16	0.0340	0.0000	0.0391	3.96%

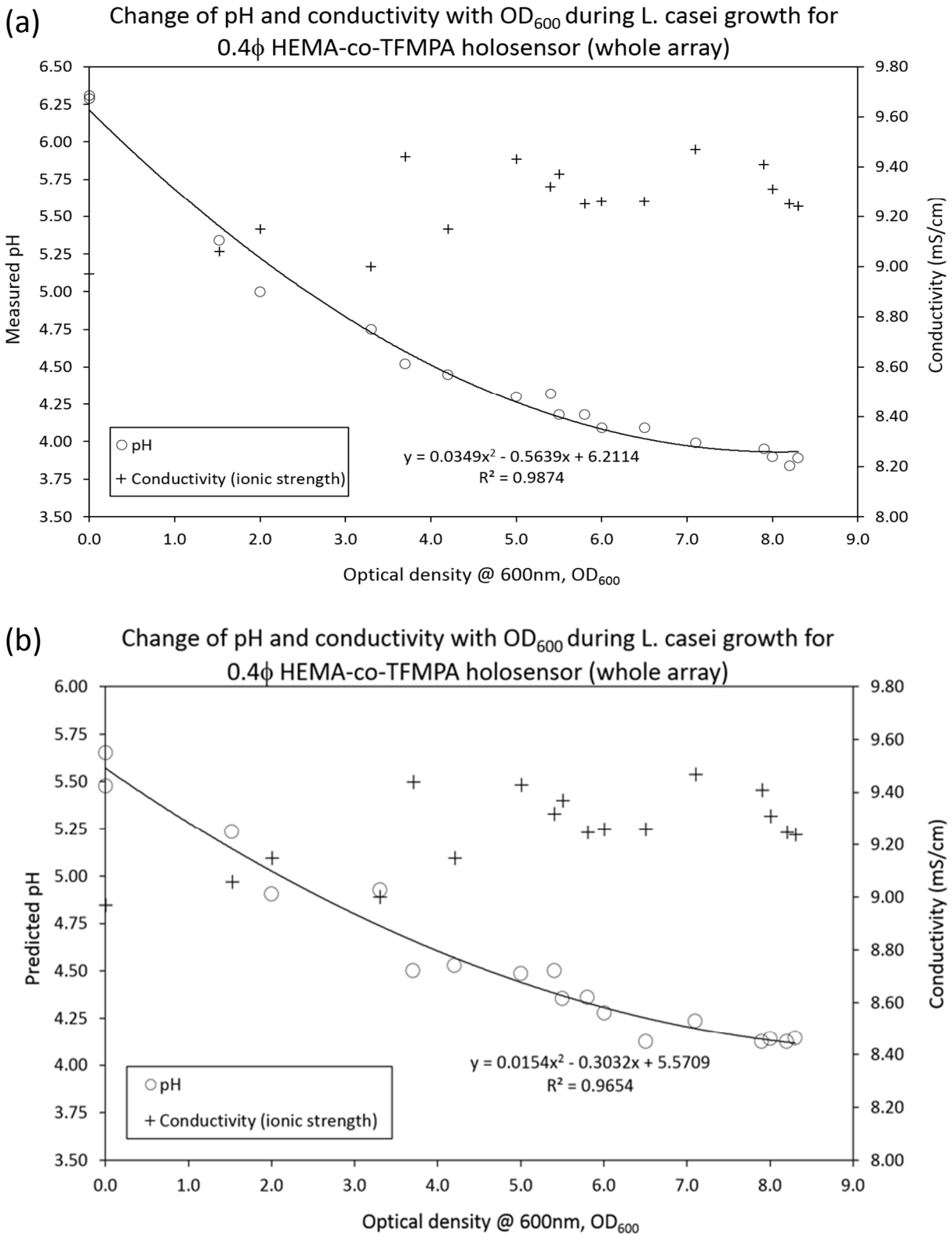

Figure 4-22: ***(a)*** *(Ideal case) Measured pH and conductivity (ionic strength) of the batch media (broth) containing live L. casei at increasing OD_{600} values,* ***(b)*** *predicted pH (from Equation 4.4) and measured conductivity plotted against increasing OD_{600} of the bacterial media (broth)*

4.19 Discussion – Concentric ring patterns

A distinctive difference between the holographic signals of the 0.4ϕ holosensors compared to that of the 3.0ϕ ones were the concentric patterns observed on the gel during holosensor interrogation. In addition, for the 0.4ϕ holosensor, a dark spot coincided with the lowest portion of the gel together with a pointed feature (Figure 4-3). These observations were unique to that of the 0.4ϕ holosensors. However bright a hologram the 3.0ϕ gel produced, these dark circular patterns were only observed, if any, at the edges of bright 3.0ϕ holosensors. In this section (§4.19), a few possible explanations for the existence of the concentric ring patterns were examined.

4.19.1 Point scatterers and spherical waves

A concentric ring interference pattern can form when defects like dust particles or other small scatterers reradiate a weak scattered spherical wave. Such a wave could then interfere with the primary wave to form concentric interference patterns [152]. In “elastic scattering”, an oscillating dipole acts as an emitter of an electromagnetic wave of the same wavelength as the incident one and follows the time-modulation of the electric wave vector. Where the scatterer is larger than 20 nm, several of these oscillating dipoles are created simultaneously within one given particle, which causes some of the emitted light waves to inherit a significant phase difference. Smaller scatterers impart only a negligible phase difference between light emitted from the various scattering centres within the given particle [153] (Figure 4-23(a)).

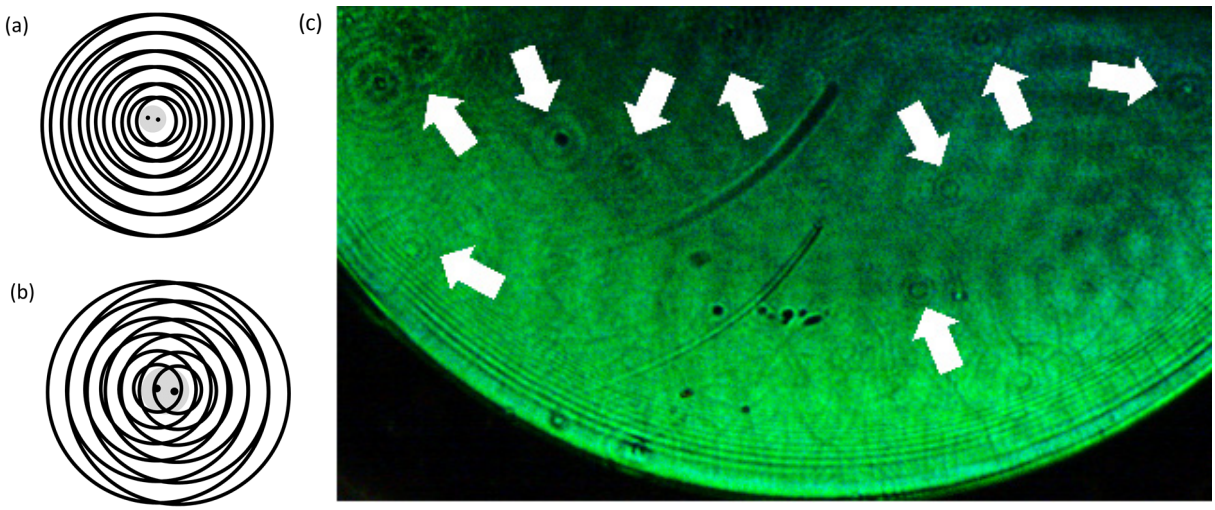

*Figure 4-23: Interference pattern from **(a)** a small scatterer and **(b)** large scatterer, depicted with only 2 scattering centres within the particle, for simplicity. **(c)** Picture of a 3.0ϕ HEMA-co-TFMPA hologram with random occurrences of point scatterers depicted by the ripples indicated by the white arrows*

Although the interference pattern in this illustration was concentric, random occurrences of small particles at different parts of the gel should result in a much more randomised pattern and would not be the main contributor of the diametric concentric rings pattern observed with the 0.4ϕ holosensors.

4.19.2 Diffraction of light from nano-periodic structures

Recently, Laskar *et al.* studied the diffraction of light from self-assembled colloidal magnetic particles exhibiting periodic structures with different beam path lengths [154]. It was found that path length (L) dictated light-matter interaction (diffraction of scattering pattern). Where a single corona-like light scattered ring for the longer path length (L = 1 mm) was observed, a concentric diffraction ring pattern for shorter path length (L = 80 μm) was observed when the condition for maintaining temporal coherence, and therefore constructive interference was satisfied.

There was a possibility that the short polyHEMA gel height could be displaying the same type of diffusion described, but did not explain why a larger 3.0ϕ hologram would not possess such a pattern.

4.19.3 Air wedge interference and Newton's rings

Wedge fringes form when two glass plates are placed face-to-face with one end separated by a thin spacer such as a piece of tissue or hair. The resultant air-wedge interference pattern are straight-line, evenly spaced fringes parallel to the line along which they touch. The interference is brought about by a division of amplitude, where the path length difference between light reflected off the top surface of the top plate and the top surface of the bottom plate result in interference.

Similarly, Newton's rings form when a curved surface is placed on an optically flat surface while interference occurs between the light impinging on the curved surface and the light reflected off the bottom flat surface.

A schematic diagram for a typical air-wedge interference setup and Newton's rings setup are illustrated in Figure 4-24. Both phenomena, however, require a small angle – typically about 4 minutes of arc to see the fringes clearly – since the interference pattern is not well defined for path differences of more than a few hundred wavelengths. Optomechanical components in the hologram fabrication setup were placed at much larger distances away from each other.

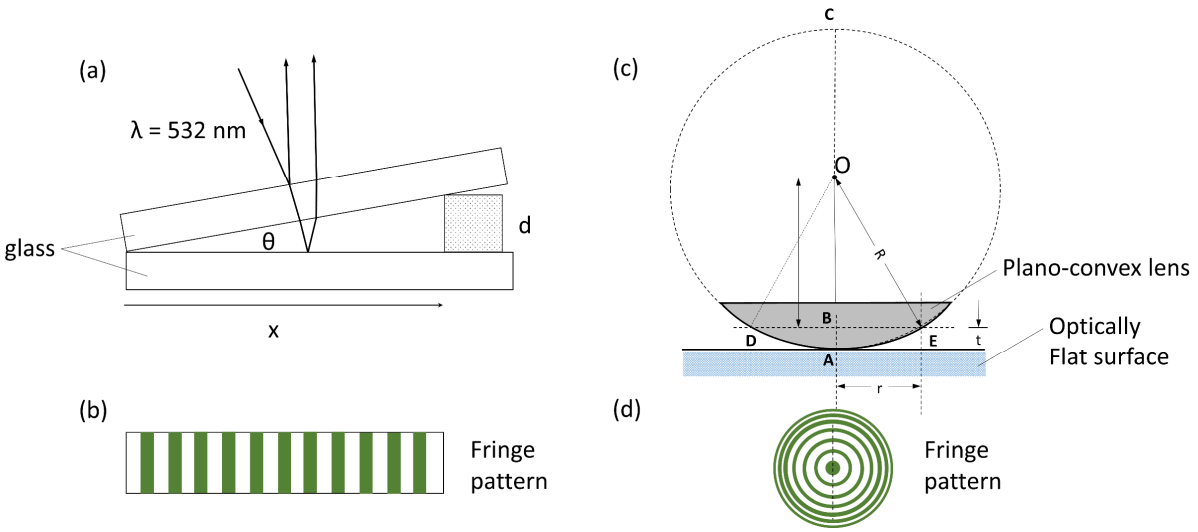

*Figure 4-24: Schematic diagram of the **(a)** air-wedge setup, and **(b)** its fringe pattern; **(c)** Newton's rings setup with its **(d)** fringe pattern*

4.19.4 Effect of Airy disk

The concentric ring patterns and the use of a pinhole (circular aperture) during hologram fabrication resemble the diffraction pattern resulting from a uniformly illuminated circular aperture with a bright region in the centre, known as the airy disk.

An airy disk is a far field diffraction of light and the formation of concentric ring patterns with a bright central circular disk surrounded by alternately bright and dark rings whose intensity decreases rapidly as distance from centre increases. The observed fringes on the 0.4ϕ holosensors, however, were typically evenly spaced out with no attenuation.

4.19.5 Effect of multiple reflections and interference

A Michelson interferometer consists of two mirrors, a beam splitter, and a screen or camera. The beam splitter partially reflects and transmits the beam of uniform intensity onto mirrors, for which the path difference of the reflected and transmitted beam result in an interference pattern that can be captured on a screen. Where the image of mirror 2 is parallel to M1, the image of source S_1' and S_2' will be in-line but separated as depicted in Figure 4-25. In order to observe the concentric ring pattern, the imaging system or camera has to have its focus set to infinity. If the light were to be collimated, an arrangement known as the Twyman-Green interferometer, interference will occur everywhere in the output beam with real, non-localised fringes. This would make it possible to view the concentric ring patterns on a card everywhere in the output beam.

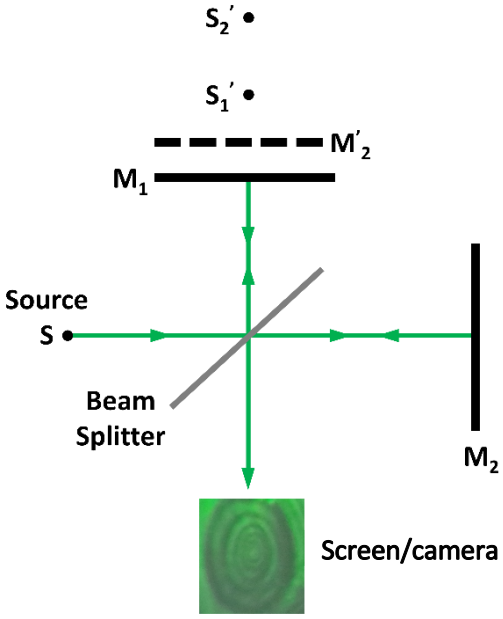

Figure 4-25: Schematic diagram of the Michelson Interferometer

4.19.6 Effect of the Laguerre Gaussian mode

The concentric ring patterns are similar to the Laguerre Gaussian mode shapes observed in a cylindrical resonator. As the 0.4ϕ holosensor gel was located in between two front surface mirrors, its cylindrical shape could have functioned as an optical cavity, and the laser would resonate inside the cavity where its length is an integer number of the laser beam wavelength. A length drift of the laser resonator would shift the resonator mode frequencies without also shifting the gain maximum, also known as mode hopping.

If the resonator symmetry is mostly circular, the modes exhibit a cylindrical symmetry described by the Laguerre polynomials [155]. Laguerre-Gauss (LG) modes are solutions to the paraxial wave equation in cylindrical polar coordinates [156].

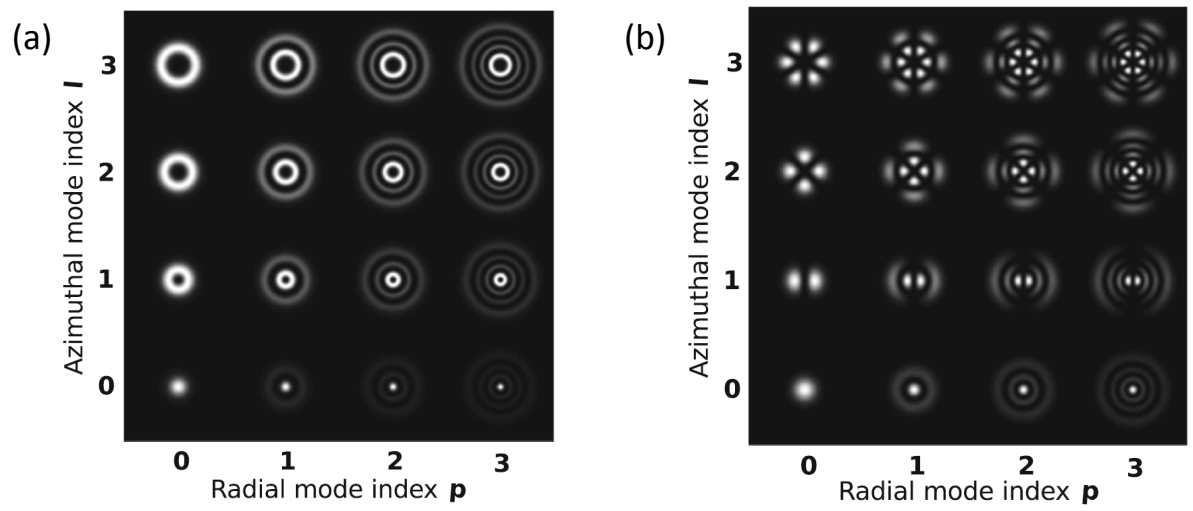

*Figure 4-26: Intensity distributions for the modes up to the 9th order of the **(a)** helical and **(b)** sinusoidal LG mode sets. Republished with permission of Springer, from ref.* [156]*. Copyright© 2014, Springer International Publishing*

A cylindrical waveguide would exhibit field configurations that illustrate a concentric ring configuration (Figure 4-27) for transverse modal field distribution TE_{01}, TE_{02} and TE_{03} [157], [158].

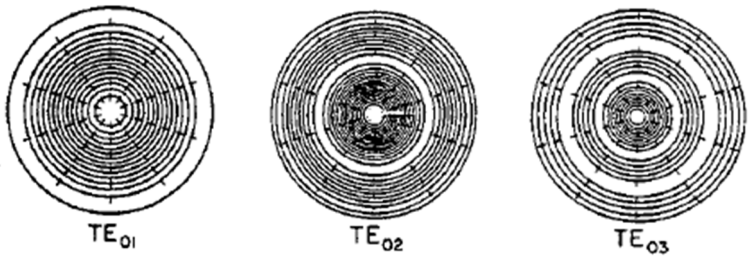

Figure 4-27: Transverse modal field distribution TE_{01}, TE_{02} and TE_{03} for a circular waveguide. Extracted from ref. [155] with permission granted by IEEE. Copyright© 1985 IEEE. The actual collation of all the studied transverse modal field distribution from ref. [155] can be found in Appendix W.

The concentric ring patterns on the 0.4ϕ gel were a composite (not purely just concentric rings with a bright spot at the centre), probably a combination of the aforementioned phenomena. The resolution of the pattern on the gel would have to be improved in order to have a more representative conclusion about the origin of the pattern. Evidence suggests, that the main contributions to the pattern was from the Twyman-Green interferometer arrangement (§4.19.5) and circular waveguide mode (§4.19.6).

The images of the laser source in the hologram fabrication setup were adjusted to be intentionally separated (Figure 2-19(b)) and the real, non-localised interference pattern could be captured by a screen. The explanation of mode hopping and resonance within a circular waveguide seemed to explain the interference pattern well, with its transverse mode field distribution resembling the photographed gel patterns.

5 Chapter 5 Further holosensor developments

Analogous to resonance, the strength of a holographic signal is dependent on the magnitude and concordance of the recorded Bragg reflection planes. With better spatial uniformity and more Bragg planes that constructively interfere to reflect selectively a wavelength band of illuminated light, the hologram brightness and monochromatic quality can be optimised. Following the success of integrating miniaturised holosensor spots and an array into a microfluidic system, the next step forward is to control the variation of gel height (flatness) across its diameter.

Lactobacillus casei monitoring was utilised as a platform to evaluate the viability of cell monitoring in a microfluidic system as the bacterium has a predictable homo-fermentative metabolism. A higher value application for the integrated miniaturised holosensor was mammalian cell monitoring. These cells typically thrive in an environment around pH 7.0. Instead of using the acidic 2-(trifluoromethyl) propenoic acid (TFMPA) pH moiety, the basic 2-(dimethylamino) ethyl methacrylate (DMAEM) pH ligand could be incorporated into the HEMA-co-EDMA (polyHEMA) gel matrix to monitor mammalian cell lines. The apparent pK_a of DMAEM in polyHEMA was pH 6.93 [80]. Gel-bound DMAEM buffers efficiently at ± 1 pH unit from its pK_a, which makes it ideal for pH monitoring of mammalian cells. As a starting point, a miniaturised HEMA-co-EDMA-co-DMAEM gel could be fabricated and a hologram recorded within its volume to demonstrate a proof-of-concept for a miniaturised DMAEM holosensor embedded in a PDMS-glass microfluidic chip.

In this chapter, a method of obtaining flat gel profiles is explored, followed by a proof-of-concept for a miniaturised 0.4ϕ DMAEM holosensor with a flat gel profile. Developments involving an alternative substrate (for the holosensor) and a dye-free hologram fabrication method are also investigated and discussed.

5.1 Flat gel profile exploration

The technique of employing a polymerisation inhibitor (or terminator) into the gel precursor solution worked well in controlling the gel diameter during photo-polymerisation; similar work had been performed utilising a terminator for the production of thermosensitive microgels [133], albeit not for the application described in this thesis. However, no work has been done on the fabrication of a flat-top gel profile, or controlling the gel height variation, to the best of the author's knowledge.

Controlling the gel height variation optimises the holosensor by introducing uniformity with regard to the formation of Bragg reflection planes following the development of Ag^0 fringes within the gel matrix.

As illustrated in Figure 5-1, it can be clearly seen that there would be a loss of Bragg planes in the non-uniform region compared to the ideal gel profile. The Ag^0 fringes at the edges would also tend to be distorted compared to the bulk of the gel. The lack of Bragg plane quality and consistency, together with a decreased number of fringes available for constructive interference would adversely affect the resulting hologram brightness and monochromatic quality.

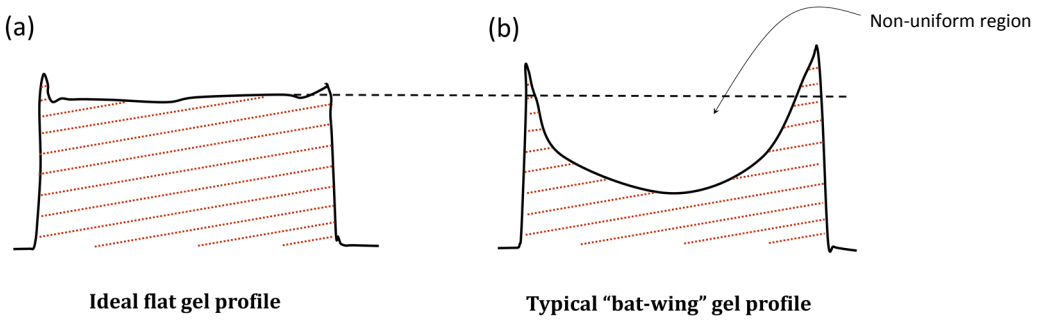

*Figure 5-1: Schematic diagram comparing **(a)** an ideal flat gel profile and **(b)** a typical "bat-wing" gel profile. The brown dotted lines represent the Ag^0 fringes, which form the Bragg reflection planes.*

5.1.1 "Bat-wing" gel profile

The occurrence of the "bat-wing" gel profile most likely results from the diffusion and reaction kinetics of photo-polymerisation with a photomask [133], and is exacerbated by the use of a polymerisation inhibitor. During UV exposure, the concentration of inhibitor near the centre of the photo-polymerised gel decreases sharply due to the inactivation by the exponentially increasing number of free radicals and radicalised methacrylate groups of the gel precursor ingredients (monomers, cross-linkers and pH moieties) within the UV-illuminated area. Unreacted monomers, cross-linkers and pH moieties are less inhibited at the edges of the illuminated region since diffusion continually feeds the edges with more polymerisation products. However, since the gel precursors would not be able to diffuse to the centre region before being polymerised, there is a tendency for the gel to be taller at the edges than at the middle, leading to the formation of the "bat-wing" gel profile.

Park *et al.* [133] developed a simplified diffusion-reaction kinetics model for such a photo-polymerisation process and predicted a few observations from the simulation model, which were corroborated with experimental findings illustrated in Figure 5-2. Increased exposure time and monomer concentration formed larger (diameter) gels; while increased exposure intensity, terminator concentration, monomer concentration and exposure time amplified the "bat-wing" effect.

Using these results, exposure intensities and terminator concentration were experimentally minimised but to no significant improvement. Other identified experimental parameters were varied to explore the possibilities of fabricating a gel with flat profile.

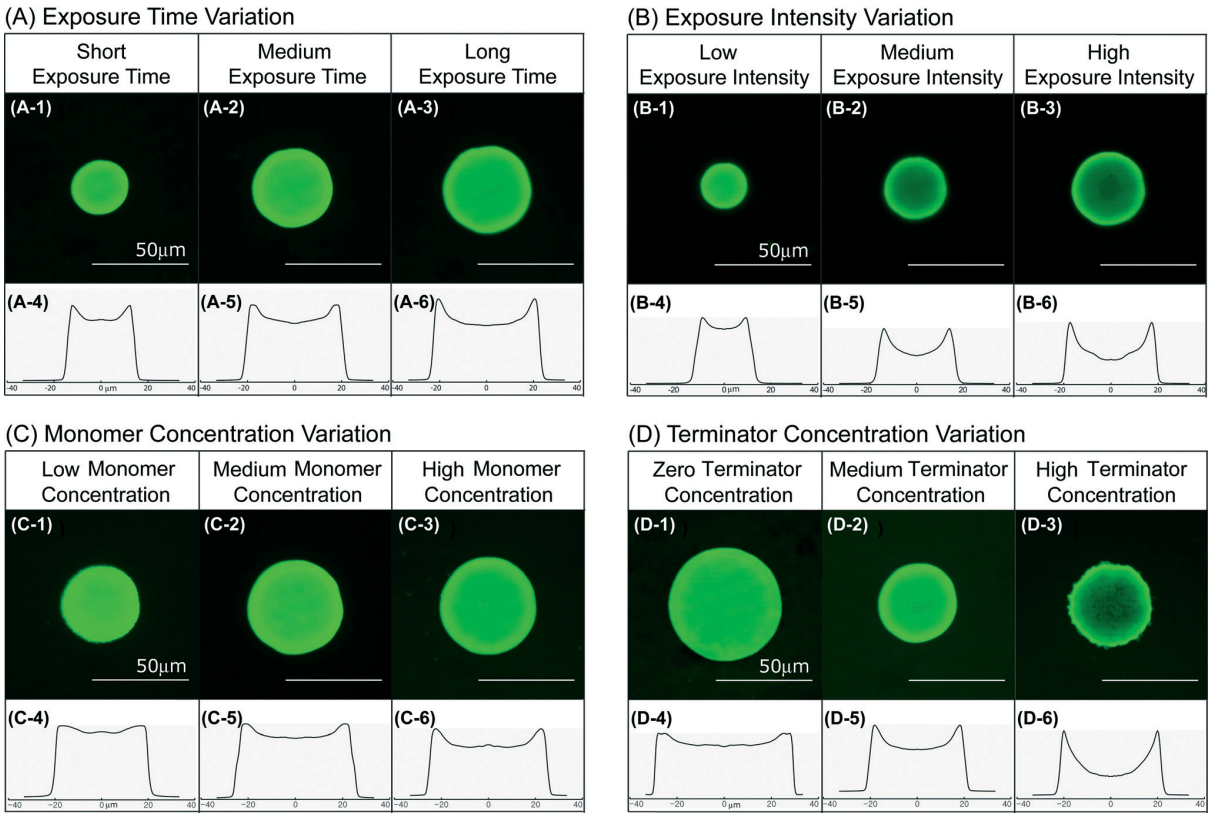

Figure 5-2: Experimental results from ref. [133]. *Concentration profile of photo-polymerised poly-N-isopropylacrylamide (polyNIPAAM) gels illustrating the gel profile with* ***(A)*** *exposure time variation,* ***(B)*** *exposure intensity variation,* ***(C)*** *monomer concentration variation, and* ***(D)*** *terminator concentration variation. Reproduced in part from ref.* [133] *with permission of The Royal Society of Chemistry. Copyright© 2014.*

5.1.2 Flatness ratio (FR)

Before proceeding to examine various experimental techniques and parameters, it was important to first define the criteria for a flat gel profile. Experimentally, since no holograms could be observed for gels below 3 µm in height (due to the insufficient number of fringes required for adequate constructive interference), this number would be utilised as a benchmark for desired gel height variation, i.e. difference in the maximum and minimum gel height ($h_{max} - h_{min}$). It meant that a height variation of 3 µm should not have a significant convoluting influence on the hologram signal. For relative comparisons amongst gels of different dimensions, this difference was normalised as a percentage ratio to the minimum gel height (h_{min}) as shown in Equation 5.1.

$$Flatness\ ratio, FR = \frac{(h_{max} - h_{min})}{h_{min}} \times 100\% \tag{5.1}$$

5.1.3 Effect of UV power intensity

Considering UV intensity directly influences the diffusion and reaction kinetics, the power intensity of the UV LED was varied across the 0 – 100% (corresponding to a maximum of 185.5 mW/cm^2) range to

observe its effect on gel height variation. As illustrated in Figure 5-3, the gel exhibited a pronounced "bat-wing" effect when photo-polymerised beyond 30% UV power (55.8 mW/cm^2), and formed a ring at and above 60% UV power (111.1 mW/cm^2).

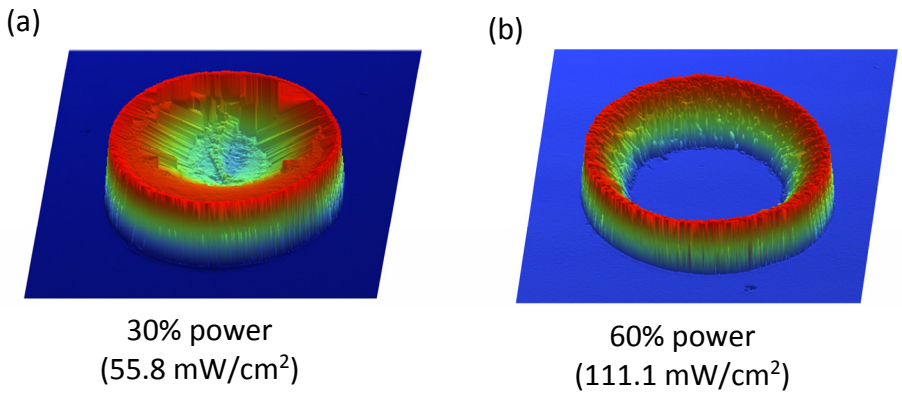

Figure 5-3: 3D digital elevation model (data gathered from the white light profiler) of the photopolymerised DMAEM gel with ***(a)*** *30% power and* ***(b)*** *60% power respectively.*

The change observed from Figure 5-3 was substantial compared to what was reported in reference [133], due in part to the much higher concentration of gel precursors present in 1 mL of solvent. 8 mmol per mL of IPA solvent was utilised compared to about 2.99 mmol of gel precursors in 1 mL of methanol from Figure 5-2, where the UV power was varied between 110 mW/cm^2 to 440 mW/cm^2. The reaction kinetics for the 0.4ϕ DMAEM holosensor would thus be significantly more pronounced.

Increasing UV power intensity does still increase the gel height variation as depicted in Appendix R-2(a), especially when the intensity was increased significantly.

5.1.4 Effect of cover substrate

Special care was given when choosing the cover substrate material. The experimental setup differed from previous work where UV radiation would propagate through the cover substrate depicted and labelled as "COC cover" (instead of the gel substrate) before interacting with the gel precursor solution as illustrated in Figure 2-17(b). This configuration enables the interchangeability of substrate for the gel.

5.1.4.1 Choice of cover substrate

Cyclic olefin copolymer (COC) was experimentally determined to be the best cover substrate for gel fabrication due to its high UV transparency and relatively inert and hydrophobic surface compared to glass, polyethylene terephthalate (PET, or widely known as Mylar®), polycarbonate (PC) and poly(methyl methacrylate) (PMMA). The UV attenuation and transmittance of the mentioned substrates were displayed in Appendix J(c) and Appendix J(d) respectively.

5.1.4.2 Hydrophilicity and hydrophobicity of cover substrate

Hydrophobicity was important to prevent the gel from polymerising on the cover substrate instead. Although fluorinated ethylene propylene (FEP), polytetrafluoroethylene (PTFE) (more widely known as Teflon^{TM}) and polydimethylsiloxane (PDMS) are more hydrophobic than COC, they are gas-permeable compounds. Oxygen (O_2) could diffuse through the substrates, inhibiting the free radical polymerization reaction.

5.1.4.3 Difference between both sides of injection moulded COC

COC was injection-moulded into disc-form at SIMTech and possessed a slightly different surface profile on either side. Each side of the diced COC exhibited a different Newton ring pattern when placed on a glass substrate (as shown in Appendix R-1(c)) The photopolymerised gels using the 2 different sides sometimes produced gels with significantly disparate gel dimensions, as illustrated in Appendix R-2(b).

5.1.5 Effect of varying DMPA:HQ ratio

By varying the free radical initiator to inhibitor (DMPA: HQ) ratio, it was conceivable that with a lower DMPA: HQ ratio, the reaction kinetics of polymerisation would be slower. Yet, even a 1:2 DMPA: HQ ratio did not improve the flatness ratio (FR) significantly. The difference in FR between a 2:1 and 10:1 ratio, reported in Appendix R-2(c), was not significant enough.

5.1.6 Effect of evaporation and solvent

Evaporation was thought to be a contributing factor in the gel profile as the isopropyl alcohol (IPA) solvent in the gel precursor solution was volatile, relative to DI water. During UV photo-polymerisation, the evaporating solvent could be introducing certain convection, which if encouraged, could promote mixing. However, when the much less volatile 1-butanol was utilised as the solvent instead, there was no significant and consistent improvement in the gel height variation.

The temperature of the gel precursor solution was also thought to have an effect on the gel height variation. Gel precursor solutions that were kept around 4°C (by storing the solution vial in an insulated foam container with ice) until just before photo-polymerisation also produced gels of similar non-ideal flatness ratios, although the gel diameters were notably smaller.

70% (v/v) ethanol (EtOH) was typically used as a disinfectant to kill bacteria, though it was utilised with great effect for appraising gel adhesion strength to the substrate due to its large expansion potential for a polyHEMA holosensor as illustrated in Figure 5-4. A 12 min 70% (v/v) EtOH immersion after photo-polymerisation was thought to not only verify the gel adhesion to its substrate in lieu of its expansion, it also dissolves the top gel layer which was newly formed (including the undesired built-up edges). The consequence to the 70% (v/v) EtOH immersion was trivial – the maximum diameter,

minimum gel height and maximum gel height decreased in about equal proportions, as shown in Appendix R-2(d).

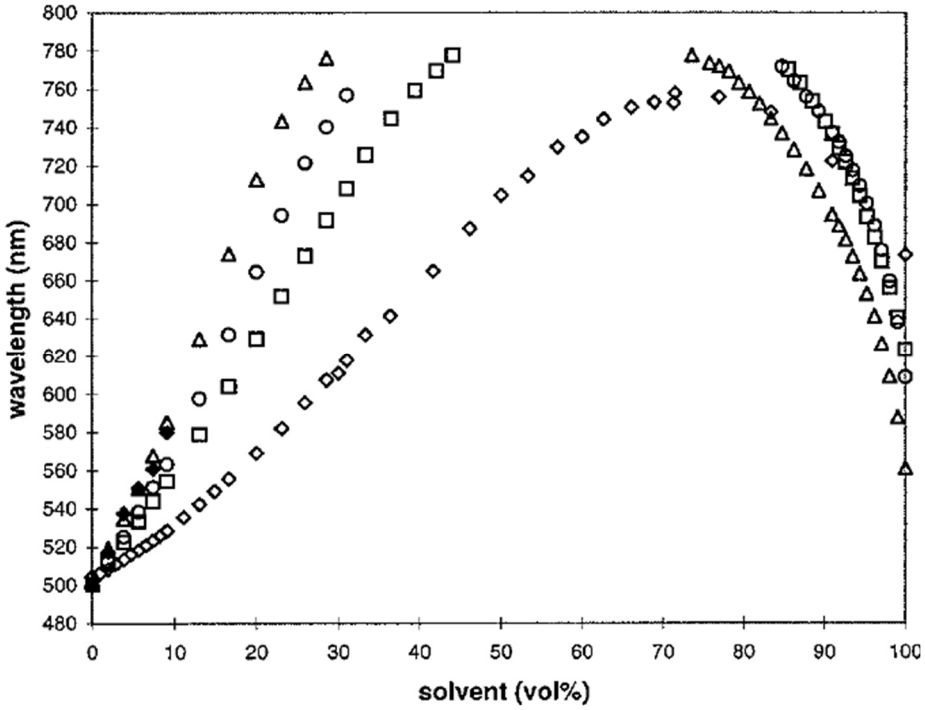

Figure 5-4: Swelling of a poly (HEMA) hologram containing 5% (w/w) EDMA as a function of alcohol concentration (vol%) for a range of different alcohols: methanol (◇), ethanol (□), propan-1-ol(Δ), propan-2-ol(○), and butan-1-ol (◆). Reprinted (adapted) with permission from ref. [92]. Copyright© 1999 American Chemical Society.

5.1.7 Effect of O_2 plasma treatment

The application of oxygen (O_2) plasma creates hydrophilic groups on the plasma-treated surface. The increase in hydrophilicity could cause the diffusion kinetics to favour uniform polymerisation. Nevertheless, comparisons made between photo-polymerisation on a single plasma-treated surface, on both substrate surfaces and just the pristine surfaces, depicted in Appendix R-2(e) (with gel dimensional averages and standard deviations of three samples each) showed negligible effects on the flatness ratio of the polymerised gels.

5.1.8 Effect of extrinsic experimental factors

5.1.8.1 Solvent overflow technique

A small reservoir of solvent outside the substrate interface was thought to continually wick the solution from between the interface during photo-polymerisation by capillary action, and minimise diffusion in the opposite direction into the UV transparent region of the photomask. Some

experimental techniques utilised to mitigate this potential occurrence were the lift-press technique, or the inside-edge vs over-edge techniques (described in Appendix R-1(a-b & e-f)).

5.1.8.2 Vibration length and frequencies

There was a possibility that long or short frequency mechanical vibrations could couple with the gel precursor solution to form turbulent eddies and encourage mixing to aid diffusion to all parts of the exposed region. A mobile phone vibration app was utilised to introduce vibrations of various length and frequencies during photo-polymerisation. Certain samples initially exhibited flat gel profiles, but after the same vibration frequency was reproduced and repeated more than 5X, it was found that it had little effect on the final profile of the gel.

5.1.8.3 N_2 purge and reverse-pipetting technique

Gel precursor solutions with different dissolved oxygen (O_2) contents would exhibit different polymerisation rates and chemistry. Additional inhibition by dissolved O_2, on top of the added hydroquinone (as the inhibitor) would result in more gel height variation due to an increased consumption of inhibitor under the illuminated regions and less polymerisation. Once the monomers were fully consumed, any additional polymerisation could only arise from the non-illuminated regions. The newly formed monomer radical would not survive long enough to diffuse to the middle of the illuminated region and would thus build up at the edges.

Consequently, N_2 purge (bubbling of N_2 through the solution to displace any dissolved oxygen) was performed into the solution for 5 min prior to photo-polymerisation. The reverse-pipetting technique was also utilised to aspirate and dispense the purged solution to avoid inadvertently introducing air (and O_2) into the solution.

Some of the extrinsic factors mentioned appeared to have an effect on the flatness ratio, with some of the FR significantly dropping to the teens (in %) from its typical 40%. Further tests later showed that the occurrence of the low FR anomalies were predominantly caused by a separate coincidental phenomenon.

5.1.9 Flat profile (FR) anomaly

During the evaluation of the aforementioned extrinsic parameters, a few disparate gel profiles emerged. The top surface of these gel anomalies were unusually flat, and the gel diameters were notably larger compared to others which were fabricated with the same experimental parameters, as illustrated in Figure 5-5(a).

Comparing the average gel dimensions for the six typical samples (#1, #2, #5 - #8 of Figure 5-5(b)) to that of the two samples (#3F and #4F of Figure 5-5(b)) exhibiting the flat profiles, the flatness ratio (FR) was substantially different. Taking into account all the experimental conditions that were kept constant, the flat profile anomaly should not have occurred. The only explanation left was that, one or more of the experimental conditions were changing but had gone unnoticed.

Additional gels were photopolymerised with the same parameters, which incidentally produced more gels with flat profiles. Sometimes, all 10 samples in a single run had flat gel profiles, while other runs had gels with FRs that were “in between”. These gels mostly had flat tops with steeper corners, and were allocated the term “transition gels”.

During that period, the COC cover substrates were cut with different methods, namely, (1) laser-cut, (2) milled, (3) cut with scissors, (4) snapped off with a hot sharp metal press and (5) diced. The quality of the cut edges and waviness of the substrate varied quite a bit. Consequently, the surface roughness of these different substrates were studied with the white light profiler.

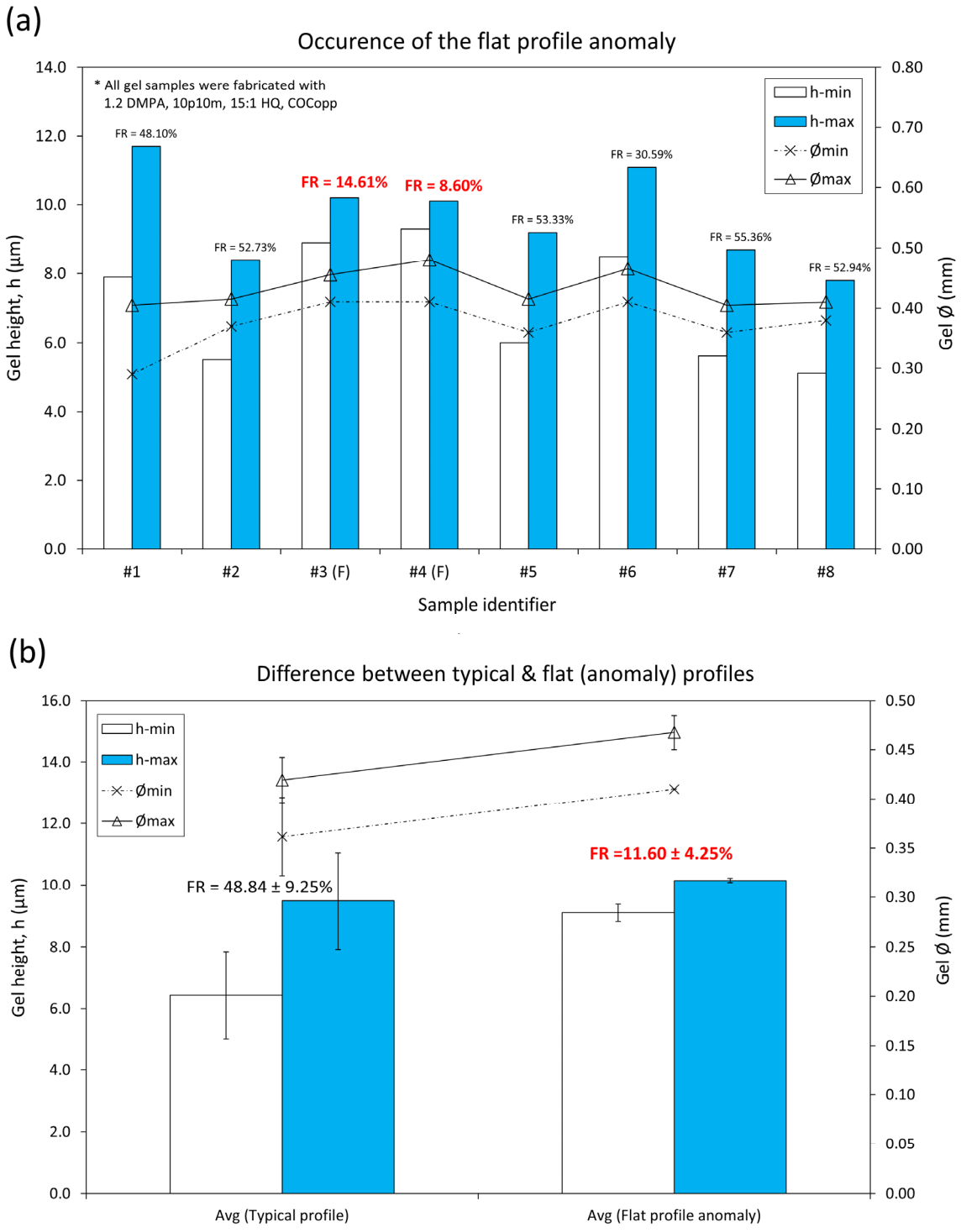

Figure 5-5: Emergence of the flat profile anomaly. ***(a)*** *2 out of 8 gels fabricated with the same parameters exhibiting unusually low flatness ratio (FR).* ***(b)*** *Average dimensions (6 samples) of the typical gel profiles compared to the average (2 samples) of the flat gel anomaly. The fabrication recipe was 8DH-2 (8 mmol total gel constituents in 1 mL IPA), 6D4E (6 mol% DMAEM & 4 mol% EDMA), 1.2DMPA (0.08484 mmol DMPA), 15:1 HQ (0.00471 mmol HQ), 10p10m (18.79 mW/cm2 UV@ 365 nm for 10 mins), COCopp, 3 µL*

5.2 Surface roughness

Surface roughness is a measure of periodic or random deviations from a nominal surface which forms its three dimensional topographical profile [159]. It consists of high frequency micro/nano-scale roughness, medium frequency waviness (macro roughness) and low frequency form (general shape). The different frequencies can be measured separately by using cut-off filters to reduce the amplitude of the other frequencies. Roughness is denoted as **R** and waviness is designated **W**.

5.2.1 Roughness and waviness parameters

Several roughness parameters can be used to characterise the high frequency variations. The most commonly used roughness parameter is the arithmetical mean roughness, or R_a. It is the arithmetic average deviation from the mean line. R_q, the geometric mean roughness, is the root mean square (rms) value of roughness. It takes into account the occasional spikes or troughs more than R_a, which only calculates the average. R_t is the sum total of the maximum peak (R_p) and maximum (R_v) of the roughness, and R_z is the ten-point mean roughness by calculating the average height difference between the five highest peaks and five lowest valleys of roughness. R_t and R_z are thus more relevant when the entire range of variations is required for analysis. These measurements are calculated within the assessment length (L_a) which is what is left for analysis after filtering. The medium frequency (waviness) parameters are simply denoted with **W** in place of **R**. Appendix S-1 illustrates the profile and equations for the aforementioned roughness parameters.

5.2.2 Cut-off wavelength, λ_c (ISO 4288-1996)

To separate the medium frequency variations (waviness) from the high frequency variations (roughness), filter cut-offs with a cut-off wavelength (λ_c) were utilised. It was chosen based on the characteristics of the surface to be analysed. For standardisation, the cut-off wavelength (λ_c) was chosen based on the internationally recognised ISO 4288-1996 standard (table shown in Appendix S-2(b)). This standard also recommended the evaluation length (L_e) required for a true representation of the measured roughness.

For devices smaller than the recommended evaluation length (L_e), cut-off wavelength (λ_c) had to be determined using a different method. The evaluation length (L_e) was typically divided into equal sample lengths (L_s) for roughness measurements. At least five of these sample lengths, each of which was equal to the chosen cut-off wavelength (λ_c), were required for good statistical analysis. The maximum (upper limit) chosen cut-off wavelength (λ_c) would therefore be one-fifth of the evaluation length (L_e). The lower limit for cut-off wavelength (λ_c) was determined by observing the resulting profile reported by the white light profiler and identifying the corresponding cut-off wavelength (λ_c)

where the roughness profile started to appear on the waviness profile, which would indicate the point of inadequacy with regard to the chosen λ_c.

5.2.2.1 Determination of cut-off wavelength for < 0.4 mm evaluation length

As an example, the long and short pass Gaussian regression filters at various cut-off wavelengths (λ_c) were utilised and examined to determine the cut-off wavelength (λ_c) for a 0.4ϕ HEMA-co-DMAEM gel. Table 5-1 illustrates the R_a readings for the short pass filter corresponding to the various λ_c.

To take away any edge effects, only the central two-thirds (67%) of the 0.4 mm gel diameter was assigned as the evaluation length by applying a digital mask. The upper limit of λ_c, as earlier discussed, was thus 0.05 mm. As shown in Appendix T, the roughness profile was observed starting to appear on the long pass filtered profile at 0.03 mm, and therefore set as the lower limit. A collation of 3D digital elevation models with their corresponding cross-sectional profile at the edges of the evaluation length was shown in Appendix T.

Table 5-1: Determination of cut-off wavelength below 0.4 mm evaluation length

Cut-off λ_c (mm)	R_a (nm)	
0.01	9	
0.02	14	
0.025	16	
0.03	18	Lower limit (Obtained from appearance of high frequency roughness in form)
0.035	19	
0.04	20	Chosen median cut-off value
0.045	21	
0.05	22	
0.06	30	Upper limit (⅕th evaluation length) $(0.67 \times 0.4) \times \frac{1}{5} = 0.0536$
0.07	48	
0.08	84	

The chosen cut-off wavelength (λ_c) was the median value between the upper and lower limits. It is important to note that the variation of R_a readings also narrowed within the identified limits. This showed convergence towards the chosen cut-off wavelength (λ_c) value. Taking these limits as the uncertainty, the uncertainty for the R_a measurements would therefore be ± 2 nm (difference of 2 nm if the upper or lower limits were chosen instead). A simple gauge for a representative cut-off wavelength (λ_c) would be 1/10th of the gel diameter. For a more representative R_a, this procedure can be followed to determine the cut-off wavelength (λ_c) and its associated accuracy.

5.3 Cover substrate surface texture analysis

The arithmetical mean roughness (R_a), geometric mean or root mean square (rms) roughness (R_q), ten-point mean roughness (R_z) and R_t (sum total of the maximum peak (R_p) and maximum valley (R_v) measurements of the roughness) of the cover substrates were measured and scrutinised to detect a pattern for successful flat gel profile fabrication. It was found that R_q and W_q were the parameters that most accurately predicted which cover substrate would reproduce the flat gel anomaly. Both sides of the cover substrate were interrogated with the white light profiler, with chosen cut-off wavelengths (λ_c) specified by ISO 4288-1996 (Appendix S-2(b)). The relevant results for selected representative cover substrates were summarised in Figure 5-6. Data points joined by a line in Figure 5-6(a) indicated the same tested substrate.

Initially, it was thought that only the waviness parameter (W_q) was important, and that substrates had to be as flat as possible. In other words, W_q had to be below a certain threshold value (1.5 μm). Surprisingly, when a few commercially (comm) purchased single-crystal quartz substrates were tested and verified for their role in producing a flat gel profile, none of the gels had flat profiles. It turned out that R_q values also had to be above a certain support threshold (62 nm) for the anomaly to happen.

Whether the COC cover substrate was milled or diced, the dimensions of the substrate seemed to matter. Larger samples tended to have a higher W_q, regardless the symmetry of the cut substrate. Other methods of cutting the substrates (such as laser cut and heat-press-cut) were left out of this analysis as they were too warped (possessed high W_q).

Engineered diffusers were also utilised above a quartz cover substrate to introduce some UV scattering, with the expectation that the higher R_q promoted scattering that should result in the flat gel profile anomaly. No such flat gel profiles were produced this way.

Another requirement was a definite substrate form (or cross-sectional shape). Sample #3 exhibited a profile that was a mix of the convex (CX) and concave (CV) form, reported as “undetermined” in Figure 5-6(b), and could not produce gels with flat profiles.

The substrates that satisfied these criteria could only be reused until a certain point. Sample #10 was an example that “expired”. Hence, another criterion was required – for which the difference between R_q for both sides of the substrate should not exceed 12 nm.

5.3.1 Flat gel profile anomaly criteria

To sum up, for the production of flat gel profiles:

(1) W_q of both sides had to be < 1.5 µm

(2) R_q of both sides had to be > 62 nm

(3) R_q difference of both sides < 12 nm

(4) Substrate form must be definite – either curved upwards (concave) or downwards (convex)

(a)

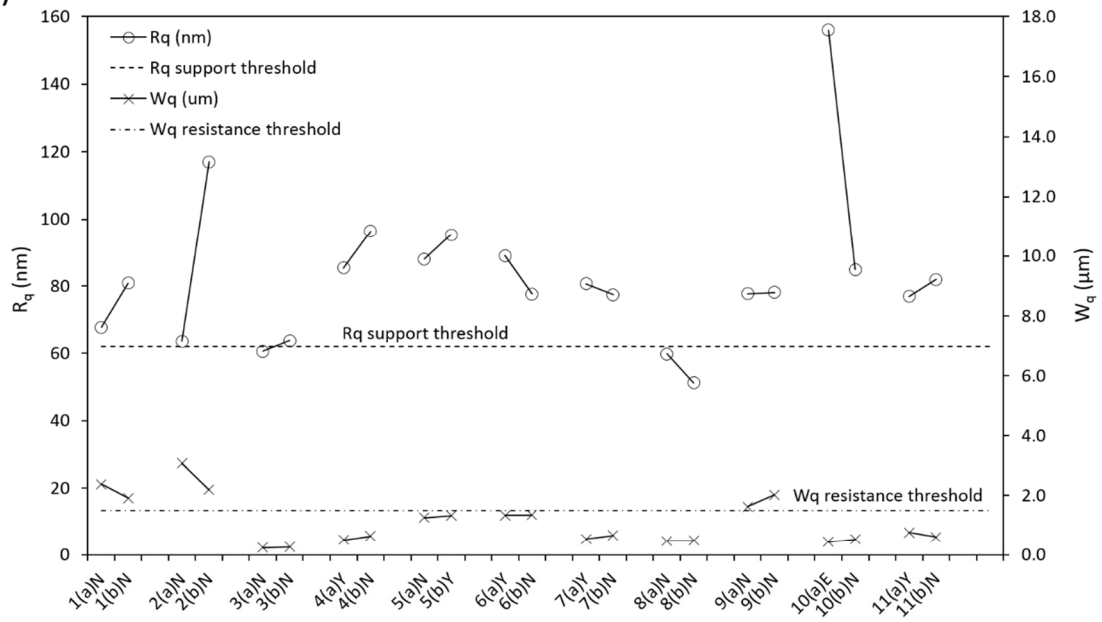

(b)

	Substrate identifier	Side	Size	Method	Form Shape	Flatness Outcome
1 (a)	COC	opp	16x11	milled	CV	N
1 (b)		ww			CX	
2 (a)	COC	opp	16x11	diced	CV	N
2 (b)		ww			CX	
3 (a)	COC-2	opp	8x8	diced	undet.	N
3 (b)		ww			CV	
4 (a)	COC-4	opp	8x8	diced	CX	Y
4 (b)		ww			CV	N
5 (a)	COC	opp	10x8	milled	CX	N
5 (b)		ww			CX	Y
6 (a)	COC-1	opp	10x8	milled	CV	Y
6 (b)		ww			CX	N
7 (a)	COC-5	opp	8x8	diced	CX	Y
7 (b)		ww			CV	N
8 (a)	Quartz	a	8x8	comm	undet.	N
8 (b)		b			undet.	
9 (a)	COC	opp	14x14	diced	CV	N
9 (b)		ww				
10 (a)	COC-12	opp	8x8	diced	CX	E
10 (b)		ww			CV	N
11 (a)	COC-2a	opp	8x8	diced	CV	Y
11 (b)		ww			CX	N

(c)

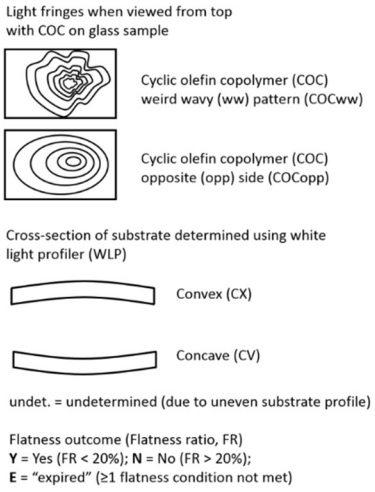

Figure 5-6: COC cover substrate information. ***(a)*** *Graph of R_q and W_q plotted against substrate identifiers depicted with R_q support threshold line and W_q resistance threshold line. Both sides of the substrate had to be below the W_q resistance threshold and above the R_q support threshold in order to generate flat gel profiles.* ***(b)*** *Table summarising the identification of the various substrates, which side was utilised, their sizes, method of cutting, form (or shape) of the substrate and whether or not it resulted in a flat gel profile.* ***(c)*** *Pictorial representation of fringes and substrate form.*

5.4 Types of gel profiles

During the flat profile exploration period, 241 0.4ϕ HEMA-co-DMAEM gels were fabricated, while 119 0.4ϕ HEMA-co-DMAEM gels were produced after the flat gel profile anomaly criteria was discovered. Figure 5-7 shows the probabilities of obtaining various types of gel profiles during the first exploration phase, and the numbers in brackets showed the probabilities after the surface texture of the cover substrates was linked to the formation of these flat gel profiles. There was a 3-fold increase in the likelihood of obtaining the flat gel profiles. The numbers would have been even better if not for the expendability of the cover substrate in terms of producing the flat profile.

Suitably, six different recipes with different DMPA mol% were optimised; the corresponding fabricated flat gel profiles were illustrated in Appendix U.

Most of the flat gel profiles had a flatness ratio (FR) smaller than 20%. The "transition" profile would also be flat if the edges were ignored. As a general guideline, gel height variations ($h_{max} - h_{min}$) smaller than 3 μm typically possessed a low FR, while transition profiles had gel height variations ranging from about 3 to 4 μm.

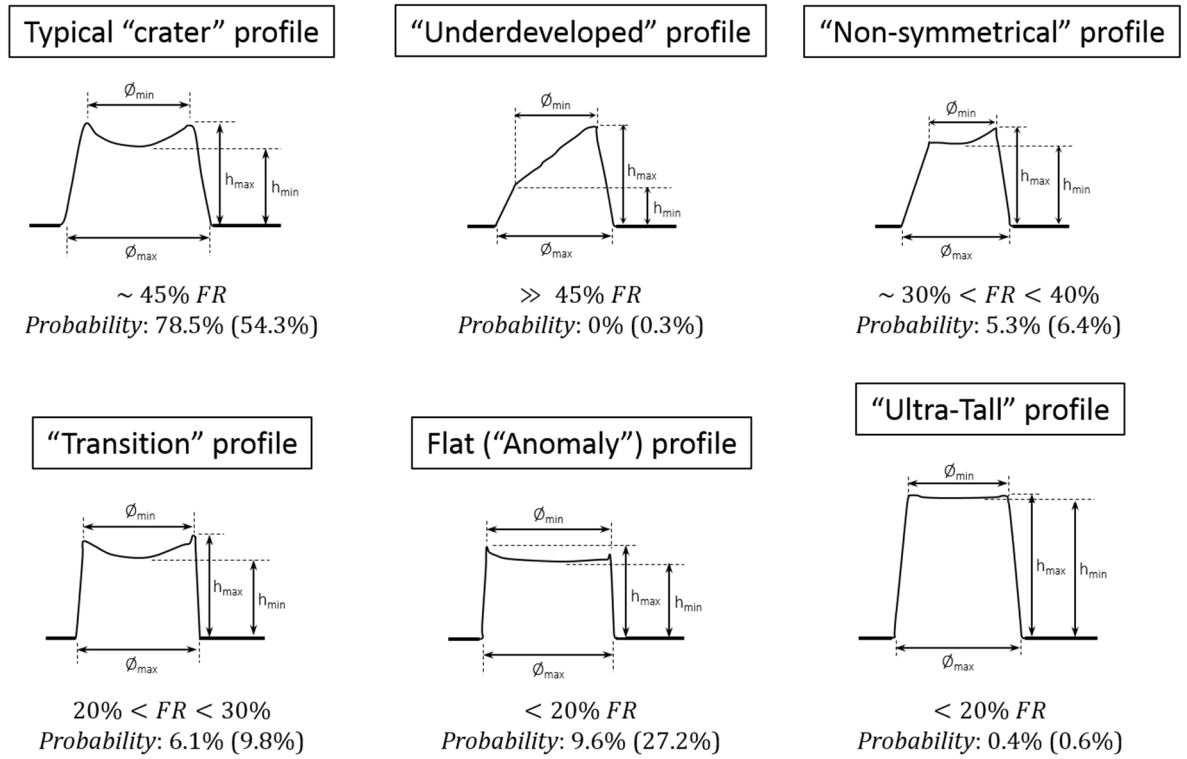

** Probabilities were tabulated in 2 distinct phases – exploration phase, and (in brackets) flat profile correlation confirmation phase*

Figure 5-7: Schematic diagram for the different types of gel profiles.

5.4.1 HEMA-co-DMAEM gel nano-indentation

Nano-indentation was performed on the gel surface for the 3.0ϕ and 0.4ϕ DMAEM gels. The purpose of nano-indentation was to find out the difference in reduced modulus (or elasticity) across the gel diameter. Typically, a force 15 mN was applied to travel 1000 nm with a loading/unloading rate of 0.25 mN/s.

Nano-indentation, a destructive testing method that utilises a hard tip with mechanical properties that are known, to penetrate the specimen until a specified value (1000 nm). The load was held for 60s and the area of the residual indentation was measured to determine hardness, where hardness $= \frac{P_{max}}{A_r}$. P_{max} was the maximum load and the residual indentation area A_r. The slope of the unloading curve, $\frac{dP}{dh}$, was determined to obtain the stiffness value. The reduced modulus, E_r, was then calculated with Equation 5.2 in Figure 5-8(b).

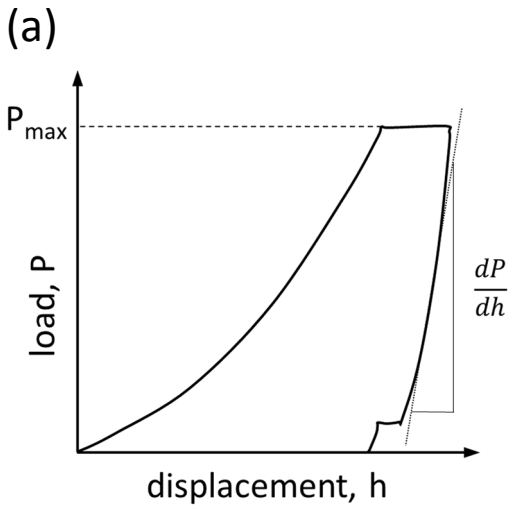

$$E_r = \sqrt{\frac{\pi}{4A}}\left(\frac{dp}{dh}\right) \qquad (5.2)$$

- E_r is the reduced (elastic) modulus
- $\left(\frac{dp}{dh}\right)$ is the tangent stiffness, viz. the slope of the P-h graph
- A is projected contact area

Figure 5-8: Determination of hardness and reduced modulus.

5.4.1.1.1 3.0ϕ HEMA-co-DMAEM gels

Comparing three samples of 3.0ϕ HEMA-co-DMAEM gel nano-indentation runs, there were slight variations in the reduced modulus, 5.20 ± 0.74 GPa (average ± 1 s.d.), though with negligible differences for their hardness, 0.12 ± 0.01 GPa (Appendix V-1(a)). From Appendix V-1(c), it was noticed that the overdeveloped region of the 3.0ϕ gel a_10p8m had a consistently higher reduced modulus, 4.06 ± 1.06 GPa, compared to the gel bulk, which was 2.59 ± 0.10 GPa. The right edge of 3.0ϕ gel b_5p6m had a reading that was far off (5.24 GPa), as compared to the rest of the gel, 4.51 ± 0.41 GPa (average ± 1 s.d.), indicating a difference in cross-linking. Yet, another 3.0ϕ gel c_2p6m exhibited no significant difference with its reduced modulus across the gel, 3.34 ± 0.17 GPa. The better gel

uniformity could be due to the lower power of 4.03 mW/cm^2 for Gel c compared to 9.55 mW/cm^2 for Gel b.

5.4.1.1.2 0.4ϕ HEMA-co-DMAEM gels

0.4ϕ gels fabricated from different mol% DMPA concentrations (Appendix V-2) were a lot more consistent in terms of reduced moduli compared to that of the 3.0ϕ gels, even though the DMPA concentration, UV power and exposure durations between the 0.4ϕ samples differed significantly. The three tested 0.4ϕ samples had reduced moduli of 3.94 ± 0.14 GPa, 3.80 ± 0.04 GPa and 3.68 ± 0.12 GPa – with an overall average of 3.81 ± 0.15 GPa.

From these preliminary results, it was suggested that 0.4ϕ gels were more robust to fabricate, and were less prone to gel non-uniformity.

5.5 Miniaturised 0.4ϕ HEMA-co-DMAEM holosensor

A hologram was fabricated with one of the 0.4ϕ HEMA-co-DMAEM gels that appeared flat but had a FR of 36.7% because of its steep edges. This DMAEM holosensor was unique in the sense that only 0.5 mol% EDMA crosslinker was utilised (typically 4 mol% EDMA). The purpose was to enable the hologram to display blue all the way to red across the evaluating pH range of pH 3.5 to 8.5.

It was worth highlighting that the hologram fabrication parameters were also different. This was the only 0.4ϕ HEMA-co-DMAEM gel that displayed a hologram after being exposed to 8.645 mW, or 5.5 mW/cm^2 (typically 0.290 mW) of the 532 nm CW laser. Figure 5-9 illustrates the digital elevation models, cross-sectional profiles, schematic gel diagram and high-resolution hologram picture of the 0.4ϕ HEMA-co-EDMA (0.5 mol%)-co-DMAEM (6 mol%) holosensor.

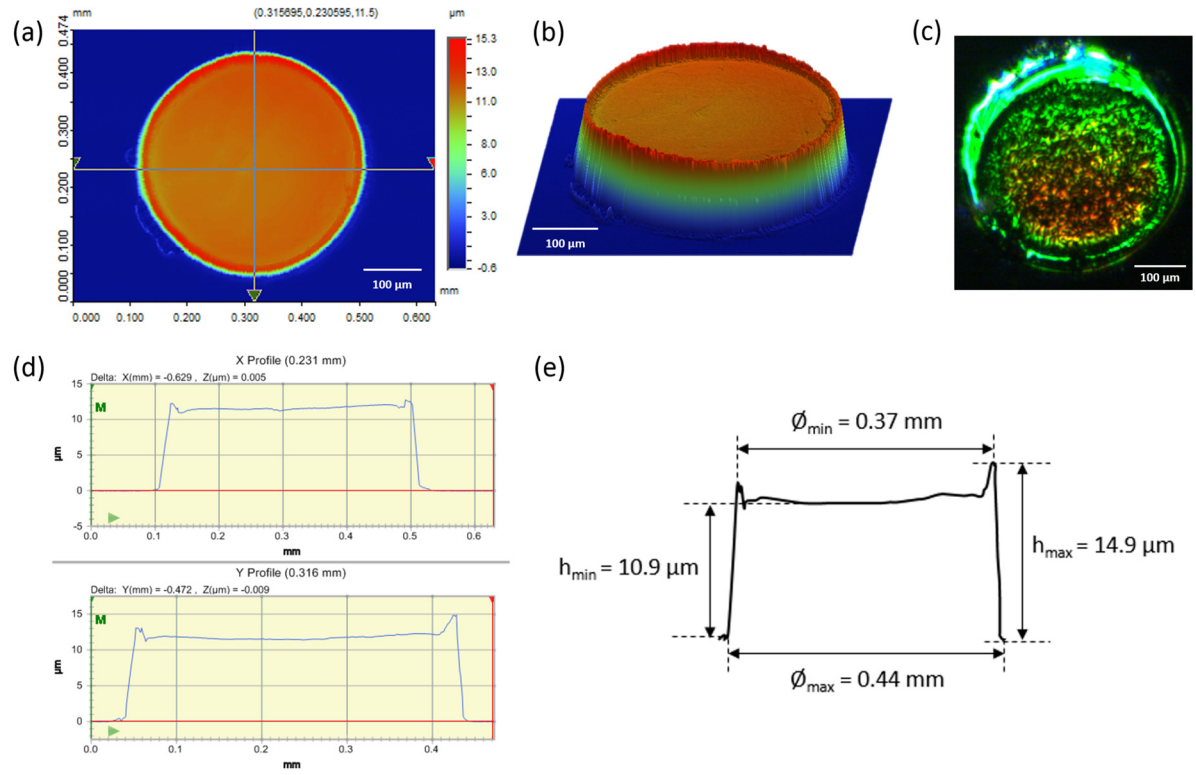

Figure 5-9: Collation of 0.4ϕ HEMA-co-DMAEM holosensor information. ***(a & b)*** *2D and 3D digital elevation model of the chosen 0.4ϕ HEMA-co-DMAEM holosensor recorded after hologram fabrication respectively.* ***(c)*** *Picture of the hologram taken by the high-resolution camera at 36X magnification while the 0.4ϕ microfluidic chip embedded holosensor on PC was immersed in pH 6.0 McIlvaine buffer.* ***(d)*** *Cross-sectional x and y profile of the 0.4ϕ holosensor on PC along the crosshair depicted on the 2D digital elevation model.* ***(e)*** *Picture of the LED illuminated hologram taken by a Samsung S7 mobile phone with pH 6.0 McIlvaine buffer inside the microfluidic chip.* ***(f)*** *Reproduced y profile of the 0.4ϕ gel with measured white light profiler data.*

It was observed that this holosensor did not exhibit any concentric ring patterns. Taking into account that most of the DMAEM gels did not display any holograms, this particular hologram could be one recorded by the interference of scattered laser light. A flatter gel profile could be the reason for the absence of the concentric ring pattern. Further work is required to arrive at a more definitive conclusion.

5.5.1 pH characterisation of 0.4ϕ HEMA-co-DMAEM holosensor

The 0.4ϕ HEMA-co-EDMA (0.5 mol%)-co-DMAEM (6 mol%) holosensor was characterised with ionic strength balanced (to 15 mS/cm) McIlvaine pH buffers from pH 3.5 to 8.5. Another light source, a 6500K LED (from Prizmatic) was utilised as a high-power alternative to the Xenon light source. The pH response (peak wavelength) of the DMAEM holosensor was normalised to the total intensity normalised value of the area under the curve (calculated using trapezium rule) for the spectral intensity distribution of the LED source.

The resulting spectrophotometric data, hologram pictures taken with a high-resolution industrial camera, and the associated CIExyY chromaticity diagram plot were illustrated in Figure 5-10.

It was noted that there was a +12 nm shift in the peak wavelength correction for the intensity normalisation for pH 7.5. Only further tests with more DMAEM holosensors would indicate if the correction was representative of the actual holosensor response, or that a more broadband light source such as the tungsten-halogen or Xenon lamp was a requirement for accurate characterisation and interrogation.

Similar to the TFMPA holosensors, after a certain extent of contraction, the blue colour of the holosensor started to fade as if the signal was moving out of the gel in a particular direction. This indicated a possible angular shift in the Ag^0 Bragg reflection plane. The gel itself could also have been expanded beyond its axis and only returned back when contracted. It was challenging to obtain a gel profile when it was immersed in a pH buffer because the average refractive index of the polyHEMA ($\eta_{HEMA} = 1.43$) gel matrix was close to that of water ($\eta_{water} = 1.33$). White light profiling and ellipsometry were not able to detect the gel expansion when hydrated.

RGB values extracted from the hologram pictures in Figure 5-10(b) were transformed to the xyY colour space (described in Appendix B) and plotted on the CIE 1931 chromaticity diagram. The pH change inscribed a path (or locus) in the diagram, which was indicative of a blue to green colorimetric shift.

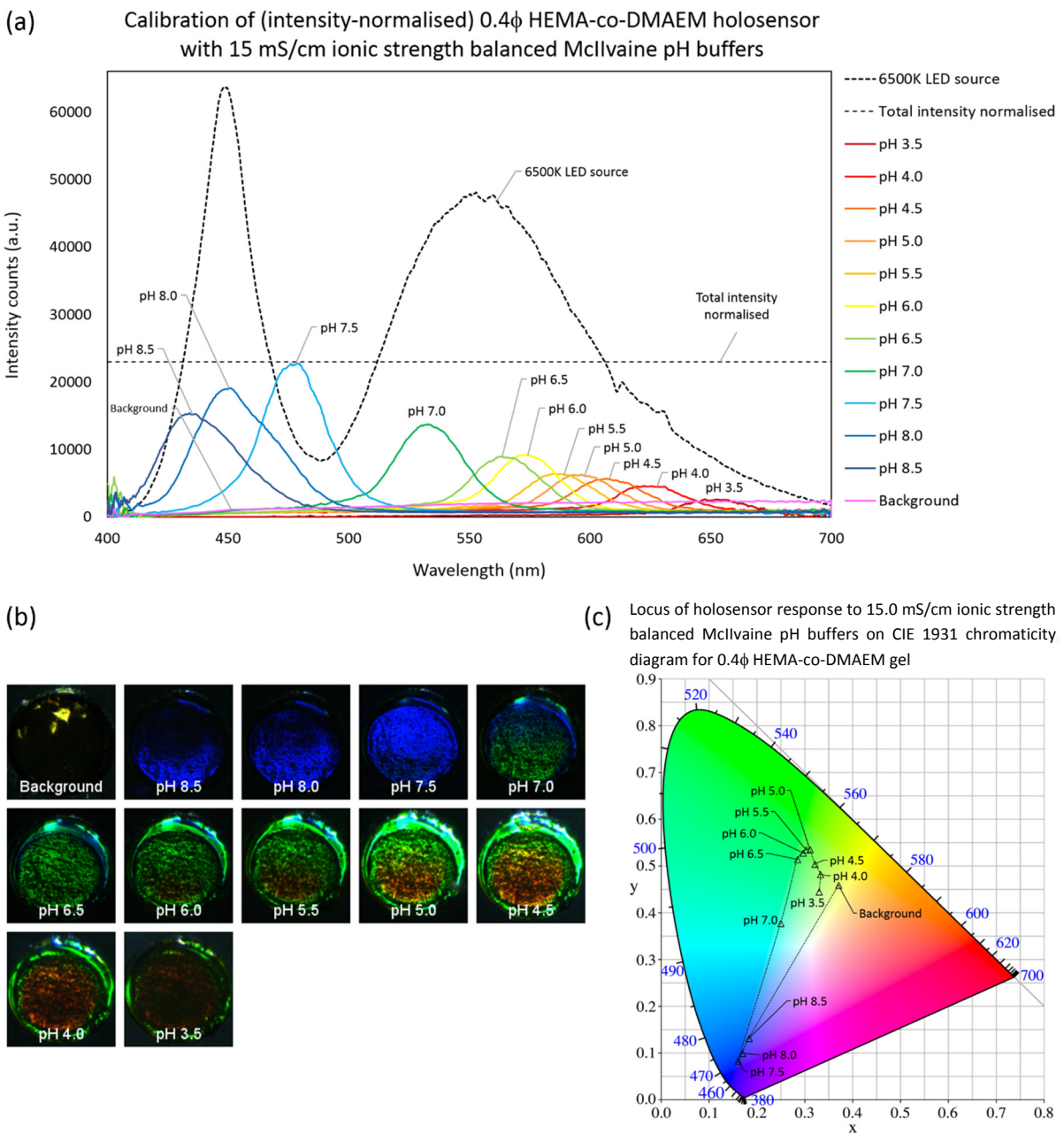

Figure 5-10: pH characterisation information of the 0.4ϕ HEMA-co-DMAEM holosensor. ***(a)*** *Total intensity-normalised peak wavelength holosensor pH responses obtained from pH 8.5 down to pH 3.5. The height of the peaks represents the corresponding spectral intensity recorded by the spectrophotometer. Note that the illumination source was a 6500K LED* ***(b)*** *Picture montage of holograms captured by the high-resolution camera at 36X magnification when immersed in correspondingly decreasing pH starting from pH 8.5 to pH 3.5 just before the spectrophotometric data of (a) was collected.* ***(c)*** *Visualisation of colour change with locus for holosensor response to McIlvaine pH buffers corresponding to the RGB-xyY transformed values from (b) plotted onto the CIE 1931 chromaticity diagram.*

5.5.2 Calibration curve for 0.4ϕ HEMA-co-DMAEM holosensor

The modified Henderson-Hasselbalch (H-H) curve for the basic DMAEM pH moiety was slightly different in that the gel contracted at high pH and expands at low pH, opposite to that of the acidic TFMPA pH moiety. The calibration curve was governed by Equation 5.3 (derived in Appendix I as I.25), while its derivative (Equation 5.4) was used to estimate the apparent pK_a (when pH = pK_a).

$$\lambda = \frac{\lambda_{max} + \lambda_{min} \cdot (10^{pH - pK_a})}{1 + 10^{pH - pK_a}} \tag{5.3}$$

$$\frac{d\lambda}{dpH} = (\lambda_{min} - \lambda_{max}) \left(\frac{\ln 10}{4}\right) \tag{5.4}$$

The pK_a and wavelength values (λ_{min} and λ_{max}) were then tweaked in steps of 0.05 pH units and 1 nm respectively to achieve the best fit to the data.

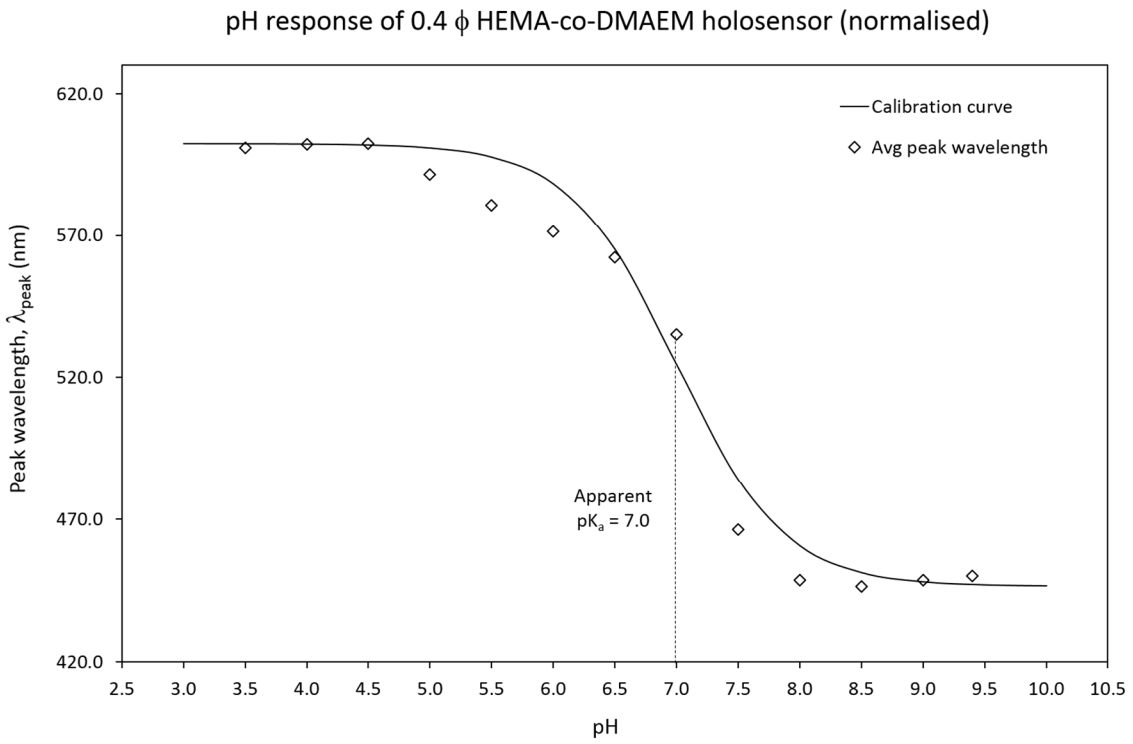

Figure 5-11: Modified Henderson-Hasselbalch (H-H) pH calibration curve for 0.4ϕ HEMA-co-DMAEM holosensor. The apparent pK_a of the holosensor was pH 7.0

There was no significant holosensor response (peak wavelength) with regard *to L. casei* growth as its pK_a with the ionic strength balanced pH buffer, and maximum buffering capacity of DMAEM (pH 7.0 ± 2.0) was too far from the pH growth range of *L. casei*. Regardless, it would be useful for monitoring mammalian cells, which grow around pH 7.0 – 7.5, the optimal range for this DMAEM holosensor.

5.6 Miniaturised 0.4ϕ HEMA-co-TFMPA holosensor on PC

Polycarbonate (PC) is one of the engineering polymers, which is widely used as a substrate for microfluidic chips due to its low cost, high optical transparency, high glass transition temperature (suitable for DNA processing), and ease of fabrication. It is however, a challenge to use PC as the alternative substrate to glass for the polyHEMA holosensors due to its chemical incompatibility to polyHEMA and PDMS. Even with oxygen plasma treatment, which renders the surface hydrophilic, PC does not readily bond with polyHEMA or PDMS.

5.6.1 Adhesion of gel to PC substrate

Acrylate crosslinkers were thought to be the solution for this problem due to their reactivity and quick UV–activated polymerisation. The concept was to use crosslinkers as the intermediate interlinking layer.

The crosslinker was made to adsorb on the activated (via UV@254 nm for 15 min or oxygen plasma treated) PC surface for 5 min. N_2 was then utilised to spread the adsorbed crosslinker. The gel precursor solution was then dispensed on the flattened adsorbed crosslinker layer. With the photomask, only the UV-transparent regions will activate the adsorbed crosslinker to react and slightly dissolve the top surface of PC to bond covalently the methacrylate groups onto the acrylate crosslinker. The adsorbed crosslinkers at the non UV-irradiated regions will be easily dissolved with IPA and washed away, leaving the polyHEMA gel connected to the PC surface via the multi-acrylate groups of the crosslinker.

Most acrylate crosslinkers can quickly dissolve or react with polymers, even without the proposed mechanism. A series of acrylate and methacrylate crosslinkers were tested for their reactivity (as described in Table 5-2) with the PC surface; the ones that do not after 5 min would be tested. After that, the gel precursor solution (co-TFMPA, co-DMAEM and co-MAA were tested) was photo-polymerised and the polyHEMA gel immersed in 70% (v/v) EtOH for 12 min to test PC-polyHEMA adhesion quality. The three crosslinkers that worked well with no notable issues were DPEPHA, PETA and PETTA (see Table 5-2).

Optical transparency was critical for the holosensor; those that cause cloudiness, even if only slightly, would greatly hamper the quality of the hologram. The cloudy regions would act as scattering centres and disrupt interference.

It was observed that PC-PDMS and PC-polyHEMA bonding was of better quality when 0.60 mm thick injection moulded PC was used compared to that of the 1 mm thick cast PC sheets. This could be due to the lower surface roughness of injection-moulded PC that promoted bonding.

Table 5-2: List of tested crosslinkers depicted with their chemical structures and reaction with PC surfaces

Acronym	Chemical	Chemical structure	Observations
DMAEA	2-(Dimethylamino)ethyl acrylate	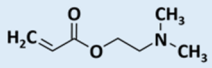	Turned cloudy quickly
DPEPHA	Dipentaerythritol penta-/hexa-acrylate	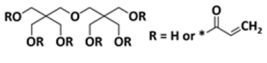	No issues
EDMA	ethylene glycol dimethacrylate	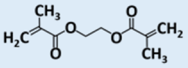	Turned cloudy after 1 min
GDMA	glycerol dimethacryate	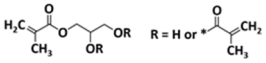	Not cloudy, but failed 70% EtOH immersion
PEA	2-phenoxyethyl acrylate (Ethylene glycol phenyl ether acrylate)	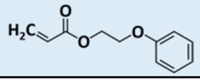	Became spotty after adding gel precursor solution
PEGDA	Poly(ethylene glycol) diacrylate, Mn 250	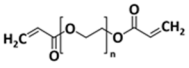	Turned a little cloudy after 15 mins
PEGPEA	poly(ethylene glycol) phenyl ether acrylate (average Mn ~ 324)	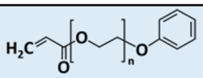	Turned cloudy after adding gel precursor solution
PETA	Pentaerythritol triacrylate	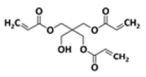	No issues
PETTA	Pentaerythritol tetraacrylate	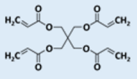	No issues
Silane A174	3-(Trimethoxysilyl) propylmethacrylate (TMPMA)	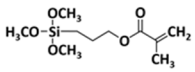	Turned cloudy after 1 min
tBAEM	2-(tert-butylamino)ethyl methacrylate	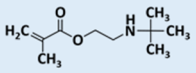	Became very slightly cloudy
TTEGDA	Tetra(ethylene glycol) diacrylate	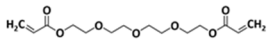	Became lightly and evenly cloudy

5.6.2 Adhesion of PC to PDMS

Sunkara *et al.* [127] introduced a method suitable for large area at room temperature for PC-PDMS bonding. This highly effective method was adapted for the bonding of PC-PDMS. It involved treating both the PC and PDMS surfaces with 60W oxygen plasma for 60s at 50 sccm flowrate and 2 x 10^{-1} Torr (recipe #8 of Table 2-1). The substrates were then immersed in 1% aq. v/v APTES (plasma-treated side up) for 20 min. Both the substrates were then carefully taken out, dried with N_2 gun and placed back into the plasma machine for the same plasma treatment. The two surfaces were then brought together and carefully pressed. Force was prudently applied to prevent the middle portion of the microfluidic chamber on the PDMS from sagging and bonding with the glass, or worse, with the holosensor itself.

5.6.3 Visualisation of the PC-embedded 0.4ϕ HEMA-co-TFMPA holosensor

The PC-embedded 0.4ϕ TFMPA holosensor was interrogated by the white light profiler, spectrophotometer and high-resolution industrial camera to provide the montage of 2D and 3D digital elevation models, cross-sectional profiles, schematic diagram and 36X magnified high-resolution picture of the hologram illustrated in Figure 5-12.

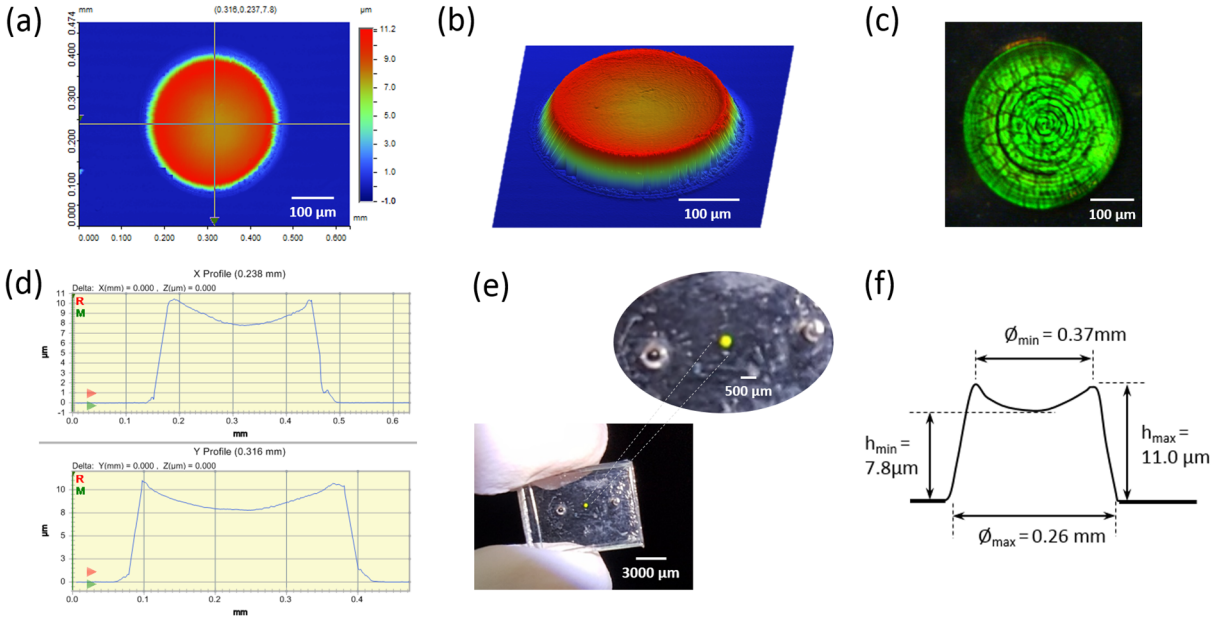

Figure 5-12: Collation of 0.4ϕ HEMA-co-TFMPA holosensor on PC substrate. ***(a & b)*** *2D and 3D digital elevation model of the chosen 0.4ϕ HEMA-co-TFMPA holosensor on PC substrate recorded after hologram fabrication respectively.* ***(c)*** *Picture of the hologram taken by the high-resolution camera at 36X magnification while the 0.4ϕ microfluidic chip embedded holosensor on PC was immersed in pH 6.0 McIlvaine buffer.* ***(d)*** *Cross-sectional x and y profile of the 0.4ϕ holosensor on PC along the crosshair depicted on the 2D digital elevation model.* ***(e)*** *Picture of the LED illuminated hologram taken by a Samsung S7 mobile phone with pH 6.0 McIlvaine buffer inside the microfluidic chip.* ***(f)*** *Reproduced y profile (schematic diagram) of the 0.4ϕ gel with measured white light profiler data.*

5.6.4 Utilising the PC-embedded 0.4ϕ HEMA-co-TFMPA holosensor

Initially, the PC-embedded holosensor was able to react to pH changes and expand or contract, as illustrated by a few screenshots of a video grab in Figure 5-13. Unfortunately, for unknown reasons, the holosensor stopped reacting to pH change after a few trials with the first run of the pH characterisation and remained bright green no matter the pH or even the addition of IPA, which should expand the polyHEMA itself due to its high alcohol affinity. Another observation was the background ring of blue (t=0 of Figure 5-13) that would not go away even when thoroughly rinsed with DI water, IPA and 70% (v/v) EtOH. Conceivably, the intermediate residual PETTA (crosslinker) layer could be causing these inconsistencies.

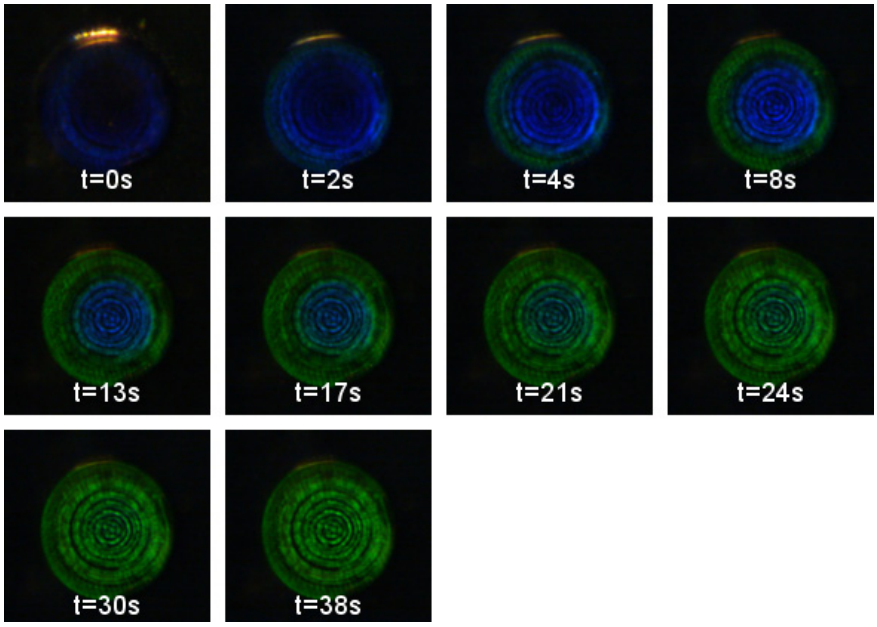

Figure 5-13: Video grab of 0.4ϕ HEMA-co-TFMPA holosensor on PC during gel expansion with pH 6.00 (9.50 mS/cm) McIlvaine buffer

Further work will be performed to investigate these strange occurrences, improve on the suggested method and justify its utility as a pH holosensor.

5.7 Violet laser for hologram fabrication

Silver nanoparticles (Ag NPs) absorb strongly between 400 – 500 nm. This absorption property can be exploited to fabricate a hologram without the need of dyes to absorb the 532 nm laser for hologram fabrication. The whole hologram fabrication procedure could then be performed with all the chemicals in aqueous solutions. This would also enable the tuning of holosensor colour at a particular analyte concentration. For instance, it could be utilised as an end-point colour for pH 3.0 so that the holosensor would replay in violet at pH 3.0 and red shift for acidic pH moieties. The problem of holosensors contracting beyond the visible spectrum could be resolved. Also, this method would eliminate the possibility of residual dyes (after hologram fabrication) affecting the holosensor by continually absorbing more green light and darken (printout), fog the hologram, and/or affect its diffraction efficiency.

Figure 5-14 illustrates a green laser exposed PDMS-masked HEMA-co-MAA gel and hologram compared to that of a hologram generated with a violet (411 nm) laser. The difficulty in visualising violet, especially when the hologram is small and dim, made it extremely challenging to reproduce. The gel had to be typically immersed in alcohol to replay in green. The violet laser absorption could have been overwhelming, which would have directly reduced the Ag^{+} to Ag^{0}, creating latent images regardless of interference and compromising the hologram fabrication process. Much work is still

required to make this work as a holosensor, though this did demonstrate the feasibility of producing a hologram without dyes.

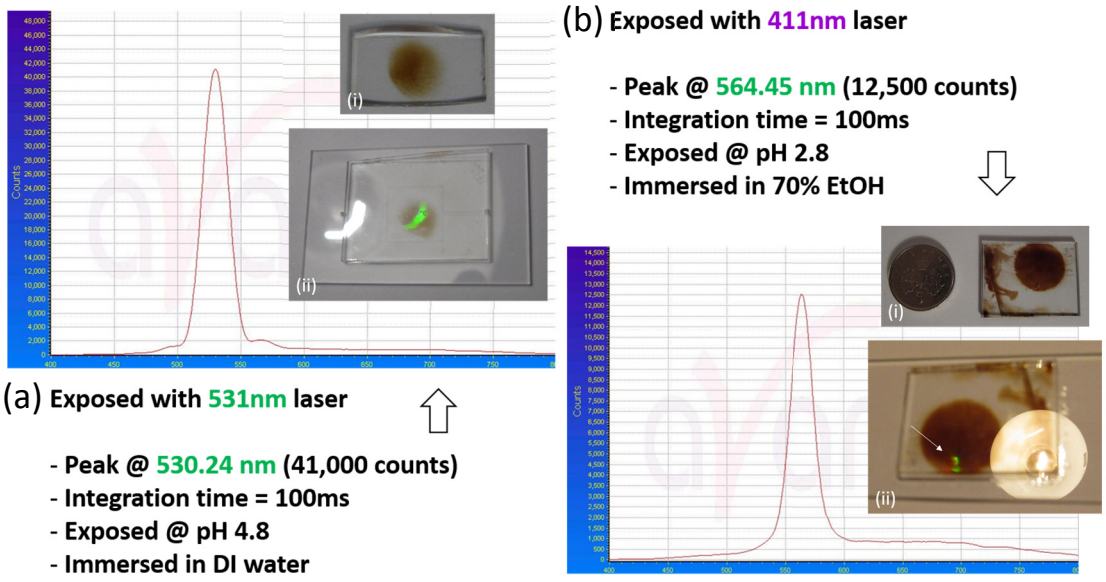

Figure 5-14: Spectrophotometric information with peak wavelength, intensity counts, integration time and laser exposure parameters for the samples exposed with the ***(a)*** *531 nm laser superimposed with (i) a picture of the gel and (ii) hologram, and* ***(b)*** *411 nm laser superimposed with (i) picture of the gel and (ii) hologram indicated by the white arrow.*

5.8 Outcomes

A flat gel profile fabrication method based on the surface texture of the cover substrate was explored and successfully implemented. The determination of cut-off wavelength for an evaluation length less than 0.4 mm was also analysed. Gel characterisation with a devised flatness ratio parameter was performed and appraised. A miniaturised 0.4ϕ DMAEM pH holosensor capable of exhibiting colours across the visible spectrum (blue to red) within its evaluation pH range (pH 3.5 – 8.5) was demonstrated. The modified H-H curve for the basic pH moiety DMAEM was presented. PC-embedded miniaturised 0.4ϕ TFMPA holosensor was introduced and integrated into a microfluidic system, and a dye-free hologram fabrication technique utilising a violet laser was discussed.

6 Chapter 6 Final Discussion

Understanding the growth mechanisms of microorganisms is critical in bioprocessing [160]. Used substantially in therapeutic protein production, the growth of animal cells and their expression of these proteins depends heavily on the extracellular environment [5]. Increasing the yield of such products requires bioprocesses to be optimised quickly and inexpensively with multiplexed capabilities [19], [161], [162]. Microbioreactor platforms integrated with highly sensitive detection systems to monitor key variables such as pH and biomass have been utilised to screen and optimise conditions for high-throughput processes [19]. However, with decreasing working volumes for monitoring smaller numbers of cells, monitoring the cellular environment and obtaining accurate process information becomes challenging [8]. Non-invasive optical techniques are preferred over electrochemical methods since they do not require electrical connections and electrodes that may be prone to biofouling and corrosion [54]. In addition, it is crucial that the sensor does not consume the analyte(s) it is measuring, especially when using a small volume to monitor cells for heterogeneity or single cell analysis. There is thus a technological need to gather as much information as possible for a cell residing in a small volume of media to establish accurately what goes on around a cell on a nanolitre scale.

6.1 Current bioreactor sensors

Currently, most pH, DO and biomass sensors utilised in microbioreactors rely on lifetime detection of fluorescence quenching [20], [32], [54], fluorescent dyes [20] such as phenol red [47], [54] and electrochemical sensors such as ion-selective field effect transistor (ISFET) sensors [39], [40], [55].

Fluorescent dyes, including the widely used phenol red as a pH indicator, can exhibit certain phototoxic or undesirable effects. For example, while the fluorescence signal gradually decreases with each light exposure, the free radicals generated during fluorophore photobleaching can result in adverse effects on live cells [56], [57]. Phenol red is a known weak estrogen [58], [59], which could also lead to detrimental, non-estrogenic effects [60]–[62] on cells. The difficulty in miniaturising electrochemical biosensors inexpensively and replicably [101] results in a bottleneck for the development of reliable miniaturised biosensors for nanobioreactors.

Commercialised systems utilise microtitre plates and miniaturised shake flasks with non-invasive sensors for the real-time monitoring of cell cultures. These systems typically miniaturise the existing 500 mL shake flasks to less than 10 mL, usually including options for running experiments in parallel, such as the Micro24 MicroReactor system from Pall Life Sciences, which is capable of aerobic and

anaerobic microbial fermentations (7 mL working volume) with independent control. Another single-use microbioreactor widely used by major pharmaceutical and biotech companies, academic and research institutes is the ambr® (Advanced Microscale Bioreactor System) cell culture system from The Automation Partnership (TAP). It utilises 24 disposable reactors with a 10 – 15 mL working volume each, for pH and DO measurement using patch sensors [5], [27]. A fully automated miniaturised bioreactor, SimCell™ (Seahorse Bioscience) [20] allows up to 1500 independently controlled cell cultivation devices, with reactor chambers each of 300 – 700 μL working volume. The lack of nanobiosensors in these commercialised systems also point to a limit to how small these microbioreactors can currently go, due to a lack of reliable sensors that can be used in small volumes.

In this respect, microfluidic systems offer an attractive solution for the miniaturisation of biological assays. Sample volumes can be reduced up to a million-fold, facilitating highly parallelised assays with drastically increased throughput and reduced cost [75]. Pharmaceutical and biotech industries are constantly pressured to reduce development costs and accelerate process development. Having a small scale system would enable multiple reactions to be run in parallel with automated sampling and, when integrated to purification, would provide significant improvement to developmental timelines [27]. The substantial reduction in the use of media in microfluidic systems contributes to the cost savings as well by reducing the cost and enabling multiple experiments to be conducted at the same time.

For small reaction volumes (in the μL range), the most widely used non-invasive sensors are the pH and DO sensor spots from PreSens Precision Sensing GmbH [14]. The sensors utilise a Dual Lifetime Referenced (DLR) method, which enables internally referenced measurements, and are typically small enough to be attached to the sides of shake flasks or microfluidic chips. Even so, the size of the PreSens sensor spot is 2 mm in diameter and a minimum of 150 μm in height, which translates to about 0.47 μL in sensor volume. Although there are smaller sensors, these are only for oxygen monitoring. Additionally, it is expensive to use these sensors, especially if the microfluidic chips are disposable.

6.2 Current holographic sensor technology

In our group, Lowe *et al.* (2004) hypothesised that 3 mm "spot" holographic sensors could be fabricated using a contact-printing process involving a hydrophobic FEP mask to inhibit polymerisation at the masked regions where it was oxygen-rich [163]. In 2007, Dobson fabricated flake holograms under 1 μL in volume [124], but only in suspensions or as random spots on a substrate. Bell utilised a tape mask to fabricate a spot holosensor of area about 1cm^2 (10 μL, 11.3 mm diameter, 100 μm height) and incorporated it into a microfluidic chip to monitor the growth of *Lactobacillus casei* [79].

A holographic sensor consists of a hologram recorded within the volume of a stimuli-responsive "smart hydrogel" (gel). The colour of the hologram changes according to the expansion (red shift) or contraction (blue shift) of the gel due to the change in spacing between reduced Ag^0 fringe planes formed during the hologram (recording) fabrication process. They have been utilised to detect analytes ranging from, but not limited to, pH [79] [80], ionic strength [81] and other biological metabolites and parameters, to water in solvents [91] and alcohol concentrations [92].

The most useful advantage of a holographic sensor is it operates by an equilibrative mechanism, i.e. does not consume the analyte it is measuring. Compared to other conventional analyte-measuring methods, the holographic sensor is the ideal candidate for miniaturisation. It is non-invasive, non-consumptive and inexpensive to fabricate.

The research work described in this thesis aimed to miniaturise the pH holographic sensor in a replicable manner, for application in a nanobioreactor. Two major challenges needed to be overcome in order to achieve the interrogation of a miniaturised holosensor in a microfluidic chip: (1) controlling the gel volume, and (2) maximising the holosensor signal-to-noise ratio.

6.3 Controlling the gel volume

Controlling the gel volume was important for the miniaturisation of the holosensor in view of the buffering capacity of the sensor itself. Although it is non-consumptive and does not use up the measured analyte, the equilibrative mechanism of the holosensor necessitated temporary "borrowing" of protons from the solutions to balance the charges within the gel. This is especially evident near the pK_a of the pendant ionisable functional group, where a small change in pH will result in a large change in charge for the pH moiety. The buffering capacity was calculated to be negligible as long as the embedded amount of pH-sensitive ligand (in mols) in the gel only took up a fraction (5%, or for even better accuracy, 1%) of the L-lactic acid production by *L. casei* within the microfluidic cell chamber. In the case of the reported work in this thesis, the utilised 75 μm height chamber and assumed 80 g/L acid production translated to a required minimum chamber diameter of 1.69 mm and 5.40 mm for the 0.4ϕ and 3.0ϕ holosensor respectively.

To control the gel volume, a quartz-chrome photomask was utilised together with the addition of a polymerisation inhibitor, hydroquinone, in the gel precursor solution to achieve a photo-polymerised pattern with excellent mask fidelity. The method adapted from photolithography provided tight tolerances and fabrication robustness for the 3.0ϕ spot, 0.4ϕ spot and 0.4ϕ array, as demonstrated in §3.2, §4.2.3 and §4.13 respectively. It was noted that in 2014, Park *et al.* demonstrated a similar method for producing microgels, albeit for a different type of gel (poly-N-isopropylacrylamide (pNIPAAM)) [133].

The research work described in this thesis went a step further to control the flatness of the gel as well. According to the literature, no work has yet been done to investigate and fabricate a hydrogel with a flat top, likely due to a lack of applications requiring this specification. Almost all photo-polymerised gels form with a "bat-wing profile", especially when high UV power was utilised for rapid gel polymerisation. Even with uniform UV intensities, the gel was formed with the characteristic bat-wing shape. Accordingly, a flatness requirement was defined and many parameters studied to attain the desired profile. It was thought that a flat profile would minimise the chances of obtaining polychromatic holograms resulting from a difference in diffraction efficiency of fringes at the centre compared to the edge of the gel. A roughness and waviness requirement for an injection-moulded cyclic olefin copolymer (COC) cover substrate was defined based on the experimental findings required for obtaining a flat gel profile (§5.3.1). It was found that the results were not as intuitive as might be anticipated by utilising a cover substrate that was as flat and smooth as possible. There was also a band, or "sweet spot" of root mean square roughness (R_q) where the flat gel profile anomaly was observed.

6.4 Maximising the signal-to-noise ratio

While the gel portion of the holographic sensor (holosensor) was miniaturised, serious thought was directed at how it might be possible to interrogate such a holosensor. Although previous work had shown the application of pH holographic sensors for monitoring *L. casei*, the holosensor spot was large enough for its signal to be picked up by a spectrophotometer. A larger sensor possesses higher tolerance to diminished holographic signals and variations since the total signal intensity is read over a large area. When miniaturised further, the quality and brightness of the hologram would accordingly be critical to the detection and interrogation of the holographic signal.

Every step of the hologram fabrication method [80], [131], [164] and set up (Figure 1-9) was scrutinised and modified as described in Appendix G (procedure) and §2.4.2.8 (method and set up) to maximise the signal-to-noise ratio. The existing ablation technique had the advantage of robustness, but the power could not be accurately adjusted for each pulse. It was then decided on the account of safety and controllability, that a high-powered continuous wave (CW) laser could be utilised instead. The major drawback of the CW laser was the exposure time, which had to be in the range of milliseconds to seconds compared to about 10 ns for the pulsed laser. Many contingencies were put in place to minimise the possibility of movement, which even down to half the wavelength of the laser (266 nm for the case of a 532 nm laser), would destroy the interference pattern. The whole setup was tightly fixed onto an optical table covered by an acrylic housing and encircled with thick lightproof and

draught-proof curtains. The lights and airflow in the darkroom area were independently controlled so that there was minimal interruption during equilibration and laser exposure.

A half-wave plate was placed in front of the laser to ensure only one type of light polarisation progressed to the sample. It was also utilised as a means for controlling the laser power by changing the attenuation of the laser with the integrated polarising filter. Only first-surface mirrors with $\frac{\lambda}{4}$ scratch-dig specifications for optimal flatness were utilised for the reflection and object beams. Samples were taped to a customised microfabricated jig to ensure that the recording angle was as consistent as possible. The lens train was adjusted such that the retroreflection was just offset to the left of the laser source to ensure parallelism to the table. This offset adjustment included all the optomechanical components. An alignment method adapted from the Michelson interferometer setup was utilised to ensure that the offsets were the same for subsequent samples (more details in Figure 2-19, §2.4.2.8.2). Although appreciable laser power was thought to be required for higher diffraction efficiency, it turned out that the laser power had to be adjusted as low as possible (0.290 mW for a 9 mm diameter beam), to prevent stray reflections from disturbing the interference pattern. It also minimised the possibility of interference from the scattering of laser light off the AgBr particles within the gel during hologram fabrication. These adjustments to methodology were realised after numerous experiments where the holograms turned out to be polychromatic, having only a ring of hologram at the edges, random spot holograms and appearing with no holograms at all. These issues were resolved by the strict adherence to the above-mentioned derived procedures.

A customised holographic signal interrogation system was established for this specific application. The angular intolerance made it extremely challenging to find the holographic signal. In trying to produce a quality hologram, however, the visible window would be even smaller. Optomechanical stages with six degrees of freedom (accomplished with a combination of tilt-yaw mirror adaptors, x-y-z axis adjustments and rotary or goniometric stages and adaptors) were utilised for the illumination and stage module, while keeping the interrogation module vertical with only one degree of freedom. A 12X zoom lens was also integrated with a high-resolution camera to take pictures of the hologram. The camera could also be interchanged with a fibre optic cable to direct the holographic signal to a spectrophotometer. A 150W Xenon source was utilised because of its favourable spectral characteristics across the visible range (~380 nm – 780 nm).

To avoid the convolution of ionic strength readings during pH measurements, the pH buffers utilised for holosensor calibration were prepared with known concentrations and ionic strength balanced to the average of ionic strength observed during *L. casei* growth. The peak wavelength responses were also intensity-corrected based on the spectrum of the illumination source to enable the holosensor to

be compared with those utilising a different light source. The high-resolution pictures and videos of the hologram were used for colour space conversion from RGB to xyY for visualisation of colour change on the CIE 1931 chromaticity diagram. They also provided indications about the gel expansion and contraction behaviour in real-time. The peak wavelength response from four pH characterisation runs, of which the first was discarded, were recorded with their hologram pictures.

L. casei samples from the same batch and growth phase were frozen and prepared for the demonstration of bacterial cell monitoring. Ionic strength, OD_{600} and pH readings were taken before introducing a 50 μL aliquot of the media containing live *L. casei* cells into the microfluidic system for interrogation.

6.5 Performance comparison of the miniaturised holosensors

The working volume for the nanobioreactor described in this work was 235.6 nL (2.0 mm diameter cylindrical chamber with 75 μm height), with the holosensor at about 3.11 nL (0.4mm diameter cylindrical sensor with about 18.7 μm height). The working volume reported in this thesis was ~ 4200X smaller than a typical 1 mL bioreactor, ~212X smaller than the smallest working volume (50 μL) of the commercial microbioreactors (BioLector, m2p Labs) reviewed in §1.1.3, or ~98X smaller than the smallest working volume for a screen printed electrode [44]. Although the smallest microbioreactor reviewed in §1.1.4.2 (Balagaddé *et al.* [45]) was 16 nL, there were no integrated sensors in the microfluidic system.

Structures less than 10 μm has been produced using photolithography. Assuming the method could be further miniaturised to around 20 μm (for a 1:1 gel diameter:height ratio), for instance, the holosensor would be about 25 pL, with a working volume (assuming the chamber diameter is 5X that of the holosensor – 100 μm) of about 2.4 nL.

According to a devised accuracy parameter calculations in §3.12, §4.12 and §4.18, the respective 3.0ϕ, 0.4ϕ and 0.4ϕ holosensor arrays displayed accuracies for monitoring pH of 99.08%, 99.38% and 97.77%, compared to the commercial pH meter.

Previous work with *L. casei* using pH holographic sensors utilised the slope, $\frac{d\lambda}{dpH}$, to report the sensitivity [80] and accuracy [79] of the pH holosensor. The slope values were 165 nm/pH unit (pH resolution of 0.0061) and 41 nm/pH unit (pH resolution of 0.0244, reported as ±0.02 accuracy) respectively. The pH resolution was calculated based on the possibility of measuring wavelength to a resolution of 1 nm. The sensitivity of the miniaturised holosensors described in this thesis are 58.10 nm/pH unit (pH resolution of 0.01721), 63.42 nm/pH unit (pH resolution of 0.01576), and 89.86 nm/pH unit (pH resolution of 0.01113) for the 3.0ϕ HEMA-co-EDMA (3 mol%)-co-TFMPA (6 mol%), 0.4ϕ

HEMA-co-EDMA (3 mol%) TFMPA (6 mol%), and 0.4ϕ HEMA-co-EDMA (0.5 mol%)-co-DMAEM (6 mol%) respectively. The slope values of the 0.4ϕ HEMA-co-EDMA (3 mol%) TFMPA (6 mol%) holosensor array were collated in Table 4-1 (§4.18), with an average of 40.3 nm/pH unit (pH resolution of 0.02481) when the array was interrogated as a whole.

The reproducibility of pH measurement was demonstrated by Marshall *et al.* [80] with the visual error bars in the calibration graph by using 3 independent samples, which was comparable to those reported in this thesis. Marshall *et al*. utilised constant ionic strength across all pH calibration buffers in order to mitigate the effects of ionic strength during pH measurement. The holosensors miniaturised and fabricated in this thesis, went a step further to obtain a light intensity-normalised wavelength response to enable a light source-independent comparison between the peak wavelength responses of different pH holosensors.

Additionally, it was reported by Bell [79] that there was a 44 min delay to the pH response of the holosensor. This was believed to be attributable to the thicker and larger holosensor volume, which would take time to equilibrate. To put the holosensor volume into perspective, Marshall *et al.* [80] and Bell [79] produced slide (76 mm x 26 mm) holosensors (10 μm gel height; ~19.76 μL gel volume) and spot (1 cm^2) holosensors (100 mm height, 11.3 mm diameter; ~10 μL gel volume) respectively. In contrast to the 3.0ϕ (18.9 μm height; 158.73 nL gel volume) and miniaturised 0.4ϕ (18.7 μm height; 3.11 nL gel volume) holosensors discussed in this thesis, the gel volume was significantly smaller, which resulted in a short equilibration time of 5 min and 1 min respectively for the 3.0ϕ and 0.4ϕ pH holosensors. This enabled the miniaturised holosensors to be utilised for near real-time cell culture monitoring.

Since the majority of pharmaceutical activities involved mammalian cell culture, a different pH holosensor was also fabricated as a proof-of-concept for monitoring animal cells. The miniaturised HEMA-co-DMAEM holosensor was customised with 0.5 mol% EDMA in order to exhibit the full range of hologram colours from blue all the way to red corresponding to reduction in pH from pH 8.5 to 3.5.

Bonding procedures for PDMS-glass and PC-PDMS [127] were adopted and modified from discussions with the plasma machine vendor and literature, while a plastic-holosensor gel bonding technique was devised to demonstrate the possibility of utilising an alternative substrate other than glass for holosensors. Preliminary results using a violet (411 nm) CW laser for hologram fabrication were also reported to realise the possibility of dye-free hologram fabrication.

6.6 Final Conclusions

In this thesis, a miniaturised pH holographic sensor (holosensor) was integrated into a PDMS-glass nanolitre bioreactor (or nanobioreactor). It has been demonstrated that a miniaturised spot (3.11 nL in volume) and a holosensor array of volumes smaller than 5 nL could be fabricated and utilised with high signal-to-noise ratio and accuracy comparable to a conventional pH meter. While the smallest known pH meter (micro-pH electrode) has a limit to the minimum volume (5 μL) required to obtain a reading, the miniaturised pH holosensor was able to obtain pH readings in a 0.27 μL microfluidic chamber. Even if the smallest non-invasive PreSens pH sensors were utilised, the volume of the sensor itself (0.47 μL, 2 mm diameter, 150 μm height) would be larger than the desired working volume. Whereas the technology for process control and monitoring was not widely available in a microbioreactor below 200 μL, it was shown that pH measurements could be read accurately in a nanobioreactor more than 700X smaller. Furthermore, the holosensors could be in principle, inexpensively produced, and could withstand plasma treatment and sterilisation (autoclaving) without delamination from its substrate.

The fed-batch growth of a 'model' microorganism, *Lactobacillus casei* Shirota *(L. casei)* from Yakult was monitored with the miniaturised holosensor and compared against the pH meter for accuracy. *L. casei* almost exclusively produces lactic acid from its metabolic activity of consuming glucose [126]. The lowering of pH during its growth was correlated to the peak wavelength of the holosensor response.

The consequence of this capability is far-reaching. Not only could other analyte-sensitive holosensors be miniaturised using the same method, the potential of multiplexing experiments within a nanobioreactor is limited only to the quality of fluidic interconnects and photomask resolution. With the brightness of the developed holosensor, it could be further miniaturised to fit thousands of these holosensors into an intricate network of nanobioreactors integrated into a microfluidic chip the size of a credit card. The optical setup could be automated to find the maximum holographic signal, and move from spot to spot in order to take readings from different microfluidic chambers. Arrays of holosensors could act as redundancies to ensure measurement accuracy. The sensor volume and associated nanobioreactor working volume are already orders of magnitude smaller than commercially available microbioreactors involving integrated sensors, and there is still a possibility of further miniaturisation to the limit of photolithography.

This brings us one step closer towards the ultimate aim of long-term real-time monitoring of a single mammalian cell in a mass-producible polymeric nanobioreactor.

Appendices

Appendix A: Absorbance graphs

A-1 Absorbance spectra of chemicals for gel fabrication

(a)

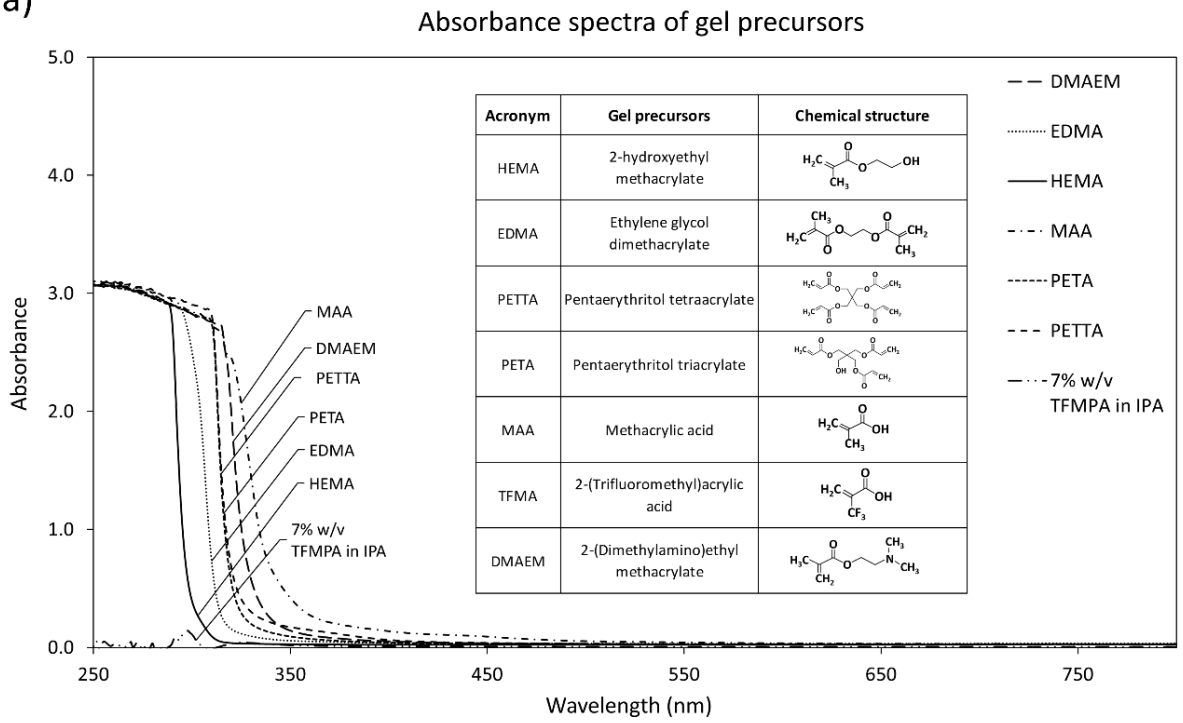

Acronym	Gel precursors	Chemical structure
HEMA	2-hydroxyethyl methacrylate	
EDMA	Ethylene glycol dimethacrylate	
PETTA	Pentaerythritol tetraacrylate	
PETA	Pentaerythritol triacrylate	
MAA	Methacrylic acid	
TFMA	2-(Trifluoromethyl)acrylic acid	
DMAEM	2-(Dimethylamino)ethyl methacrylate	

(b)

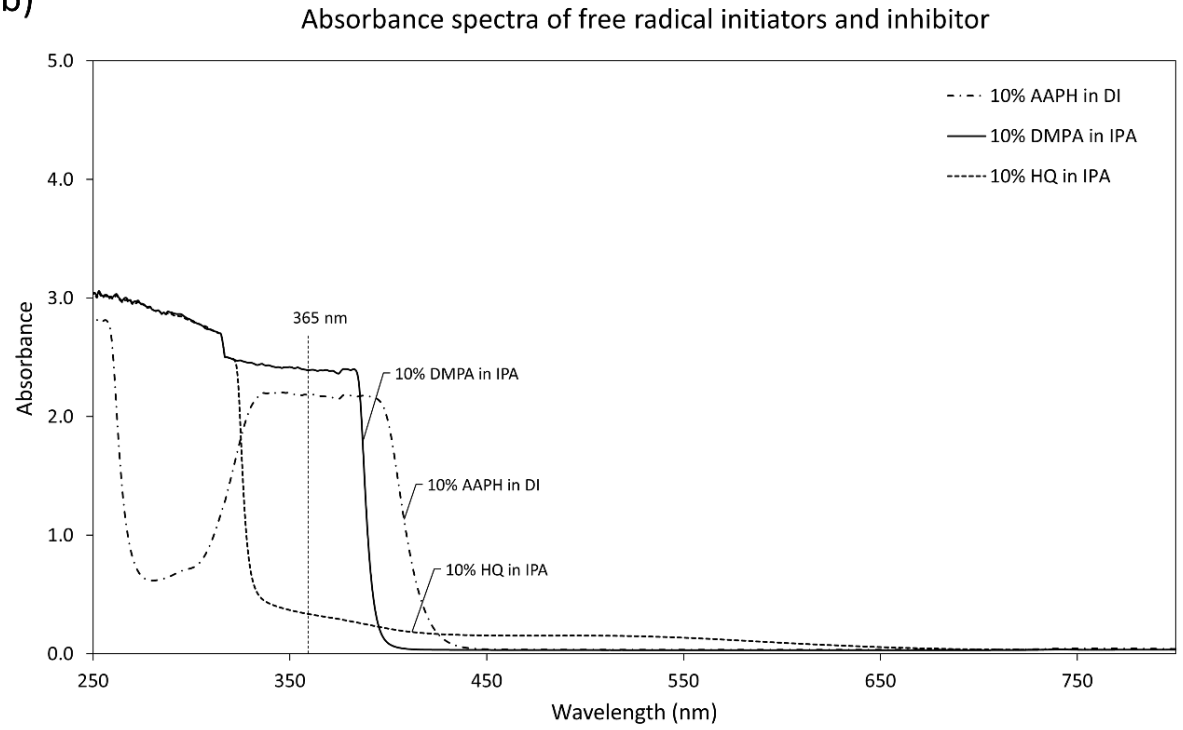

*Figure A-1: Absorbance spectra of **(a)** gel precursors, and **(b)** free radical initiators and inhibitor*

A-2 Absorbance spectra of gel and dyes

(c)

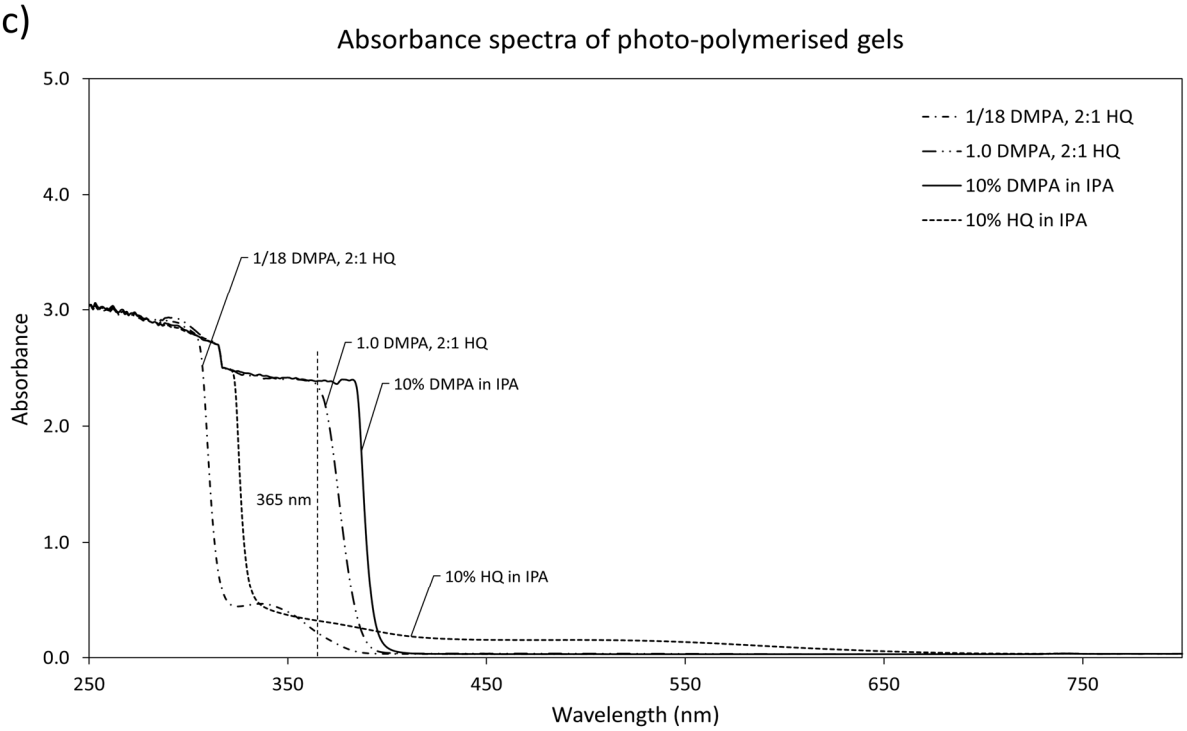

(d)

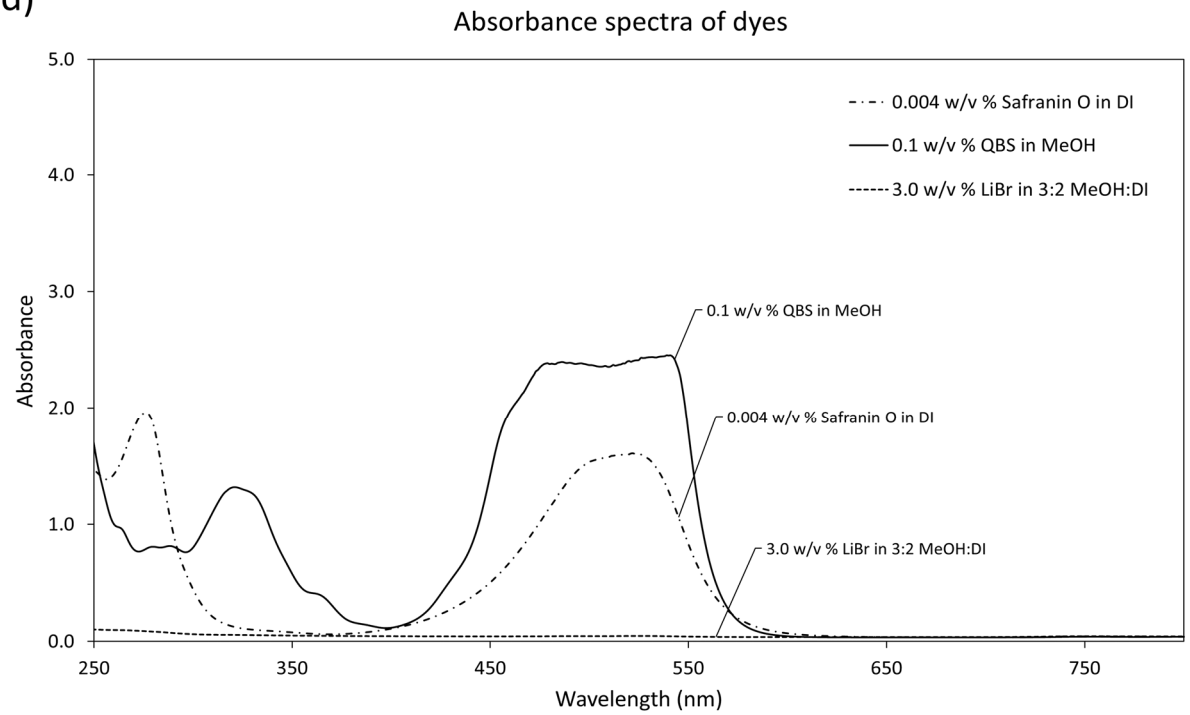

*Figure A-2: Absorbance spectra of **(a)** photo-polymerised gels (1.0 DMPA and 1/18 DMPA described their DMPA molar concentration (in 1 mL IPA solvent) in the gel precursor solution corresponding to 0.7070 mmol and 0.00393 mmol respectively), and **(b)** various dyes.*

Appendix B: RGB to xyY conversion

RGB (or standard sRGB (IEC 61966-2-1, 1999)) values occupy a certain region (colour gamut) defined by its reference white, D65 as shown on the chromaticity diagram below.

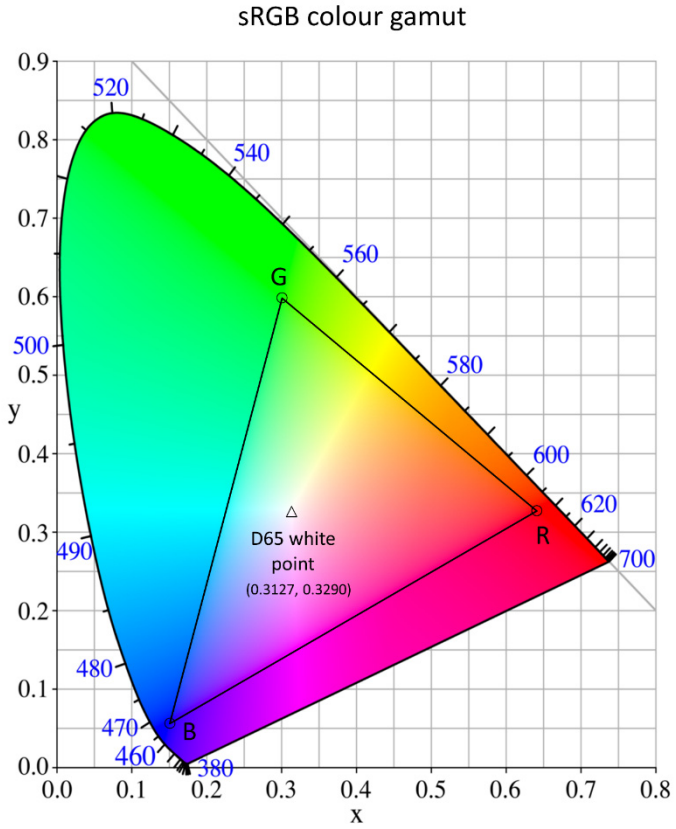

Figure B: sRGB gamut on the CIE 1931 chromaticity diagram

The RGB values must first be normalised to [0, 1] from [0, 255] by simply dividing each component by 255. The non-linear RGB, denoted $\boldsymbol{V} \epsilon \{R, G, B\}$, is inverse sRGB companded and converted to linear RGB with respect to energy, denoted $\boldsymbol{v} \epsilon \{r, g, b\}$, with Equation B.1 [141], [142] as follows:

$$\boldsymbol{v} = \begin{cases} \boldsymbol{V}/12.92 & \boldsymbol{V} \leq 0.04045 \\ [(\boldsymbol{V} + 0.055)/1.055]^{2.4} & \boldsymbol{V} > 0.04045 \end{cases} \quad \text{(B.1)}$$

The resulting linear RGB is then transformed to the XYZ colour space with transformation matrix, [M], obtained from D65 reference white (since sRGB was defined relative to D65 white) using the standard 2° observer (Equation B.3). The xyY coordinates can be obtained using the conversion described in Equation B.4.

$$\begin{bmatrix} X \\ Y \\ Z \end{bmatrix} = [M] \begin{bmatrix} r \\ g \\ b \end{bmatrix} \quad \text{(B.2)}$$

$$\begin{bmatrix} X \\ Y \\ Z \end{bmatrix} = \begin{bmatrix} 0.4124 & 0.3575 & 0.1804 \\ 0.2126 & 0.7151 & 0.0721 \\ 0.0193 & 0.1191 & 0.9503 \end{bmatrix} \begin{bmatrix} r \\ g \\ b \end{bmatrix} \quad \text{(B.3)}$$

$$x = \frac{X}{X + Y + Z}, \qquad y = \frac{Y}{X + Y + Z}, \qquad Y = Y \quad \text{(B.4)}$$

Appendix C: Using tape as a mask for gel fabrication

C-1 Preliminary work on holosensors

(a) Whole-slide photo-polymerised HEMA-co-MAA gel samples

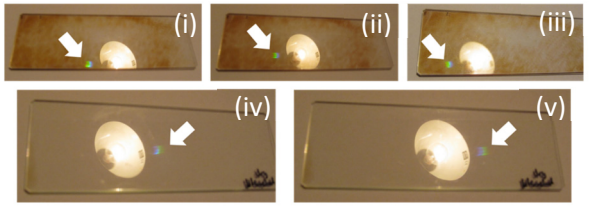

*Figure C-1(a): Recorded dry (i.e. without any buffers**), (i-iii)** a hologram was observed on the same sample at different parts of the slide when changing the viewing or illumination angle. **(iv & v)** Another holosensor bleached with iodine to form silver iodide (AgI) to render the gel colourless. A hologram, albeit polychromatic, was observed at different locations at a different viewing angle.*

(b) Masked photo-polymerised HEMA-co-MAA gel samples

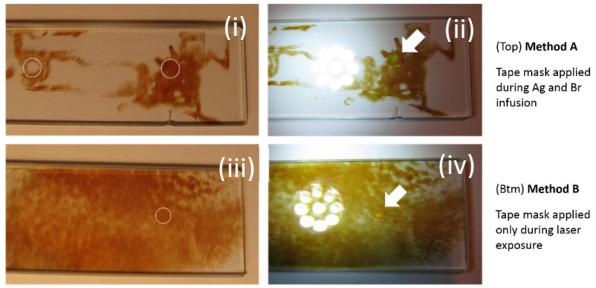

*Figure C-1(b): **(i)** A fabricated holosensor with dotted circle depicting unmasked area from a tape mask. **(ii)** A hologram observed at the unmasked region. The brown reduced Ag^0 does not spread uniformly throughout gel as the slide was immersed in agitated LiBr, causing uneven diffusion of silver and bromide. **(iii-iv)** fabricated holosensor with dotted circle representing position of tape mask that was applied during laser exposure.*

(c) (d)

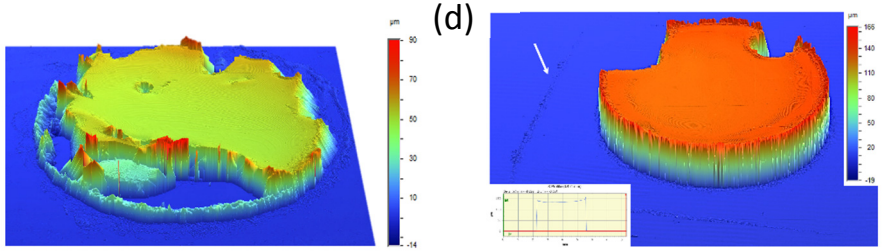

*Figure C-1: 3.0ϕ HEMA-co-DMAEM gels damaged during **(c)** the removal of quartz cover substrate, and **(d)** the removal of the tape mask. The white arrow indicates the presence of residue after using the tape mask for photo-polymerisation.*

(e)

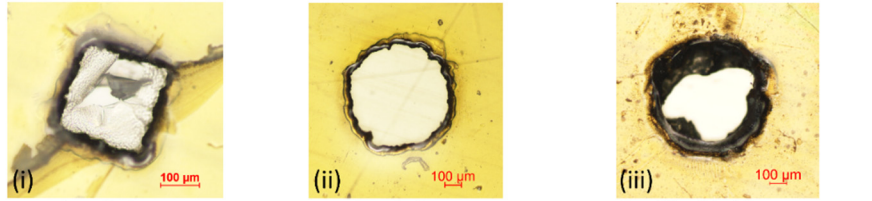

(f)

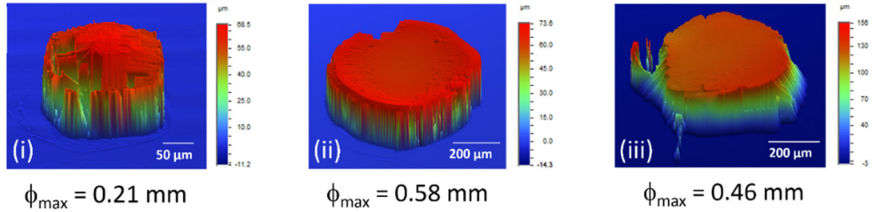

*Figure C-1: **(e)** Kapton tapes cut using CO_2 laser machine with parameters described in Appendix D were used as masks for photo-polymerisation and **(f)** the resultant gels formed in the well created by the tape between the quartz cover and glass substrate.*

C-2 Preliminary work on 5.0ϕ holosensor

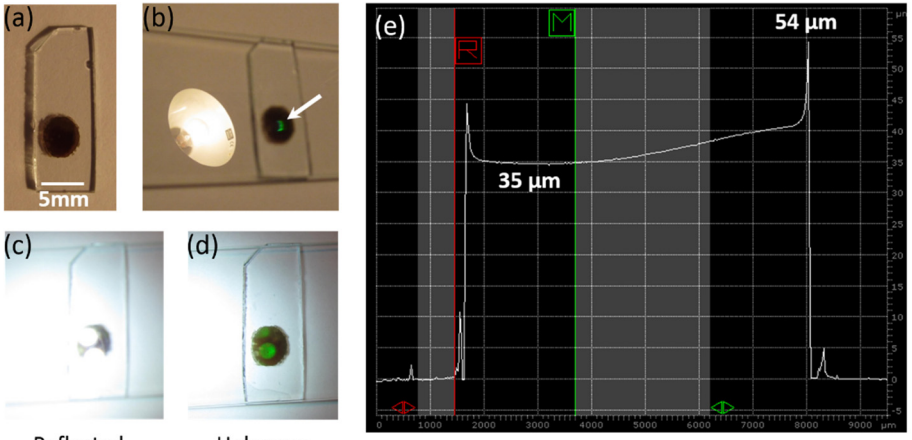

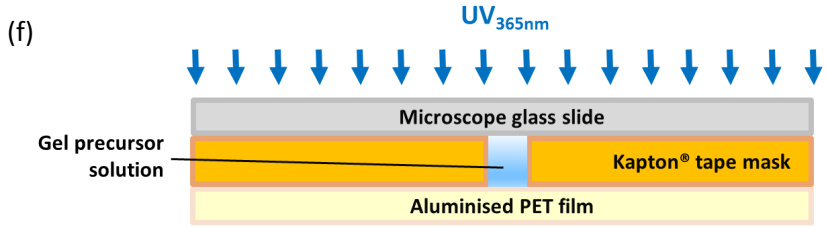

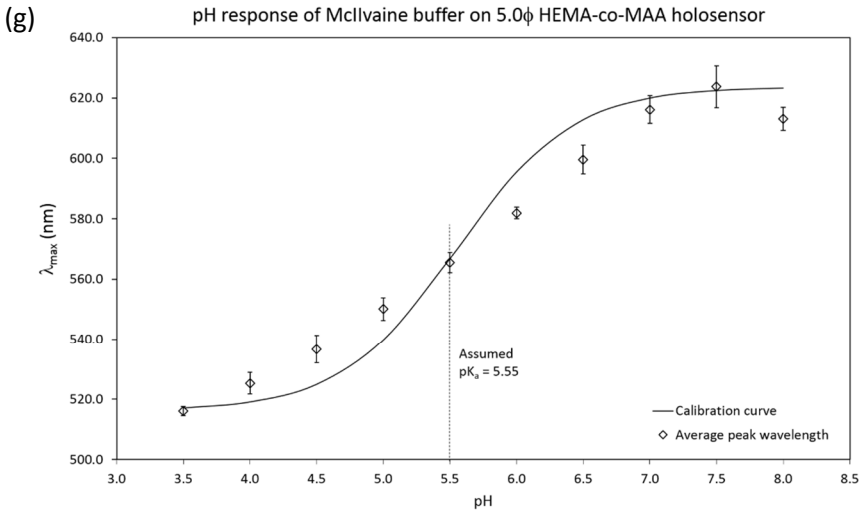

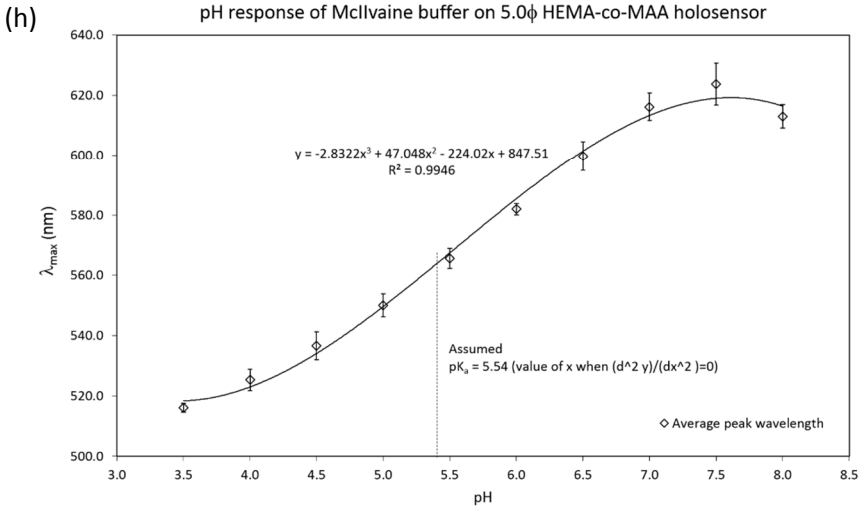

Figure C-2: ***(a)*** *5.0 mm diameter HEMA-co-EDMA (5 mol%)-co-MAA (6 mol%) fabricated using a 50 µm thick electric insulation tape with punched 5.0 mm hole.* ***(b)*** *Hologram indicated by the white arrow,* ***(c)*** *reflection of the illumination beam and then* ***(d)*** *a hologram observed at an offset angle away.* ***(e)*** *Profile of the gel measured by a stylus surface profiler.* ***(f)*** *Schematic diagram for gel fabrication with tape mask.* ***(g)*** *A calibration curve derived and modified from the Henderson-Hasselbalch equation to determine the assumed (or apparent) pK_a of the pH sensitive ligand within the gel matrix.* ***(h)*** *The data points were curve fitted and the curve equation differentiated twice to find out its pK_a.*

Appendix D: CO_2 laser cutting machine recipes for various substrates

Table D: Optimised CO_2 laser cutting parameters for various substrates and thicknesses

Material	Thickness (mm)	Power (%)	Speed	Pixels per inch (PPI)	Focal point above (mm)
	0.25	3.0	2.0	300	0.3
	0.50	6.0	2.0	300	0.5
	0.50	20.0	4.0	1000	0.5
	1.0	40.0	4.5	1000	1.0
	2.0	40.0	2.0	1000	2.0
	3.0	90.0	2.0	1000	3.0
	4.0	50.0	1.0	1000	4.0
	5.0	90.0	1.2	1000	5.0
	6.0	90.0	1.0	1000	6.0
	10.0	90.0	0.3	1000	10.0
Polystyrene (PS) petri dish	1.0	20.0	5.0	1000	1.0
Injection-moulded cyclic olefin copolymer (COC)	0.60	90.0	9.0	300	0.5
Kapton (double sided tape)	0.14	10.0	15.0	1000	
	0.035	10.0	15.0	1000	0.25
	0.060	10.0	15.0	1000	0.25
	0.005	3.0	4.0	1000	0.25
	0.010	5.0	4.0	1000	0.25
	0.050	10.0	4.0	1000	0.25
Teraoka Tape (silicone adhesive)	0.050	3.0	4.0	1000	0.25
Coloured red tape	0.14	20.0	4.0	1000	0.14
3M 3000LSE Tape 9472FL	0.127	20.0	4.0	1000	0.2

Appendix E: PDMS Mould Fabrication

SU-8 glass mould

A standard microscope glass slide (76 mm x 25 mm x 1mm) was taken out from its packaging, cut into 2 using the "scribe-and-snap method" (§2.4.1.1.2) and placed into a clean glass beaker. The slide is further cleaned with 3-minute acetone immersion in a clean glass beaker placed inside an ultrasonic bath, followed by an IPA rinse and then a 3 min ultrasonic IPA immersion in the same beaker. The cleaning step is concluded with a 3 min ultrasonic DI water immersion in the same beaker that had been rinsed with DI water. The excess water was blown away with an N_2 air gun.

Next, the cleaned glass slide was positioned in the Laurel spin coater (or customised spin coater) with a drop (~1 mL) of SU-8 2025 on the middle of the slide. Cleanroom wipes (or tissue) were placed around the spindle to capture any excess SU-8 during the spin coating process. Before the SU-8 resist was put on the glass substrate, about 4 drops (from a plastic pipette) of an adhesion promoter, hexamethyldisilazane (HMDS), was spun at 3000 rpm @ 100 rpm/s for 40s. To achieve about 80 μm thick SU-8 layer on the glass substrate, the spin coater was programmed or manually adjusted (in the case of the customised spin coater via voltage adjustment) to spin at 500 rpm @ 100 rpm/s for 10s and then 1000 rpm @ 100 rpm/s for 45s (the acceleration cannot be accurately adjusted for the customised spin coater). After the spin-coating process, a toothpick was used to scrap away the built-up SU-8 at the edge of the glass substrate to minimise contamination of the hotplate at the next step. By removing the edge bead, the photomask can be physically closer to the SU-8 layer during the exposure step, which will result in improved resolution.

The SU-8 resist on glass substrate was then placed on a 65°C hotplate for 3 min, followed by 9 min on another 95°C hotplate. The heated substrate was then left on a non-metal surface to cool for 3 min. This prebake process at 65°C and 95°C removes most of the solvent from the SU-8 resist, making it more solid. The purpose of a 2-stage temperature ramp and subsequent slow cooling rate was to decrease internal mechanical stress, without which the SU-8 would most likely curl up and delaminate from the substrate easily during the post-exposure bake or hard-bake process. A convection oven should not be utilised for the prebake process due to the formation of a skin layer, which inhibits the evaporation of solvent.

The cooled substrate was then exposed to UV through a photomask with the desired pattern using the mask aligner (with UV intensity ~21 mW/cm^2) for 16s. This exposure duration was specific to glass (1.5X that of silicon wafers) because of its high UV transmittance.

After that, the UV-exposed substrate was then placed on the 65°C and 95°C hotplate for 2 min and 7 min respectively as part of the post exposure bake process to complement the crosslinking process of the UV exposure.

The substrate was developed by immersion (and constant agitation by manual swirling) in propylene glycol monomethyl ether acetate (PGMEA) or SU-8

developer (preferred for better results) in a clean glass beaker for 9 min. Spray and rinse the developed SU-8 on glass substrate with IPA. If a white film appears during the IPA rinse, it is an indication that the resist was underdeveloped. Continue to develop with PGMEA or SU-8 developer to remove the white film until a point where an IPA rinse would not yield a white film. An ultrasonic bath can be used to quicken the development process, but was not utilised because the resist may develop too quickly. After the finish IPA rinse, the substrate was dried with the N_2 air gun.

The developed substrate was then placed on a hotplate @ 150°C for 15 min to anneal any surface cracks that may have appeared after development, as well as to prevent any further changes to the resist properties.

The SU-8 glass mould was then placed in the desiccator with a 2 μL drop of 1H-1H-2H-2H-Perfluorodecyltriethoxysilane (FDTS) on another glass slide. A vacuum pump was utilised to create a vacuum within the desiccator, after which the desiccator was sealed and contained and left in the fumehood overnight. FDTS was meant to be create a non-stick layer on the SU-8 glass mould for easy removal of PDMS after casting.

Nickel-plated glass mould

The 7" (~170 mm) diameter glass wafer was first sputtered with the Quorum Q300T Ni sputter tool with sputter current and sputter time 55 – 70 mA and 100 – 120s respectively. The Ni-sputtered wafer was then laminated with three layers of 25 μm dry film photoresist using the 105°C hot roller of the SI-L610 Dry Film Laminator. The 15 μm Mylar sheet of the top layer is left unpeeled so that the photomask can be pressed against the photoresist without staining. Subsequently, UV exposure was performed with the vacuum UV exposure machine (having a measured 1.5 mW/cm^2 UV intensity) for 110s under -20 cmHg vacuum. After the exposure, the sample was left untouched for 10 to 15 minutes for the photochemical reaction to stabilise. The non-exposed areas are not cross-linked, and are dissolved and washed off by placing the sample onto the Laurel spin coater spinning at 100 rpm for about 13.5 min with a custom made spray system to dispense 1% sodium carbonate (Na_2CO_3). After development, nickel was sputtered to provide a seed layer before surfactant was sprayed onto the wafer. It was then immersed into the nickel sulfamate bath. The power, voltage and temperature were set at 35A, 18.9V and 56.5°C respectively. The nickel-plating process was performed for 3 to 4 hours, before the wafer was immersed into 1% aq. NaOH to strip the resist away (lift-off) and reveal only the patterned areas. The eventual nickel mould thickness was around 0.6 mm. Tape was used to stick on the edges as the mould was sharp at its edges and posed as a safety hazard. 60 μL of FOTS was dispensed on a separate glass petri dish to render the nickel surface hydrophobic to make it easier for PDMS de-moulding. The nickel-plated glass mould was then put into the customised FOTS oven (§2.2.2.5) at 100°C under about -25inHg vacuum overnight.

Appendix F: Calculation for gel precursor ratio

Table F: HEMA-co-TFMPA gel precursor solution recipe

01/11/2016 - 1.0 DMPA (2:1 HQ) | For 0.4D gel | 8TH-2 | 6T3E

HEMA-TFMPA - pH sensitive

DMPA	HQ
2	1

*Reciprocal of DMPA fraction

DMPA			Check
1	/	1.000	1.0

Total no. of mmol = 8 mmol (We want 8mmol constituents in 1ml IPA)

		mw (g/mol)	desired mol%	Total amt (mmol)	weight (g)	w/v % made	Density (g/cm3) (g/ml)	1 vol (ml) (for 1ml)	1000 vol (in ul) for 1ml	500 vol (in ul) for 500ul	300 vol (in ul) for 300ul	200 vol (in ul) for 200ul	1400 vol (in ul) for 600ul	For 500
2-Hydoxyethyl methacrylate	HEMA	130.14	91.00%	7.28000	0.94742	100	1.073	0.8830	882.96	441.48	264.89	176.59	529.78	
Ethylene glycol dimethylacrylate	EDMA	198.22	3.00%	0.24000	0.04757	100	1.051	0.0453	45.26	22.63	13.58	9.05	27.16	
2-(Trifluoromethyl) propenoic acid	TFMPA	140.06	6.00%	0.48000	0.06723	99999999	-	0.0000	0.00	0.00	0.00	0.00	0.00	0.03361 g
2,2-Dimethoxy-2-phenylacetophenone	DMPA	256.30	-	0.07070	0.01812	10	-	0.1812	181.20	90.60	54.36	36.24	108.72	
Hydroquinone	HQ	110.11	-	0.03535	0.00389	10	-	0.0389	38.92	19.46	11.68	7.78	23.35	
Total		-	100%	8.000	1.08423	-	-	0.2201	220.13	110.06	66.04	44.03	132.08	
				8.10605										
2,2-Dimethoxy-2-phenylacetophenone	DMPA	256.30	66.67%	0.07070	0.01812	10		0.1812	181.20	90.60	54.36	36.24	108.72	
Hydroquinone	HQ	110.11	33.33%	0.03535	0.00389	10		0.0389	38.92	19.46	11.68	7.78	23.35	

This Row = tot solvent vol (ADD ALL non-100% & non-9999999 vol)

Monomers-to-solvent ratio = 1.06222 g/ml Total reagents-to-solvent ratio = 1.084234 g/ml

IPA (to make it 1ml)	IPA	60.10	-	-	-	-	0.785	0.7799	779.87	389.94	233.96	155.97	467.92	

First, the molar ratio (mol%) of crosslinking (EDMA) and pH-sensitive ligand (TFMPA) were decided. The total amount of each constituent (HEMA, EDMA and TFMPA) were calculated based on their molecular weight and number of moles required per mL of solvent (8 mmol constituents in 1 mL IPA). Next, the fraction of DMPA normalised to past recipes was designated (i.e. 1.0 DMPA would be 0.07070 mmol of DMPA. The molar ratio of HQ was arbitrarily fixed at half the amount of DMPA, hence the term "1.0 DMPA (2:1 HQ)". Since TFMPA was solid crystals, it was weighed (0.03361g – highlighted in green) in a transparent 1.2 mL eppendorf tube together with the other constituents and required amount of 10% w/v DMPA and 10% w/v HQ in IPA, and vortexed before transferring to a 2 mL amber vial. Additional IPA (389.94ul) was added to make up the 500 µL required to achieve the designated ratio. This recipe involved **8** mmol **H**EMA-co-**T**FMPA and was abbreviated "8TH", the suffix "-2" represented method #2 for calculating the constituents based on a total moles of constituents per mL of solvent basis. It is slightly different to determining the volume of constituents (1 mL) added to the same volume (1 mL) of 2% w/v free radical initiator (DMPA) based on molar ratio as utilised previously. A condensed version of this recipe would thus be "8TH-2, 6T3E, 1.0 DMPA (2:1 HQ)".

Appendix G: Summarised procedure for hologram fabrication

Table G: Optimised hologram fabrication experimental procedures

#	Procedure	Chemical	Amount	Duration	Type	Remarks
1	Cleaning	70% EtOH / O_2 plasma	5 ml	1 min / 3mins	Immersion / ion-dominant plasma	gel side face up / 250W, 4 x 10^{-1} Torr (55% Ar, 45% O_2), 3mins
2	Dehydration	N_2 dry	1 bar	5s	Air gun	dry both sides
3	Ag infusion	0.1M $AgClO_4$	80 µl	1 min	Blob immersion	blob covering gel side up
4	Dehydration	N_2 dry	1 bar	5s	Air gun	dry both sides
5	Br & dye infusion	20:1 3% w/v LiBr in 2:1 MeOH:DI w/ 0.5% w/v QBS dye in MeOH	4 ml	1 min	Immersion	keep bromide solution in air-tight µ-dish to minimise evaporation
6	Washing	70% EtOH	5 ml	1 min	Agitated immersion	gel side face up with swirling
7	Dehydration	N_2 dry	1 bar	5s	Air gun	dry both sides
8	Washing	DI water	copious amounts	30s	Inundation	flush with DI water tap gel side up
9	Dehydration	N_2 dry	1 bar	10s	Air gun	dry both sides thoroughly
10	Equilibration	2% w/v L-ascorbic acid (adjusted to pH 4.5 w/ NaOH)	20 µl	12 mins	chamber immersion	wash w/ DI and dry again if air bubbles form in chamber
11	Laser Exposure	N.A.	N.A.	3s exposure @ 0.290 mW	N.A.	power was measured with 9.0 mm diameter laser beam
12	Development	1:1 Saxby A: Saxby B	4.75 ml	18s	Immersion	Top cover was to touch and cover the solution surface to minimise oxidation
13	Stop development	5% v/v Acetic acid (Stop bath)	20 ml	30s	Agitated immersion	swirl substrate with tweezer inside stop bath
14	Washing	DI water	copious amounts	10s	Inundation	flush with DI water tap gel side up
15	Dehydration	N_2 dry	1 bar	10s	Air gun	dry both sides thoroughly
16	pH response test	McIlvaine buffer (at diff pH levels accordingly)	12 µl	1 min	covered immersion	cover with any other substrate and test holosensor for colour (green) w/ TH or LED torch
17	Dye cleansing	100% IPA	4.75 ml	1 min	Immersion	dry and wash w/ DI for 5s after this step
18	Fixing	1:1 20% $Na_2O_3S_2$: DI water (fixer)	4.75 ml	1 min	Immersion	unexposed AgBr gets dissolved away
19	Dehydration	N_2 dry	1 bar	3s	Air gun	dry both sides sparingly
20	Washing	DI water	copious amounts	10s	Inundation	flush with DI water tap gel side up to dissolve any residual fixer
21	Fixing and dye cleansing	6.7% v/v $Na_2O_3S_2$ in 33% EtOH	4.5 ml	3 mins	Immersion	Clean up any residual dye and AgBr

Appendix H: Recipe for ionic strength balanced (9.50 mS/cm) 0.1M McIlvaine buffers

Table H: Recipe for obtaining 9.50 mS/cm normalised ionic strength 0.1M McIlvaine buffers

pH	original conductivity (mS/cm)	0.1M Citric Acid (ml)	0.1M Na_2HPO_4 (Base) (ml)	Add Acid (ml)	Add 3M NaCl (ml)	Add Base (ml)	Final conductivity (mS/cm)
6.00	9.60	9.75	31.00	0.00	0.00	0.05	9.60
5.75	9.23	10.00	30.00	0.65	0.05	0.03	9.51
5.50	8.91	11.00	29.00	0.60	0.10	0.05	9.52
5.25	8.64	12.00	28.00	0.49	0.14	0.10	9.49
5.00	8.37	13.00	27.00	0.35	0.19	0.13	9.49
4.75	8.05	14.00	26.00	0.30	0.24	0.30	9.51
4.50	7.81	15.00	25.00	0.35	0.25	0.20	9.50
4.25	7.32	16.50	23.50	0.10	0.32	0.23	9.48
4.00	6.87	18.00	22.00	0.10	0.35	0.28	9.49
3.75	7.04	19.50	20.50	0.20	0.38	0.33	9.50
3.50	5.84	21.00	19.00	0.70	0.58	0.60	9.55
3.25	5.27	23.50	16.50	0.00	0.65	0.80	9.48
3.00	4.56	26.00	14.00	1.90	0.79	0.90	9.47

The buffer was made in the order of adding the experimentally determined volumes of 0.1M citric acid and 0.1M disodium hydrogen phosphate (Na_2HPO_4). The pH was monitored while the acid component (0.1M citric acid) was added to the intended pH. 3M NaCl was then added to raise the ionic strength to 9.50 mS/cm. The added NaCl would have adjusted the pH down. More base (Na_2HPO_4) with amounts stated in Table H were added to adjust the pH back to the desired value.

Appendix I: Derivation of the modified Henderson-Hasselbalch equation

A weak acid (HA) partially dissociates in water to a hydronium ion (H_3O^+) and conjugate base (A^-)

$$HA + H_2O \rightleftharpoons A^- + H_3O^+ \quad \text{(I.1)}$$

For simplification, the hydronium ion (H_3O^+) will be referred to as a proton (H^+)

The acid dissociation constant is thus,

$$K_a = \frac{[H^+][A^-]}{[HA]} \quad \text{(I.2)}$$

Taking logarithm of base 10 to both sides of the equation, it becomes

$$\log_{10} K_a = \log_{10}[H^+] + \log_{10}\frac{[A^-]}{[HA]} \quad \text{(I.3)}$$

Since $pH = -\log_{10}[H^+]$ and $pK_a = -\log_{10}[K_a]$, Equation (I.3) becomes

$$pH = pK_a + \log_{10}\frac{[A^-]}{[HA]} \quad \text{(I.4)}$$

$$\Rightarrow pH - pK_a = \log_{10}\frac{[A^-]}{[HA]}$$

This is equivalent to the following:

$$10^{pH - pK_a} = \frac{[A^-]}{[HA]} \quad \text{(I.5)}$$

Assuming the ideal case where the extent of ionization, α, within the pHEMA matrix causes a linear change in the peak diffracted wavelength, a modified Henderson-Hasselbalch calibration curve can be normalised to find out the apparent pK_a of the holosensor as follows:

$$pH = pK_a + \log_{10}\frac{\alpha}{1-\alpha} \quad \text{(I.6)}$$

$$\Rightarrow pH - pK_a = \log_{10}\frac{\alpha}{1-\alpha}$$

which then becomes

$$10^{pH - pK_a} = \frac{\alpha}{1-\alpha} \quad \text{(I.7)}$$

where α is normalised and defined by:

$$\alpha = \frac{\lambda - \lambda_{min}}{\lambda_{max} - \lambda_{min}} \quad \text{(I.8)}$$

Substituting Equation (I.8) to (I.7),

$$10^{pH-pK_a} = \frac{\left(\frac{\lambda-\lambda_{min}}{\lambda_{max}-\lambda_{min}}\right)}{1-\left(\frac{\lambda-\lambda_{min}}{\lambda_{max}-\lambda_{min}}\right)}$$

Multiplying RHS of equation by $\left(\frac{\lambda_{max}-\lambda_{min}}{\lambda_{max}-\lambda_{min}}\right)$,

$$\Rightarrow 10^{pH-pK_a} = \frac{\lambda-\lambda_{min}}{\lambda_{max}-\lambda_{min}-\lambda+\lambda_{min}}$$

$$10^{pH-pK_a} = \frac{\lambda-\lambda_{min}}{\lambda_{max}-\lambda} \quad \text{(I.9)}$$

The predicted pH can thus be found by rearranging (I.9)

$$\boxed{pH = \log_{10}\left(\frac{\lambda-\lambda_{min}}{\lambda_{max}-\lambda}\right)+pK_a} \quad \text{(I.10)}$$

To obtain the predicted wavelength, (I.9) becomes

$$\lambda_{max}\cdot(10^{pH-pK_a}) - \lambda\cdot(10^{pH-pK_a}) = \lambda-\lambda_{min}$$

$$\lambda\cdot(1+10^{pH-pK_a}) = \lambda_{max}\cdot(10^{pH-pK_a})+\lambda_{min}$$

$$\boxed{\therefore \lambda = \frac{\lambda_{max}\cdot(10^{pH-pK_a})+\lambda_{min}}{1+10^{pH-pK_a}}} \quad \text{(I.11)}$$

The apparent pK_a is found where the slope of the graph of λ against pH, $\frac{d\lambda}{dpH}$, is at its maximum.

To obtain $\frac{d\lambda}{dpH}$, the differentiation quotient rule (depicted in its general form), $\frac{dy}{dx} = \frac{v\frac{du}{dx}-u\frac{dv}{dx}}{v^2}$, is applied :

$$\frac{d\lambda}{dpH} = \frac{v\frac{du}{dpH}-u\frac{dv}{dpH}}{v^2} \quad \text{(I.12)}$$

where u and v are the numerator, $u = \lambda_{max}\cdot(10^{pH-pK_a})+\lambda_{min}$, and denominator, $v = 1+10^{pH-pK_a}$, of Equation (I.11) respectively. Equation I.10 then becomes

$$\frac{d\lambda}{dpH} = \frac{(1+10^{pH-pK_a})(\lambda_{max}\cdot(10^{pH-pK_a})\cdot\ln 10)-(\lambda_{max}\cdot(10^{pH-pK_a})+\lambda_{min})(10^{pH-pK_a}\cdot\ln 10)}{(1+10^{pH-pK_a})^2} \quad \text{(I.13)}$$

$$\frac{d\lambda}{dpH} = \frac{(10^{pH-pK_a}\cdot\ln 10)[\lambda_{max}+\lambda_{max}\cdot(10^{pH-pK_a})-\lambda_{max}\cdot(10^{pH-pK_a})-\lambda_{min}]}{(1+10^{pH-pK_a})^2}$$

$$\boxed{\therefore \frac{d\lambda}{dpH} = \frac{(10^{pH-pK_a}\cdot\ln 10)(\lambda_{max}-\lambda_{min})}{(1+10^{pH-pK_a})^2}} \quad \text{(I.14)}$$

$\frac{d\lambda}{dpH}$ is at its maximum when $pH = pK_a$. Equation (I.14) can then be subsequently simplified to:

$$\frac{d\lambda}{dpH} = \frac{(\ln 10)(\lambda_{max} - \lambda_{min})}{4} \quad \text{(I.15)}$$

The maximum slope $\frac{d\lambda}{dpH}_{max}$, , and $\lambda_{max}\ or\ \lambda_{min}$ were determined experimentally and $\frac{d\lambda}{dpH}_{max}$ was then worked out using Equation (I.25) using the experimentally deduced $\lambda_{max}\ or\ \lambda_{min}$.

By inserting it into the now known λ_{max} and λ_{min} into Equation (I.11), a calibration curve of λ against pH at a particular pK_a was then plotted. The experimental values are superimposed on the same graph and the assumed pK_a , or apparent pK_a, was determined by estimating it between two pH data points that should enclose the maximum slope $\frac{d\lambda}{dpH}_{max}$. The outcome should be a calibration curve that is the best fit to the experimental data. The predicted pH based on the calibration curve can then be determined with Equation I.10.

The above analysis is useful for holosensors which expands at higher pH and contracts at lower pH, such as gels containing pendant methacrylic acid (MAA). For holosensors which expands at lower pH and contracts at higher pH, such as those containing pendant 2-(Dimethylamino) ethyl methacrylate (DMAEM), a separate but not so dissimilar expression is extracted to obtain the calibration curve. The analysis is presented as follows:

A weak base (B) partially dissociates in water to give a hydroxide ion (OH^-) and conjugate acid (HB^+)

$$B + H_2O \rightleftharpoons HB^+ + OH^- \quad \text{(I.16)}$$

The base dissociation constant

$$K_b = \frac{[HB^+][OH^-]}{[B]} \quad \text{(I.17)}$$

Since $pOH = -\log_{10}[OH^-]$ and $pK_b = -\log_{10}[K_b]$, Equation (I.17) becomes

$$pK_b = pOH + \log_{10}\frac{[B]}{[HB^+]} \quad \text{(I.18)}$$

Since $pK_a + pK_b = 14$ and $pH + pOH = 14$, Equation (I.18) becomes

$$14 - pK_a = 14 - pH + \log_{10}\frac{[B]}{[HB^+]} \quad \text{(I.19)}$$

$$pH = pK_a + \log_{10}\frac{[B]}{[HB^+]} \quad \text{(I.20)}$$

It is worth noting that the expression for pendant basic ligands (e.g. DMAEM) is similar to that for pendant acidic ligands (e.g. MAA). The ratio

of $\frac{[A^-]}{[HA]}$ (from Equation (I.5)) and $\frac{[B]}{[HB^+]}$ (from Equation (I.20)) represents the concentration ratio of non-protonated to protonated species within the pHEMA gel matrix. The difference though, is that the ionised component for acidic ligands is in the numerator, $[A^-]$, but the ionised component for basic ligands is in the denominator, $[HB^+]$.

Assuming the ideal case where the extent of ionisation, θ, within the pHEMA matrix causes a linear change in the peak diffracted wavelength, the equation of the modified normalised Henderson-Hasselbalch calibration curve for the apparent pK_a of the holosensor is as follows:

$$pH = pK_a + \log_{10}\frac{1-\alpha}{\alpha} \tag{I.21}$$

which then becomes

$$10^{pH-pK_a} = \frac{1-\alpha}{\alpha} \tag{I.22}$$

The extent of ionisation, α, is the same as Equation (I.8), and Equation (I.22) becomes

$$10^{pH-pK_a} = \frac{\lambda_{max}-\lambda}{\lambda-\lambda_{min}} \tag{I.23}$$

The predicted pH can be derived by rearranging Equation (I.23)

$$pH = \log_{10}\left(\frac{\lambda_{max}-\lambda}{\lambda-\lambda_{min}}\right) + pK_a \tag{I.24}$$

By expanding the expression and making λ the subject, Equation (I.23) becomes

$$\boxed{\lambda = \frac{\lambda_{max} + \lambda_{min}\cdot(10^{pH-pK_a})}{1+10^{pH-pK_a}}} \tag{I.25}$$

Differentiating λ wrt to pH using the quotient rule,

$$\boxed{\frac{d\lambda}{dpH} = \frac{10^{pH-pK_a}\cdot \ln 10\,(\lambda_{min}-\lambda_{max})}{(1+10^{pH-pK_a})^2}} \tag{I.26}$$

At $\frac{d\lambda}{dpH}_{max}$, $pH = pK_a$. Equation (I.26) becomes

$$\boxed{\frac{d\lambda}{dpH} = (\lambda_{min}-\lambda_{max})\left(\frac{\ln 10}{4}\right)} \tag{I.27}$$

This equation describing the slope of the modified Henderson-Hasselbalch calibration curve for the pendant basic ligand differs from Equation (I.27) by a negative sign on the RHS of Equation (I.27). It is noteworthy that $\frac{d\lambda}{dpH}$ is negative for the calibration curve.

Appendix J: UV LED emission spectrum, power equivalence graph, substrate UV attenuation and transmittance

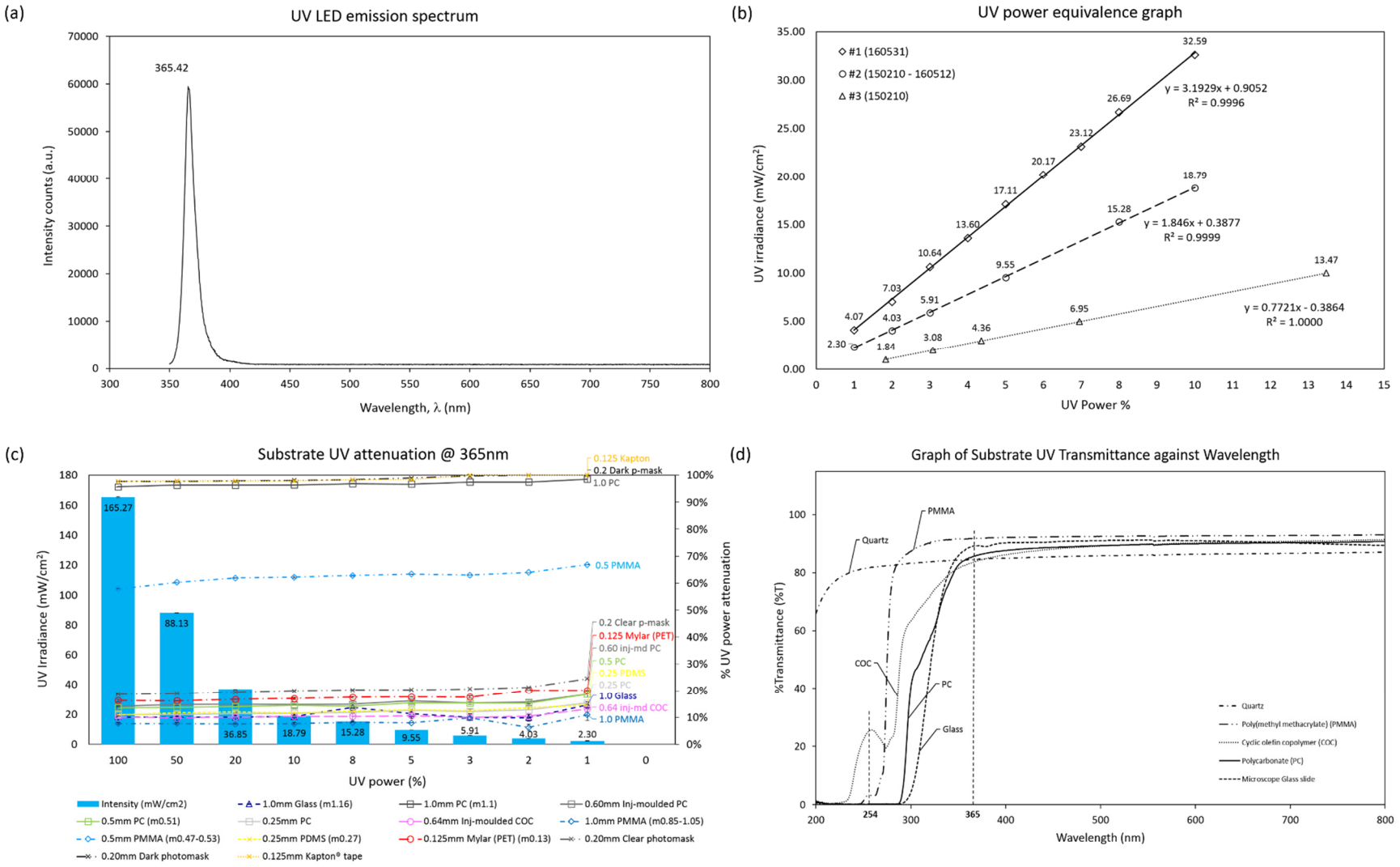

Figure J: ***(a)*** *UV LED emission spectrum.* ***(b)*** *UV LED power equivalence graph.* ***(c)*** *UV attenuation of various substrates.* ***(d)*** *UV transmittance of common substrates.*

Appendix K: Ionic strength correction for 3.0ϕ HEMA-co-EDMA-co-TFMPA (91.0:3.0:6.0 mol%) holosensor spot

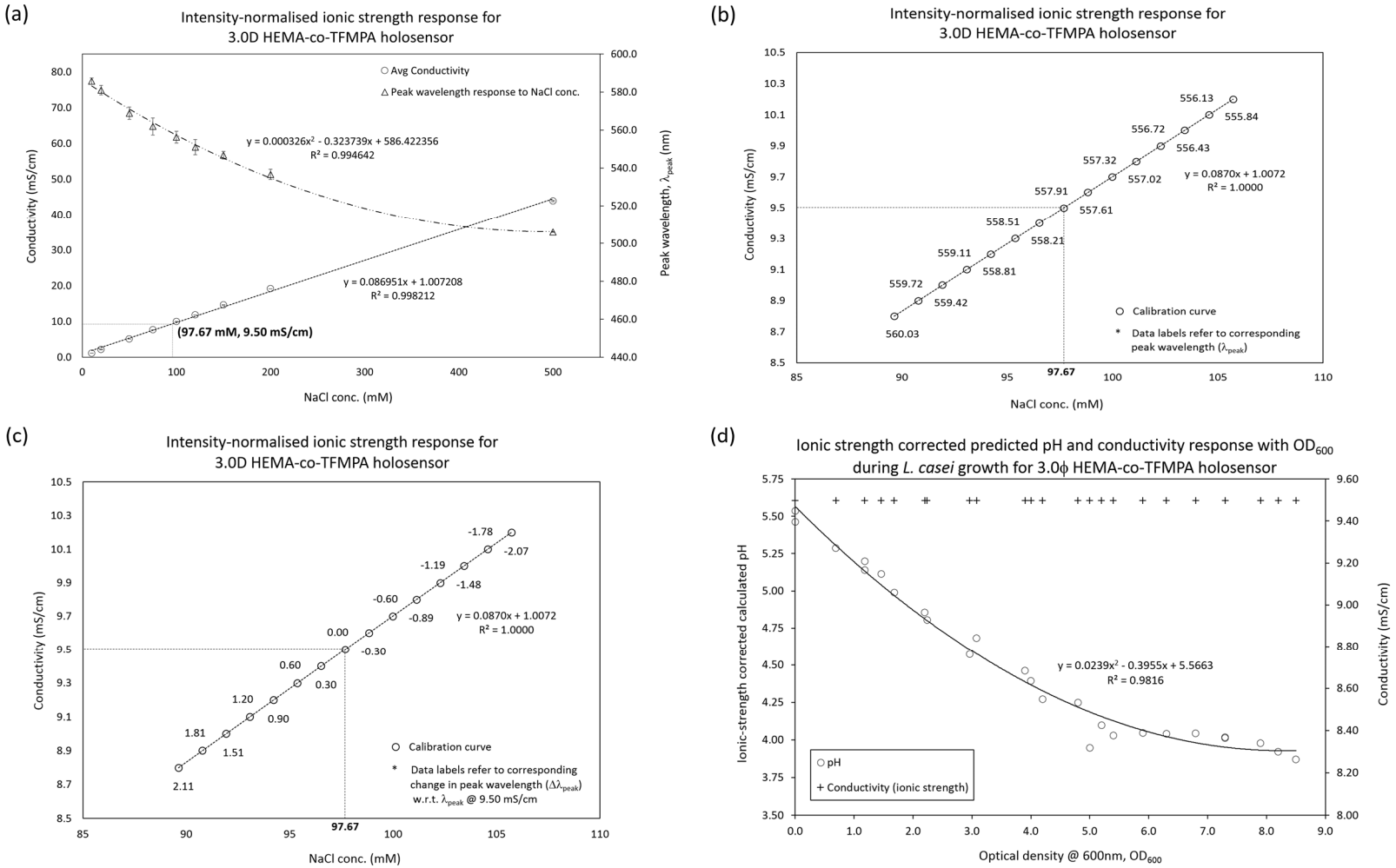

Figure K: ***(a)*** *Graph of average measured conductivity and average peak wavelength (from 3 separate runs) against varying NaCl concentrations. Error bars represents ± 1 s.d.* ***(b)*** *Graph of conductivity against corresponding NaCl and peak wavelength. The values were calculated from the equation of the best-fit curve in (a). Conductivity of 9.50 mS/cm translates to an equivalent 97.67 mM NaCl.* ***(c)*** *Graph of conductivity against normalised peak wavelength values (@ 9.50 mS/cm).* ***(d)*** *Ionic strength-corrected graph vs OD_{600} with normalised conductivity.*

Appendix L: Minimum chamber volume required to mitigate buffering capacity of holosensor

(a) **Calculation of buffering capacity of holosensor (0.46mm diameter gel)**

Measured gel height, h_{max} =	18.70	µm	
=	0.01870	mm	
Measured gel diameter, ϕ_{max} =	0.46	mm	
Resultant gel vol =	0.00311	µl	(assuming perfect cylindrical shape)
=	3.11	nl	
For TFMPA			
M_r of TFMPA =	140.06	g/mol	
%mol TFMPA (in 1ml solvent) =	6.0	%	of 8 mmol = 0.48000 mmol
Actual # mols TFMPA in gel =	1.49E-09	mols	(equiv. # mols as fraction of gel vol out of 1ml solvent)
=	1.49172	nmol	
Total weight of TFMPA in gel =	2.09E-07	g	(from M_r and actual # mols TFMPA in gel)
Conc. of TFMPA =	6.72E-17	g/L	
For L-Lactic acid			
M_r of L-Lactic acid =	90.08	g/mol	
Minimum amt of L-lactic acid (for 1% utilisation) =	149.17	nmol	(100X actual # mols TFMPA in gel)
=	1.49E-07	mols	
L-Lactic acid production by L. casei =	80.00	g/L	(Senedese et al., 2015)
Conc. of L-Lactic acid production (by L. casei) =	8.88E-01	mol/L	(from M_r of L-Lactic acid and acid production by L. casei)
For the min. L-Lactic acid amt (1% util.), corresponding vol. =	1.68E-07	L	
=	167.97	nL	
For 75um high chamber, diameter, d to neglect buffering capacity =	1.69	mm	
=	1688.6	µm	

Util %	Minimum ϕ (mm)					
	80 g/L, 75 µm chamber	L-Lactic acid prod. (10 g/L)	L-Lactic acid prod. (20 g/L)	L-Lactic acid prod. (40 g/L)	100 µm chamber	125 µm chamber
1.00%	1.69	4.78	3.38	2.39	1.46	1.31
3.00%	0.97	2.97	1.95	1.38	0.84	0.75
5.00%	0.76	2.14	1.51	1.07	0.65	0.58
10.00%	0.53	1.51	1.07	0.76	0.46	0.41

(b) **Calculation of buffering capacity of holosensor (3.27mm diameter gel)**

Measured gel height, h_{max} =	18.90	µm	
=	0.01890	mm	
Measured gel diameter, ϕ_{max} =	3.27	mm	
Resultant gel vol =	0.15873	µl	(assuming perfect cylindrical shape)
=	158.73	nl	
For TFMPA			
M_r of TFMPA =	140.06	g/mol	
%mol TFMPA (in 1ml solvent) =	6.0	%	of 8 mmol = 0.48000 mmol
Actual # mols TFMPA in gel =	7.62E-08	mols	(equiv. # mols as fraction of gel vol out of 1ml solvent)
=	76.18833	nmol	
Total weight of TFMPA in gel =	1.07E-05	g	(from M_r and actual # mols TFMPA in gel)
Conc. of TFMPA =	6.72E-17	g/L	
For L-Lactic acid			
M_r of L-Lactic acid =	90.08	g/mol	
Minimum amt of L-lactic acid (for 5% utilisation) =	1523.77	nmol	(20X actual # mols TFMPA in gel)
=	1.52E-06	mols	
L-Lactic acid production by L. casei =	80.00	g/L	(Senedese et al., 2015)
Conc. of L-Lactic acid production (by L. casei) =	8.88E-01	mol/L	(from M_r of L-Lactic acid and acid production by L. casei)
For the min. L-Lactic acid amt (5% util.), corresponding vol. =	1.72E-06	L	
=	1715.76	nL	
For 75um high chamber, diameter, d to neglect buffering capacity =	5.40	mm	
=	5397.0	µm	

Util %	Minimum ϕ (mm)					
	80 g/L, 75 µm chamber	L-Lactic acid prod. (10 g/L)	L-Lactic acid prod. (20 g/L)	L-Lactic acid prod. (40 g/L)	100 µm chamber	125 µm chamber
1.00%	12.07	34.13	24.14	17.07	10.45	9.35
3.00%	6.96	19.70	13.93	9.85	6.03	5.39
5.00%	5.40	15.27	10.79	7.63	4.67	4.18
10.00%	3.82	10.79	7.63	5.40	3.30	2.96

*Figure L: Minimum chamber volume required to minimise TFMPA (pH moiety) buffering capacity for **(a)** 0.46ϕ holosensor and **(b)** 3.27ϕ holosensor*

Appendix M: Relative proportion of DMPA (by size)

(a) TFMPA - Formula (8 mmol/ml - TH-2) 1.0 DMPA (2:1 HQ)

Density of IPA = 0.786 g/cm^3 (20°C)

Total # mmol/ml = 8 mmol/ml (We want 8mmol constituents in 1ml IPA)

mol %	Gel precursor	M_r (g/mol)	Normalised M_r	Total amt (mmol)	Total amt /ml (mmol/ml)	Relative "molecular volume"	% (in 1ml)
91.00%	HEMA	130.14	2.17	7.28000	3.77535	8.17510	50.66%
3.00%	EDMA	198.22	3.30	0.24000	0.12446	0.41050	2.54%
6.00%	TFMPA	140.06	2.33	0.48000	0.24892	0.58010	3.59%
66.67%	DMPA	256.30	4.26	0.07070	0.03666	0.15636	0.97%
33.33%	HQ	110.11	1.83	0.03535	0.01833	0.03359	0.21%
	IPA	60.10	1.00	13.07820	6.78224	6.78224	42.03%
	Total	-	-	21.18	10.98597	16.13789	100.00%

* Total volume of liquids = 1.92830 ml

(b) TFMPA - Formula (8 mmol/ml - TH-2) 1/18 DMPA (2:1 HQ)

Density of IPA = 0.786 g/cm^3 (20°C)

Total # mmol/ml = 8 mmol/ml (We want 8mmol constituents in 1ml IPA)

mol %	Gel precursor	M_r (g/mol)	Normalised M_r	Total amt (mmol)	Total amt /ml (mmol/ml)	Relative "molecular volume"	% (in 1ml)
91.00%	HEMA	130.14	2.17	7.28000	3.77535	8.17510	51.23%
3.00%	EDMA	198.22	3.30	0.24000	0.12446	0.41050	2.57%
6.00%	TFMPA	140.06	2.33	0.48000	0.24892	0.58010	3.64%
66.67%	DMPA	256.30	4.26	0.00393	0.00204	0.00869	0.05%
33.33%	HQ	110.11	1.83	0.00196	0.00102	0.00187	0.01%
	IPA	60.10	1.00	13.07820	6.78224	6.78224	42.50%
	Total	-	-	21.08	10.93403	15.95850	100.00%

* Total volume of liquids = 1.92840 ml

(c)

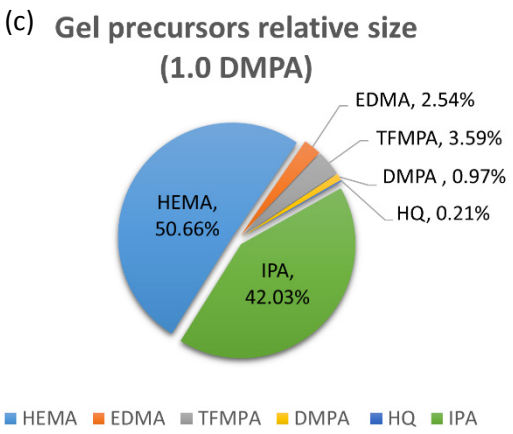

(d)

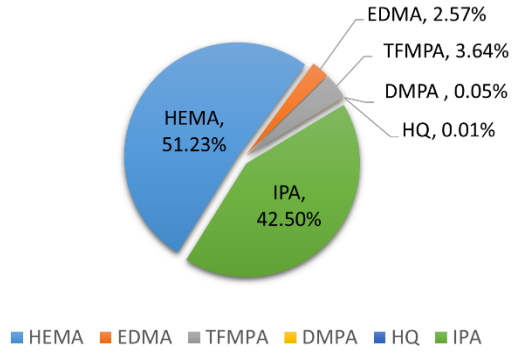

Figure M: Calculations for gel precursors' proportion (based on relative size), by normalising to the M_r of IPA. Note the % relative "molecular volume" (in 1 mL). ***(a)*** *Relative proportion of 1.0 DMPA.* ***(b)*** *Relative proportion of 1/18 DMPA.* ***(c & d)*** *Graphic representation of DMPA proportion for 1.0 and 1/18 DMPA respectively; the numbers ("1.0" and "1/18") represent the multiplier compared to previous work with pH holosensors*

Appendix N: Ionic strength correction for 0.4ϕ HEMA-co-EDMA-co-TFMPA (91.0:3.0:6.0 mol%) holosensor spot

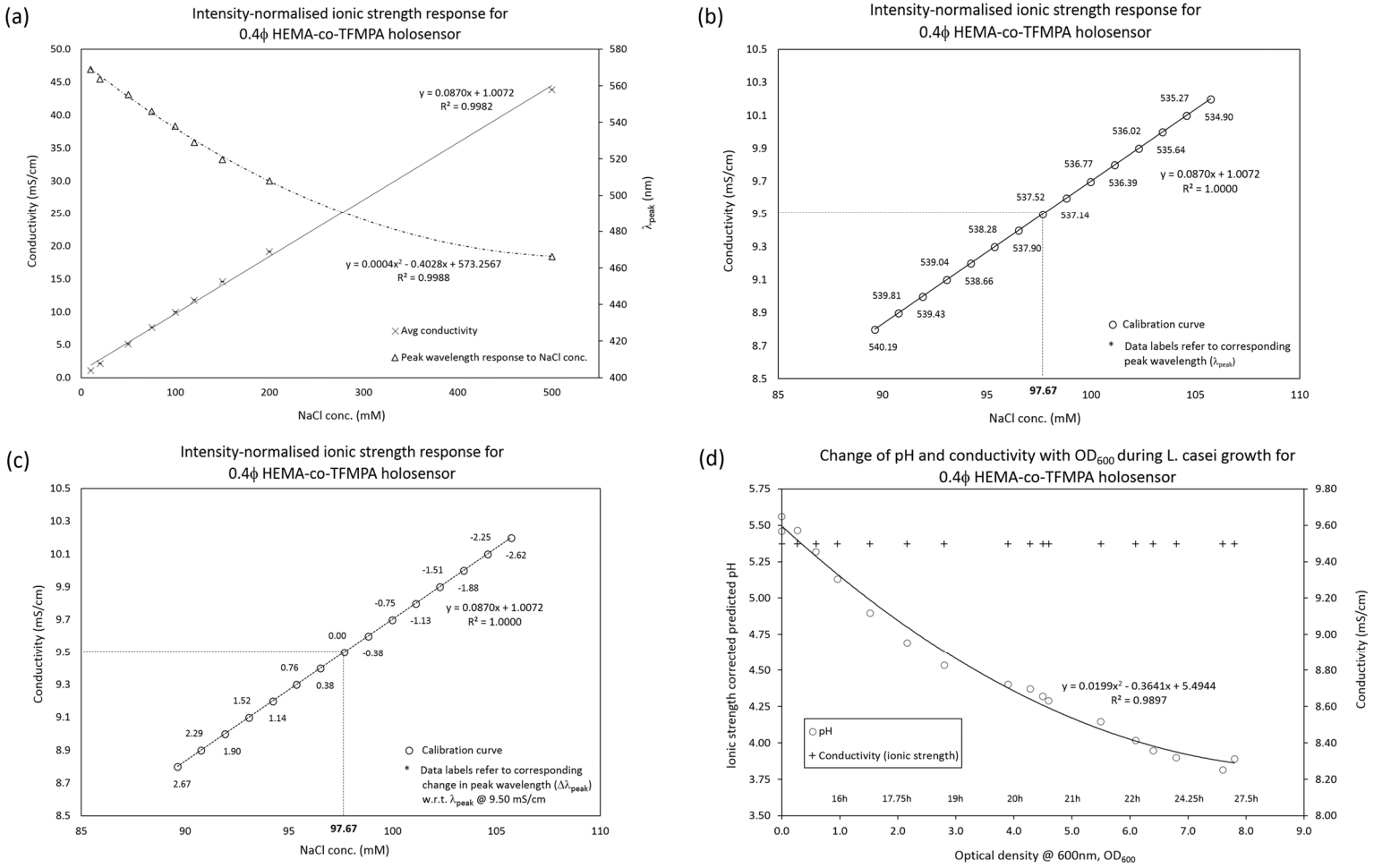

Figure N: ***(a)*** *Graph of average measured conductivity and peak wavelength against varying NaCl concentrations. Error bars represents ± 1 s.d.* ***(b)*** *Graph of conductivity against corresponding NaCl and peak wavelength. The values were calculated from the equation of the best-fit curve in (a). Conductivity of 9.50 mS/cm translates to an equivalent 97.67 mM NaCl.* ***(c)*** *Graph of conductivity against normalised peak wavelength values (@ 9.50 mS/cm).* ***(d)*** *Ionic strength-corrected graph vs OD_{600} with normalised conductivity.*

Appendix O: 0.4ϕ HEMA-co-TFMPA holosensor array

O-1 Holograms of 0.4ϕ HEMA-co-TFMPA array – pH calibration

Whole 0.4ϕ HEMA-co-TFMPA array (6.96X magnification, 5 ms exposure)

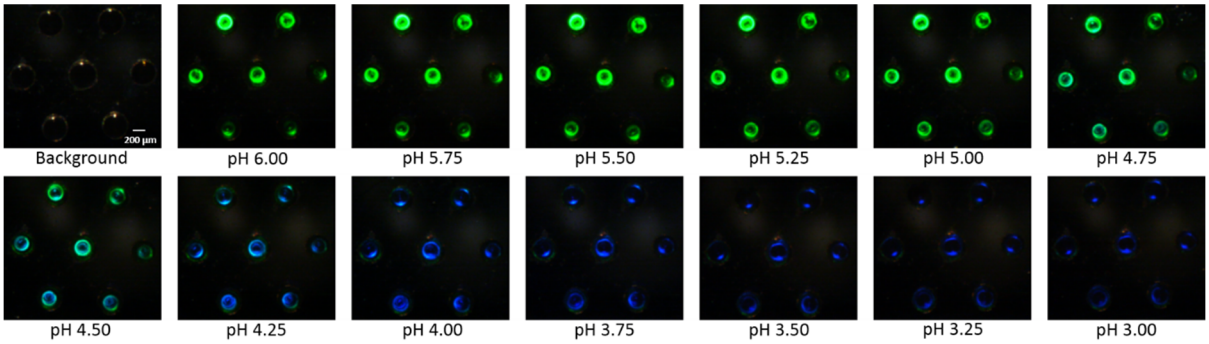

1 of 7: 0.4ϕ HEMA-co-TFMPA array (24X magnification, 2 ms exposure)

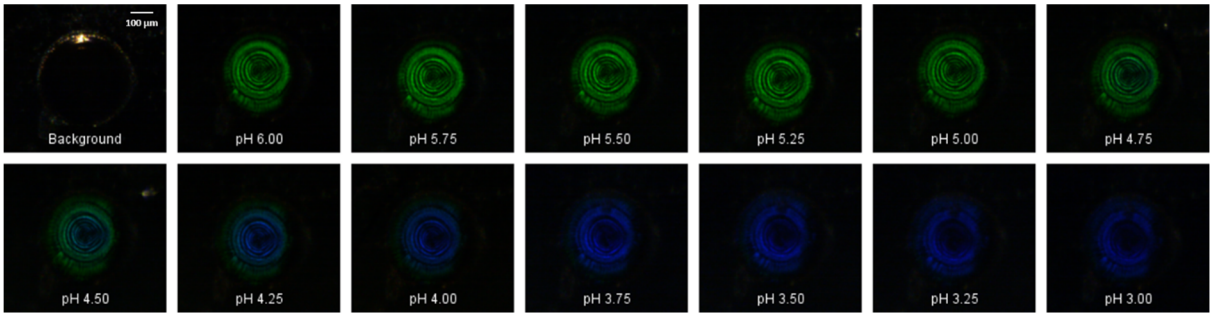

2 of 7: 0.4ϕ HEMA-co-TFMPA array (24X magnification, 2 ms exposure)

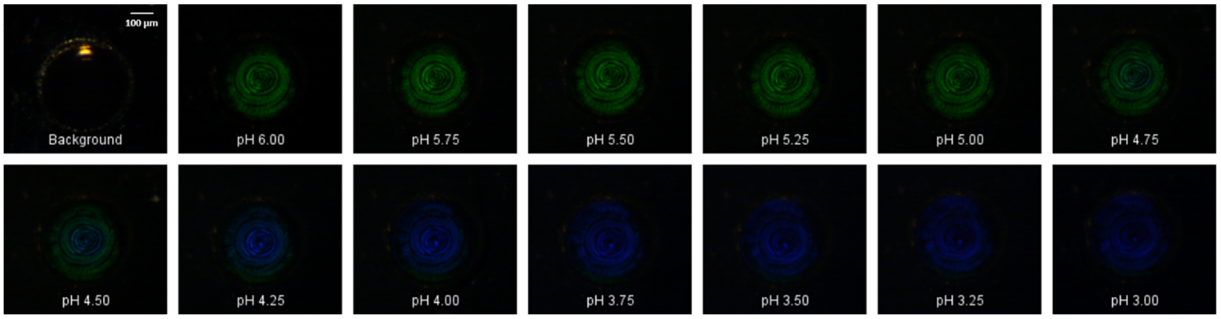

3 of 7: 0.4ϕ HEMA-co-TFMPA array (24X magnification, 2 ms exposure)

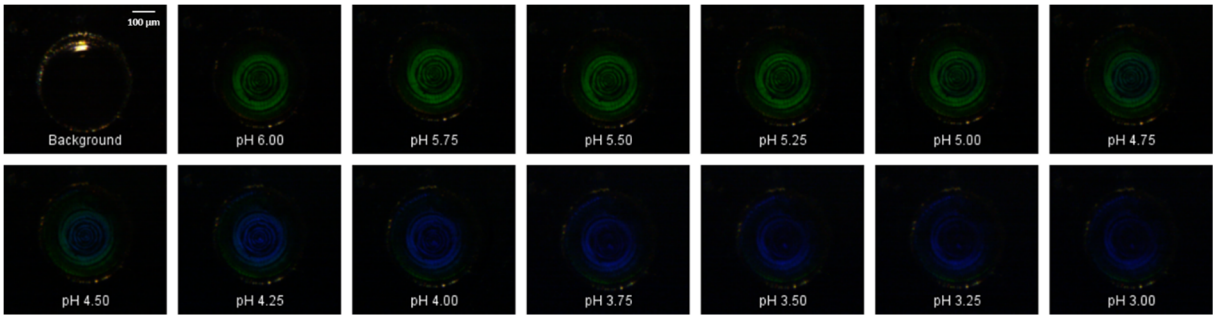

Appendix O: 0.4ϕ HEMA-co-TFMPA holosensor array

O-1 Holograms of 0.4ϕ HEMA-co-TFMPA array – pH calibration (contd.)

4 of 7: 0.4ϕ HEMA-co-TFMPA array (24X magnification, 2 ms exposure)

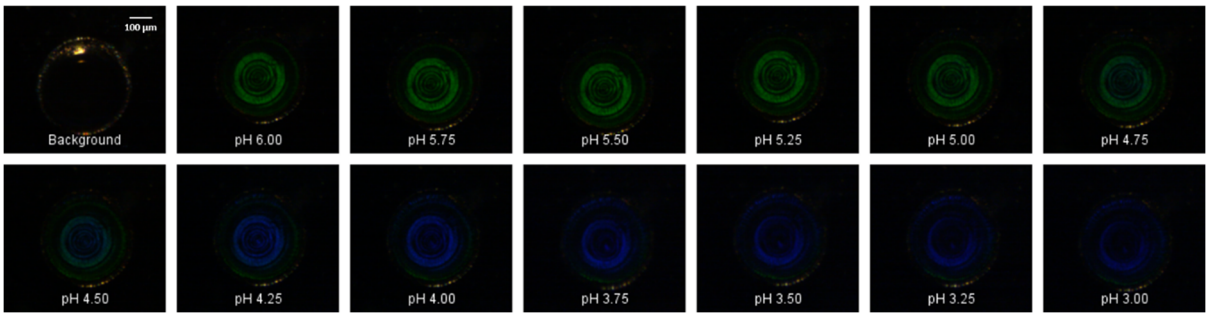

5 of 7: 0.4ϕ HEMA-co-TFMPA array (24X magnification, 2 ms exposure)

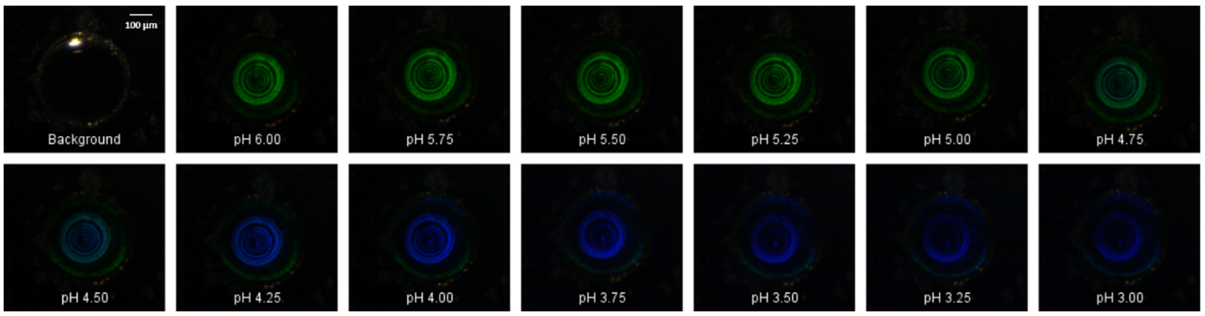

6 of 7: 0.4ϕ HEMA-co-TFMPA array (24X magnification, 2 ms exposure)

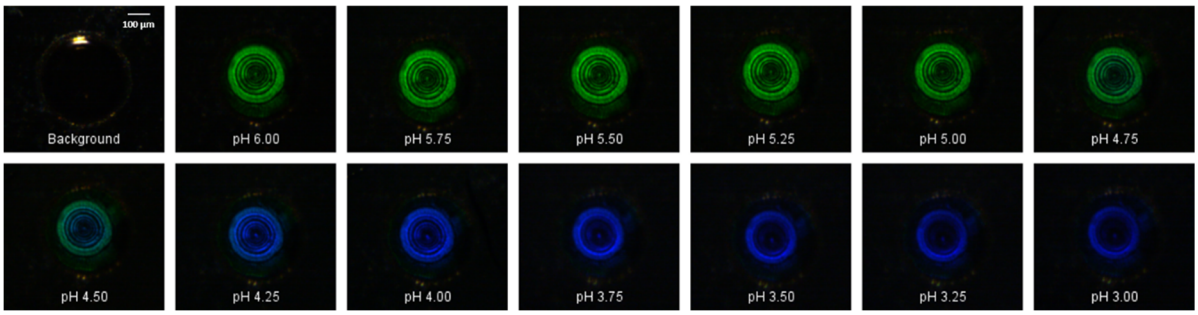

7 of 7: 0.4ϕ HEMA-co-TFMPA array (24X magnification, 2 ms exposure)

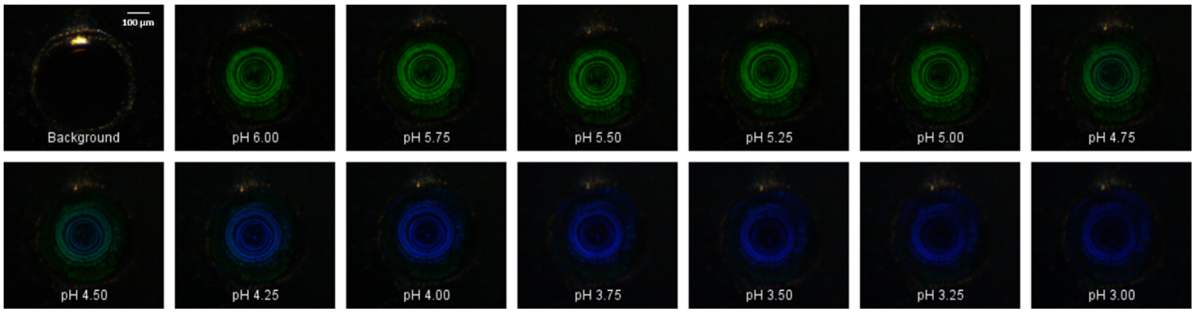

Appendix O: 0.4ϕ HEMA-co-TFMPA holosensor array

O-2 Holograms of 0.4ϕ HEMA-co-TFMPA array – Monitoring of *L. casei* growth

Whole 0.4ϕ HEMA-co-TFMPA array (6.96X magnification, 5 ms exposure)

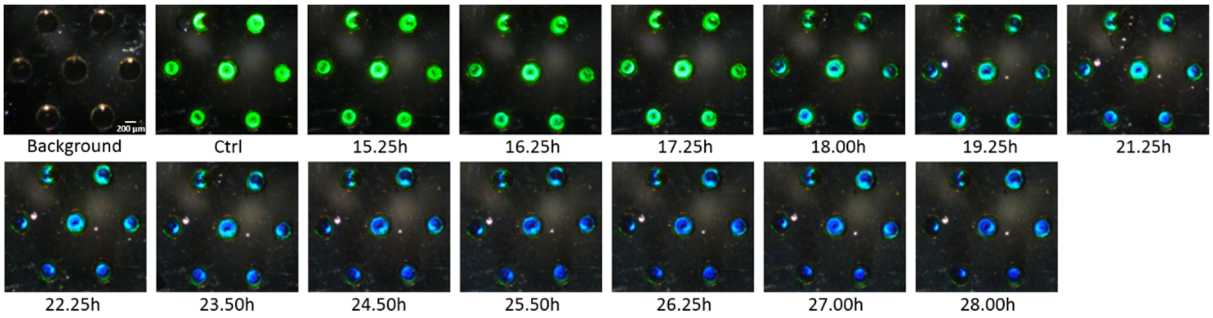

1 of 7: 0.4ϕ HEMA-co-TFMPA array (36X magnification, 5 ms exposure)

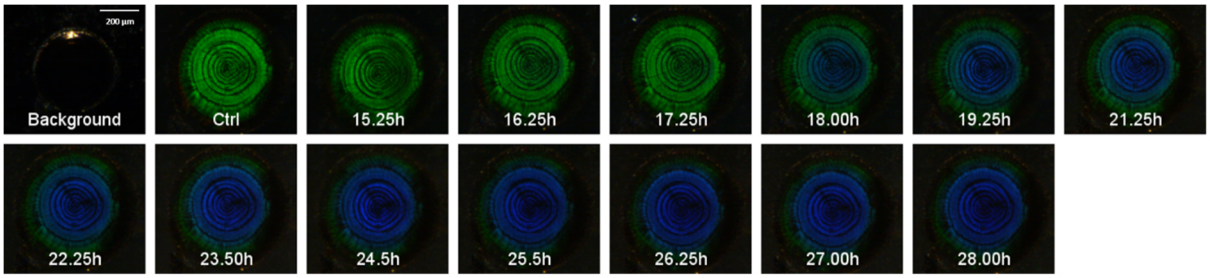

2 of 7: 0.4ϕ HEMA-co-TFMPA array (36X magnification, 5ms exposure)

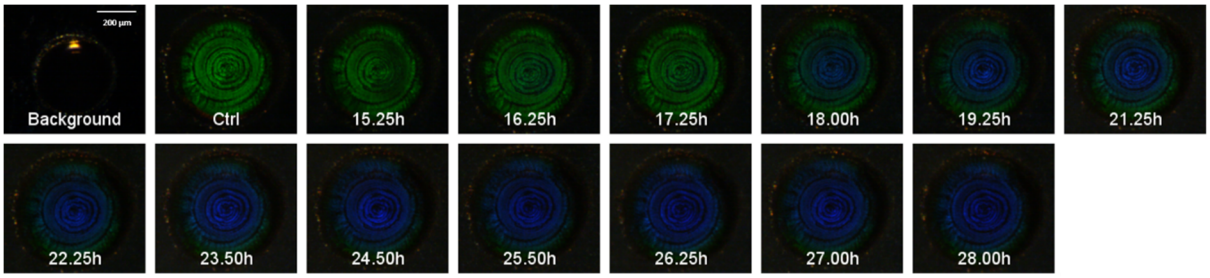

3 of 7: 0.4ϕ HEMA-co-TFMPA array (36X magnification, 5 ms exposure)

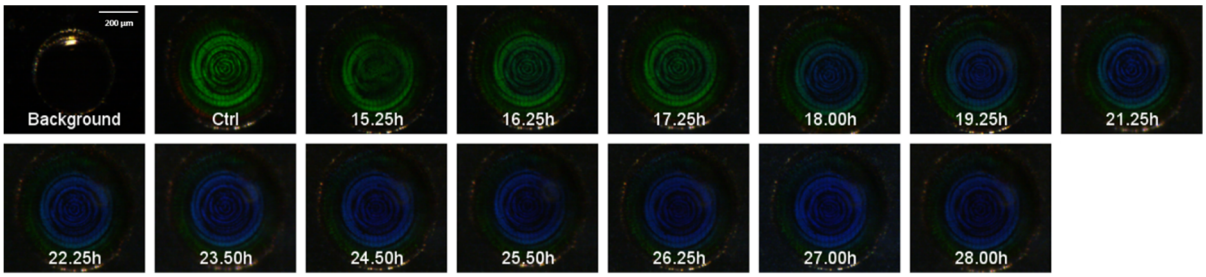

Appendix O: 0.4ϕ HEMA-co-TFMPA holosensor array

O-2 Holograms of 0.4ϕ HEMA-co-TFMPA array – Monitoring *L. casei* growth (contd.)

4 of 7: 0.4ϕ HEMA-co-TFMPA array (36X magnification, 5 ms exposure)

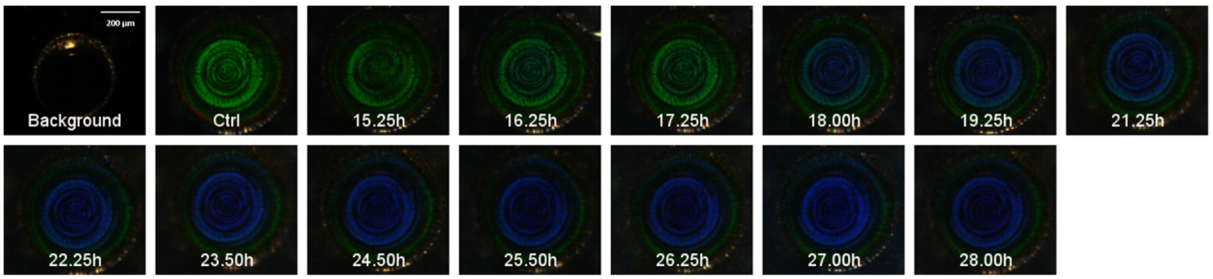

5 of 7: 0.4ϕ HEMA-co-TFMPA array (36X magnification, 5 ms exposure)

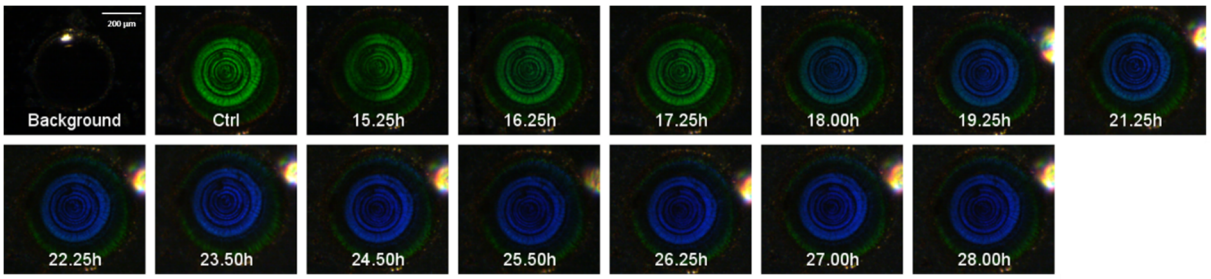

6 of 7: 0.4ϕ HEMA-co-TFMPA array (36X magnification, 5 ms exposure)

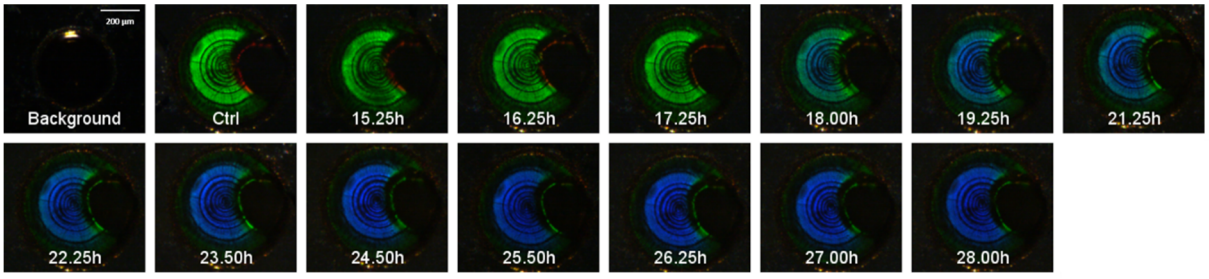

7 of 7: 0.4ϕ HEMA-co-TFMPA array (36X magnification, 5 ms exposure)

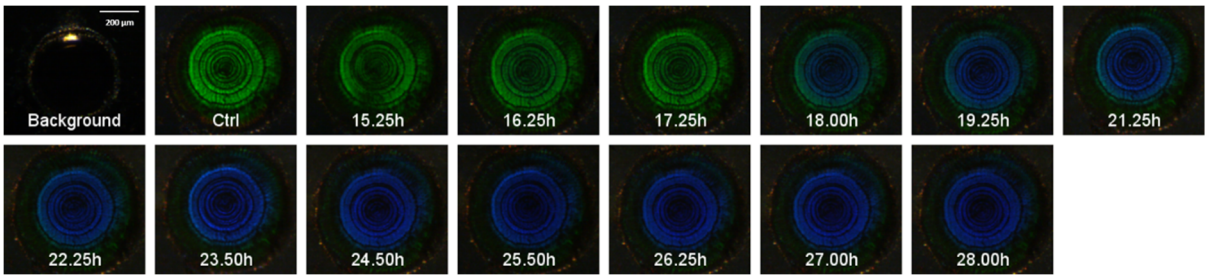

Appendix P: CIE 1931 chromaticity diagrams of 0.4ϕ HEMA-co-TFMPA holosensor array

P-1 0.4ϕ HEMA-co-TFMPA holosensor array CIExyY diagrams (pH characterisation)

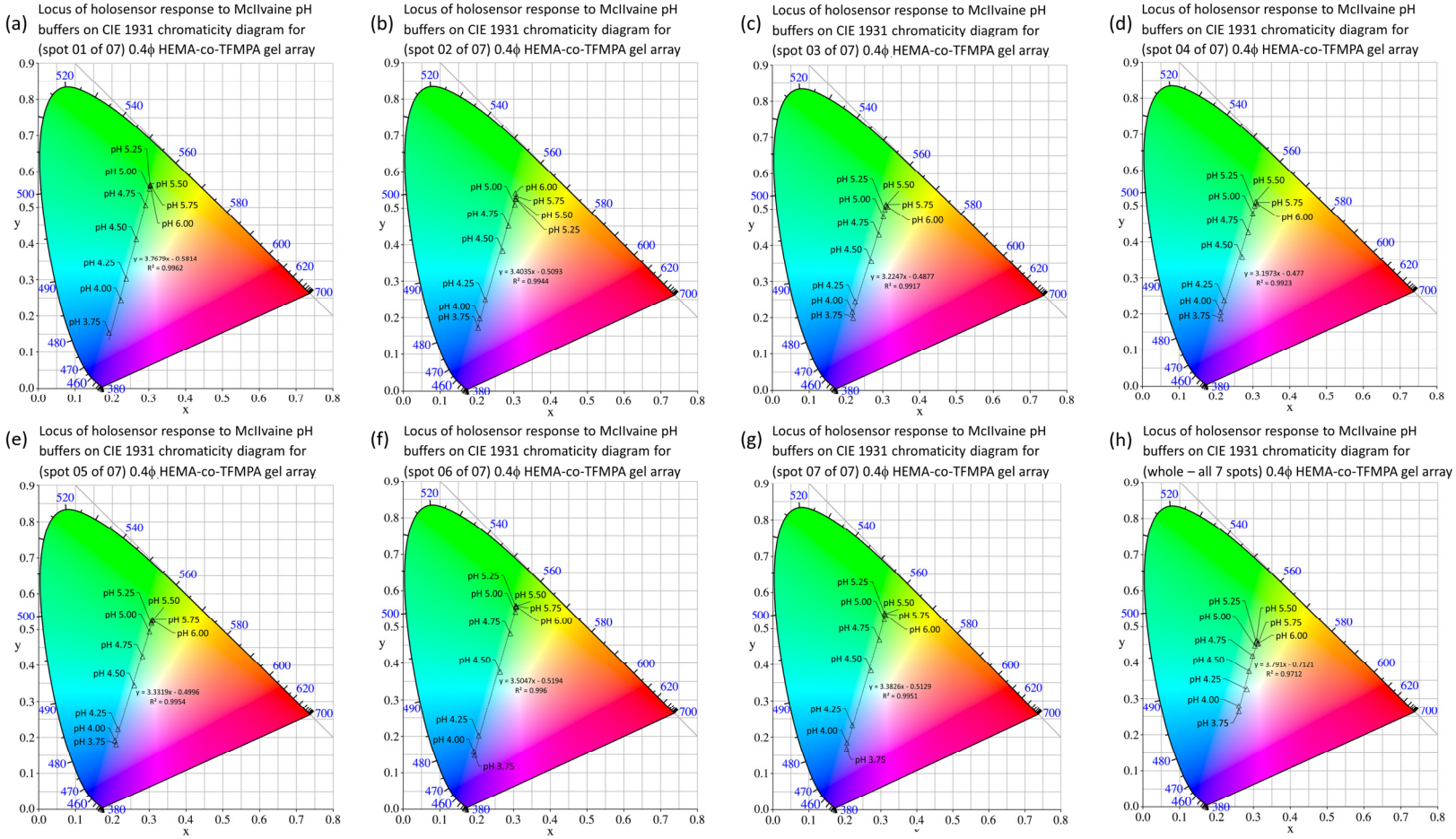

*Figure P-1: Collation of CIExyY diagrams obtained from transformed RGB values of 0.4ϕ HEMA-co-TFMPA holosensor pictures of **(a – g)** spots #1 to #7 respectively and **(h)** as a whole array during pH characterisation*

Appendix P: CIE 1931 chromaticity diagrams of 0.4ϕ HEMA-co-TFMPA holosensor array

P-2 0.4ϕ HEMA-co-TFMPA holosensor array CIExyY diagrams (*L. casei* interrogation)

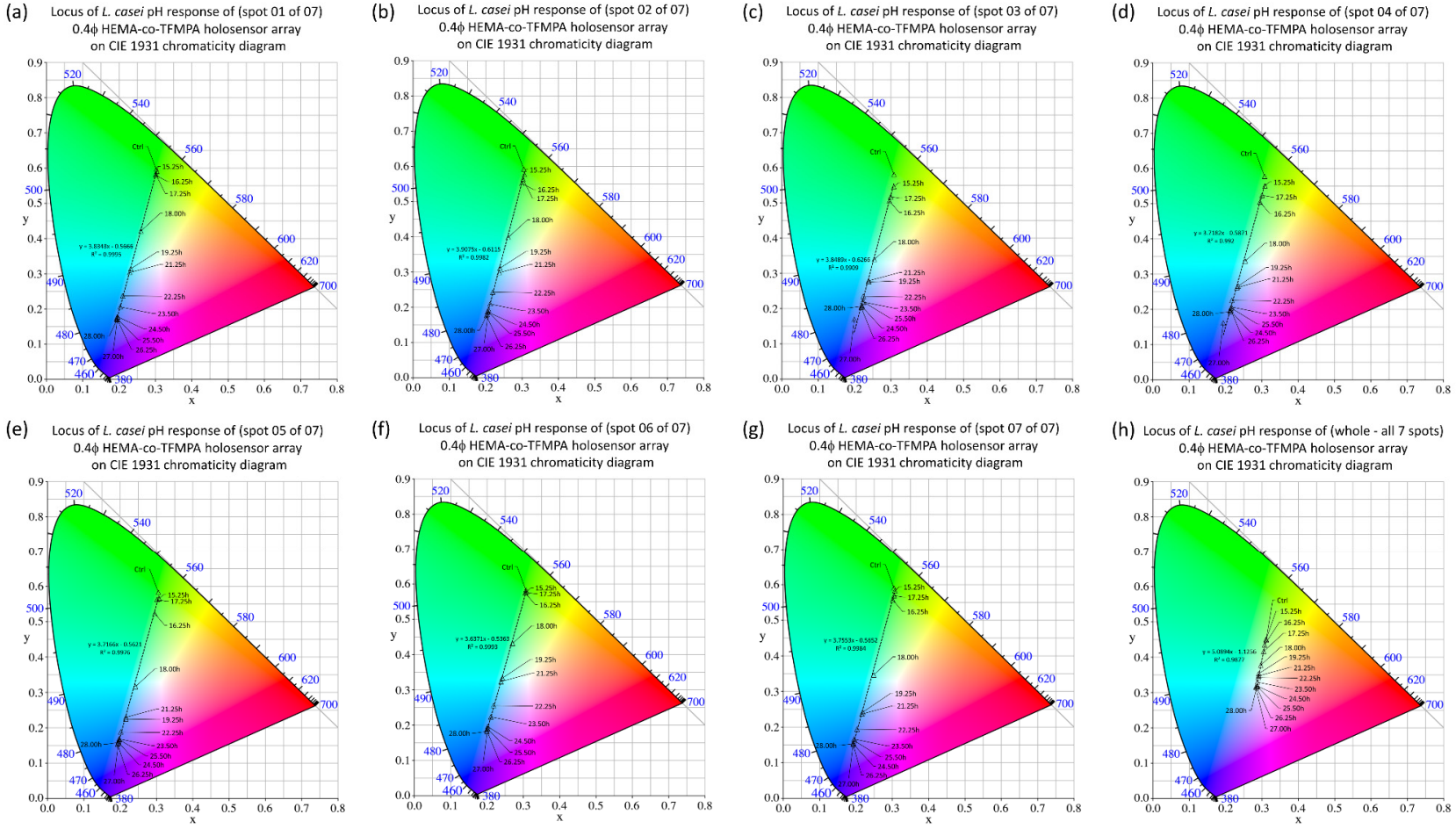

*Figure P-2: Collation of CIExyY diagrams obtained from RGB values of 0.4ϕ HEMA-co-TFMPA holosensor pictures of **(a – g)** spots #1 to #7 respectively and **(h)** as a whole array during L. casei interrogation*

Appendix Q: Graphs for 0.4ϕ HEMA-co-TFMPA holosensor array

Q-1 pH response (peak wavelength) of 0.4ϕ TFMPA holosensor array – pH calibration

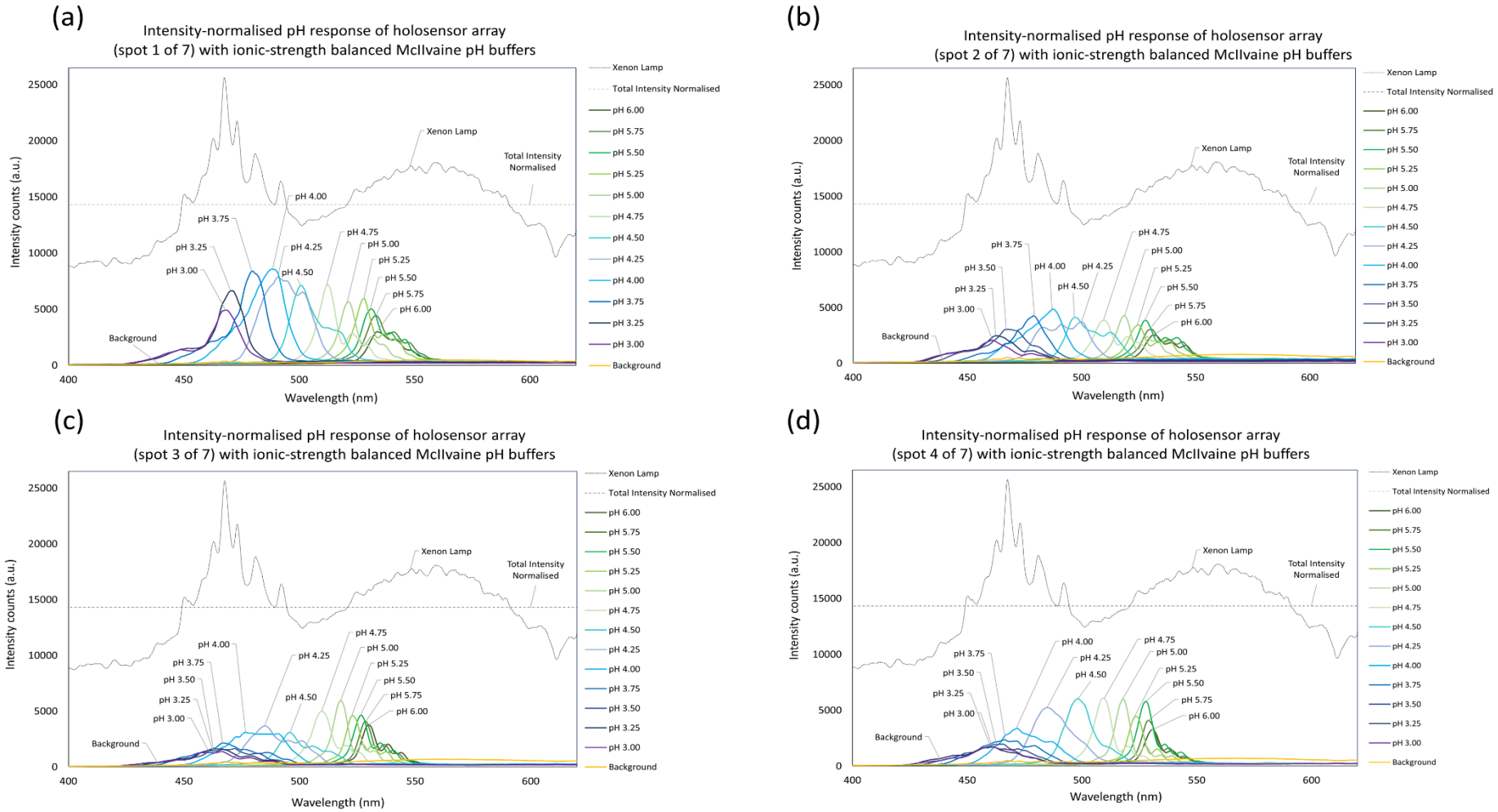

Figure Q-1: Peak wavelength pH responses of 0.4ϕ holosensor array ***(a – d)*** *spot #1 to #4 respectively (pH calibration with ionic strength balanced McIlvaine pH buffers)*

Q-1 Peak wavelength pH responses of 0.4ϕ TFMPA holosensor array – pH calibration (contd.)

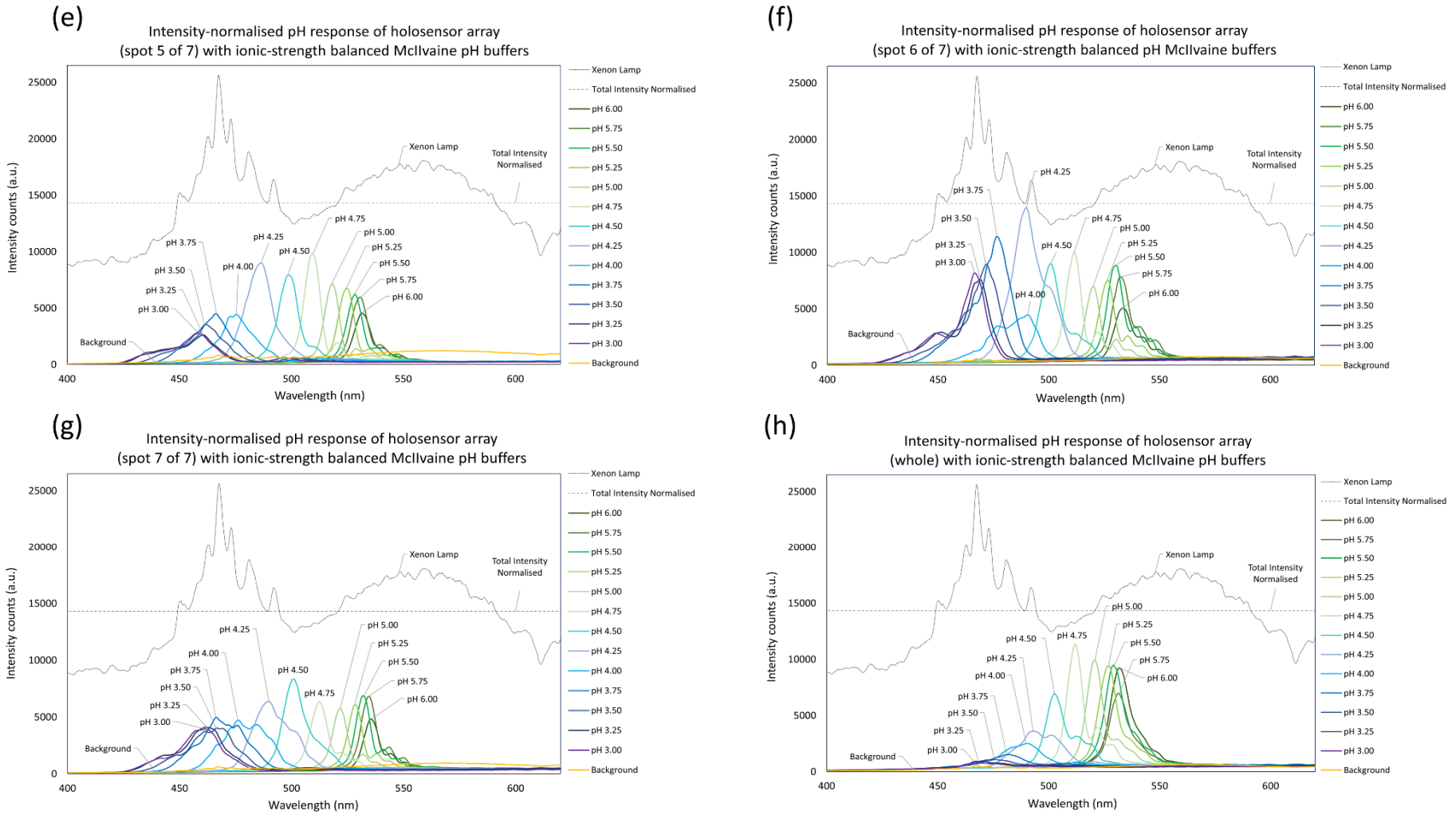

*Figure Q-1: Peak wavelength pH responses of 0.4ϕ holosensor array **(e – h)** spot #5 to #7 and of the whole array respectively (pH calibration with ionic strength balanced McIlvaine pH buffers)*

Q-2 Normalised average intensity & slope

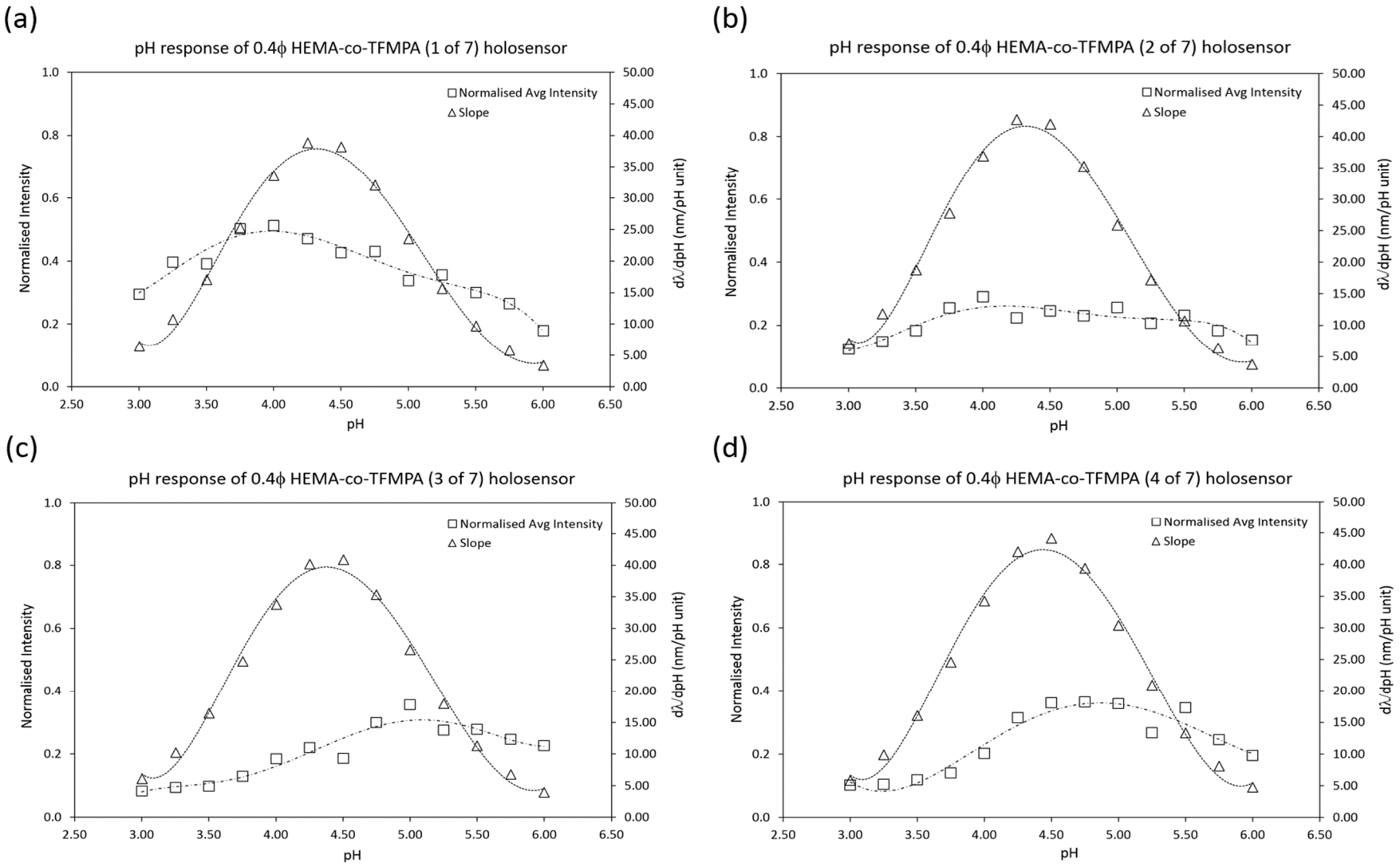

*Figure Q-2: Graphs of normalised average intensity and slope against pH for **(a – d)** 0.4ϕ holosensor array spot #1 to #4 respectively.*

Q-2 Normalised average intensity & slope (contd.)

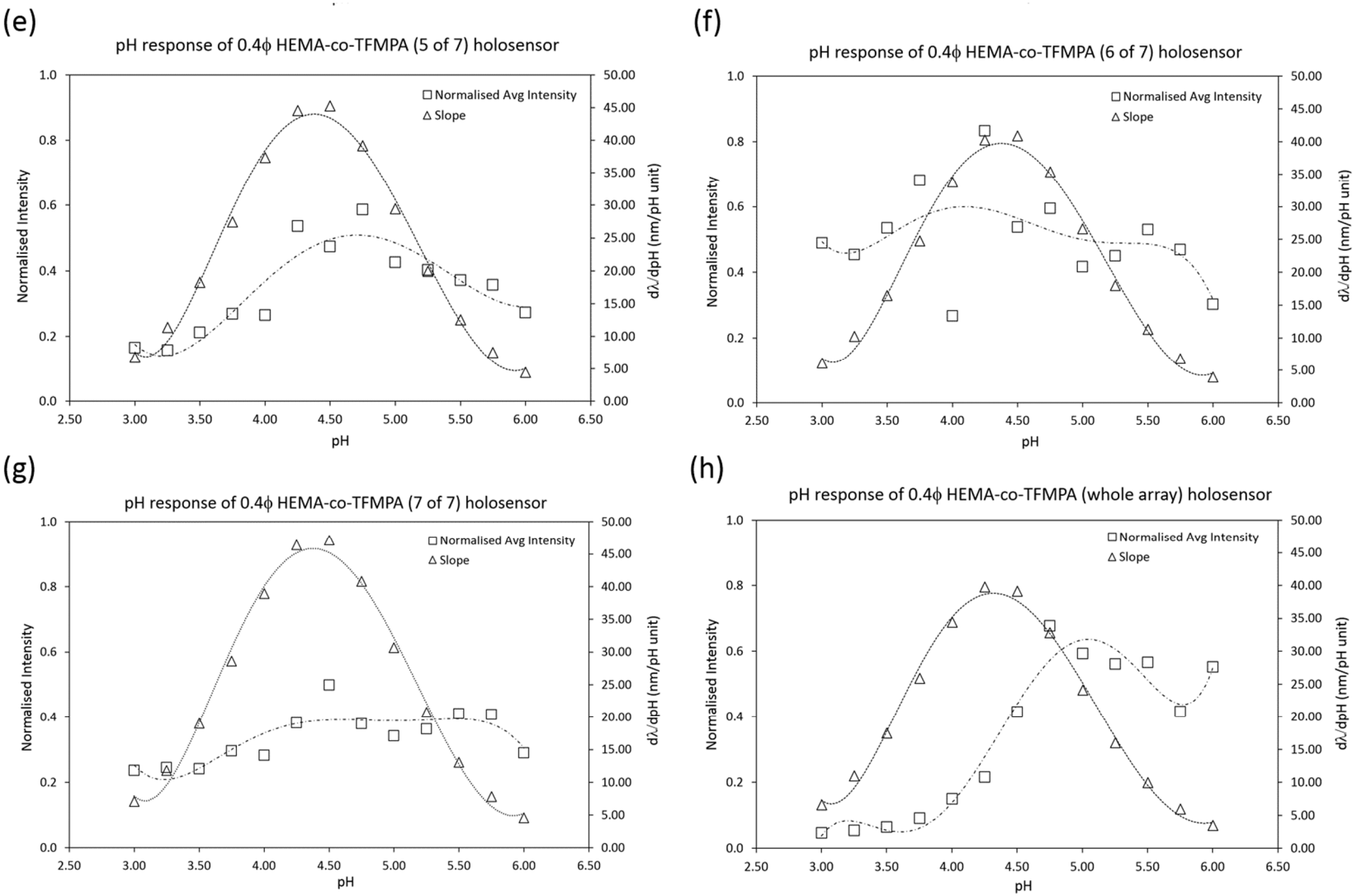

*Figure Q-2: Graphs of normalised average intensity and slope against pH for **(e - h)** 0.4ϕ holosensor array spot #5 to #7 and of the whole array respectively.*

Q-3 pH characterisation curves (using modified H-H equation)

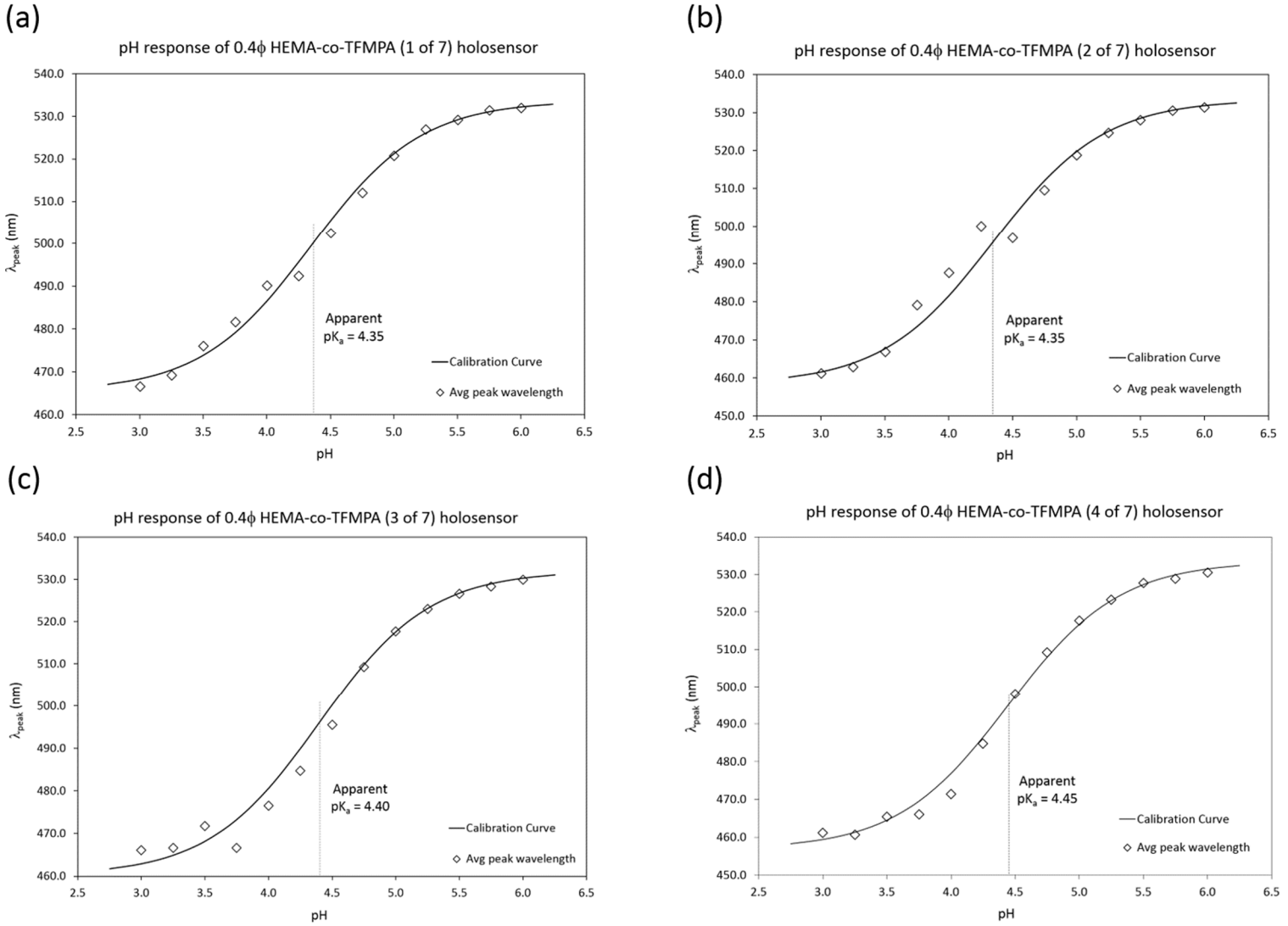

*Figure Q-3: pH calibration curve (using modified H-H equation) for **(a – d)** 0.4ϕ holosensorr array spot #1 to #4 respectively*

Q-3 pH characterisation curves (using modified H-H equation) (contd.)

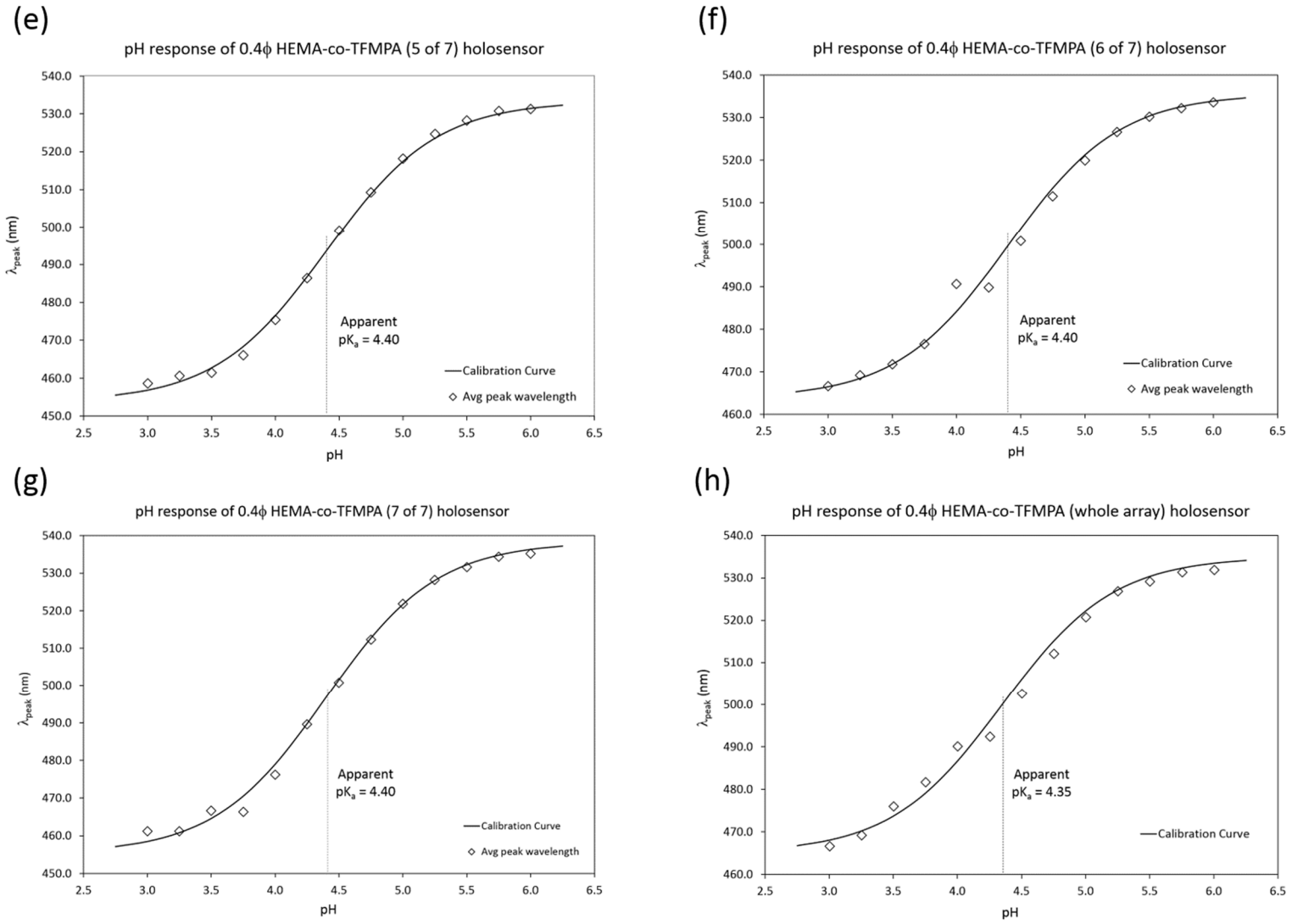

*Figure Q-3: pH calibration curve (using modified H-H equation) for **(e – h)** 0.4ϕ holosensorr array spot #5 to #7 and of the whole array respectively*

Q-4 Standard curve (Measured pH vs predicted pH)

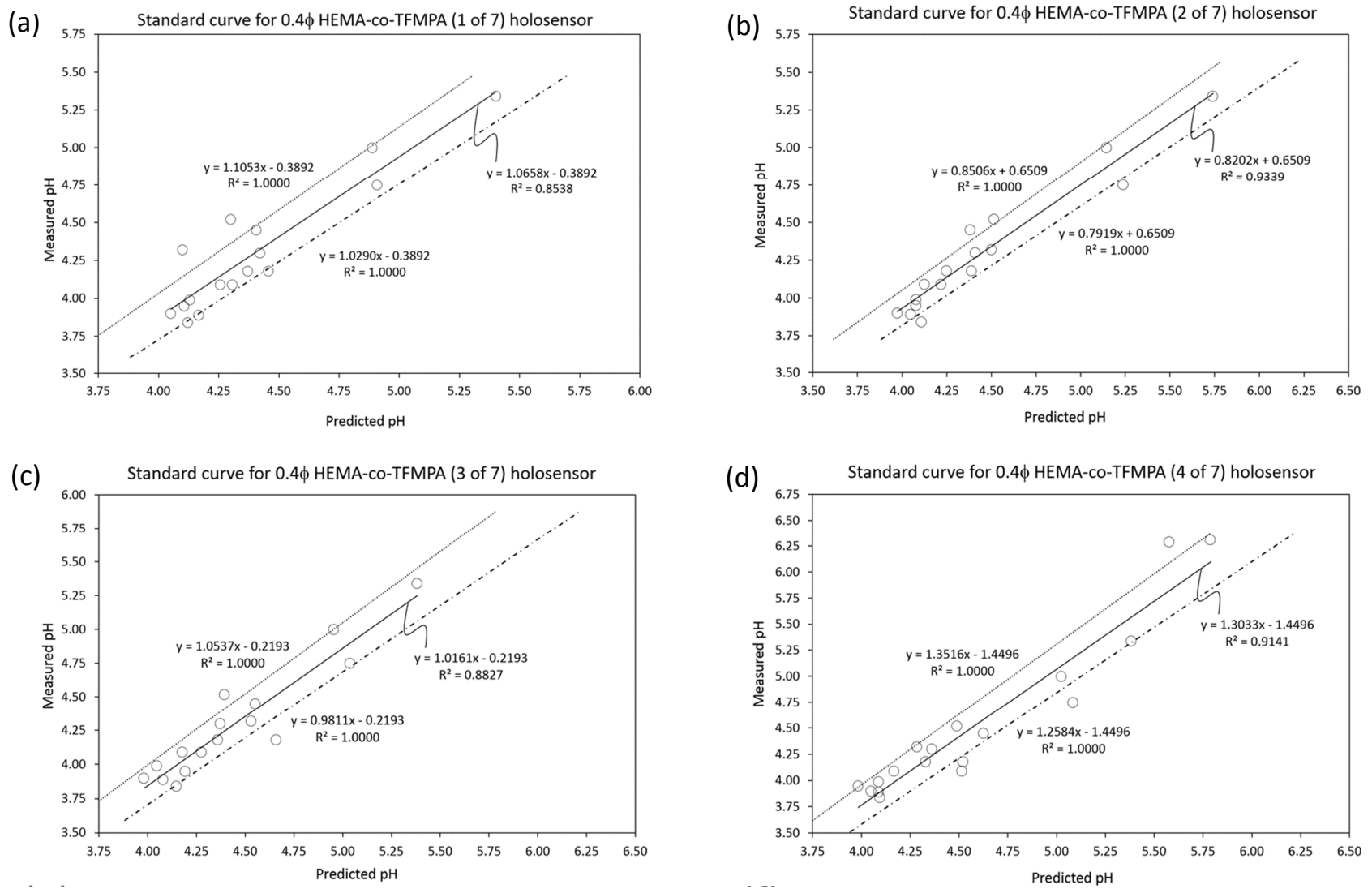

*Figure Q-4: Standard curves of measured pH vs predicted pH for **(a – d)** 0.4ϕ holosensor array spot #1 to #4 respectively*

Q-4 Standard curve (measured pH vs predicted pH) (contd.)

(e)

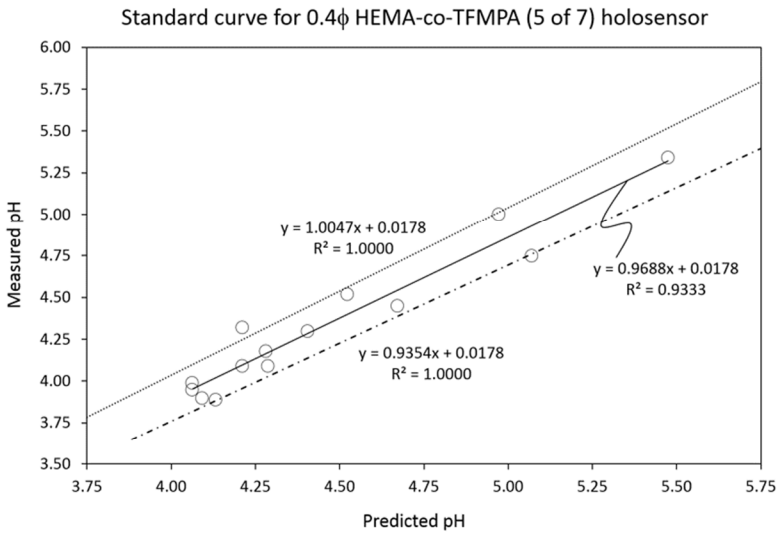

(f)

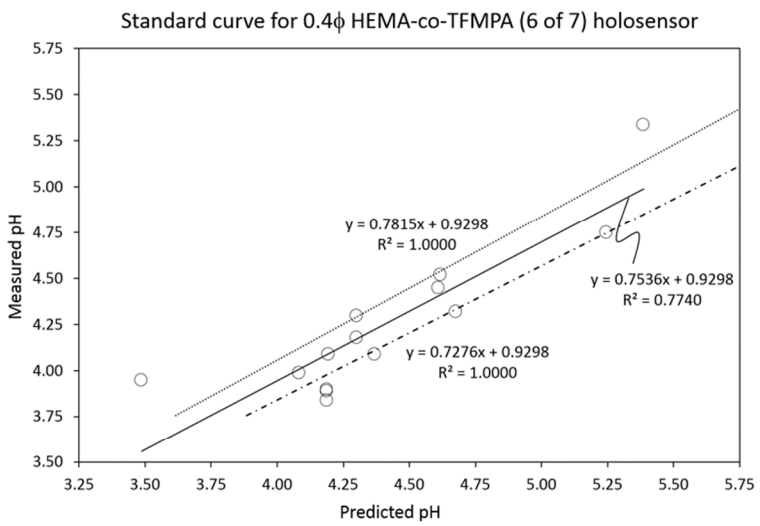

(g)

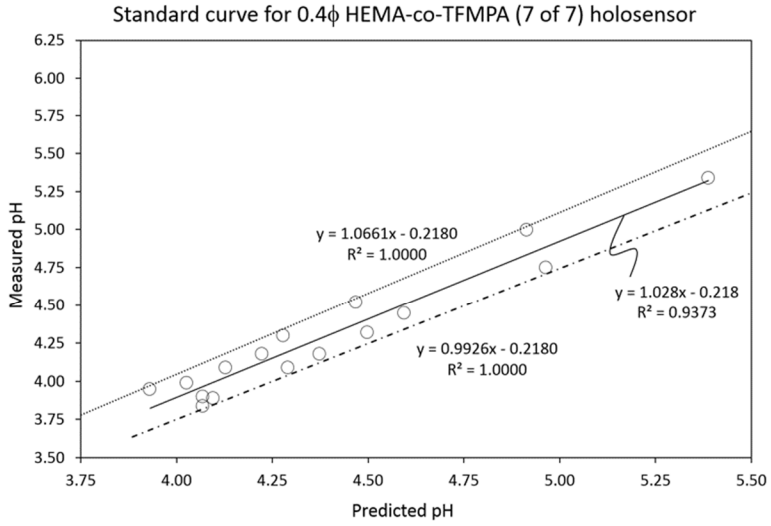

(h)

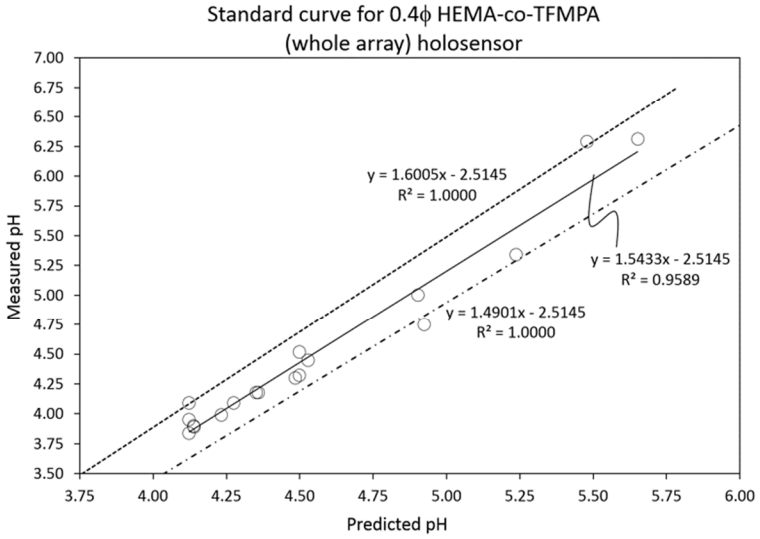

*Figure Q-4: Standard curves of measured pH vs predicted pH for **(e – h)** 0.4ϕ holosensor array spot #5 to #7 and of the whole array respectively*

Q-5 Measured pH vs OD_{600} curve (Ideal case)

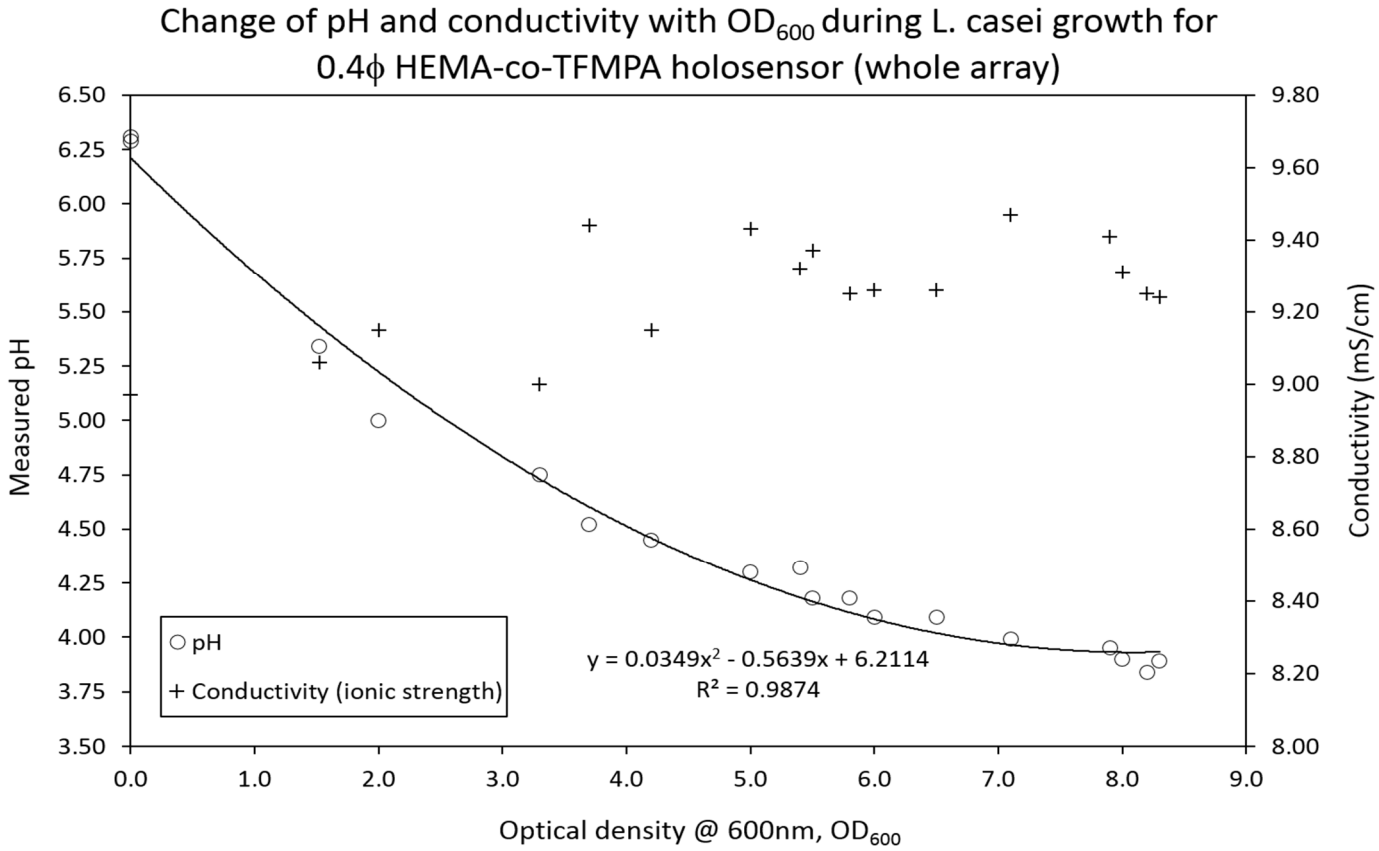

Figure Q-5: Measured pH vs OD_{600} curve (Ideal case)

Q-6 Predicted pH vs OD_{600} curves

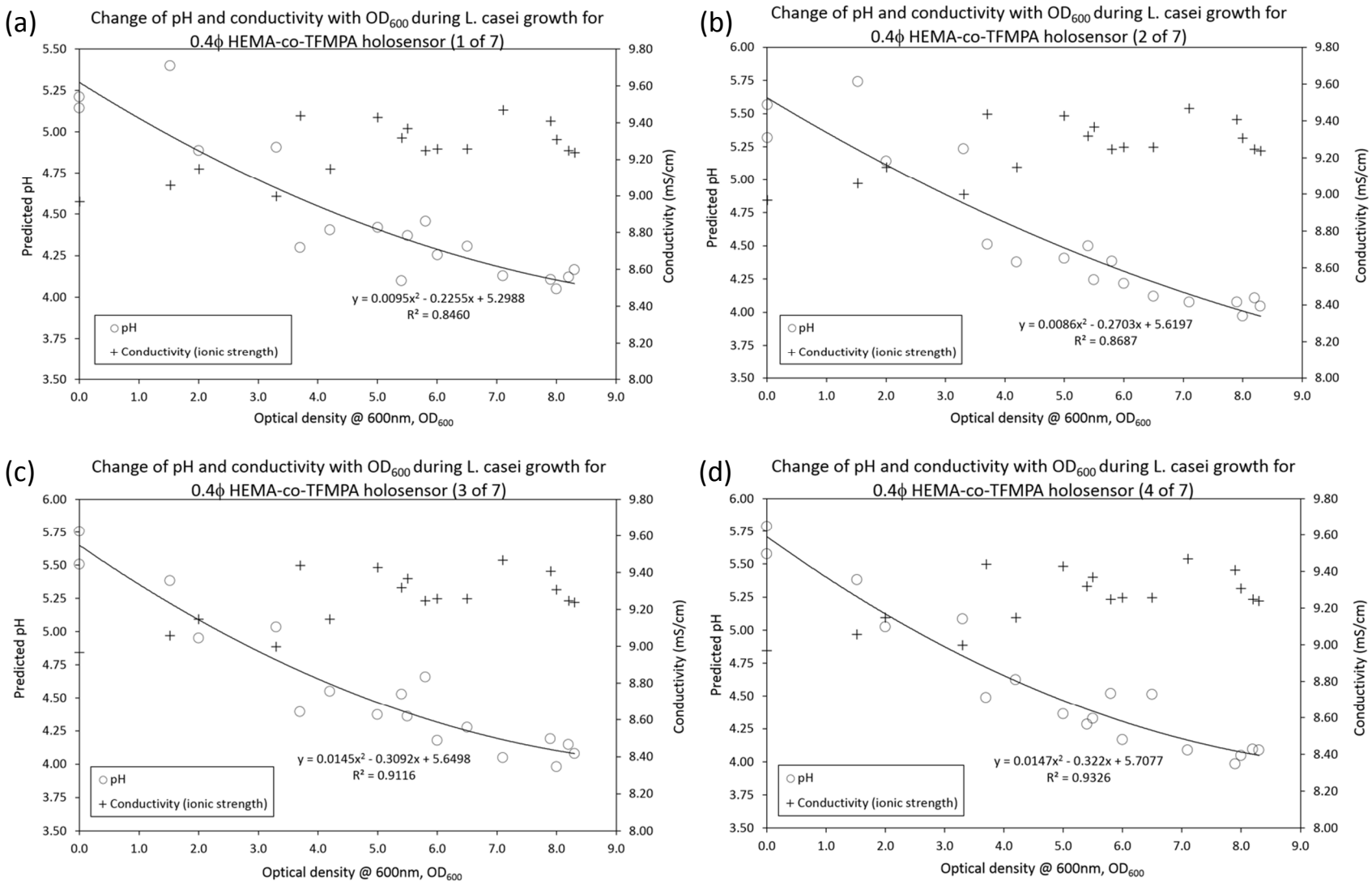

*Figure Q-6: Predicted pH vs OD_{600} curves for **(a – d)** 0.4ϕ holosensor array spot #1 to #4 respectively*

Q-6 Predicted pH vs OD_{600} curves (contd.)

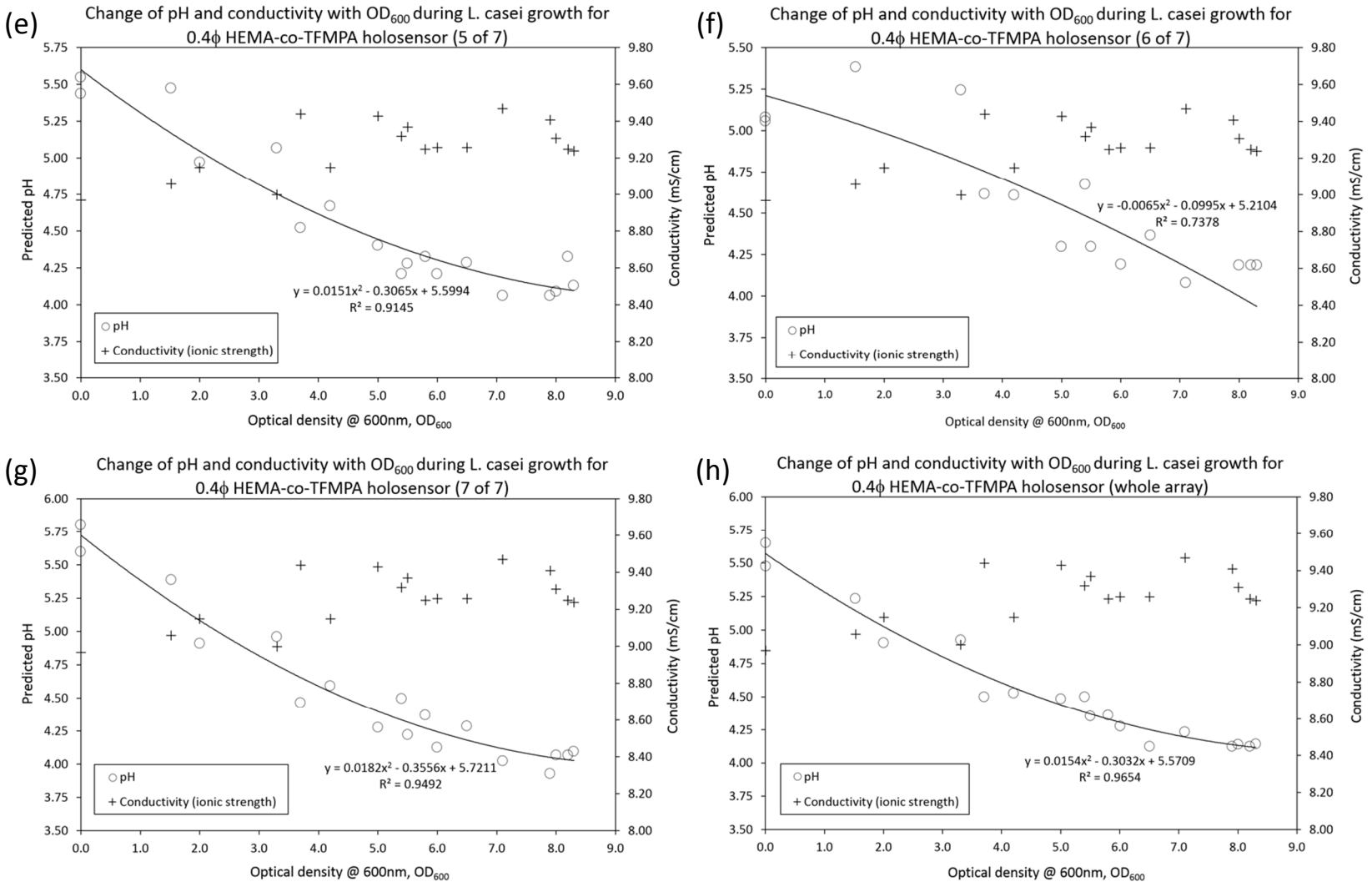

*Figure Q-6: Predicted pH vs OD_{600} curves of measured pH vs predicted pH for **(e – h)** 0.4ϕ holosensor array spot #5 to #7 and of the whole array respectively*

Appendix R: Flat profile exploration

R-1 Naming conventions and schematics for flat profile exploration

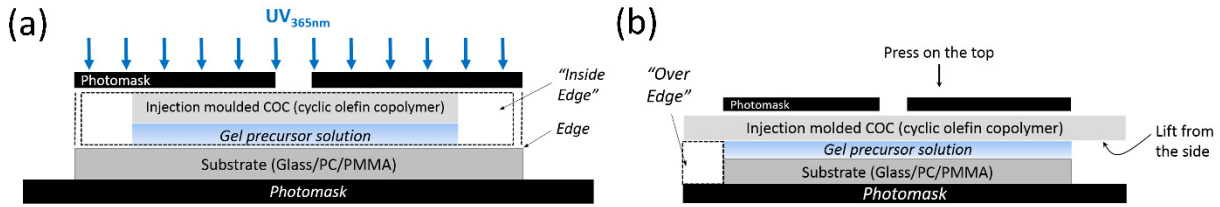

*Figure R-1: **(a)** Schematics for definition of "inside edge" and "over edge". **(b)** Schematics for location of press and lift.*

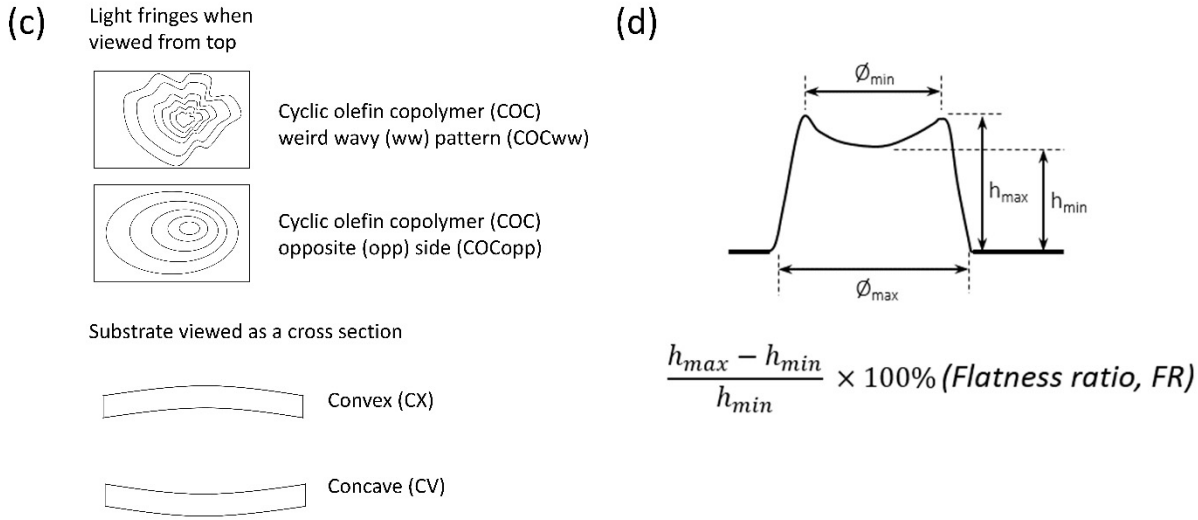

*Figure R-1: **(c)** Definition of "weird wavy" and "opposite" with regard to the difference sides of the COC substrate, and the orientation for the substrate waviness (CX or CV). **(d)** Schematics of a typical gel profile together with the equation for flatness ratio (FR).*

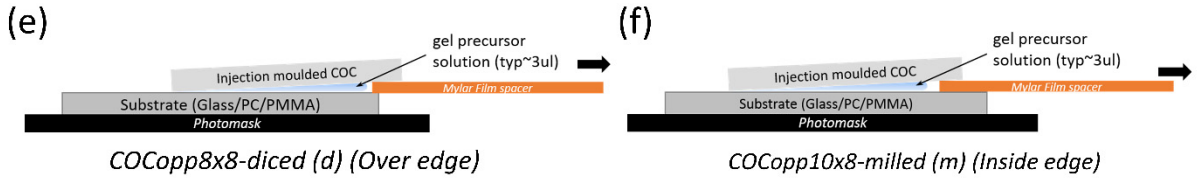

COCopp8x8-diced (d) (Over edge) *COCopp10x8-milled (m) (Inside edge)*

*Figure R-1: **(e & f)** Schematics for "inside edge" and "over edge" experimental setup for gel fabrication.*

R-2 Graphs for flat profile exploration (varying parameters)

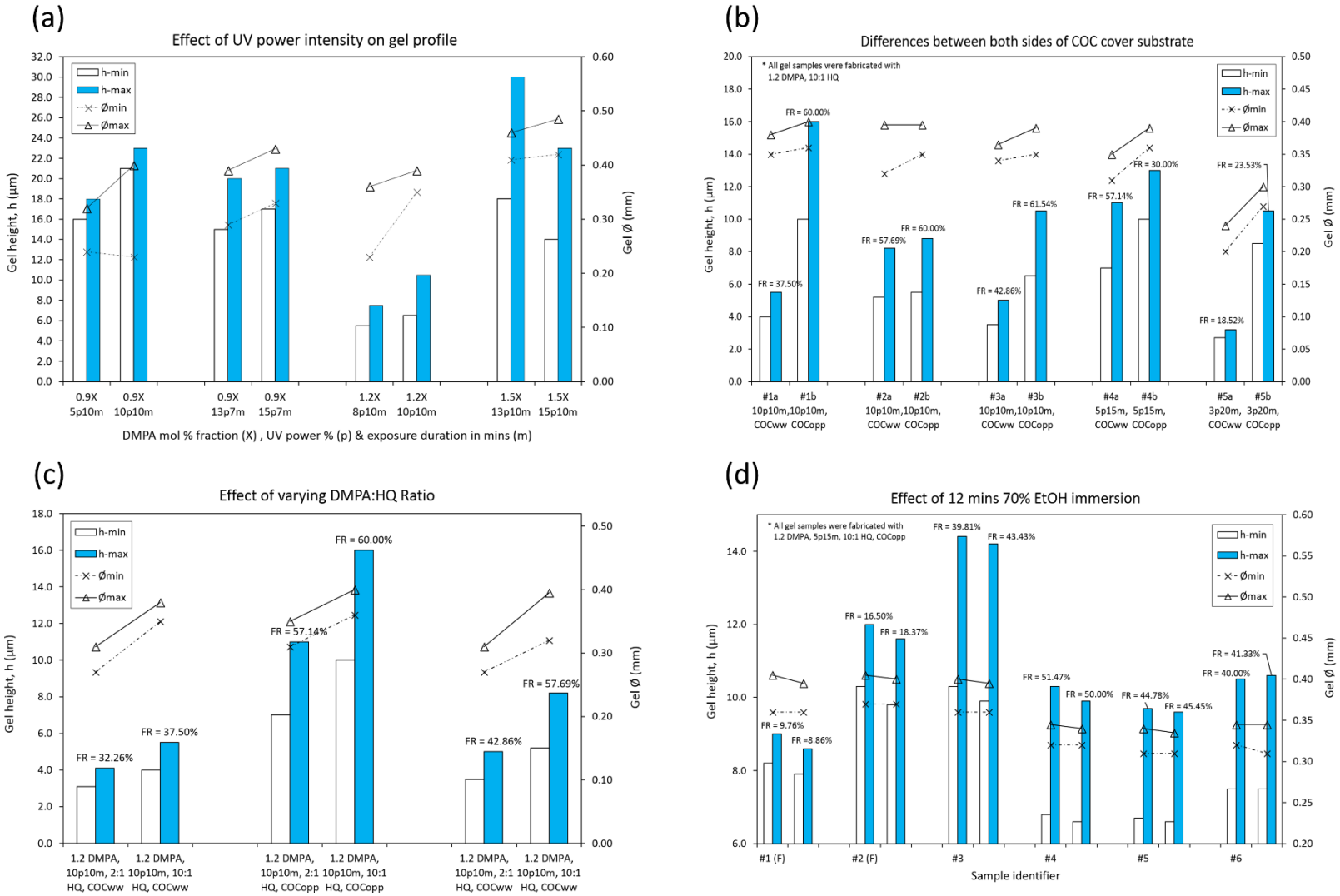

**All UV power intensities stated in (a – d) were in reference to graph #2 in Appendix J(b).*

R-2 Graphs for flat profile exploration (varying parameters) (contd.)

(e)

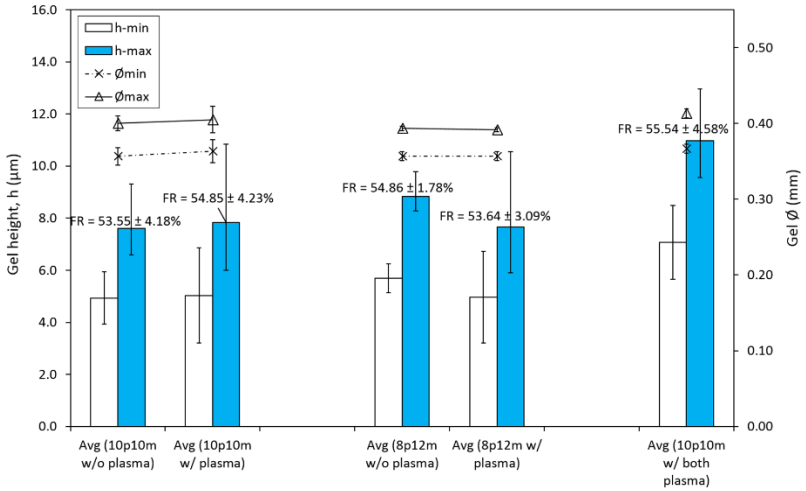

(f)

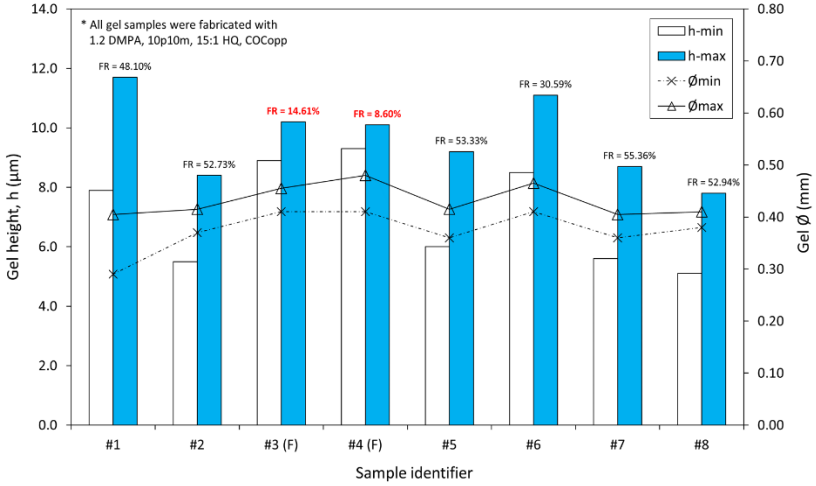

(g)

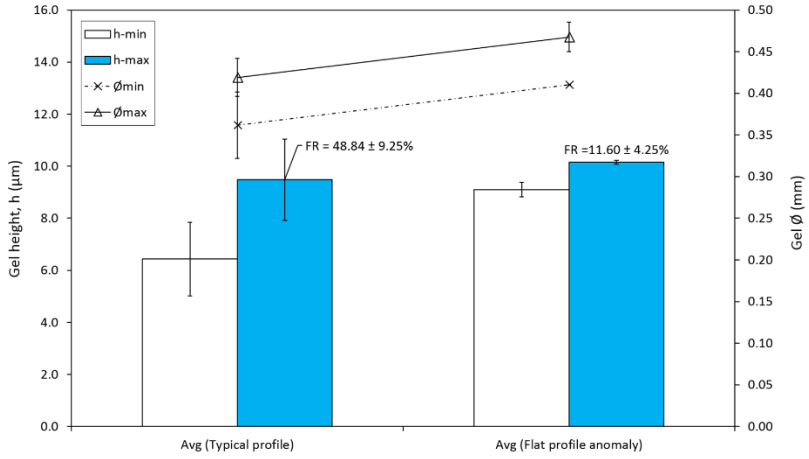

(h)

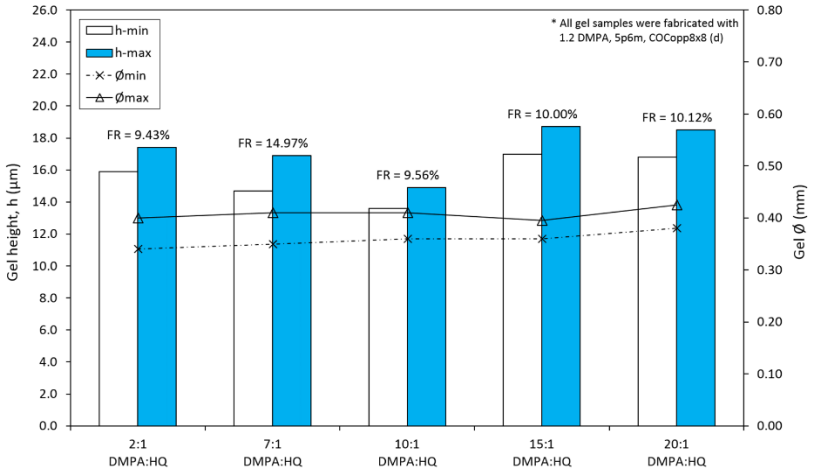

**All UV power intensities stated in (a – d) were in reference to graph #2 in Appendix J(b).*

Appendix S: Surface roughness and cut-off wavelength (λ_c)

S-1 Definitions of different surface roughness parameters

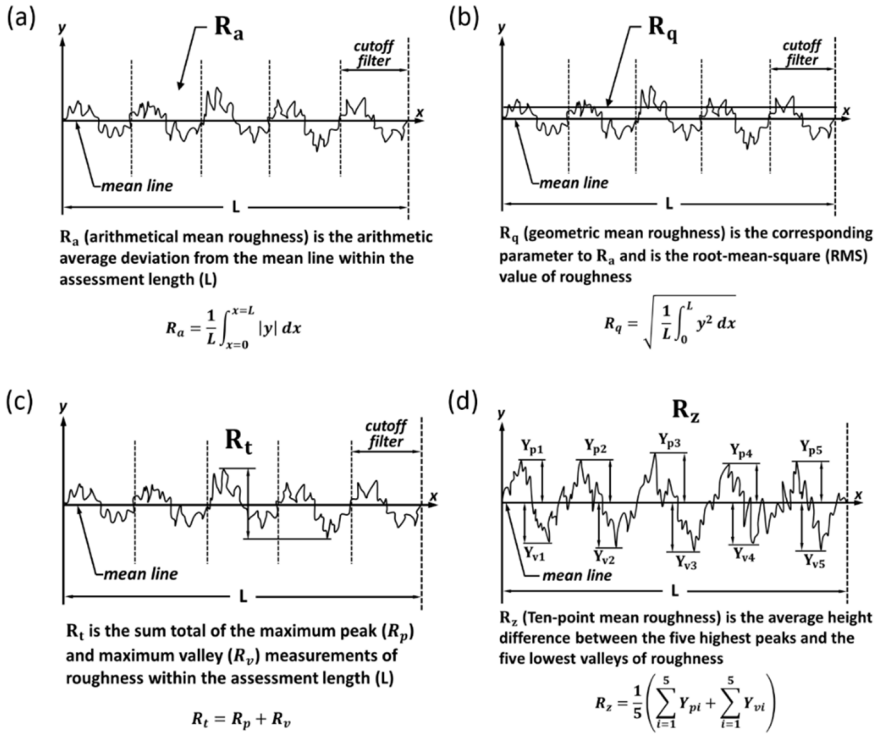

*Figure S-1**(a – d)**: Definitions of arithmetical mean roughness (R_a), geometrical mean roughness (R_q), sum total of maximum peak (R_p) and maximum valley (R_v) within the assessment length (L) (R_t), and ten-point mean roughness (R_z) respectively* [165]. *Reproduced with permission and courtesy from Bruker Nano Surface. Copyright© 2005, Bruker*

S-2 Cut-off wavelength (λ_c)

(a)

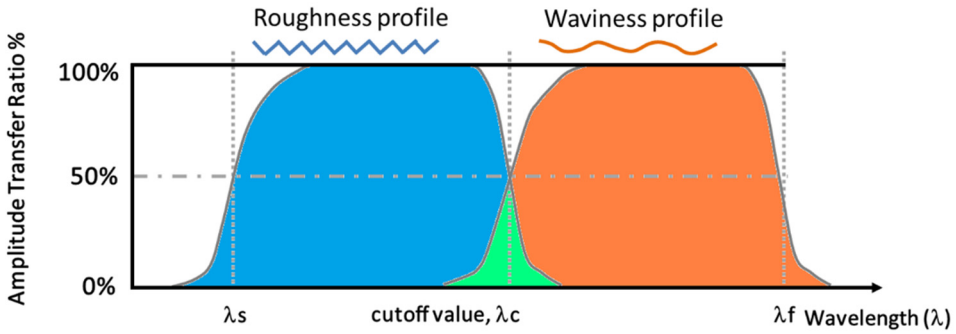

(b)

ISO 4288-1996 (for cut-off value)			
nm	R_a (um)	λ_c (mm)	L_e (mm)
6 - 20	0.006 - 0.02	0.08	0.4
> 20 - 100	> 0.02 - 0.1	0.25	1.25
> 100 - 2000	> 0.1 - 2	0.8	4
> 2000 – 10,000	> 2 - 10	2.5	12.5
> 10,000 – 80,000	> 10 - 80	8	40

*Figure S-2: **(a)** A certain cut-off wavelength (λ_c) exists for which the high frequency roughness profile can be sufficiently separated from the low frequency waviness profile. **(b)** ISO 4288-1996 table for choice of λ_c based on initial R_a measurements. L_e is the evaluation length, which is typically 5X the cut-off wavelength.*

Appendix T: Determination of cut-off wavelength (λ_c) for 0.4ϕ HEMA-co-DMAEM gels

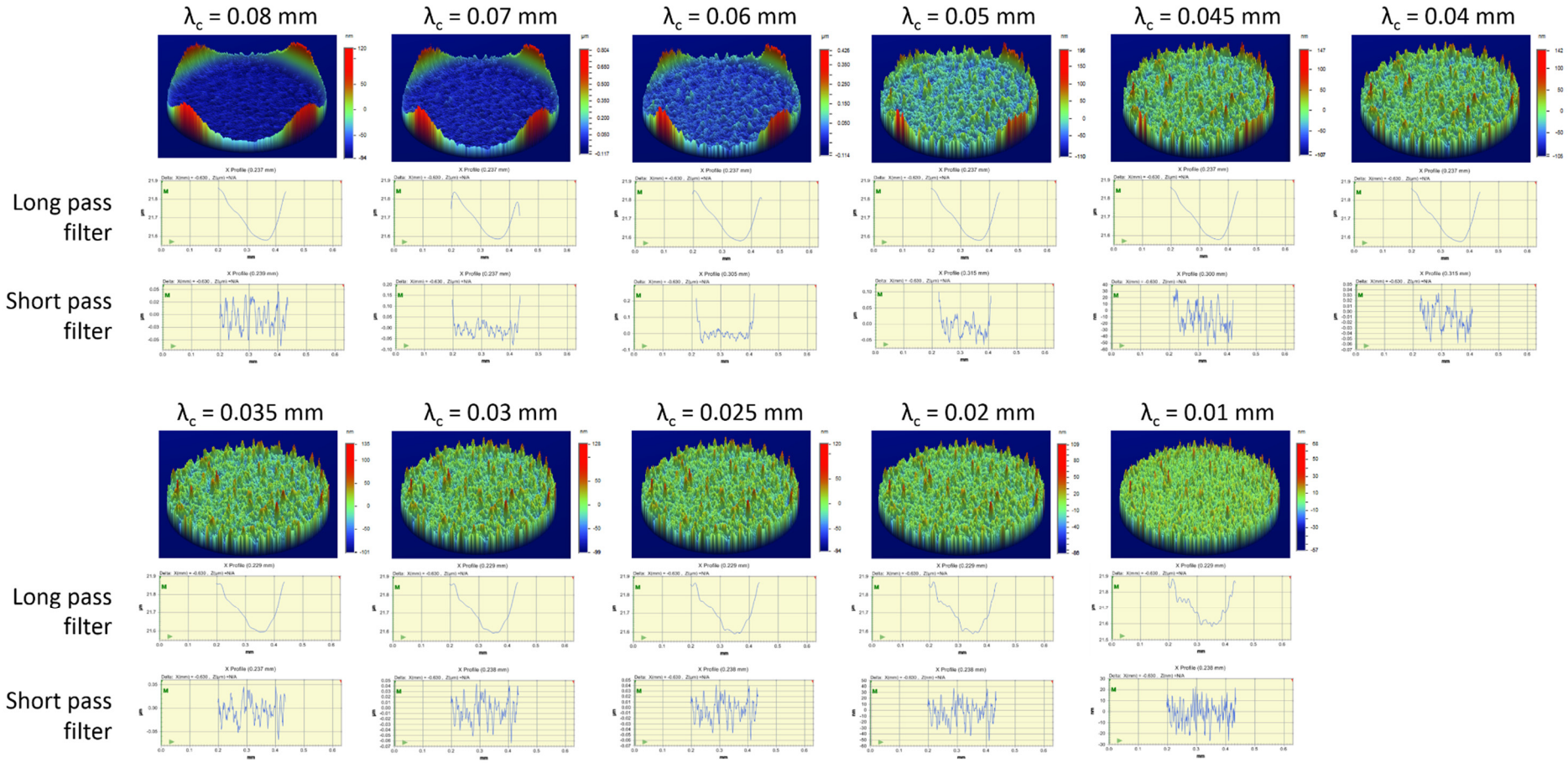

Figure T: A collection of micrographs and Gaussian regression filter graphs for 0.4ϕ HEMA-co-DMAEM gels corresponding to different cut-off wavelengths (λ_c). The long pass filters depict the low frequency waviness profiles while the short pass filters illustrate the high frequency roughness profiles. The upper limit of λ_c was determined visually by the appearance of high frequency roughness data in the long pass Gaussian regression filter graph. In this case, the limit was determined to be between λ_c = 0.03mm and λ_c = 0.025mm

Appendix U: Ideal recipes for flat gel (0.4ϕ HEMA-co-DMAEM) profiles

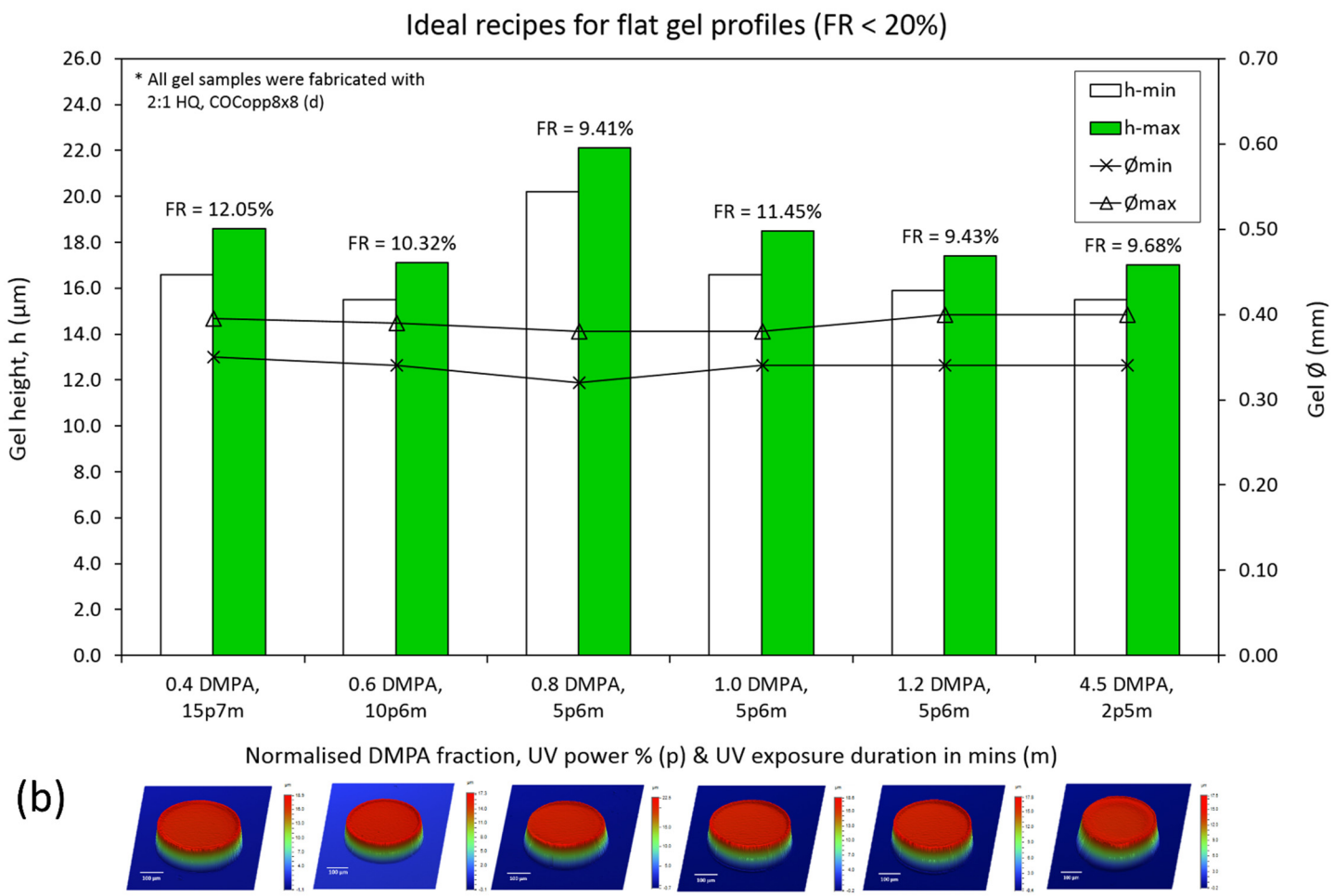

Figure U: Ideal recipes for flat gel profiles. ***(a)*** *Gel dimensions and flatness ratio, FR for different DMPA concentration.* ***(b)*** *Typical 3D digital elevation model of the corresponding gel recipe. Scale bars are 100 µm.*

Appendix V: Gel nano-indentation

V-1 3.0ϕ HEMA-co-DMAEM gel nano-indentation

(a)

	Hardness (GPa)	Reduced Modulus (GPa)	Avg Hardness -All (GPa)	Avg Hardness -Centre (GPa)	Avg Reduced Modulus - All (GPa)	Avg Reduced Modulus - Centre (GPa)
Gel 01						
left35	0.11	4.55	0.12	0.12	5.20	5.67
right35	0.11	4.45				
top800	**0.13**	**6.21**				
btm800	**0.12**	**5.19**				
centre	**0.12**	**5.60**				
Gel 02						
left35	0.13	6.08	0.13	0.12	5.84	5.38
right35	0.15	7.00				
top800	**0.12**	**5.31**				
btm800	**0.12**	**5.23**				
centre	**0.12**	**5.60**				
Gel 03						
left35	0.14	6.33	0.14	0.14	6.66	6.62
right35	0.14	7.09				
top800	**0.13**	**6.18**				
btm800	**0.14**	**6.69**				
centre	**0.14**	**6.99**				

(b)

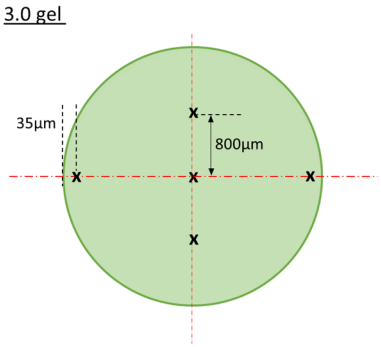

(c)

	Ra (nm) - 70% EtOH	Hardness (GPa)	Reduced Modulus (GPa)	Ra (nm) - Aft 1 min IPA rinse	Hardness (GPa)	Reduced Modulus (GPa)
Gel a_10p8m						
out_top35	40	0.0887	3.23	97		
out_btm35		0.1060	3.55			
out_left750		0.1170	5.61			
out_right750		0.0947	3.85			
in_left35		0.0853	2.59		0.0844	2.62
in_right35		0.0833	2.44		0.0893	2.63
in_top750		0.0843	2.59		0.0928	2.89
in_btm750		0.0870	2.70		0.1040	3.17
in_centre		0.0845	2.63		0.0995	3.06
Average		0.0849	2.59		0.0940	2.87
Std Dev		0.0014	0.10		0.0078	0.25
% Std Dev/Avg		1.63%	3.67%		8.34%	8.64%
Gel b_5p6m						
in_left35	43	0.111	4.28	79	0.1010	3.80
in_right35		0.1180	5.24		0.1340	6.44
in_top700		0.1110	4.32		0.1150	4.36
in_btm700		0.1070	4.30		0.1120	4.22
in_centre		0.1100	4.43		0.1110	4.53
Average		0.1114	4.51		0.1146	4.67
Std Dev		0.0040	0.41		0.0121	1.03
% Std Dev/Avg		3.62%	9.08%		10.52%	21.96%
Gel c_2p6m						
in_left35	51	0.1020	3.13	111	0.1130	3.30
in_right35		0.1040	3.20		0.1100	3.32
in_top725		0.1070	3.37		0.1130	3.38
in_btm725		0.1070	3.45		0.1160	3.58
in_centre		0.1070	3.54		0.1130	3.50
Average		0.1054	3.34		0.1130	3.42
Std Dev		0.0023	0.17		0.0021	0.12
% Std Dev/Avg		2.18%	5.12%		1.88%	3.52%

(d)

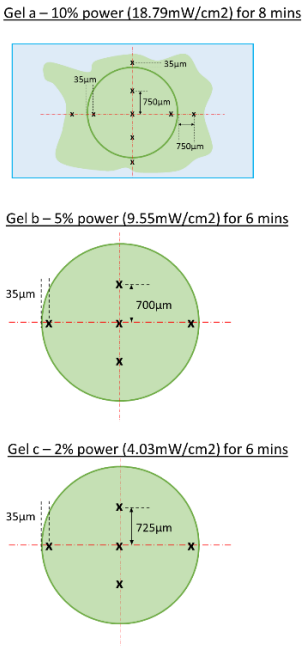

Figure V-1: 3.0ϕ HEMA-co-DMAEM gel nano-indentation test. ***(a)*** *Hardness and reduced modulus values for different parts of 3.0ϕ gel, and* ***(b)*** *schematic diagram for data collection location. Gel recipe was 8DH-2, 1/18 DMPA, 10:1 HQ, 5 µL Mylar® film, 10p8m (18.79 mW/cm^2).* ***(c)*** *Surface roughness (R_a), hardness and reduced modulus values for 3 other 3.0ϕ gels, and* ***(d)*** *schematic diagram for the nano-indentation gel data collection location for gels a, b and c.*

V-2 0.4ϕ HEMA-co-DMAEM gel nano-indentation

All data points used for calculation of Avg etc.

0.6 DMPA	(2:1 HQ, COCopp8x8d4, 10p6m)					
	Ra (nm) - 70% EtOH	Hardness (GPa)	Reduced Modulus (GPa)	Ra (nm) - Aft 1 min IPA rinse	Hardness (GPa)	Reduced Modulus (GPa)
left35		0.104	3.77		0.1190	3.88
right35		0.1090	4.16		0.1110	3.81
top89	26	0.1010	3.89	26	0.1220	4.02
btm89		0.1060	3.92		0.1180	3.89
centre		0.1040	3.94		0.1170	3.84
Average		0.1048	3.94		0.1174	3.89
Std Dev		0.0029	0.14		0.0040	0.08
% Std Dev/Avg		2.81%	3.60%		3.44%	2.07%

4.5 DMPA	(2:1 HQ, COCopp8x8d4, 2p5m)					
	Ra (nm) - 70% EtOH	Hardness (GPa)	Reduced Modulus (GPa)	Ra (nm) - Aft 1 min IPA rinse	Hardness (GPa)	Reduced Modulus (GPa)
left35		0.111	3.78		0.1640	5.11
right35		0.1120	3.86		0.1650	5.63
top88	21	0.1100	3.82	23	0.1060	3.64
btm88		0.1080	3.79		0.1120	3.82
centre		0.1090	3.76		0.1190	3.97
Average		0.1100	3.80		0.1332	4.43
Std Dev		0.0016	0.04		0.0289	0.88
% Std Dev/Avg		1.44%	1.03%		21.73%	19.89%

1.2 DMPA	(2:1 HQ, COCopp8x8d4, 5p6m)					
	Ra (nm) - 70% EtOH	Hardness (GPa)	Reduced Modulus (GPa)	Ra (nm) - Aft 1 min IPA rinse	Hardness (GPa)	Reduced Modulus (GPa)
left35		0.109	3.76		0.1270	4.69
right35		0.1010	3.47		0.1210	4.50
top86	22	0.1070	3.68	24	0.1370	4.89
btm86		0.1100	3.78		0.1420	4.79
centre		0.1080	3.71		0.1380	4.86
Average		0.1070	3.68		0.1330	4.75
Std Dev		0.0035	0.12		0.0087	0.16
% Std Dev/Avg		3.30%	3.37%		6.53%	3.32%

Only central area data used for calculation of Avg etc.

0.6 DMPA	(2:1 HQ, COCopp8x8d4, 10p6m)					
	Ra (nm) - 70% EtOH	Hardness (GPa)	Reduced Modulus (GPa)	Ra (nm) - Aft 1 min IPA rinse	Hardness (GPa)	Reduced Modulus (GPa)
left35		0.104	3.77		0.1190	3.88
right35		0.109	4.16		0.1110	3.81
top89	26	0.101	3.89	26	0.1220	4.02
btm89		0.106	3.92		0.1180	3.89
centre		0.104	3.94		0.1170	3.84
Average		0.1037	3.92		0.1190	3.92
Std Dev		0.0025	0.03		0.0026	0.09
% Std Dev/Avg		2.43%	0.64%		2.22%	2.37%

4.5 DMPA	(2:1 HQ, COCopp8x8d4, 2p5m)					
	Ra (nm) - 70% EtOH	Hardness (GPa)	Reduced Modulus (GPa)	Ra (nm) - Aft 1 min IPA rinse	Hardness (GPa)	Reduced Modulus (GPa)
left35		0.111	3.78		0.1640	5.11
right35		0.112	3.86		0.1650	5.63
top88	21	0.11	3.82	23	0.1060	3.64
btm88		0.108	3.79		0.1120	3.82
centre		0.109	3.76		0.1190	3.97
Average		0.1090	3.79		0.1123	3.81
Std Dev		0.0010	0.03		0.0065	0.17
% Std Dev/Avg		0.92%	0.79%		5.79%	4.34%

1.2 DMPA	(2:1 HQ, COCopp8x8d4, 5p6m)					
	Ra (nm) - 70% EtOH	Hardness (GPa)	Reduced Modulus (GPa)	Ra (nm) - Aft 1 min IPA rinse	Hardness (GPa)	Reduced Modulus (GPa)
left35		0.109	3.76		0.1270	4.69
right35		0.101	3.47		0.1210	4.50
top86	22	0.107	3.68	24	0.1370	4.89
btm86		0.11	3.78		0.1420	4.79
centre		0.108	3.71		0.1380	4.86
Average		0.1083	3.72		0.1390	4.85
Std Dev		0.0015	0.05		0.0026	0.05
% Std Dev/Avg		1.41%	1.38%		1.90%	1.06%

0.6DMPA – 10% power (18.79mW/cm^2), 6 mins

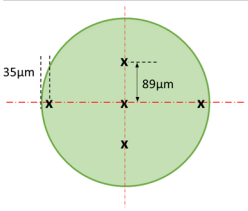

4.5DMPA – 2% power (4.03mW/cm^2), 5 mins

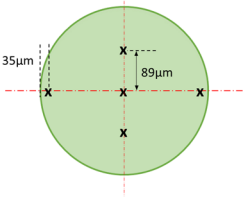

1.2DMPA – 5% power (9.55mW/cm^2), 6 mins

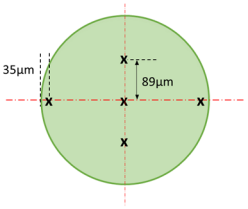

Figure V-2: Nano-indentation run with 0.4ϕ HEMA-co-DMAEM gels with schematic diagram for the collection location of gel data. Gel fabrication recipe for the 0.4ϕ gel was 8DH-2, 2:1 HQ, 6D4E, 3 µL gel precursor volume, COCopp8x8d4.

Appendix W: Transverse modal field distribution for a circular waveguide

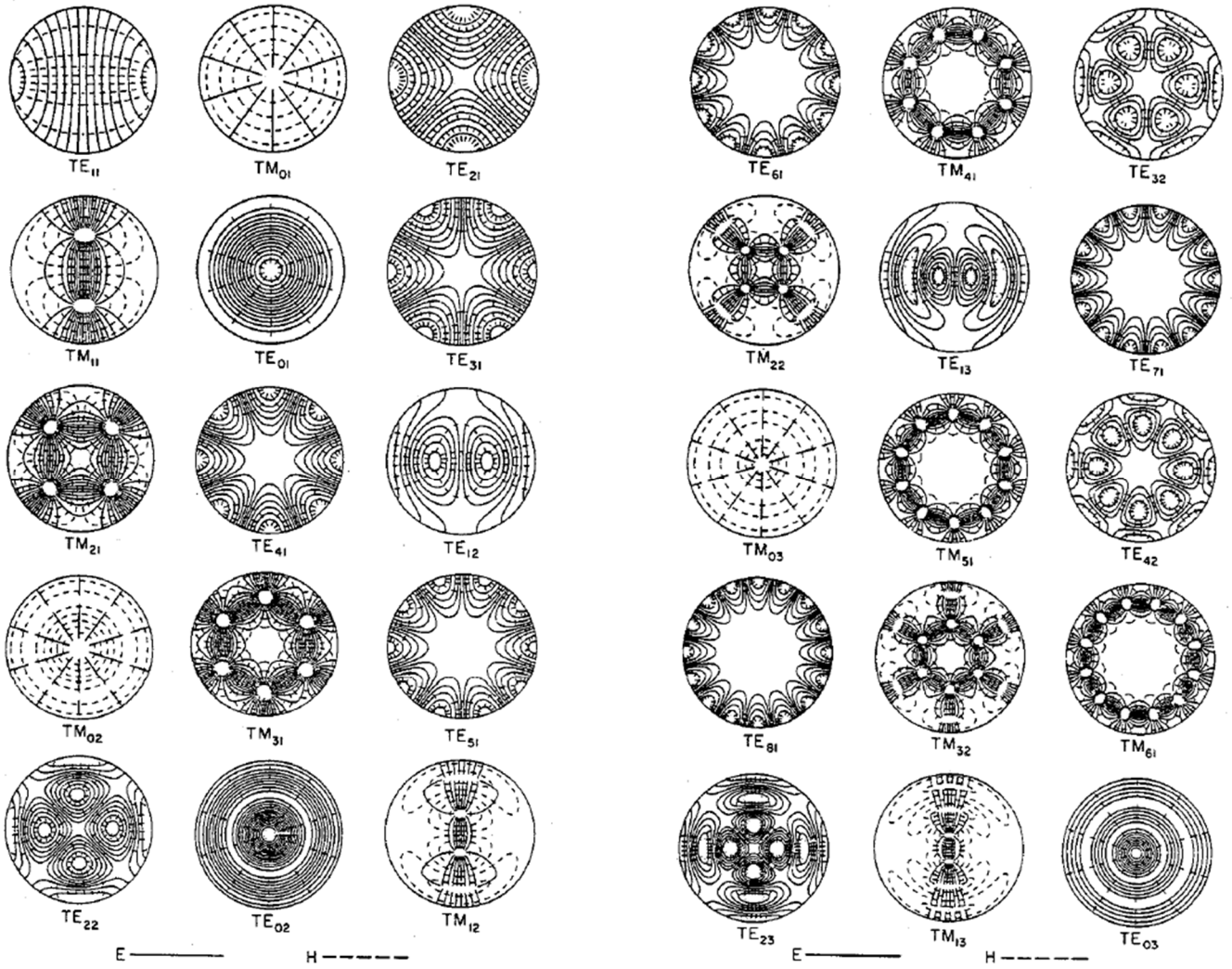

Figure W: Transverse modal field distribution for a circular waveguide. Reprinted from ref. [157] *with permission granted by IEEE. Copyright© 1985 IEEE*

Appendix X: FTIR interrogation for residual HQ/DMPA detection in DMAEM gel

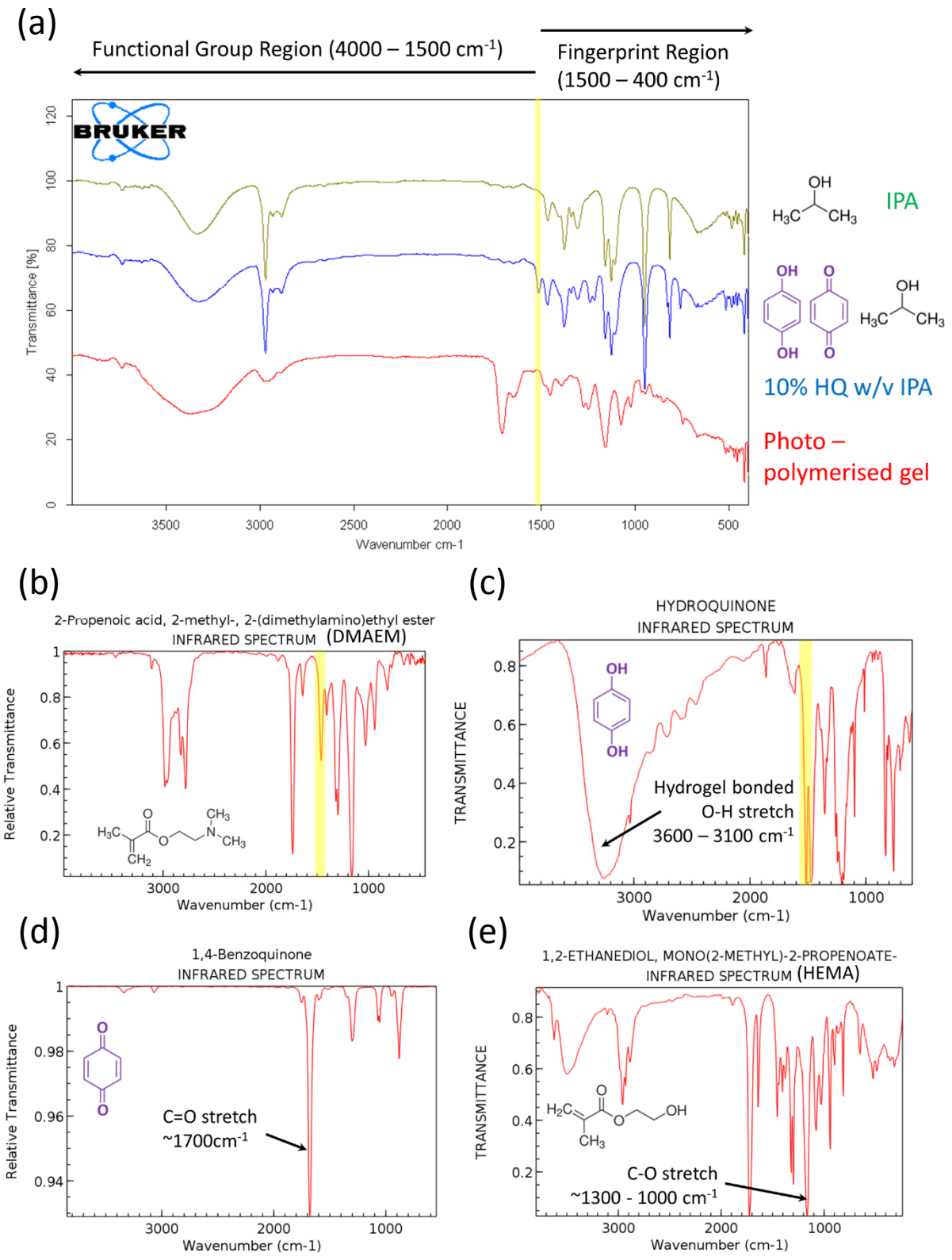

Source: NIST Chemistry WebBook (http://webbook.nist.gov/chemistry)

*Figure X: Measured FT-IR spectrum of **(a)** IPA, 10% w/v HQ in IPA and photo-polymerised polyHEMA gel. FT-IR spectrum obtained from NIST Chemistry WebBook for **(b)** DMAEM, **(c)** HQ, **(d)** BQ and **(e)** HEMA.*

Appendix Y: Obstacles and challenges

Y-1 Challenges associated with ≥ 3.0ϕ holosensors

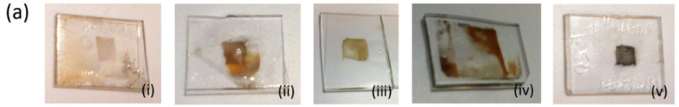

*Figure Y-1**(a)**: A collation of HEMA-co-EDMA(5mol%)-co-MAA (6mol%) gels fabricated with varying amount of reduced Ag0 within the gel matrix. The gel colour ranges from **(i)** light brown to **(iv)** black. The shape of the colour formed during hologram fabrication with a PDMS stencil having a square hole of sides 3 mm while introducing Ag and Br into the gel matrix via the hole.*

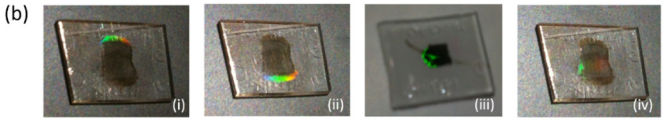

*Figure Y-1**(b)(i-iv)**: A collation of HEMA-co-EDMA(5mol%)-co-MAA (6mol%) gels with holograms appearing only at one edge*

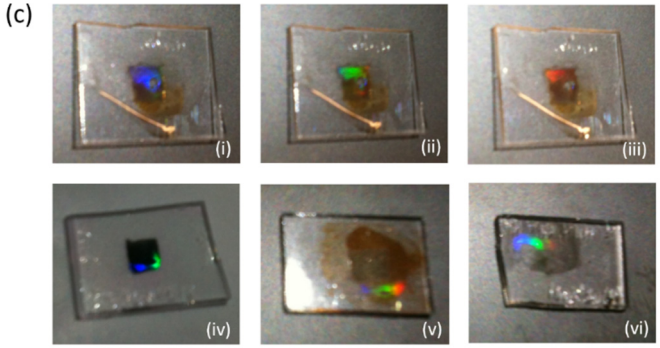

*Figure Y-1**(c)(i-iii)**: The same HEMA-co-EDMA(5mol%)-co-MAA (6mol%) gel exhibiting holograms of different colours at slightly offset angles. **(iv-vi)** Polychromatic holograms at a particular edge of different HEMA-co-EDMA(5mol%)-co-MAA (6mol%)*

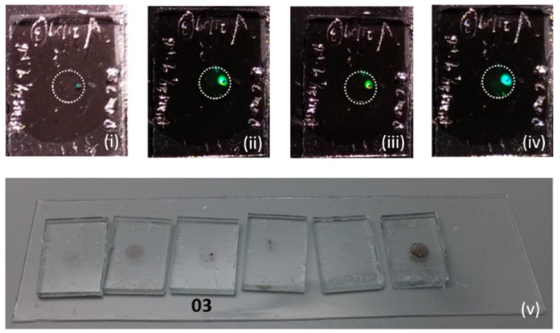

*Figure Y-1**(d)(i-iv)**: Photographs of the same 3.0ϕ HEMA-co-EDMA(3mol%)-co-DMAEM (6mol%) gel (labelled "03" in (v)) at various viewing angles with a hologram found only at a particular random spot near to the edge (circumscribed by the dotted white line) of the gel. **(v)** A collation of different holosensors which underwent the same fabrication procedures and produced a visible precipitate during hologram fabrication.*

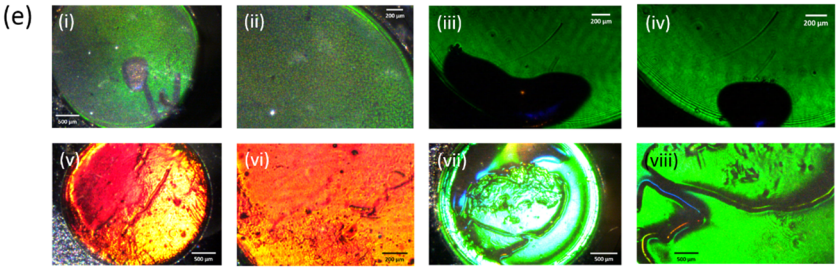

*Figure Y-1**(e)**: **(i & ii)** Dim hologram captured with 20ms integration time on 3.0ϕ HEMA-co-EDMA(3 mol%)-co-TFMPA(6 mol%) gel (1/18 DMPA, 2:1 HQ, 6T3E, 9p4m#1, COCopp8x8 (d)) recorded at pH 4.5 and tested at pH 6.0 with scale bars of 500 μm and 200 μm respectively. **(iii & iv)** Trapped bubbles in microfluidic chamber filled with pH 6.0 buffer disrupting holographic display at the black areas of two different 3.0ϕ HEMA-co-EDMA(3mol%)-co-TFMPA (6 mol%) gels (1.0DMPA, 2:1 HQ, 6T3E, 9p4m#1, COCopp8x8(d), recorded with pH 4.5 L-ascorbic acid) with 200 μm scale bars. **(v & vi)** The same, bright but polychromatic hologram captured with 5ms integration time on 3.0ϕ HEMA-co-EDMA(3 mol%)-co-DMAEM(6 mol%) gel (1/18 DMPA, 10:1 HQ, 6D3E, 10p8m#1, Mylar film, 5 μL), recorded with pH 4.5 L-ascorbic acid with scale bars of 200 μm and 500 μm respectively. **(vii & viii)** The same, bright and monochromatic hologram captured with 5ms integration time on 3.0ϕ HEMA-co-EDMA(3 mol%)-co-DMAEM(6 mol%) gel (1.0 DMPA, 2:1 HQ, 6T3E, 7p8m#1, PC film, 6 μL), polymerised with 35 μm thick Teraoka tape as a spacer and mask, tested at pH 6.0 and with scale bars of 500 μm. The centre portion of the gel was deformed while being stuck to the PDMS chamber floor.*

Y-2 Challenges associated with miniaturized 0.4ϕ holosensors

(a)

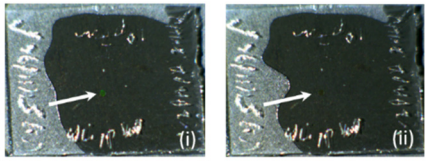

*Figure Y-2**(a)(i &ii)**: Photograph of the same, dim 0.4ϕ HEMA-co-EDMA (3 mol%)-co-DMAEM (6 mol%) gel (1.2 DMPA, 2:1 HQ, 6D3E, 5p6m#1, COCopp8x8(d)) viewed at different angles, recorded and tested with high-resolution camera*

(b)

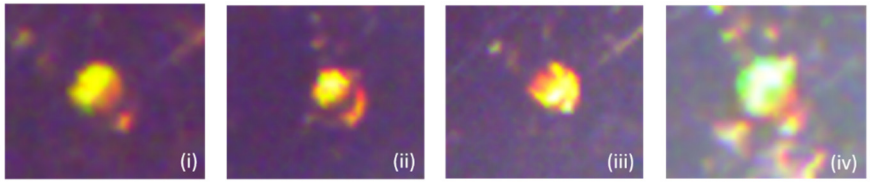

*Figure Y-2**(b)(i-iv)**: Photograph of the same, polychromatic 0.4ϕ DMAEM hologram viewed at a progressively slight offset angle from (i) to (iv)*

(c)

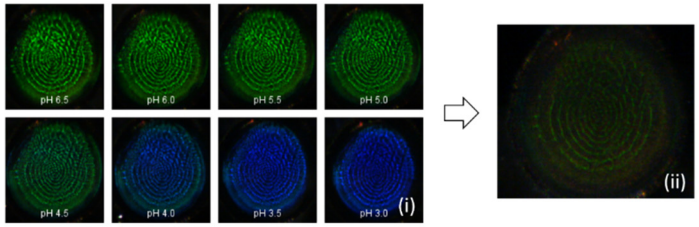

*Figure Y-2**(c)(i)**: Micrograph of the same 0.4ϕ HEMA-co-EDMA (3 mol%)-co-TFMPA (6 mol%) gel (1.0 DMPA, 2:1 HQ, 6T3E, 9p4m#1, COCopp8x8(d)) TFMPA hologram interrogated with ionic strength balanced pH buffers from pH 6.5 to 3.0. When the experiment proceeded for L. casei tests, the hologram became **(ii)** drastically dimmer*

(d)

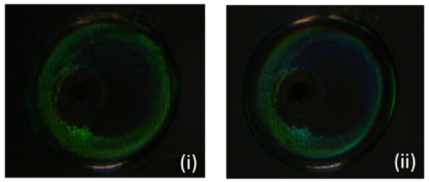

*Figure Y-2**(d)(i & ii)**: Micrographs of the same 0.4ϕ HEMA-co-EDMA (3 mol%)-co-TFMPA (6 mol%) gel (1.0 DMPA, 2:1 HQ, 6T3E, 9p4m#1, COCopp8x8(d)4c) holosensor on PC substrate tested with buffers of different pH. The background signal of the hologram was also a ring of dim hologram.*

(e)

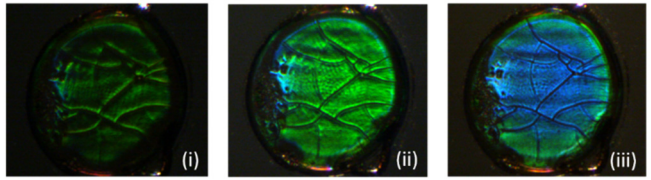

*Figure Y-2**(e)(i-iii)**: Micrographs of the same 0.4ϕ AA holosensor tested with buffers of pH 7.0, 4.0 and 3.0 respectively, displaying polychromatic (evident with double peak wavelengths observed with spectrometer) holograms and surface cracks*

Appendix Z: Spectra of light sources for hologram interrogation

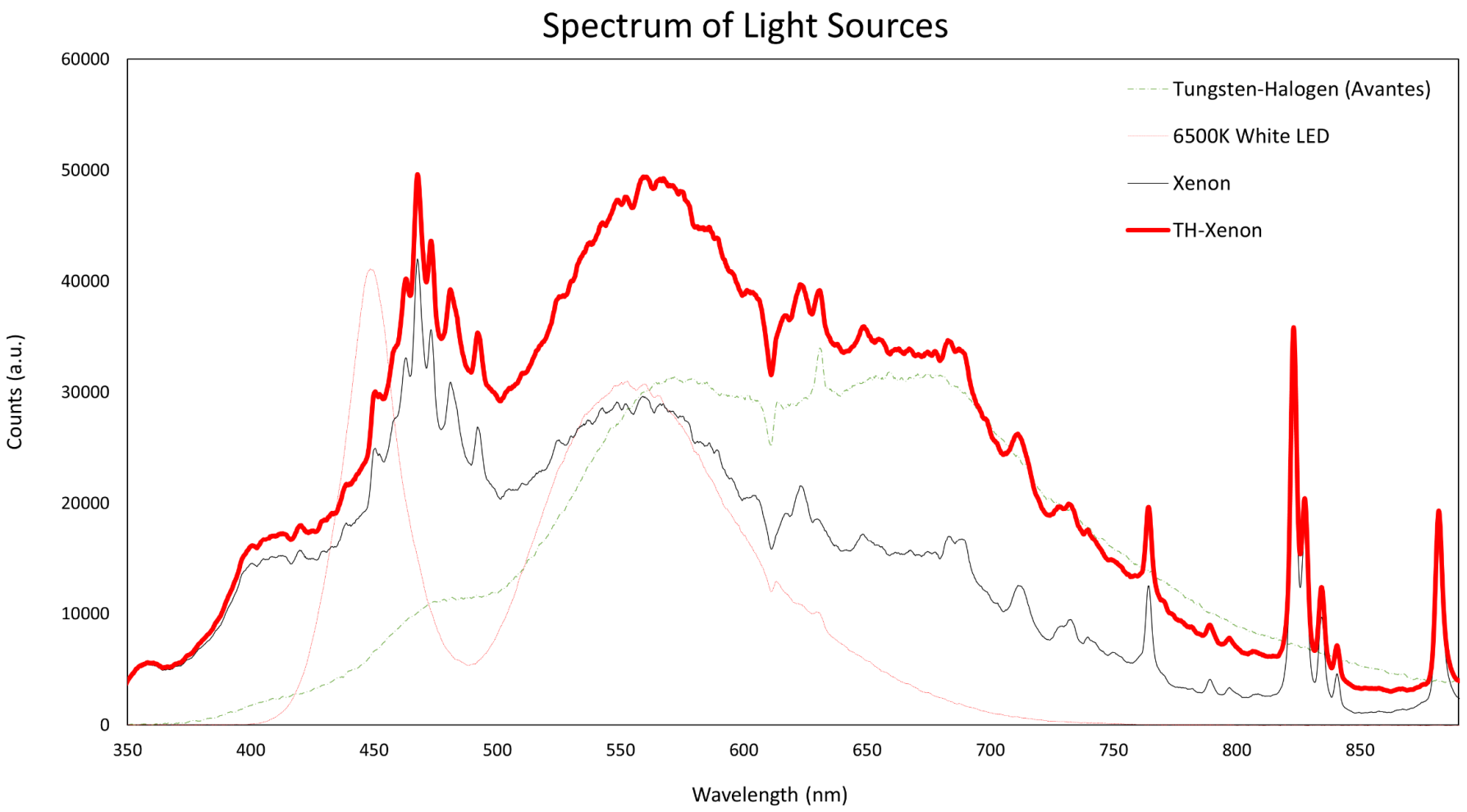

Figure Z: Spectra of tungsten-halogen (T-H), 6500K LED and Xenon light sources, together with a superimposed intensity optimised TH-Xenon hybrid spectrum when T-H and Xenon light sources were combined.

Appendix AA: Holosensor issues and challenges

3.0ϕ holosensors

Issues associated with ≥ 3.0ϕ holosensors were collated in Appendix Y-1(a – e).

Colour of reduced Ag^0 gel

Depending on how developed the gel was, the gel with reduced Ag^0 fringes would exhibit different colours ranging from light brown, to black (Appendix Y-1(a)). The darker it was, the denser the reduced Ag^0 was.

When it was light brown, there could be too little AgBr. Ag salt dissolved in 3:2 IPA:DI was required, or the gel was not dry enough after Ag^+ infusion (causing too much Ag^+ to leak out during Br^- immersion). An ascorbic acid sensitiser bath could be added to increase the sensitivity of the AgBr during exposure. Exposure time and laser power could be increased as well.

When the gel was light red after exposure, it meant that there were still substantial amounts of dye in the gel matrix. Either there were not enough Ag^+ to react with the Br^-, or exposure/development duration was too short. The pH of the developer would need to be checked as well. If the gel colour were too light, its reducing ability could be lost.

If the gel turned black too fast, the Ag^+ concentration could be too high, or an Ag^+ salt dissolved in DI should be utilised instead of the one dissolved in 3:2 IPA: DI. It could also mean that there was too little Br^- during exposure, reducing Ag^+ to Ag^0 quickly in the developer. If Ag^+ or Br^- were not the problem; exposure would have been too long, laser intensity could have been too high, or the gel was immersed too long in the developer.

Photographic density is the logarithm of the reciprocal of the transmittance. For the Goldilocks effect, i.e. a thick brown tinge of density 3.0, a good gauge would be to look through the developed gel at the developer bath in a white tray and then at the safelight. If the developer bath can be seen, it is too light; if it blocks the safelight, it is too dark [108]. A set of neutral density films would come in handy to estimate the different shades of densities at increments of 0.15 from 0 to 3. Cutting this in half lengthwise, and putting one strip over another provides 0.3 steps of 0 to 6 to be put beside the safelight as a guide.

Coffee stain (ring) effect

Some holograms exhibited the ideal density of reduced Ag^0 (brown, density around 3.0), but only displayed holograms at the edges (Appendix Y-1(b)). This could be due to a laser intensity which was too high, especially when accompanied with a dark gel, the hologram would likely be formed only

from the interference of coherent scattered laser light. Otherwise, it should be a matter of sample alignment which was different to when it was first aligned before exposure. It would also be worth measuring the gel profile before hologram fabrication as a minimum of 5 μm gel thickness was required for enough fringes to interfere constructively and produce a bright enough hologram.

Polychromatism

With the Bragg's condition, a different wavelength should be viewed from a different angle. However, it should not be of the same intensity. Appendix Y-1(c) showed 2 cases of polychromatism: a monochromatic hologram that displayed a different colour at a slightly different angle, or spot holograms showing different colours at the same angle. The latter was really just a variation of the coffee stain (ring) effect. For the former, it was thought that the formed Bragg reflection planes were distorted, either due to a slight misalignment during exposure or multiple exposures from accidental movement while the shutter was open. This multi-exposure could also be a product of scattered light interfering at different angles. These issues could be mitigated by utilising the lowest laser intensity required for interference.

Mini hologram in big spot

There were cases where a hologram formed, only at a particular spot of the gel, but not at the edges (Appendix Y-1(d)). This occurrence happened especially on those samples which did not undergo the 12 min 70% (v/v) EtOH immersion. A spot started showing at the Ag^+ and Br^- diffusion and immersion procedures, where a particular spot would darken prematurely even before the immersion in ascorbic acid. It was found out that a thorough IPA rinse followed by 70% (v/v) EtOH immersion, or a round of high power O_2 plasma could circumvent this problem.

An explanation for this phenomenon was attributed to the presence of residual initiator (DMPA) or inhibitor (HQ) which had precipitated out during DI water rinsing due to their low solubility in water. It would be more likely that it was the HQ though, due to its Ag^+ reduction capability which could have prematurely reduced Ag^+ to Ag^0 at a certain spot, causing further Ag^0 reduction to happen at that spot. A prolonged rinse in alcohol could have dissolved and washed it away, while plasma could have oxidised the hydroquinone (HQ) to benzoquinone (BQ), thereby eliminating its reduction ability.

FT-IR analysis was performed on the gel precursor constituents as shown in Appendix X. The spectrum of the IPA solvent, HQ in IPA and the photo-polymerised polyHEMA gel were compared against each other together with pre-obtained FTIR spectra of DMAEM, HQ, BQ and HEMA (Appendix X(b-e)). Either the HQ concentration was too small to be detected, or there really was no residual HQ in the gel matrix. However, to be on the safe side, all photo-polymerised gels were thoroughly rinsed with IPA, dried, and then immersed in 70% (v/v) EtOH for 12 mins before being allowed to come into contact with DI

water. Also, where possible, the 1/18 DMPA recipe was utilised to minimise the probability of precipitation within the gel matrix of the DMPA initiator and HQ inhibitor. A 1 min 70% (v/v) EtOH immersion step was added as the first step of the hologram fabrication procedure to mitigate this issue. Earlier, an additional O_2 plasma treatment step was included as a means of ensuring uniform hydrophilicity across the gel diameter, though it was not entirely necessary.

Major challenges for the 3.0ϕ holosensor

There were 5 major challenges when fabricating the TFMPA holosensor (Appendix Y-1(e)).

First, Appendix Y-1(ei & eii) depicts a dim hologram whose signal was too weak and sparse to distinguish between different pH buffers. The holographic signal could be intensified by increasing the exposure integration time. However, the signal-to-noise ratio was diminished, with the background gel colour dominating the acquired signal.

Secondly, Appendix Y-1(eiii & eiv) illustrates bubbles that were formed on the gel surface while inside the microfluidic chip, which prevented the imbibing of water over the bubble-covered region. This resulted in a loss of holographic signal and was displayed as a black “dead pixel”. One way to dislodge these bubbles was to introduce a reciprocating flow across the bubble region. Sometimes it required several rinses of DI water, IPA or 70% (v/v) EtOH to eliminate them. This would hinder real-time monitoring as the extracellular environment would have to be severely perturbed to clear up the signal disturbance. A debubbler could also be added upstream of the microfluidic system. However, as the PDMS cover of the microfluidic chip was gas-permeable, the origin to the problem could also be the chip substrate itself. Oxygenated media could be utilised with non gas-permeable substrates for future microfluidic chip designs to circumvent this problem.

Thirdly, there was an issue of bright, yet polychromatic holograms as shown in Appendix Y-1(ev & evi). Such holograms do still have utility as a qualitative, rather than quantitative sensor. Replicable sample alignment had to be ensured, while laser power had to be kept as low as possible to prevent the issue of “multi-exposures” from the interference from scattered laser light or specular reflections.

Next, a bright monochromatic hologram shown in Appendix Y-1(evii & eviii) was defaced when the expanded gel surface got stuck onto the PDMS chamber ceiling. The resulting non-uniform holographic signal made it impractical as a sensor. Several quality holograms were blemished this way.

In order to overcome this problem, a few measures could be taken. The chamber height was designated to be at least 3X the gel height. If the gel were to be fabricated using the tape mask technique, the chamber height would have to be adjusted accordingly. Also, tape with acrylic adhesives dissolved easily in IPA, the solvent used for the gel precursor solution. The dissolved

adhesive was deposited onto the gel surface, making it undesirably sticky. Other precautionary measures included being extra careful with and monitoring the PDMS-glass bonding procedure and Ni mould flatness respectively. During PDMS-glass bonding, pressing too hard at the middle of the chamber would cause the sagging chamber ceiling to stick onto the glass substrate or gel itself. Also, a concave Ni mould surface would result in a convex PDMS chamber. This small change could compromise the 3X gel height minimum criteria and cause the gel to more easily get stuck onto the PDMS chamber ceiling.

Lastly, a major challenge not shown in this Appendix was the formation of a visible hologram. The CW laser system was sensitive to minute movement down to a quarter of the laser wavelength. Small differences in alignment for the optomechanical components and relative sample alignment before and after exposure could also aggravate the null-hologram situation. Measures were put in place to minimise these vibration and alignment issues by having vibration-isolation and sample alignment redundancies.

0.4ϕ holosensors

Dim holograms

A 0.4ϕ holosensor possessing the same brightness as a 3.0ϕ holosensor would appear to be a lot dimmer due to its size. The brightness of the holosensor shown in Appendix Y-2(ai) was comparable to Appendix Y-1(eii) but due to its size, appeared many times dimmer. The integrated area under the reflectance spectrum for the 0.4ϕ holosensor was significantly smaller, since a much higher optical zoom was required to fill the field of view with the 0.4ϕ holosensor, which was about 56X smaller in surface area than the 3.0ϕ one. With this requirement, methods had to be modified to maximise brightness, and yet not increase laser intensity, as it would introduce more scattering. Interestingly, as reported in the earlier chapters, it was the low laser intensity and offset alignment that maximised the holographic signal for the holosensors.

Polychromatism and resolution

Polychromatism for 0.4ϕ holosensors most likely occurred when the laser intensity was set too high, or when there was movement. Movement would result in multiple exposures, such as the polychromatic, blurry 0.4ϕ hologram shown in Appendix Y-2(b). The 0.4ϕ holosensor also required a large zoom multiplier, but the working distance had to be large for adjustment of the illumination module at a particular angle. A customised hologram interrogation system was set up for this requirement, for a small field of view with up to 84X magnification and a working distance of about

30 – 80 mm, integrated with a high-resolution industrial camera and sample and illumination module with minute x, y, z, tilt-yaw and rotation adjustment capabilities.

Diminishing hologram brightness

Residual AgBr or dye within the gel matrix could absorb ambient light and cloud the original interference pattern. This was typically resolved by immersing the gel in IPA and sodium thiosulphate ($Na_2S_2O_3$) to remove residual dye and unreacted AgBr respectively. However, the holosensors did occasionally show delayed diminished responses such as the one shown in Appendix Y-2(c) which displayed a significantly diminished holographic signal only after four whole runs of pH characterisation buffers. Although immersion in IPA and $Na_2S_2O_3$ could ensure most of the dye and unreacted AgBr was removed, prolonged immersion, especially in $Na_2S_2O_3$, would also resulted in a loss of holographic signal due to the eventual dissolution of the reduced Ag^0 in $Na_2S_2O_3$. The optimal balance was eventually found and reported in Appendix G.

Background signal from PC-embedded holosensor

Appendix Y-2(d) illustrated pictures of a 0.4ϕ PC-embedded holosensor with a dim background ring hologram at the holosensor edges, which changed colour slightly at the edges with different pH buffers, as shown in Appendix Y-2(dii). It was believed that the adsorbed PETTA crosslinker utilised for PC-polyHEMA bonding was concentrated at the gel edge, which could be preventing the gel from expansion or contraction. The PC-polyHEMA method would have to be modified to enable the fabricated gel to work like the glass-embedded holosensors.

Polychromatic and cracked surface AAm holosensor

The 0.4ϕ AAm-co-AA holosensor, depicted in Appendix Y-2(e) exhibited surface cracks and polychromatism. A limited number of experiments were performed to optimise the poly-acrylamide (polyAAm) gel, though it was observed together with the polyHEMA gels that 100% IPA had a dehydrating effect and introduced surface cracks. These cracks would typically disappear with 70% (v/v) EtOH immersion. However, the cracks in the polyAAm gel remained thereafter. More experiments have to be conducted to investigate the cause of this occurrence.

Appendix AB: Materials and Equipment

Substrates

Glass

VWRI631-1552 76 mm (L) x 26 mm (W) x 1 mm (T) microscope glass slides were purchased from VWR while in Cambridge, UK; #7101 76 mm x 26 mm x 1 mm microscope glass slides were bought from XTI Services while in Singapore. 22 mm x 22 mm 0.13 - 0.17 mm thick cover glass slides were procured from XTI services and VWR Singapore. The OMP 170 glass substrate utilised with dry film photoresist for the fabrication of PDMS mould via nickel plating was purchased from Associate Mastering Service, Singapore. Single Crystal Quartz Wafers (Z-Cut to 8 mm x 8 mm x 0.5 mm, two side epi-polished and surface roughness < 1.0 nm) were bought from Latech Scientific Supply Pte Ltd, Singapore. Customised-design premium Quartz-Chrome Photomask with protective Poly/Nano 3M coating was manufactured by Front Range Photomask, USA.

Plastics

PM/ POLY-A (T000-Clear Colour) 1 mm, 2 mm, 3 mm, 4 mm, 5 mm, and 6 mm thick poly (methyl methacrylate) (PMMA) sheets, together with SABIC Innovative Plastics Lexan 1 mm thick Polycarbonate (PC) sheets, 0.5 mm and 0.25 mm thick polycarbonate films, were procured from Professional Plastics Pte Ltd, Singapore. 0.5 mm thick poly (methyl methacrylate) (PMMA) sheets were bought from GoodFellow, UK. SABIC® PC (Polycarbonate) resin PC4800 was supplied by Acumen Engineering Pte Ltd, Singapore and TOPAS 5013L-10 (Cyclic olefin copolymer) (COC) was procured from Inabata Singapore Pte Ltd. 0.64 mm (measured with digital callipers) thick COC and 0.60 mm (measured with a digital callipers) thick PC injection-moulded discs were produced by the Netsal Discjet injection moulding machine. While in Cambridge, UK, biaxial orientated ES301400 (0.1 mm thickness) Polyethylene terephthalate (PET) Mylar® film was purchased from GoodFellow Cambridge Ltd. 125 μm thick MEX02C single-sided metallised polyester sheets (with mirror finish) were purchased from HiFi Industrial Film. SU-8 2025 permanent epoxy negative photoresist was obtained from MicroChem, U.S. In Singapore, HK-31 125 mm thick poly (ethylene terephthalate) (PET) film was procured from Innox Higa Singapore Pte Ltd. Mylar® film photomasks were designed and sent for fabrication by J.D. Phototools UK while in Cambridge, UK and produced by Infinite Graphics Pte Ltd while in Singapore. Costar® 3516 sterile polystyrene 6-well cell culture dishes were supplied by Biopolis Shared Facilities (BSF). 25 μm thick NIT3025U dry film photoresist was purchased from CircuitWorks Asia Pte Ltd. 0.5 mm thick fluorinated ethylene propylene (FEP) film was procured from GoodFellow, UK.

Silicone elastomers

1673921 Dow Corning Sylgard® 184 silicone elastomer kit, poly(dimethylsiloxane) (PDMS) was purchased from element14, Singapore. 0.50 mm and 0.25 mm thick BISCO® HT-6240 transparent solid silicone (40 durometer shore A material) were procured from Rogers Technologies (Singapore) Inc.

Chemical reagents

In Singapore, chemical reagents were procured mostly from Sigma Aldrich (abbr. Sigma), Aik Moh Paints and Chemicals Pte Ltd (local distributor for Arcos Organics) (abbr. Aik Moh), VWR (local distributor for Alfa Aesar), Kanto Kagaku Singapore Pte Ltd (abbr. Kanto) and Tee Hai Chem Pte Ltd (local distributor for Tokyo Chemical Industry Pte Ltd) (abbr. Tee Hai).

Gel precursors

The monomer and crosslinker, 477028-100µ 2-hydroxyethyl methacrylate (HEMA) and 335681-100ML ethylene glycol dimethacrylate (EDMA) respectively, together with pH-sensitive 369144-5G (2-(trifluoromethyl) acrylic acid (TFMPA) and 235466-100G 1-vinylimidazole (VI) were supplied by Sigma Aldrich. An earlier recipe utilised the crosslinker (44151 EDMA), from VWR (local distributor for Alfa Aesar). pH-sensitive 21584-2500 2-(dimethylamino) ethyl methacrylate (DMAEM) and 16831-2500 methacrylic acid (MAA), together with free radical initiator 40156-0250 2,2'-azobis(2-methylpropionamidine) dihydrochloride (AAPH) and 18784-2500 2-2-dimethoxy-2-phenylacetophenone (DMPA), were obtained from Aik Moh Paints and Chemicals Pte Ltd (local distributor for Acros Organics). The free radical terminator (inhibitor), H17902-500G hydroquinone (HQ), was purchased from Sigma Aldrich.

The same monomer (HEMA), crosslinker (EDMA), pH-sensitive moiety (MAA), inhibitor (HQ) and free radical initiator (DMPA) were obtained from Sigma Aldrich, UK.

Substrate modification and bonding

While in Cambridge, UK, 440140-100ML 3-aminopropyl triethoxysilane (APTES), 30957-100ML 2-(dimethylamino) ethyl acrylate (DMAEA), 407283-100ML dipentaerythritol penta-/hexa-acrylate (DPEPHA), 335681-100ML ethylene glycol dimethacrylate (EDMA), 436895-100ML glycerol dimethacrylate, mixture of isomers (GDM), 477028-100ML 2-hydroxyethyl methacrylate (HEMA), 408336-250ML 2-phenoxyethyl acrylate (a.k.a. ethylene glycol phenyl ether acrylate) (PEA), 469823-100ML poly(ethylene glycol) acrylate (PEGA), 475629-100ML poly(ethylene glycol) (PEG) diacrylate, average M_n ~ 250 ($PEGDA_{250}$), 475629-100ML poly(ethylene glycol) (PEG) diacrylate, average M_n ~ 575 ($PEGDA_{575}$), 407348-100ML poly(ethylene glycol) phenyl ether acrylate (PEGPEA), 246794-100G

pentaerythritol triacrylate (PETA), 408263-100ML pentaerythritol tetraacrylate (PETTA), 440159-100ML 3-(trimethoxysilyl) propylmethacrylate (Silane A174), 444332-100ML 2-(tert-butylamino)ethyl methacrylate (t-BAEM), 398802-250ML tetra(ethylene glycol) diacrylate (TTEGDA), and 658758-5G 1H,1H,2H,2H-perfluorodecyltriethoxysilane (FDTS) were obtained from Sigma Aldrich UK.

While in Singapore, L16584 1H-1H-2H-2H-perfluorodecyltrichlorosilane (FDTS) and 15705 pentaerythritol triacrylate (PETA) were procured from VWR. 667420-5G 1H,1H,2H,2H-perfluorooctyltriethoxysilane (FOTS), APTES, DMAEA, DPEPHA, EDMA, HEMA, PEGDA575, PETTA, PETA, and Silane A174 of the same part numbers as the ones used in UK were purchased from Sigma Aldrich, Singapore.

Hologram fabrication

Saxby developer

15680-5000 4-methylaminophenol sulphate (Metol) was procured from Aik Moh and R0-01452-00-KJ L-ascorbic acid was purchased from Kanto. 791768-1KG sodium carbonate (Na_2CO_3) anhydrous was obtained from Sigma and BDH AnalaR 99% sodium hydroxide (NaOH) pellets were supplied by VWR Singapore.

Formation of Ag^0 nanoparticles (NPs)

21021-0250 silver perchlorate hydrate ($AgClO_4.xH_2O$) from Aik Moh Paints and Chemicals Pte Ltd (local distributor for Acros Organics) and later on 674583-25G silver perchlorate anhydrous ($AgClO_4$) were obtained from Sigma (due to unavailability from Aik Moh). 37079-32 silver (I) perchlorate ($AgClO_4$) was purchased from Kanto.

13408.36 Lithium bromide anhydrous (LiBr) was purchased from VWR and TCID4486 1-1-diethyl-2-2-cyanine iodide (QBS dye) was supplied by Tee Hai. 695092-500ML glacial acetic acid and 217263 sodium thiosulphate ($Na_2S_2O_3$) were both procured from Sigma Aldrich.

Holosensor calibration

pH buffers

In both the UK and Singapore, 791725-1KG citric acid anhydrous and 795410-500G sodium phosphate dibasic (also known as disodium hydrogen phosphate) anhydrous (Na_2HPO_4) were purchased from Sigma Aldrich.

Biologics

CM0361 M.R.S. (de Man, Rogosa and Sharpe) agar and CM0359B M.R.S. (de Man, Rogosa and Sharpe) broth were supplied by Thermo Scientific Microbiology Pte Ltd. *Lactobacillus casei* (*L. casei*) Shirota strain was extracted from Yakult that was purchased from local grocery store in Singapore.

Commercially-available equipment

Substrate preparations

General

ME204 analytical weighing balance (Mettler-Toledo) was purchased from Gaia Science Pte Ltd. The MM1E/65 GTI MiniMatcher® Lightbox was purchased from Cathay Photo Store (Pte) Ltd.

Substrate patterning

The DAD 341 Automatic Dicing Saw Machine and DCS 141 Automatic Cleaning System were both obtained from Disco Hi-Tec (Singapore) Pte Ltd. The VERSA VLS 2.30 30W continuous wave (CW) 10,600 nm CO_2 laser-cutting machine was purchased from Universal Laser Systems, USA. The CNC Mini-Mill 3 Pro Micro-milling machine was acquired from Minitech Machinery Corporation, USA. The ARE-250 Thinky Conditioning Mixer Machine was obtained from Millice Pte Ltd. The VOS-301SD Eyela vacuum oven was purchased from Fisher Scientific Pte Ltd. The minivacuum vacuum packing machine was acquired from Minipack®-torre S.p.A, Italy.

Mould fabrication and injection moulding

In the UK, the Laurell WS-650-23B spin coater and customised spin coater were utilised. In Singapore, the SI-L610 dry film laminator was purchased from Taiwan, ROC. Q300TT Quorum sputter tool was procured from Image Transforms Singapore Pte Ltd (now Ellipsiz DSS Pte Ltd). The WS-400BZ-6NPP/Lite spin coater was purchased from Laurell Technologies Corporation in Singapore. The injection-moulding machine was obtained from Netsal Discjet. The ES-EA3244 automatic self-integrated UV exposure machine was purchased from Yin Hsing Studio Photoengraving Manufacturing, Taiwan. Modec.eps TechnoTrans AG nickel-plating machine (21 kW, 32 A, 50 Hz, 400 V) was obtained from Technotrans Technologies Pte Ltd.

Surface treatment

In the UK, the Diener Femto (100W, 50 kHz, 45 sccm) plasma machine was obtained from Henniker Plasma. LF-206-LS 6W UV dual wavelength (254 nm/365 nm) transilluminator was acquired from Syngene UK. In Singapore, the AP-1000 March Nordson (600W, 13.56 MHz, 500 sccm) plasma machine

was purchased from Dniv System Pte Ltd and the COVANCE-2MPR (300W, 50 kHz, 100 sccm) plasma system was procured from Femto Science Inc, Korea. L12530-01 EX-mini Hamamatsu flat excimer UV ozone treatment machine was purchased from Hakuto Singapore Pte Ltd. The Clear View CSLUVTSDUO dual wavelength (254 nm & 365 nm) UV transilluminator (Max: 1200W) from Cleaver Scientific Ltd was purchased from Techcomp (Singapore) Pte Ltd.

Gel fabrication

UV photo-polymerisation

In the UK, the LF-206-LS dual wavelength (254 nm / 365 nm) UV transilluminator was supplied by Syngene UK and LQ-400 high-powered mercury lamp UV with light guides was from Dr. Gröbel UV-Elektronik GmbH, Germany. The mask aligner and UV intensity meter used were MicroTech MJB4 and #300AA101 UV intensity meter from Karl SUSS respectively. (130422-130724 Cleanroom Lab Book)

In Singapore, the 860604 narrow-band UV (365 nm) programmable light-emitting diode (LED) smart torch with parallel beam adaptor (abbr. UV-LED smart) was purchased from Opsytec Dr. Gröbel, Germany. The CSLUVTSDUO dual wavelength UV transilluminator from Cleaver Scientific was purchased from Techcomp (Singapore) Pte Ltd. A-02-D12-USB Laserpoint laser power measurement kit was procured from Acexon Technologies Pte Ltd. The AG350-6N-D-S-A-V mask aligner was obtained from M & R Nano Technology Co. Ltd, Taiwan.

Gel characterisation

In the UK, the DU® 800 ultraviolet-visible (UV-VIS) spectrophotometer was obtained from Beckman Coulter. The Dektak 6M stylus profilometer was obtained from Veeco (now under Bruker Singapore). Micrographs were captured using the Olympus BX-51 phase contrast microscope.

In Singapore, the Vertex 80v FTIR (bench unit) coupled with Hyperion 3000 micro-FTIR (microscope unit) was supplied by Bruker USA. The Contour-GT white light interferometric 3D (three-dimensional) surface profiler was obtained from Bruker Singapore Pte Ltd. The NanoTest nanoindentation system was purchased from Micro Materials Ltd, Wrexham UK. MM-800 Nikon measuring microscope was utilised for capturing of micrographs.

Holosensor fabrication

In the UK, the 531 nm and 411 nm green and violet laser pointers were purchased from Amazon, UK. The Quantel 'Brilliant B' Q-switched Nd:YAG (350 mJ, 532 nm) pulsed laser was used. The FieldMaster™ laser power meter was acquired from Coherent Inc.

In Singapore, the Integrated Optics (Lithuania) Matchbox 532L-21 50 mW 532 nm continuous wave (CW) Class 3b diode-pumped solid state (DPSS) single longitudinal mode (SLM) green laser was purchased from Acexon Technologies Pte Ltd. The optomechanical components (details in §2.2.1.2) were also procured from Acexon. The vibration isolation optical table was acquired from Newport.

Holosensor interrogation

In the UK, the AvaSpec ULS 2048 spectrophotometer and Avalight-Hal (halogen-tungsten) light source, together with the fibre optic cables for signal transmission, were acquired from Knight Photonics, UK.

In Singapore, the AvaSpec ULS 2048 spectrophotometer with ATTN-DA-HAL-KP direct attachment attenuator and Avalight-Hal-S (Halogen-Tungsten) light source, both supplemented with fiber optic cables, were purchased from Knight Photonics Ltd. The 150W Xenon lamp was purchased from PhotoniTech (Asia) Pte Ltd. The UI-3590CP-C-HQ-Rev.2 high-resolution CMOS colour camera from IDS (Imaging Development Systems) GmbH was purchased from iSolutions Technology Pte Ltd.

Holosensor characterisation and validation

In the UK, the Accumet Basic AB15 pH meter was purchased from Fisher Scientific UK. The HI-8733 conductivity meter was acquired from Hanna Instruments. In Singapore, the 51302601 Mettler Toledo Seven GO-SG23-ELK pH meter with the 51344102 InLab Expert Pro-ISM and InLab 738-ISM conductivity electrodes were purchased from Gaia Science (local distributor for Mettler Toledo).

Biologics

In the UK, a 900W Panasonic NN-T543W microwave was used. In Singapore, the BD115 Binder 115L natural convection incubator was purchased from Tritech Scientific Pte Ltd. RLPR05042A 160L spark free, lockable laboratory Labcold refrigerator and was obtained from ThermoFisher Scientific Pte Ltd. The same spectrophotometer (§Gel characterisation), pH meter and conductivity meter (§Holosensor characterisation and validation) were utilised. An LG MS-192W (230V AC 50 Hz 1200W; 800W power output with 2450 MHz frequency) microwave was used. Model B wavelength-adjustable monochromator was acquired from PhotoniTech Pte Ltd, Singapore. The Hirayama HG-50 autoclave and HPM-16 portable autoclave were procured from ITS Science & Medical Pte Ltd.

Consumables

The P1A85 SDC320R10MB01 diamond tipped blade was obtained from Disco Hi-Tec (Singapore) Pte Ltd. EXTECH-SD700 Barometric Pressure/Humidity/Temperature data logger was purchased from Region Suppliers (Pte) Ltd. AD-22CAS-00-X0 Gel-Pak 0 boxes were obtained from CCD Enterprise Pte Ltd for sample storage during sample transportation between processes. Tapes of various thicknesses

were purchased from Nitto Denko (Singapore) Pte Ltd, Teraoka Seisakusho Co., Ltd and 3M Singapore (3000LSE). WITEG 2410500 500 mL Drechsel bottle, SM-L800/04 GL14 Samco PVC tubing (8 mm ID, 2 mm wall thick) and NT-HC 16mm diameter hose clips were acquired from Newton 101 Pte Ltd. Red LED safelight was obtained from Appliance Innovation Pte Ltd. The Standa 5OM60 and 5OM61 optic mounts were obtained from Acexon Technologies Pte Ltd. 284 QG 10.00mm 2 mL Quartz UV-cuvettes used were obtained from Hellma UK Ltd. QG15100-2 100 μL ES quartz glass cuvettes (10mm path length) were acquired from Aireka Scientific Co., Ltd. The 206-820009-91 cuvette cell holder was procured from Shimadzu (Asia Pacific) Pte Ltd. The different gel precursor chemicals were mixed and stored in 2 mL amber capsules (purchased from Newton 101 Pte Ltd, Singapore). 1 mL Plastic cuvettes, standard 4" and 2" polystyrene petri dishes, 0.25 μm (pore size) hydrophilic syringe filters, polystyrene 6-well plates, 50 mL transfer stripettes and plastic bacteria spreader were purchased from Biopolis Shared Facilities (BSF), Singapore. 50 mL skirted plastic tubes, 30 mL and 2 mL amber bottles were supplied by BD Biosciences Singapore. MCT-150-X Axygen 1.5 mL amber microtubes were purchased from Corning, USA. Neodymium magnets of various shapes and sizes, 715-7718 P4BM and 715-7709 P3BM LED lenser flashlights, 394-217 diamond tipped scribes, 498-1060 3M Tape 810, and 103-4947 alligator clips were purchased from RS Components Pte Ltd. The X-Rite MSCCPP ColourChecker® was obtained from Cathay Photo (Pte) Ltd and the #87-413 X-Rite Pico Glossy ColourChecker® (ColorGauge Target) was acquired from Edmund Optics Singapore Pte Ltd. 0.50 mm Harris Uni-Core PDMS puncher was obtained from Sigma Aldrich.

Software

Solidworks 2013 was licensed and purchased from SeaCAD Singapore. The VERSA CO_2 laser-cutting machine runs on the VLS 2.30 software, which imported the design file from AutoCAD Mechanical 2008. The smartUV 1.1.1 software was utilised to adjust the parameters for the UV-LED smart. The Contour-GT-K white light profiler was run on Vision 64 ver 5.3, which captured micrographs, 2D contour plots (digital elevation models) and 3D surface profiles, of gels, holosensors, and cyclic olefin copolymer (COC) cover substrates. The μEye software for the high-resolution CMOS colour camera was used to capture the red, green and blue (RGB) light intensities of the holosensor. In the UK, Avasoft 7.2 software from Avantes (purchased from Knight Photonics Ltd) was utilised to obtain holosensor peak wavelength data, while the Avasoft 8.0 software with Soft-COL add-on software (also from Knight Photonics Ltd) for colour analysis was used in Singapore for OD_{600} measurements (with the customised spectrophotometer in §2.2.2.4) and holosensor peak wavelength assessment. The xyY (colour space) values were converted from RGB values using MATLAB®R2012a with the algorithm coded by Dr Gita Moghaddam.

References

[1] D. M. Wuest, S. W. Harcum, and K. H. Lee, “Genomics in mammalian cell culture bioprocessing.,” *Biotechnol. Adv.*, vol. 30, no. 3, pp. 629–38, 2012.

[2] F. Kensy, C. Engelbrecht, and J. Büchs, “Scale-up from microtiter plate to laboratory fermenter: evaluation by online monitoring techniques of growth and protein expression in Escherichia coli and Hansenula polymorpha fermentations.,” *Microb. Cell Fact.*, vol. 8, p. 68, Jan. 2009.

[3] N. Reis, C. N. Gonc, A. A. Vicente, and J. A. Teixeira, “Proof-of-Concept of a Novel Micro-Bioreactor for Fast Development of Industrial Bioprocesses,” no. 2001, 2006.

[4] R. Bareither and D. Pollard, “A review of advanced small-scale parallel bioreactor technology for accelerated process development: current state and future need.,” *Biotechnol. Prog.*, vol. 27, no. 1, pp. 2–14, 2011.

[5] B. J. Kim, J. Diao, and M. L. Shuler, “Mini-scale bioprocessing systems for highly parallel animal cell cultures.,” *Biotechnol. Prog.*, vol. 28, no. 3, pp. 595–607, May 2012.

[6] D. M. Bower, K. S. Lee, R. J. Ram, and K. L. J. Prather, “Fed-batch microbioreactor platform for scale down and analysis of a plasmid DNA production process.,” *Biotechnol. Bioeng.*, vol. 109, no. 8, pp. 1976–86, Aug. 2012.

[7] J. Hogan, “A little goes a long way,” *Nat. Publ. Gr.*, vol. 442, no. July, pp. 27–28, 2006.

[8] J. I. Betts and F. Baganz, “Miniature bioreactors: current practices and future opportunities.,” *Microb. Cell Fact.*, vol. 5, p. 21, Jan. 2006.

[9] S. Kumar, C. Wittmann, and E. Heinzle, “Minibioreactors,” *Biotechnol. Lett.*, vol. 26, pp. 1–10, 2004.

[10] H. Andersson and A. van den Berg, “Microtechnologies and nanotechnologies for single-cell analysis.,” *Curr. Opin. Biotechnol.*, vol. 15, no. 1, pp. 44–9, Feb. 2004.

[11] P. C. Blainey, “The future is now: single-cell genomics of bacteria and archaea.,” *FEMS Microbiol. Rev.*, Jan. 2013.

[12] R. L. Fernandes, M. Nierychlo, L. Lundin, a E. Pedersen, P. E. Puentes Tellez, A. Dutta, M. Carlquist, A. Bolic, D. Schäpper, a C. Brunetti, S. Helmark, A.-L. Heins, a D. Jensen, I. Nopens, K. Rottwitt, N. Szita, J. D. van Elsas, P. H. Nielsen, J. Martinussen, S. J. Sørensen, a E. Lantz, and K. V Gernaey, “Experimental methods and modeling techniques for description of cell population heterogeneity.,” *Biotechnol. Adv.*, vol. 29, no. 6, pp. 575–99, 2011.

[13] D. Gao, H. Liu, Y. Jiang, and J.-M. Lin, “Recent developments in microfluidic devices for in vitro cell culture for cell-biology research,” *TrAC Trends Anal. Chem.*, vol. 35, pp. 150–164, May 2012.

[14] R. Pörtner, *Animal Cell Biotechnology: Methods and Protocols*, 3rd ed. Humana Press, 2014.

[15] L. Tolosa, Y. Kostov, P. Harms, and G. Rao, “Noninvasive measurement of dissolved oxygen in shake flasks,” *Biotechnol. Bioeng.*, vol. 80, no. 5, pp. 594–597, 2002.

[16] P. Rohe, D. Venkanna, B. Kleine, R. Freudl, and M. Oldiges, “An automated workflow for enhancing microbial bioprocess optimization on a novel microbioreactor platform,” *Microb. Cell Fact.*, vol. 11, no. 1, p. 144, 2012.

[17] D. Schäpper, M. N. H. Z. Alam, N. Szita, A. Eliasson Lantz, and K. V Gernaey, “Application of microbioreactors in fermentation process development: a review.,” *Anal. Bioanal. Chem.*, vol. 395, no. 3, pp. 679–95, Oct. 2009.

[18] S. Goh and R. J. Ram, “Impedance Spectroscopy for In Situ Biomass Measurements in Microbioreactors,” in *14th Interntational Conference on Miniaturized Systems for Chemistry and Life Sciences*, 2010, no. October, pp. 1556–1558.

[19] G. Pasirayi, V. Auger, S. M. Scott, P. K.S.M. Rahman, M. Islam, L. O’Hare, and Z. Ali, “Microfluidic Bioreactors for Cell Culturing: A Review,” *Micro Nanosyst.*, vol. 3, no. 2, pp. 137–160, Jul. 2011.

[20] A. Amanullah, J. M. Otero, M. Mikola, A. Hsu, J. Zhang, J. Aunins, H. B. Schreyer, J. A. Hope, and A. P. Russo, “Novel micro-bioreactor high throughput technology for cell culture process development: Reproducibility and scalability assessment of fed-batch CHO cultures,” *Biotechnol. Bioeng.*, vol. 106, no. 1, pp. 57–67, 2010.

[21] J. Hogan, “Lab on a chip: A little goes a long way,” *Nature*, vol. 442, no. 7101, pp. 351–352, 2006.

[22] A. Zanzotto, N. Szita, P. Boccazzi, P. Lessard, A. J. Sinskey, and K. F. Jensen, “Membrane-aerated microbioreactor for high-throughput bioprocessing,” *Biotechnol. Bioeng.*, vol. 87, no. 2, pp. 243–254, 2004.

[23] W. A. Duetz, “Microtiter plates as mini-bioreactors: miniaturization of fermentation methods,” *Trends Microbiol.*, vol. 15, no. 10, pp. 469–475, 2007.

[24] S. R. C. Warr, J. Patel, R. Ho, and K. V. Newell, “Use of Micro Bioreactor systems to streamline cell line evaluation and upstream process development for monoclonal antibody production.,” *BMC Proc.*, vol. 5, no. (Suppl 8), p. P14, 2011.

[25] J. P. J. Betts, S. R. C. Warr, G. B. Finka, M. Uden, M. Town, J. M. Janda, F. Baganz, and G. J. Lye, “Impact of aeration strategies on fed-batch cell culture kinetics in a single-use 24-well miniature bioreactor,” *Biochem. Eng. J.*, vol. 82, pp. 105–116, 2014.

[26] A. Chen, R. Chitta, D. Chang, and A. Amanullah, “Twenty-four well plate miniature bioreactor system as a scale-down model for cell culture process development,” *Biotechnol. Bioeng.*, vol. 102, no. 1, pp. 148–160, 2009.

[27] R. Bareither and D. Pollard, “A review of advanced small-scale parallel bioreactor technology for accelerated process development: current state and future need.,” *Biotechnol. Prog.*, vol. 27, no. 1, pp. 2–14, 2011.

[28] R. Bareither and D. Pollard, “A review of advanced small-scale parallel bioreactor technology for accelerated process development: Current state and future need,” *Biotechnol. Prog.*, vol. 27, no. 1, pp. 2–14, 2011.

[29] P. Boccazzi, Z. Zhang, K. Kurosawa, N. Szita, S. Bhattacharya, K. F. Jensen, and A. J. Sinskey, “Differential gene expression profiles and real-time measurements of growth parameters in Saccharomyces cerevisiae grown in microliter-scale bioreactors equipped with internal stirring,” *Biotechnol. Prog.*, vol. 22, no. 3, pp. 710–717, 2006.

[30] Z. Zhang, N. Szita, P. Boccazzi, A. J. Sinskey, and K. F. Jensen, “A well-mixed, polymer-based microbioreactor with integrated optical measurements,” *Biotechnol. Bioeng.*, vol. 93, no. 2, pp. 286–296, 2006.

[31] A. Zanzotto, N. Szita, P. Boccazzi, P. Lessard, A. J. Sinskey, and K. F. Jensen, "Membrane-aerated microbioreactor for high-throughput bioprocessing.," *Biotechnol. Bioeng.*, vol. 87, no. 2, pp. 243–54, Jul. 2004.

[32] A. Zanzotto, P. Boccazzi, N. Gorret, T. K. Van Dyk, A. J. Sinskey, and K. F. Jensen, "In situ measurement of bioluminescence and fluorescence in an integrated microbioreactor," *Biotechnol. Bioeng.*, vol. 93, no. 1, pp. 40–47, 2006.

[33] K. S. Lee, P. Boccazzi, A. J. Sinskey, and R. J. Ram, "Microfluidic chemostat and turbidostat with flow rate, oxygen, and temperature control for dynamic continuous culture.," *Lab Chip*, vol. 11, no. 10, pp. 1730–9, May 2011.

[34] R. E. Holcomb, L. J. Mason, K. F. Reardon, D. M. Cropek, and C. S. Henry, "Culturing and investigation of stress-induced lipid accumulation in microalgae using a microfluidic device," *Anal. Bioanal. Chem.*, vol. 400, no. 1, pp. 245–253, 2011.

[35] M. N. H. Z. Alam, D. Schäpper, and K. V Gernaey, "Embedded resistance wire as a heating element for temperature control in microbioreactors," *J. Micromechanics Microengineering*, vol. 20, no. 5, p. 55014, 2010.

[36] R. Willaert and K. Goossens, *Microfluidic Bioreactors for Cellular Microarrays*, vol. 1, no. 1. 2015.

[37] Z. F. Cui, X. Xu, N. Trainor, J. T. Triffitt, J. P. G. Urban, and U. K. Tirlapur, "Application of multiple parallel perfused microbioreactors and three-dimensional stem cell culture for toxicity testing," *Toxicol. Vitr.*, vol. 21, no. 7, pp. 1318–1324, 2007.

[38] S. Halldorsson, E. Lucumi, R. Gómez-Sjöberg, and R. M. T. Fleming, "Advantages and challenges of microfluidic cell culture in polydimethylsiloxane devices," *Biosens. Bioelectron.*, vol. 63, pp. 218–231, 2015.

[39] M. M. Maharbiz, W. J. Holtz, R. T. Howe, and J. D. Keasling, "Microbioreactor Arrays with Parametric Control for High-Throughput Experimentation," *Biotechnol. Bioeng.*, vol. 85, no. 4, pp. 376–381, 2004.

[40] M. van Leeuwen, E. E. Krommenhoek, J. J. Heijnen, H. Gardeniers, L. A. M. van der Wielen, and W. M. van Gulik, "Aerobic batch cultivation in micro bioreactor with integrated electrochemical sensor array," *Biotechnol. Prog.*, vol. 26, no. 1, pp. 293–300, 2010.

[41] M. N. H. Z. Alam, M. Pinelo, K. Samanta, G. Jonsson, A. Meyer, and K. V. Gernaey, "A continuous membrane microbioreactor system for development of integrated pectin modification and separation processes," *Chem. Eng. J.*, vol. 167, no. 2–3, pp. 418–426, Mar. 2011.

[42] T. Y. Seo, K. W. Eum, S. O. Han, S. W. Kim, J. H. Kim, K. H. Song, and J. Choe, "Immobilized cell microchannel bioreactor for evaluating fermentation characteristics of mixed substrate consumption and product formation," *Process Biochem.*, vol. 47, no. 6, pp. 1011–1015, 2012.

[43] S. H. Au, S. C. C. Shih, and A. R. Wheeler, "Integrated microbioreactor for culture and analysis of bacteria, algae and yeast," *Biomed. Microdevices*, vol. 13, no. 1, pp. 41–50, 2011.

[44] J. R. McKenzie, A. Cognata, A. N. Davis, J. P. Wikswo, and D. E. Cliffel, "Real-Time Monitoring of Cellular Bioenergetics with a Multi-Analyte Screen-Printed Electrode," *Anal. Chem.*, p. 150630093637003, 2015.

[45] F. K. Balagaddé, L. You, C. L. Hansen, F. H. Arnold, and S. R. Quake, “Long-term monitoring of bacteria undergoing programmed population control in a microchemostat.,” *Science*, vol. 309, no. 5731, pp. 137–40, Jul. 2005.

[46] H. E. Abaci, R. Devendra, Q. Smith, S. Gerecht, and G. Drazer, “Design and development of microbioreactors for long-term cell culture in controlled oxygen microenvironments.,” *Biomed. Microdevices*, vol. 14, no. 1, pp. 145–52, Feb. 2012.

[47] D. Matteau, V. Baby, S. Pelletier, and S. Rodrigue, “A small-volume, low-cost, and versatile continuous culture device,” *PLoS One*, vol. 10, no. 7, pp. 1–13, 2015.

[48] T. V. Kirk and N. Szita, “Oxygen transfer characteristics of miniaturized bioreactor systems,” *Biotechnol. Bioeng.*, vol. 110, no. 4, pp. 1005–1019, 2013.

[49] K. S. Lee, P. Boccazzi, A. J. Sinskey, and R. J. Ram, “Microfluidic chemostat and turbidostat with flow rate, oxygen, and temperature control for dynamic continuous culture.,” *Lab Chip*, vol. 11, no. 10, pp. 1730–1739, 2011.

[50] L. A. Tribe, C. L. Briens, and A. Margaritis, “Communication to the Editor Determination of the Volumetric Mass Transfer Coefficient (k,a) Using the Dynamic " Gas Out-Gas In " Method: Analysis of Errors Caused by Dissolved Oxygen Probes,” *Biotechnol. Bioeng.*, vol. 46, no. 4, pp. 388–392, 1995.

[51] S. Schaepe, A. Kuprijanov, C. Sieblist, M. Jenzsch, R. Simutis, and A. Lübbert, “KLa of stirred tank bioreactors revisited,” *J. Biotechnol.*, vol. 168, no. 4, pp. 576–583, 2013.

[52] S. Suresh, V. C. Srivastava, and I. M. Mishra, “Techniques for oxygen transfer measurement in bioreactors: A review,” *J. Chem. Technol. Biotechnol.*, vol. 84, no. 8, pp. 1091–1103, 2009.

[53] J. Gottschamel, L. Richter, A. Mak, C. Jungreuthmayer, G. Birnbaumer, M. Milnera, H. Brückl, and P. Ertl, “Development of a disposable microfluidic biochip for multiparameter cell population measurements,” *Anal. Chem.*, vol. 81, no. 20, pp. 8503–8512, 2009.

[54] S. A. M. Shaegh, F. De Ferrari, Y. S. Zhang, M. Nabavinia, N. B. Mohammad, J. Ryan, A. Pourmand, E. Laukaitis, R. B. Sadeghian, A. Nadhman, S. R. Shin, A. S. Nezhad, A. Khademhosseini, and M. R. Dokmeci, “A microfluidic optical platform for real-time monitoring of pH and oxygen in microfluidic bioreactors and organ-on-chip devices,” *Biomicrofluidics*, vol. 10, no. 4, 2016.

[55] Z. Zhang, P. Boccazzi, H.-G. Choi, G. Perozziello, A. J. Sinskey, and K. F. Jensen, “Microchemostat-microbial continuous culture in a polymer-based, instrumented microbioreactor.,” *Lab Chip*, vol. 6, no. 7, pp. 906–13, Jul. 2006.

[56] A. Ettinger and T. Wittmann, “Flourescence Live Cell Imaging,” *Methods Cell Biol.*, vol. 123, pp. 77–94, 2015.

[57] K. Jacobson, Z. Rajfur, E. Vitrol, and K. Hahn, “Chromophore-assisted laser inactivation in cell biology,” *Trends Cell Biol.*, vol. 18, no. 9, pp. 443–450, 2008.

[58] Y. Berthois, J. A. Katzenellenbogent, and B. S. Katzenellenbogen, “Phenol red in tissue culture media is a weak estrogen : Implications concerning the study of estrogen-responsive cells in culture,” vol. 83, no. April, pp. 2496–2500, 1986.

[59] X. Liu, B. Chen, L. Chen, W. T. Ren, J. Liu, G. Wang, W. Fan, X. Wang, and Y. Wang, “U-Shape Suppressive Effect of Phenol Red on the Epileptiform Burst Activity via Activation of Estrogen Receptors in Primary Hippocampal Culture,” *PLoS One*, vol. 8, no. 4, 2013.

[60] K. Still, L. Reading, and A. Scutt, “Effects of phenol red on CFU-f differentiation and formation,” *Calcif. Tissue Int.*, vol. 73, no. 2, pp. 173–179, 2003.

[61] L. H. Grady, D. J. Nonneman, G. E. Rottinghaus, and W. V. Welshons, “pH-dependent cytotoxicity of contaminants of phenol red for MCF-7 breast cancer cells,” *Endocrinology*, vol. 129, no. 6, pp. 3321–3330, 1991.

[62] M. M. Walsh-Reitz and F. G. Toback, “Phenol red inhibits growth of renal epithelial cells,” *Am. J. Physiol. - Ren. Physiol.*, vol. 262, no. 4, pp. F687--F691, 1992.

[63] F. K. Balagaddé, L. You, C. L. Hansen, F. H. Arnold, and S. R. Quake, “Long-term monitoring of bacteria undergoing programmed population control in a microchemostat.,” *Science (80-.).*, vol. 309, no. 5731, pp. 137–140, 2005.

[64] W. B. J. Zimmerman, *Microfluidics: History, Theory and Applications*. Springer Science & Business Media, 2006, 2006.

[65] D. C. Duffy, J. C. McDonald, O. J. Schueller, and G. M. Whitesides, “Rapid Prototyping of Microfluidic Systems in Poly(dimethylsiloxane).,” *Anal. Chem.*, vol. 70, no. 23, pp. 4974–84, Dec. 1998.

[66] S. K. Sia and G. M. Whitesides, “Microfluidic devices fabricated in poly(dimethylsiloxane) for biological studies.,” *Electrophoresis*, vol. 24, no. 21, pp. 3563–76, Nov. 2003.

[67] P. Jothimuthu, A. Carroll, A. A. S. Bhagat, G. Lin, J. E. Mark, and I. Papautsky, “Photodefinable PDMS thin films for microfabrication applications,” *J. Micromechanics Microengineering*, vol. 19, pp. 1–9, 2009.

[68] A. Kumar and G. M. Whitesides, “Features of gold having micrometer to centimeter dimensions can be formed through a combination of stamping with an elastomeric stamp and an alkanethiol ‘ink’ followed by chemical etching,” *Appl. Phys. Lett.*, vol. 63, no. 14, pp. 2002–2004, 1993.

[69] F. Liu, A. N. Nordin, and I. Voiculescu, “Multiparametric MEMS Biosensor for Cell Culture Monitoring,” in *Design, Test, Integration and Packaging of MEMS/MOEMS (DTIP)*, no. April, 2013, pp. 1–5.

[70] H. Ceylan Koydemir, H. Külah, C. Özgen, A. Alp, and G. Hasçelik, “MEMS biosensors for detection of methicillin resistant Staphylococcus aureus.,” *Biosens. Bioelectron.*, vol. 29, no. 1, pp. 1–12, Nov. 2011.

[71] J. Melin, “Single-Molecule Detection and Optical Scanning in Miniaturized Formats,” Uppsala University, Sweden, Sweden, 2006.

[72] B. El-Kareh, *Fundamentals of Semiconductor Processing Technology*, 1st editio. Springer Science+Business Media, LLC, 1995.

[73] M. L. Kovarik, P. C. Gach, D. M. Ornoff, Y. Wang, J. Balowski, L. Farrag, and N. L. Allbritton, “Micro total analysis systems for cell biology and biochemical assays.,” *Anal. Chem.*, vol. 84, no. 2, pp. 516–40, Jan. 2012.

[74] J. Pihl, M. Karlsson, and D. T. Chiu, “Microfluidic technologies in drug discovery microfluidic systems and technologies in the process of drug discovery,” *Drug Discov. Today*, vol. 10, no. 20, pp. 1377–1383, 2005.

[75] S. Vyawahare, A. D. Griffiths, and C. A. Merten, “Miniaturization and parallelization of biological and chemical assays in microfluidic devices,” *Chem. Biol.*, vol. 17, no. 10, pp. 1052–1065, 2010.

[76] T. M. Squires, “Microfluidics Fluid physics at the nanoliter.pdf,” vol. 77, no. July, 2005.

[77] C. E. Sims and N. L. Allbritton, “Analysis of single mammalian cells on-chip.,” *Lab Chip*, vol. 7, no. 4, pp. 423–40, Apr. 2007.

[78] D. R. Thevenot, K. Toth, R. A. Durst, and W. G. S, “IUPAC Recommended Definitions and Classification,” *Pure Appl. Chem.*, vol. 71, no. 12, pp. 2333–2348, 1999.

[79] L. L. Bell, “Optically Interrogated Biosensors in Microfluidics (PhD Thesis),” University of Cambridge, 2011.

[80] A. J. Marshall, J. Blyth, C. A. B. Davidson, and C. R. Lowe, “pH-sensitive holographic sensors.,” *Anal. Chem.*, vol. 75, no. 17, pp. 4423–31, Sep. 2003.

[81] C. R. Lowe, “Holographic Sensors,” in *Handbook of Biosensors and Biochips*, John Wiley & Sons, Ltd, 2008.

[82] S. Kabilan, J. Blyth, M. C. Lee, A. J. Marshall, A. Hussain, X.-P. Yang, and C. R. Lowe, “Glucose-sensitive holographic sensors.,” *J. Mol. Recognit.*, vol. 17, no. 3, pp. 162–6, 2004.

[83] X. Yang, M. Lee, F. Sartain, X. Pan, and C. R. Lowe, “Designed Boronate Ligands for Glucose-Selective Holographic Sensors,” pp. 8491–8497, 2006.

[84] R. Hu, A. C. Stevenson, and C. R. Lowe, “An acoustic glucose sensor.,” *Biosens. Bioelectron.*, vol. 35, no. 1, pp. 425–8, May 2012.

[85] A. J. Marshall, D. S. Young, J. Blyth, S. Kabilan, and C. R. Lowe, “Metabolite-sensitive holographic biosensors.,” *Anal. Chem.*, vol. 76, no. 5, pp. 1518–23, Mar. 2004.

[86] F. K. Sartain, X. Yang, and C. R. Lowe, “Holographic Lactate Sensor,” vol. 78, no. 16, pp. 5664–5670, 2006.

[87] F. K. Sartain, X. Yang, and C. R. Lowe, “Complexation of l-Lactate with Boronic Acids : A Solution and Holographic Analysis,” pp. 4060–4067, 2008.

[88] R. B. Millington, A. G. Mayes, J. Blyth, and C. R. Lowe, “A Holographic Biosensor,” *Proc. Int. Solid-State Sensors Actuators Conf. - TRANSDUCERS ’95*, vol. 1, pp. 509–512, 1995.

[89] R. B. Millington, A. G. Mayes, J. Blyth, and C. R. Lowe, “A hologram biosensor for proteases,” *Sensors Actuators B*, vol. 33, pp. 55–59, 1996.

[90] D. M. Disley, J. Blyth, D. C. Cullen, H. X. You, S. Eapen, and C. R. Lowe, “Covalent coupling of immunoglobulin G to a poly(vinyl)alcohol-poly(acrylic acid) graft polymer as a method for fabricating the interfacial-recognition layer of a surface plasmon resonance immunosensor.,” *Biosens. Bioelectron.*, vol. 13, no. 3–4, pp. 383–96, Mar. 1998.

[91] J. Blyth, R. B. Millington, A. G. Mayes, E. R. Frears, and C. R. Lowe, “Holographic sensor for water in solvents.,” *Anal. Chem.*, vol. 68, no. 7, pp. 1089–94, Apr. 1996.

[92] A. G. Mayes, J. Blyth, M. Kyro, R. B. Millington, and C. R. Lowe, “A Holographic Alcohol Sensor,” *Anal. Chem.*, vol. 71, no. 16, pp. 3390–3396, 1999.

[93] A. G. Mayes, J. Blyth, R. B. Millington, and C. R. Lowe, “Metal ion-sensitive holographic sensors.,” *Anal. Chem.*, vol. 74, no. 15, pp. 3649–57, Aug. 2002.

[94] B. Madrigal González, G. Christie, C. a. B. Davidson, J. Blyth, and C. R. Lowe, “Divalent metal ion-sensitive holographic sensors,” *Anal. Chim. Acta*, vol. 528, no. 2, pp. 219–228, Jan. 2005.

[95] J. L. Martínez-Hurtado, C. A. B. Davidson, J. Blyth, and C. R. Lowe, “Holographic detection of hydrocarbon gases and other volatile organic compounds,” *Langmuir*, vol. 26, no. 19, pp. 15694–15699, Oct. 2010.

[96] X. Luo and J. J. Davis, “Electrical biosensors and the label free detection of protein disease biomarkers.,” *Chem. Soc. Rev.*, vol. 42, no. 13, pp. 5944–62, Jul. 2013.

[97] S. Herber, J. Bomer, W. Olthuis, P. Bergveld, and A. van den Berg, “A miniaturized carbon dioxide gas sensor based on sensing of pH-sensitive hydrogel swelling with a pressure sensor.,” *Biomed. Microdevices*, vol. 7, no. 3, pp. 197–204, Sep. 2005.

[98] R. Gracia and D. Mecerreyes, “Polymers with redox properties: materials for batteries, biosensors and more,” *Polym. Chem.*, vol. 4, no. 7, p. 2206, 2013.

[99] J. C. Pickup, F. Hussain, N. D. Evans, O. J. Rolinski, and D. J. S. Birch, “Fluorescence-based glucose sensors.,” *Biosens. Bioelectron.*, vol. 20, no. 12, pp. 2555–65, Jun. 2005.

[100] N. D. Lourenço, J. a Lopes, C. F. Almeida, M. C. Sarraguça, and H. M. Pinheiro, “Bioreactor monitoring with spectroscopy and chemometrics: a review.,” *Anal. Bioanal. Chem.*, vol. 404, no. 4, pp. 1211–37, Sep. 2012.

[101] L. M. Bellan, D. Wu, and R. S. Langer, “Current trends in nanobiosensor technology.,” *Wiley Interdiscip. Rev. Nanomed. Nanobiotechnol.*, vol. 3, no. 3, pp. 229–46, 2011.

[102] A. Mateescu, Y. Wang, J. Dostalek, and U. Jonas, “Thin Hydrogel Films for Optical Biosensor Applications,” *Membranes (Basel).*, vol. 2, no. 4, pp. 40–69, Feb. 2012.

[103] M. Ebara, Y. Kotsuchibashi, R. Narain, N. Idota, Y. J. Kim, J. M. Hoffman, K. Uto, and T. Aoyagi, *Smart Biomaterials*. Springer Japan, 2014.

[104] V. Mucci and C. Vallo, “Efficiency of 2 , 2-Dimethoxy-2-phenylacetophenone for the Photopolymerization of Methacrylate Monomers in Thick Sections,” *J. Appl. Polym. Sci.*, vol. 123, pp. 418–425, 2011.

[105] H. Fischer, R. Baer, R. Hany, I. Verhoolen, and M. Walbiner, “2,2-Dimethoxy-2-phenylacetophenone: Photochemistry and Free Radical Photofragmentation,” *J. Chem. Soc. Perkin Trans. 2*, pp. 787–798, 1990.

[106] S. Ruebel and M. Stuemke, “Preparation for the photodynamic control of micro-organisms and use thereof,” US 20070254349 A1, 2004.

[107] A. M. and C. L. J Blyth, RB Millington, “A diffusion method for making silver bromide based holographic recording material,” *Imaging Sci. J.*, vol. 47, pp. 87–91, 1999.

[108] G. Saxby and S. Zacharovas, *Practical Holography, Fourth Edition*. CRC Press, 2015.

[109] P. Hariharan, *Basics of Holography*. Cambridge University Press, 2002.

[110] D. Gabor, “A New Microscopic Principle,” *Nature*, vol. 161, pp. 777–778, 1948.

[111] E. N. Leith and J. Upatnieks, “Reconstructed Wavefronts and Communication Theory,” *J. Opt. Soc. Am.*, vol. 52, no. 10, pp. 1123–1130, Oct. 1962.

[112] A. K. Yetisen, I. Naydenova, F. da Cruz Vasconcellos, J. Blyth, and C. R. Lowe, “Holographic Sensors: Three-Dimensional Analyte-Sensitive Nanostructures and Their Applications,” *Chem. Rev.*, Sep. 2014.

[113] H. M. Hegab, A. ElMekawy, and T. Stakenborg, “Review of microfluidic microbioreactor technology for high-throughput submerged microbiological cultivation,” *Biomicrofluidics*, vol. 7, no. 2, pp. 1–14, 2013.

[114] G. Saxby, “The basic types of hologram,” in *Practical Holography, Third Edition*, Taylor & Francis, 2003, pp. 46–56.

[115] S. Kabilan, A. J. Marshall, F. K. Sartain, M.-C. Lee, A. Hussain, X. Yang, J. Blyth, N. Karangu, K. James, J. Zeng, D. Smith, A. Domschke, and C. R. Lowe, “Holographic glucose sensors.,” *Biosens. Bioelectron.*, vol. 20, no. 8, pp. 1602–10, Feb. 2005.

[116] D. Bhatta, G. Christie, J. Blyth, and C. R. Lowe, “Holographic sensors for the detection of bacterial spores,” vol. 23, pp. 520–527, 2007.

[117] E. V. Tan and C. R. Lowe, “Holographic enzyme inhibition assays for drug discovery.,” *Anal. Chem.*, vol. 81, no. 18, pp. 7579–89, Sep. 2009.

[118] C. R. Lowe, “Holographic Sensors and their Production,” US 2007/0036674 A1, 2004.

[119] J. Blyth, C. R. Lowe, A. G. Mayes, and R. B. Millington, “Holographic Sensors and their Production,” US 6689316 B1, 1999.

[120] K. Jacqueline, “Optical Immunoassays for Pregnancy (PhD Thesis),” University of Cambridge, 2015.

[121] A. K. Yetisen, “Holographic Point-of-Care Diagnostic Devices (PhD Thesis),” Univerisity of Cambridge, 2014.

[122] J. L. Martinez-Hurtado, “Gas-Sensitive Holographic Sensors (PhD Thesis),” University of Cambridge, 2012.

[123] A. K. Yetisen, M. M. Qasim, S. Nosheen, T. D. Wilkinson, and C. R. Lowe, “Pulsed laser writing of holographic nanosensors,” *J. Mater. Chem. C*, 2014.

[124] C. A. Dobson, “The design, fabrication and characterization of holographic optical elements (PhD Thesis),” University of Cambridge, 2007.

[125] “pH: Are You in Control of a Moving Target? .” [Online]. Available: http://www.pharmamanufacturing.com/articles/2011/044.html. [Accessed: 03-Sep-2013].

[126] P. Gaynor, “Generally Recognized as Safe (GRAS) Determination for the Use of Lactobacillus casei Strain Shirota As a Food Ingredient,” 2012.

[127] V. Sunkara, D.-K. Park, H. Hwang, R. Chantiwas, S. A. Soper, and Y.-K. Cho, “Simple room temperature bonding of thermoplastics and poly(dimethylsiloxane),” *Lab Chip*, vol. 11, no. 5, pp. 962–965, Mar. 2011.

[128] J. R. Vig, “Ultraviolet-Ozone Cleaning of Semiconductor Surfaces,” Fort Monmouth, NJ, 1992.

[129] A. T. Augousti, N. White, and N. M. White, Eds., “Sensors and Their Applications VIII, Proceedings of the eighth conference on Sensors and their Applications,” 1997, p. 276.

[130] S. Sutton, “Counting Colonies,” *The Microbiology Network*, 2006. [Online]. Available: http://www.microbiol.org/resources/monographswhite-papers/counting-colonies/.

[131] L. L. Bell, A. A. Seshia, C. A. B. Davidson, and C. R. Lowe, “Integration of holographic sensors into microfluidics for the real-time pH sensing of L. casei metabolism,” *Procedia Eng.*, vol. 5, pp. 1352–1355, Jan. 2010.

[132] C. A. B. Davidson, J. Blyth, and B. Madrigal Gonzalez, “Holographic Sensors and their Production,” EP 1602013 B1, 2004.

[133] S. Park, D. Kim, S. Y. Ko, J.-O. Park, S. Akella, B. Xu, Y. Zhang, and S. Fraden, “Controlling uniformity of photopolymerized microscopic hydrogels,” *Lab Chip*, 2014.

[134] C. Barner-Kowollik, T. P. Davis, and M. H. Stenzel, “Probing mechanistic features of conventional, catalytic and living free radical polymerizations using soft ionization mass spectrometric techniques,” *Polymer (Guildf).*, vol. 45, no. 23, pp. 7791–7805, 2004.

[135] A. Tiwari and A. Polykarpov, *Photocured Materials*. Royal Society of Chemistry, 2014.

[136] P. Glöckner, *Radiation Curing: Coatings and Printing Inks ; Technical Basics, Applications and Trouble Shooting*. Vincentz Network, 2008.

[137] ISO 2768-1, “Tolerances for linear and angular dimensions without individual tolerance indications,” 1989.

[138] H. I. Bjelkhagen, *Silver-Halide Recording Materials: for Holography and Their Processing*. Springer Berlin Heidelberg, 1995.

[139] J. Zhou, W. Tang, and D. Liu, “Analysis of polarization properties of reflection volume holographic grating,” *Opt. Commun.*, vol. 196, no. 1–6, pp. 77–84, 2001.

[140] A. Edlich, V. Magdanz, D. Rasch, S. Demming, S. Aliasghar Zadeh, R. Segura, C. Kähler, R. Radespiel, S. Büttgenbach, E. Franco-Lara, and R. Krull, “Microfluidic reactor for continuous cultivation of Saccharomyces cerevisiae.,” *Biotechnol. Prog.*, vol. 26, no. 5, pp. 1259–70, 2010.

[141] B. J. Lindbloom, “Accurate Color Reproduction for Computer Graphics Applications,” in *Proceedings of the 16th Annual Conference on Computer Graphics and Interactive Techniques*, 1989, vol. 23, no. 3, pp. 117–126.

[142] F. Mendoza, P. Dejmek, and J. M. Aguilera, “Calibrated color measurements of agricultural foods using image analysis,” *Postharvest Biol. Technol.*, vol. 41, no. 3, pp. 285–295, 2006.

[143] G. W. C. Kaye, G. W. C. Kaye, and T. H. Laby, *Tables of physical and chemical constants and some mathematical functions*, 15th editi. Longman, 1986.

[144] A. L. C. Senedese, R. M. Filho, and M. R. W. Maciel, “L-Lactic Acid Production by Lactobacillus rhamnosus ATCC 10863,” *Sci. World J.*, vol. 2015, no. Article ID 501029, p. 6 pages, 2015.

[145] I. V Khudyakov and N. J. Turro, “Cage Effect Dynamics under Photolysis of Photoinitiators,” *Des. Monomers Polym.*, vol. 13, no. October 2014, pp. 487–496, 2010.

[146] A. Zellander, C. Zhao, M. Kotecha, R. Gemeinhart, M. Wardlow, J. Abiade, and M. Cho, "Characterization of pore structure in biologically functional poly(2-hydroxyethyl methacrylate) - Poly(ethylene glycol) diacrylate (PHEMA-PEGDA)," *PLoS One*, vol. 9, no. 5, pp. 1–8, 2014.

[147] N. Annabi, J. W. Nichol, X. Zhong, C. Ji, S. Koshy, A. Khademhosseini, and F. Dehghani, "Controlling the porosity and microarchitecture of hydrogels for tissue engineering.," *Tissue Eng. Part B. Rev.*, vol. 16, no. 4, pp. 371–83, 2010.

[148] Wiley-VCH, *Ullmann's Polymers and Plastics: Products and Processes*. John Wiley & Sons, 2016.

[149] N. B. C. Engineers, *Synthetic Resins Technology Handbook*. NIIR Project Consultancy Services, 2005.

[150] A. N. Wilkinson and A. J. Ryan, *Polymer Processing and Structure Development*. Springer Netherlands, 1998.

[151] A. N. Martin, P. J. Sinko, and Y. Singh, *Martin's Physical Pharmacy and Pharmaceutical Sciences: Physical Chemical and Biopharmaceutical Principles in the Pharmaceutical Sciences*, Sixth Edit. Lippincott Williams & Wilkins, 2011.

[152] A. E. Siegman, *Lasers*. University Science Books, 1986.

[153] W. Schärtl, *Light Scattering from Polymer Solutions and Nanoparticle Dispersions*. Springer Berlin Heidelberg, 2010.

[154] J. M. Laskar, B. Raj, and J. Philip, "Path length tunable light-matter interaction in magnetic nano fluid based field-induced photonic crystal-glass structure," *New J. Phys.*, vol. 18, no. 10, pp. 1–13, 2016.

[155] S. Forget, "Optical Resonators and Gaussian Beams," *Laser and non-linear optics*, 2007. [Online]. Available: http://www.optique-ingenieur.org/en/courses/OPI_ang_M01_C03/co/Contenu_14.html.

[156] P. Fulda, "Laguerre-Gauss Beams for Test Mass Thermal Noise Reduction," in *Precision Interferometry in a New Shape: Higher-order Laguerre-Gauss Modes for Gravitational Wave Detection*, Cham: Springer International Publishing, 2014, pp. 17–39.

[157] C. S. Lee, S. W. Lee, and S. L. Chuang, "Plot of Modal Field Distribution in Rectangular and Circular Waveguides," *IEEE Trans. Microw. Theory Tech.*, vol. 33, no. 3, 1985.

[158] C. A. Balanis and E. Holzman, "Circular Waveguides," in *Encyclopedia of RF and Microwave Engineering*, John Wiley & Sons, Inc., 2005.

[159] B. Bhushan, "Surface Roughness Analysis and Measurement Techniques," in *Modern Tribology Handbook, Two Volume Set*, CRC Press, 2000.

[160] M. M. Schuler and I. W. Marison, "Real-time monitoring and control of microbial bioprocesses with focus on the specific growth rate: current state and perspectives.," *Appl. Microbiol. Biotechnol.*, vol. 94, no. 6, pp. 1469–82, Jun. 2012.

[161] S. Carneiro, E. C. Ferreira, and I. Rocha, "Metabolic responses to recombinant bioprocesses in Escherichia coli.," *J. Biotechnol.*, vol. 164, no. 3, pp. 396–408, Apr. 2013.

[162] D. M. Disley, P. R. Morrill, K. Sproule, and C. R. Lowe, “An optical biosensor for monitoring recombinant proteins in process media.,” *Biosens. Bioelectron.*, vol. 14, no. 5, pp. 481–93, May 1999.

[163] C. R. Lowe, C. A. B. Davidson, J. Blyth, A. J. Marshall, and A. P. James, “Holographic Sensors and their Production,” US 7443553 B2, 2004.

[164] A. K. Yetisen, H. Butt, F. da Cruz Vasconcellos, Y. Montelongo, C. a. B. Davidson, J. Blyth, L. Chan, J. B. Carmody, S. Vignolini, U. Steiner, J. J. Baumberg, T. D. Wilkinson, and C. R. Lowe, “Light-Directed Writing of Chemically Tunable Narrow-Band Holographic Sensors,” *Adv. Opt. Mater.*, vol. 2, pp. 250–254, Dec. 2014.

[165] Veeco Instruments Inc., “Dektak 8 Advanced Development Profiler Manual.” 2005.